

REPORT DOCUMENTATION PAGE

Public reporting burden for this collection of information is estimated to average 1 hour per response, including the time for reviewing the data needed, and completing and reviewing the collection of information. Send comments and suggestions for reducing this burden, to Washington Headquarters Services, Directorate for Information Operations and Reports, 1215 Jefferson Davis Highway, Suite 1204, Arlington, VA 22202-4302, and to the Office of Management and Budget, Paperwork Reduction Project (0704-0188) Washington, DC 20503.

0797

ring
1 of
1

1. AGENCY USE ONLY (Leave Blank)		2. REPORT DATE December, 1994	3. REPORT TYPE AND DATES COVERED Final
4. TITLE AND SUBTITLE USAF Summer Research Program - 1994 Graduate Student Research Program Final Reports, Volume 11, AEDC, FJSRL, and WHMC			5. FUNDING NUMBERS
6. AUTHORS Gary Moore			
7. PERFORMING ORGANIZATION NAME(S) AND ADDRESS(ES) Research and Development Labs, Culver City, CA			8. PERFORMING ORGANIZATION REPORT NUMBER
9. SPONSORING/MONITORING AGENCY NAME(S) AND ADDRESS(ES) AFOSR/NI 4040 Fairfax Dr, Suite 500 Arlington, VA 22203-1613			10. SPONSORING/MONITORING AGENCY REPORT NUMBER
11. SUPPLEMENTARY NOTES Contract Number: F49620-93-C-0063			
12a. DISTRIBUTION AVAILABILITY STATEMENT Approved for Public Release			12b. DISTRIBUTION CODE
13. ABSTRACT (Maximum 200 words) The United States Air Force Graduate Student Research Program (USAF- GSRP) is designed to introduce university, college, and technical institute graduate students to Air Force research. This is accomplished by the graduate students being selected on a nationally advertised competitive basis during the summer intersession period to perform research at Air Force Research Laboratory Technical Directorates and Air Force Air Logistics Centers. Each participant provided a report of their research, and these reports are consolidated into this annual report.			
14. SUBJECT TERMS AIR FORCE RESEARCH, AIR FORCE, ENGINEERING, LABORATORIES, REPORTS, SUMMER, UNIVERSITIES			15. NUMBER OF PAGES
			16. PRICE CODE
17. SECURITY CLASSIFICATION OF REPORT Unclassified	18. SECURITY CLASSIFICATION OF THIS PAGE Unclassified	19. SECURITY CLASSIFICATION OF ABSTRACT Unclassified	20. LIMITATION OF ABSTRACT UL

UNITED STATES AIR FORCE
SUMMER RESEARCH PROGRAM -- 1994
GRADUATE STUDENT RESEARCH PROGRAM FINAL REPORTS

VOLUME 11

ARNOLD ENGINEERING DEVELOPMENT CENTER
FRANK J. SEILER RESEARCH LABORATORY
WILFORD HALL MEDICAL CENTER

RESEARCH & DEVELOPMENT LABORATORIES
5800 Uplander Way
Culver City, CA 90230-6608

Program Director, RDL
Gary Moore

Program Manager, AFOSR
Major David Hart

Program Manager, RDL
Scott Licoscas

Program Administrator, RDL
Gwendolyn Smith

Program Administrator, RDL
Johnetta Thompson

Submitted to:

AIR FORCE OFFICE OF SCIENTIFIC RESEARCH
Bolling Air Force Base
Washington, D.C.
December 1994

DTIC QUALITY INSPECTED 4

19981204 043

PREFACE

Reports in this volume are numbered consecutively beginning with number 1. Each report is paginated with the report number followed by consecutive page numbers, e.g., 1-1, 1-2, 1-3; 2-1, 2-2, 2-3.

This document is one of a set of 16 volumes describing the 1994 AFOSR Summer Research Program. The following volumes comprise the set:

VOLUME

TITLE

1	Program Management Report
	<i>Summer Faculty Research Program (SFRP) Reports</i>
2A & 2B	Armstrong Laboratory
3A & 3B	Phillips Laboratory
4	Rome Laboratory
5A & 5B	Wright Laboratory
6	Arnold Engineering Development Center, Frank J. Seiler Research Laboratory, and Wilford Hall Medical Center
	<i>Graduate Student Research Program (GSRP) Reports</i>
7	Armstrong Laboratory
8	Phillips Laboratory
9	Rome Laboratory
10	Wright Laboratory
11	Arnold Engineering Development Center, Frank J. Seiler Research Laboratory, and Wilford Hall Medical Center
	<i>High School Apprenticeship Program (HSAP) Reports</i>
12A & 12B	Armstrong Laboratory
13	Phillips Laboratory
14	Rome Laboratory
15A&15B	Wright Laboratory
16	Arnold Engineering Development Center

GSRP FINAL REPORT TABLE OF CONTENTS

i-xiv

1. INTRODUCTION	1
2. PARTICIPATION IN THE SUMMER RESEARCH PROGRAM	2
3. RECRUITING AND SELECTION	3
4. SITE VISITS	4
5. HBCU/MI PARTICIPATION	4
6. SRP FUNDING SOURCES	5
7. COMPENSATION FOR PARTICIPANTS	5
8. CONTENTS OF THE 1994 REPORT	6

APPENDICIES:

A. PROGRAM STATISTICAL SUMMARY	A-1
B. SRP EVALUATION RESPONSES	B-1

GSRP FINAL REPORTS

SRP Final Report Table of Contents

Author	University/Institution Report Title	Armstrong Laboratory Directorate	Vol-Page
MS Jennifer M Ball	Wright State University , Dayton, , OH Relation Between Detection and Intelligibility in	AL/CFBA	7- 1
MR. Richard G Best	Southwest Missouri State Univ. , Springfield, , MO The Effects of Socialization on Vocational Aspirat	AL/HRMJ	7- 2
MR. Daniel A Brown	Grand Canyon University , Phoenix, , AZ Toward Modeling Higher Level Control Systems: Inc	AL/HRAU	7- 3
MS. Susan T Chitwood	Bowling Green State University , Bowling Green, , OH Further Explorations in Epistemological Space	AL/CFHP	7- 4
John E Cisneros	California State University , Los Angeles , CA Aurally Directed Search: A Comparison Between Syn	AL/CFBA	7- 5
Candace E Clary	Duke University , Durham , NC Intra-Ocular Laser Surgical Probe (ILSP) for Vitre	AL/OEO	7- 6
Robert M Colbert	Villanova University , Villanova , PA Finite Element Modeling of Manikin Necks for the A	AL/CFBV	7- 7
MR. Mark C Delgado	University of Georgia , Athens, , GA Determination of the Oxidative Redox Capacity of A	AL/EQC	7- 8
MR. Steven J Essler	North Dakota State University , Fargo, , ND Estimation of Four Arterial Vascular Parameters fo	AL/AOCIY	7- 9
Lawrence R Gottlob	Arizona State University , Tempe , AZ Accuracy Curves in a Location-Cuing Paradigm for V	AL/HRAT	7- 10
MS. Jennifer L Greenis	Michigan State University , East Lansing, , MI ITS Evaluation: A Review of the Past and Recommen	AL/HRTE	7- 11

SRP Final Report Table of Contents

Author	University/Institution Report Title	Armstrong Laboratory Directorate	Vol-Page
MS. Patricia M Harn	University of Washington , Seattle , WA Testing R-Wise: Reading and Writing in a Supporti	AL/HRTI	7- 12
Jason E Hill	University of Scranton , Scranton , PA Rapid Bacterial DNA Fingerprinting by the Polymer	AL/AOEL	7- 13
Mr. Rod J Hughes	Oregon Health Sciences University , Portland , OR Melatonin, Body Temperature and Sleep in Humans:	AL/CFTO	7- 14
Mr Roman G Longoria	Rice University , Houston , TX The Measurement of Work Experience: Issues and Im	AL/HRTE	7- 15
Uyen A Luong	Trinity University , San Antonio, , TX Millimeter Wave-Induced Hypertension Does Not Invo	AL/OER	7- 16
MR. Scott A Macbeth	University of Dayton , Dayton, , OH Using Electronic Brainstroming Tools to Visually	AL/HRG	7- 17
MR. Nicholas F Muto	University of Scranton , Scranton, , PA Rapid Bacterial DNA Fingerprinting by the Polymera	AL/AOEL	7- 18
Kevin P Nau	Kent State University , Kent , OH Proposal for the Establishment of a Comprehensive	AL/CFTF	7- 19
MR. Eric O Riise	Cal State Univ/Chico , Chico, , CA A Study of Interaction in Distance Learning	ALL/HRT	7- 20
Ms Heather E Roberts	Virginia Tech , Blacksburg , VA Gender and RAcial Equity of the Air Force Officer	AL/HRMM	7- 21
MR. Dale F Rucker	West Virginia University , Morgantown, , WV Improved Numerical Modeling of Groundwater Flow an	ALAEQC	7- 23

SRP Final Report Table of Contents

Author	University/Institution Report Title	Armstrong Laboratory Directorate	Vol-Page
Arthur M Ryan	Wright State University , Dayton , OH The Workload Assessment Monitor: Progress Towards	AL/CFHP	7- 24
Mark J Schroeder	North Dakota State University , Fargo , ND Arterial Elastance in the Maximization of External	AL/AOCIY	7- 25
MS. Katherine M Specht	Ohio State University , Columbus , OH Tactile Perception in a Virtual Environment	AL/CFBA	7- 26
MR. Joseph M Stauffer	University of Iowa , Iowa City , IA Predicting Pilot Training Success with Logistic or	AL/HRMA	7- 27
DR. Scott G Stavrou	University of Central Arkansas , Conway , AR Analysis of the Absorption and Metabolism of Trich	AL/OET	7- 28
MS. Virginia K Stromquist	Michigan Technological Inst. , Houghton , MI Solid Phase Microextraction as a Method for Quanti	AL/EQC	7- 29
MR. Eric S Wieser	Trinity University , San Antonio , TX Millimeter Wave-Induced Hypotension Does Not Invol	AL/OER	7- 30
MR. Gregory S Zinkel	Georgia Institute Technology , Atlanta , GA A Study of the Use Predictive Modeling for Dynamic	AL/AO	7- 31

SRP Final Report Table of Contents

Author	University/Institution Report Title	Phillips Laboratory Directorate	Vol-Page
MR. William W Brocklehurst	University of Cincinnati , Cincinnati , OH Effect of Dissolved Gases on the Discharge Coeffic	PL/RKFA	8- 1
MR. Stephen E Clarke	Utah State University , Logan , UT REPORT NOT AVAILABLE AT PRESS TIME	PL/VTRP	8- 2
Peyman Ensaf	University of Denver , Denver , CO Influence of Model Complexity and Aeroelastic Cont	PL/WSA	8- 3
MR. Frank S Gulczinski	University of Michigan , Ann Arbor , MI Interior Spectroscopic Investigation of Plasma Com	PL/RKCO	8- 4
MR. Derik C Herpfer	University of Cincinnati , Cincinnati , OH Drop Sizing of a Like-Impinging Element Injector I	PL/RKFA	8- 5
MR. Phillip N Hutton	Old Dominion University , Norfolk , VA Effectiveness of Thermionic Heat Pipe Module	PL/VTPN	8- 6
MR. Robert J Leiweke	Ohio State University , Columbus , OH A Single Temperature/Material Ablation Algorithm f	PL/WSP	8- 7
MR. John I Lipp	Michigan Technological Univ , Houghton , MI Estimation of Tilts Extended Images in the Presenc	PL/LIAE	8- 8
MR. Stephen A Luker	University of Alabama , Tuscaloosa , AL Determining Cloud Coverages for Input to Thermal C	PL/GPAA	8- 9
MR. Daniel T Moriarty	MIT , Cambridge , MA Laboratory Experiments with the Versatile Toroidal	PL/GPSG	8- 10
MR. Tim C Newell	University of North Texas , Denton , TX Synchronization Using Control Chaotic Diode Resona	PL/LIDN	8- 11

SRP Final Report Table of Contents

Author	University/Institution Report Title	Phillips Laboratory Directorate	Vol-Page
Jeffrey W Nicholson	University of New Mexico , Albuquerque , NM Relaxation Processes in Gain Switched Iodine Laser	PL/LIDB	8- 12
MR. Sean R Olin	Boston University , Boston, , MA An Investigation of Flight Characteristics of the	PL/SX	8- 13
MS. Janet M Petroski	Cal State Univ/Northridge , Northridge , CA Thermoluminescence of Simple Species in Solid Mole	PL/RKFE	8- 14
MR. Aaron J Ridley	University of Michigan , Ann Arbor, , MI The Dynamic Convection Reversal Boundary	PL/GPIA	8- 15
MR. Richard M Salasovich	University of Cincinnati , Cincinnati , OH Fabrication and Mechanical Testing of Mixed-Matrix	PL/VTSC	8- 16
MR. Kevin L Scales	University of New Mexico , Albuquerque , NM A Study of Numerical Methods in Atmospheric Light P	PL/LIMI	8- 17
Greg T Sharp	University of New Mexico , Albuquerque , NM Further Studies of High Temperature Cs-Ba Tacitron	PL/WSP	8- 18
MR. Joseph M Sorci	Massachusetts Inst. Technology , Cambridge, , MA A Study of Low Frequency Weak Turbulence in a Holl	PL/GPID	8- 19
Jonathan Stohs	University of New Mexico , Albuquerque , NM Radiation Exposure of Photonic Devices	PL/VTET	8- 20
MR. Jose Suarez	Florida Inst. of Technology , Patrick AFB, , FL Meteoroid & Orbital Debris Collision Hazard Analys	PL/WSC	8- 21
MR. Tony F von Sadvosky	University of Nevada, Reno , Reno, , NV PICLL: A Portable Parallel 3D PIC Code Impleme	PL/WSP	8- 22

SRP Final Report Table of Contents

Author	University/Institution Report Title	Rome Laboratory Directorate	Vol-Page
MR. John C Bertot	Syracuse University , Syracuse, , NY Transferring Technology Via the Internet	RL/XPP	9- 1
MR. Jerry M Couretas	University of Arizona , Tucson, , AZ Analysis of Extraction and Aggregation Techniques	RL/IRDO	9- 2
MR. Frederick L Crabbe	Univ California/Los Angeles , Los Angeles, , CA Using Self-Organization to Develop Vector Represen	RL/IRDO	9- 3
MS. Julie Hsu	Louisiana State University , Baton Rouge, , LA An Assignment Based Approach to Parallel-Machine S	RL/C3CA	9- 4
Andrew J Laffely	Univ. of Maine , Orono , ME Automatic Extraction of Drainage Network from Di	RL/IRRP	9- 5
MR. Daniel K Lee	Southern Illinois University , Carbondale , IL Mutual Coupling Effect of Square Microstrip Patch	RL/ERA	9- 6
Slawomir J Marcinkowski	Syracuse University , Syracuse , NY Transferring Technology Via the Internet	RL/XPP	9- 7
MR. Sean S O'Keefe	Cornell University , Ithaca, , NY Integration of Optoelectronic Devices with Microwa	RL/OCBP	9- 8
MR Robert L Popp	University of Connecticut , Storrs , CT Multisensor-Multitarget Data Fusion Using an S-Dim	RL/OCTM	9- 9
MR. Steven J Pratt	Syracuse University , Syracuse, , NY Analysis and Comparison of the Performance/Life Co	RL/C3AB	9- 10
Francis X Reichmeyer	Syracuse University , Syracuse , NY Local Area ATM Network Interfaces	RL/C3AB	9- 11

SRP Final Report Table of Contents

Author	University/Institution Report Title	Rome Laboratory Directorate	Vol-Page
MR. David H Sackett	Rochester Institute of Technol , Rochestter , NY Self-Sustained Pulsation and High Speed Optical Ne	RL/OCPA _____	9- 12
ME. Paul E Shames	Univiersity of Cal/San Diego , San Diego, , CA A Study of High Speed Polarization Rotators for Us	RL/IRAP _____	9- 13
Terrence W Towe	Univ of Arkansas-Fayetteville , Fayetteville , AR REPORT NOT AVAILABLE AT PRESS TIME	RL/ERX _____	9- 14
Okechukwu C Ugweje	Florida Atlantic University , Boca Raton, , FL A Program Plan for Transmitting High-Data-Rate ATM	RL/C3BA _____	9- 15
MR. Martin A Villarica	Syracuse University , Syracuse, , NY A Study of the Application of Fractuals and Kineti	RL/ERDR _____	9- 16
Stanley J Wenndt	Colorado State University , Fort Collins , CO An Investigation of Cepstrum Based Speaker Identif	RL/IRAA _____	9- 17

SRP Final Report Table of Contents

Author	University/Institution Report Title	Wright Laboratory Directorate	Vol-Page
MS. Terri L Alexander	University of Central Florida , Orlando, , FL Design of Spectroscopic Material-Characterization	WL/MNGS	10- 1
MR. Joseph L Binford, III	University of Dayton , Dayton, , OH Thermal Stability Apparatus Design and Error Analy	WL/MLPO	10- 2
MR Jonathan A Bishop	University of Oklahoma , Norman, , OK Influence of Model Complexity and Aeroelastic Cons	WL/FIBR	10- 3
MR. Steven P Burns	Purdue University , West Lafayette, , IN The Use of Pressure Sensitive Paints on Rotating M	WL/POTF	10- 4
MR. Lance H Carter	University of Texas/Austin , Austin , TX Gain-Scheduled Bank-to-Turn Autopilot Design Using	WL/MNAG	10- 5
MR. Peng Chen	University of North Texas , Denton , TX Synthesis & Characterization of Lanthanum Phosphat	WL/MLLM	10- 6
MS. Lora A Cintavey	University of Cincinnati , Cincinnati , OH Processing and Characterization of Nonlinear Optic	WL/MLBP	10- 7
MR. William K Cope	University of Illinois/Urbana , Urbana, , IL Assessment of Gasp for the Simulation of Scramjet	WL/POPT	10- 8
Mike J Cutbirth	Oklahoma State University , Stillwater , OK A Study of the Heat Transfer for the High Flux Hea	WL/POOS	10- 9
Craig M Files	University of Idaho , Moscow , ID Using a Search Heuristic in an NP-Complete Problem	WL/AART-	10- 10
MR Edward M Friel	University of Dayton , Dayton , OH Direction Finding in the Presence of a Near Field	WL/AARM	10- 11

SRP Final Report Table of Contents

Author	University/Institution Report Title	Wright Laboratory Directorate	Vol-Page
MR. Keith D Grinstead	Purdue University , West Lafayette, , IN Obtaininnng the Correction Factors for Two-Photon I	WL/POSF _____	10- 12
MR. Jason J Hugenroth	Louisiana State University , Baton Rouge, , LA A Research Plan for Evaluating Wave Gun as a Low-L	WL/MNAA _____	10- 13
MR. Andrew Kager	University of Central Florida , Orlando, , FL A Numerical Study of the Effect of Base and Collec	WL/ELRA _____	10- 14
MR. John C Lewis	University of Kentucky , Lexington , KY A Theory for the Testing of Materials Under Combin	WL/MNM _____	10- 15
MR. Kenneth P Luke	Wright State University , Dayton, , OH Three-Dimensional Modeling Using a Calibrated Came	WL/AARF- _____	10- 16
John D Mai	Univ of Calif-Los Angeles , Los Angeles , CA Preliminary Characterization and Calibration of Mi	WL/FIME _____	10- 17
MR Mark A Manzardo	Univ of Alabama-Huntsville , Huntsville , AL High Speed Imaging Infrared Polarimetry	WL/MNGS _____	10- 18
MR. David B Maring	University of FloridaFL , Gainesville, , FL Fabrication and White-Light Characterization of An	WL/MNG _____	10- 19
MR. Joseph R Miramonti	University of Missouri/Columbi , Columbia, a , MO Scanning Image Aleghbra Networks for Vehicle Identi	WL/MNGA _____	10- 20
MS. Jennifer S Naylor	Auburn University , Auburn, , AL Automation Control Issues in the Development of an	WL/MNAG _____	10- 21
MR. Ned F O'Brien	University of Dayton , Dayton, , OH A Study of RF Fiber Optic Communication Link Techn	WL/AAAI- _____	10- 22

SRP Final Report Table of Contents

Author	University/Institution Report Title	Wright Laboratory Directorate	Vol-Page
MR. Tae W Park	Univ of Illinois/Chicago , Chicago , IL A Numerical Study of DropleVortx Interactions in a	WL/POSF	10- 23
MS Margaret F Pinnell	University of Dayton , Dayton , OH A Parametric Study of the Factors Affecting the Op	WL/MLBM	10- 24
MR. Seth M Pinsky	Oregon Grad Inst. Sci & Tech , Portland , OR S-Parameter Measurements on a GaAsFET Variable-Gai	WL/ELM	10- 25
MR. David A Ress	Tennessee Technological Univ , Cookeville , TN Modifications To The Thinker Discovery System	WL/MLIM	10- 26
Mohammed A Samad	University of New Orleans , New Orleans , LA A Study of Delamination Damage and Energy Exchange	WL/FIVS	10- 27
MR. Robert W Slater III	University of Cincinnati , Cincinnati , OH Low-Velocity Impact of Moisture-Conditioned Lamina	WL/FIBE	10- 28
Ed P Socci	University of Virginia , Charlottesville , VA X-ray Diffraction Study of Siloxane/Cholestrol Bas	WL/MLPO	10- 29
MR. Edward A Thompson	University of Cincinnati , Cincinnati , OH Annealed Fuzzy Control for a Self-Tuning Piezolect	WL/FIBG	10- 30
MR. Brent A Veltkamp	Michigan State University , East Lansing , MI Pixel Plane Design for SIMD Graphic Processor	WL/ELED	10- 31
MR. Christopher C Vogt	University of Cal San Diego , San Diego , CA The Combinatorics of Function Decomposition and Ap	WL/AART-	10- 32
MR. Ralph J Volino	University of Minnesota , Minneapolis , MN Documentation of Boundary Layer Characteristics fo	WL/POTT	10- 33

SRP Final Report Table of Contents

Author	University/Institution Report Title	Wright Laboratory Directorate	Vol-Page
MR. Jeffrey A Walrath	University of Cincinnati, Cincinnati, OH Integration of Champ Firm Macro Library with DSS	WL/AAAT- _____	10- 34

SRP Final Report Table of Contents

Author	University/Institution Report Title	Arnold Engineering Development Center Directorate	Vol-Page
MR. William A Alford	Univ. Tennessee Space Inst. , Tullahoma, , TN Design of Testing and Debugging Software for C31 N	Sverdrup	11- 1
MR. Brian C DeAngelis	University of Illinois/Urbana- , Urbana , IL Performance and Validation Studies of the Kiva-II	SVERDRU	11- 2
MR. Harold D Helsley	Univ Tennessee Space Inst , Tullahoma, , TN Development of a Monitor for a Multi-Processor Net	Sverdrup	11- 3
MR. Christopher W Humphres	University of Alabama , Tuscaloosa, , AL Parallelization of Chimera Utilizing PVM	Calspan	11- 4
MR. Curtis S Mashburn	Universtity of Tennessee Space , Tullahoma, , TN Prediction of the Performance of a 7-Stage Axial-F	Sverdrup	11- 5
MR. William S Meredith	Univ of Tennesse Sp. Inst. , Tullhoma, , TN REPORT NOT AVAILABLE AT PRESS TIME	Calspan	11- 6
MR. Michael S Moore	Vanderbilt University , Nashville , TN A Model Based Real Time Image Processing System	SVERDRU	11- 7
MR David T Pratt	Univ of Tennessee Space Inst , Tullahoma , TN Analysis and Comparison of the Performance/Life Co	Sverdrup	11- 8
MR. David B Underhill	Univ of Tenn Space Inst , Tullahoma , TN Application of Vorticity Confinement to a Delta Wi	Calspan	11- 9

SRP Final Report Table of Contents

Author	University/Institution Report Title	Frank J Seiler Research Laboratory Directorate	Vol-Page
MR. Christian S Bahn	Colorado School of Mines , Golden, , CO A Theoretical Study of Lithium and Molten Salt Gra	FJSRL/NC _____	11- 10
MR. Antonio M Ferreira	Memphis State University , Memphis, , TN Theoretical Investigations of the NLO Properties o	FJSRL/NC _____	11- 11
MS Joan Fuller	University of Alabama , Tuscaloosa , AL Investigations of Carbon Materials in Alkali Metal	FJSRL/CD _____	11- 12

SRP Final Report Table of Contents

Author	University/Institution	Wilford Hall Medical Center	Vol-Page
	Report Title	Directorate	
MR Ramachandra P Tummala	University of Miami , Coral Gables , FL	WHMC/RD	11- 13
	Effects of Temperature on Various Hematological P		

1. INTRODUCTION

The Summer Research Program (SRP), sponsored by the Air Force Office of Scientific Research (AFOSR), offers paid opportunities for university faculty, graduate students, and high school students to conduct research in U.S. Air Force research laboratories nationwide during the summer.

Introduced by AFOSR in 1978, this innovative program is based on the concept of teaming academic researchers with Air Force scientists in the same disciplines using laboratory facilities and equipment not often available at associates' institutions.

AFOSR also offers its research associates an opportunity, under the Summer Research Extension Program (SREP), to continue their AFOSR-sponsored research at their home institutions through the award of research grants. In 1994 the maximum amount of each grant was increased from \$20,000 to \$25,000, and the number of AFOSR-sponsored grants decreased from 75 to 60. A separate annual report is compiled on the SREP.

The Summer Faculty Research Program (SFRP) is open annually to approximately 150 faculty members with at least two years of teaching and/or research experience in accredited U.S. colleges, universities, or technical institutions. SFRP associates must be either U.S. citizens or permanent residents.

The Graduate Student Research Program (GSRP) is open annually to approximately 100 graduate students holding a bachelor's or a master's degree; GSRP associates must be U.S. citizens enrolled full time at an accredited institution.

The High School Apprentice Program (HSAP) annually selects about 125 high school students located within a twenty mile commuting distance of participating Air Force laboratories.

The numbers of projected summer research participants in each of the three categories are usually increased through direct sponsorship by participating laboratories.

AFOSR's SRP has well served its objectives of building critical links between Air Force research laboratories and the academic community, opening avenues of communications and forging new research relationships between Air Force and academic technical experts in areas of national interest; and strengthening the nation's efforts to sustain careers in science and engineering. The success of the SRP can be gauged from its growth from inception (see Table 1) and from the favorable responses the 1994 participants expressed in end-of-tour SRP evaluations (Appendix B).

AFOSR contracts for administration of the SRP by civilian contractors. The contract was first awarded to Research & Development Laboratories (RDL) in September 1990. After completion of the 1990 contract, RDL won the recompetition for the basic year and four 1-year options.

2. PARTICIPATION IN THE SUMMER RESEARCH PROGRAM

The SRP began with faculty associates in 1979; graduate students were added in 1982 and high school students in 1986. The following table shows the number of associates in the program each year.

Table 1: SRP Participation, by Year

YEAR	Number of Participants			TOTAL
	SFRP	GSRP	HSAP	
1979	70			70
1980	87			87
1981	87			87
1982	91	17		108
1983	101	53		154
1984	152	84		236
1985	154	92		246
1986	158	100	42	300
1987	159	101	73	333
1988	153	107	101	361
1989	168	102	103	373
1990	165	121	132	418
1991	170	142	132	444
1992	185	121	159	464
1993	187	117	136	440
1994	192	117	133	442

Beginning in 1993, due to budget cuts, some of the laboratories weren't able to afford to fund as many associates as in previous years; in one case a laboratory did not fund any additional associates. However, the table shows that, overall, the number of participating associates increased this year because two laboratories funded more associates than they had in previous years.

3. RECRUITING AND SELECTION

The SRP is conducted on a nationally advertised and competitive-selection basis. The advertising for faculty and graduate students consisted primarily of the mailing of 8,000 44-page SRP brochures to chairpersons of departments relevant to AFOSR research and to administrators of grants in accredited universities, colleges, and technical institutions. Historically Black Colleges and Universities (HBCUs) and Minority Institutions (MIs) were included. Brochures also went to all participating USAF laboratories, the previous year's participants, and numerous (over 600 annually) individual requesters.

Due to a delay in awarding the new contract, RDL was not able to place advertisements in any of the following publications in which the SRP is normally advertised: *Black Issues in Higher Education*, *Chemical & Engineering News*, *IEEE Spectrum* and *Physics Today*.

High school applicants can participate only in laboratories located no more than 20 miles from their residence. Tailored brochures on the HSAP were sent to the head counselors of 180 high schools in the vicinity of participating laboratories, with instructions for publicizing the program in their schools. High school students selected to serve at Wright Laboratory's Armament Directorate (Eglin Air Force Base, Florida) serve eleven weeks as opposed to the eight weeks normally worked by high school students at all other participating laboratories.

Each SFRP or GSRP applicant is given a first, second, and third choice of laboratory. High school students who have more than one laboratory or directorate near their homes are also given first, second, and third choices.

Laboratories make their selections and prioritize their nominees. AFOSR then determines the number to be funded at each laboratory and approves laboratories' selections.

Subsequently, laboratories use their own funds to sponsor additional candidates. Some selectees do not accept the appointment, so alternate candidates are chosen. This multi-step selection procedure results in some candidates being notified of their acceptance after scheduled deadlines. The total applicants and participants for 1994 are shown in this table.

Table 2: 1994 Applicants and Participants

PARTICIPANT CATEGORY	TOTAL APPLICANTS	SELECTEES	DECLINING SELECTEES
SFRP	600	192	30
(HBCU/MI)	(90)	(16)	(7)
GSRP	322	117	11
(HBCU/MI)	(11)	(6)	(0)
HSAP	562	133	14
TOTAL	1484	442	55

4. SITE VISITS

During June and July of 1994, representatives of both AFOSR/NI and RDL visited each participating laboratory to provide briefings, answer questions, and resolve problems for both laboratory personnel and participants. The objective was to ensure that the SRP would be as constructive as possible for all participants. Both SRP participants and RDL representatives found these visits beneficial. At many of the laboratories, this was the only opportunity for all participants to meet at one time to share their experiences and exchange ideas.

5. HISTORICALLY BLACK COLLEGES AND UNIVERSITIES AND MINORITY INSTITUTIONS (HBCU/MIs)

In previous years, an RDL program representative visited from seven to ten different HBCU/MIs to promote interest in the SRP among the faculty and graduate students. Due to the late contract award date (January 1994) no time was available to visit HBCU/MIs this past year.

In addition to RDL's special recruiting efforts, AFOSR attempts each year to obtain additional funding or use leftover funding from cancellations the past year to fund HBCU/MI associates. This year, seven HBCU/MI SFRPs declined after they were selected. The following table records HBCU/MI participation in this program.

Table 3: SRP HBCU/MI Participation, by Year

YEAR	SFRP		GSRP	
	Applicants	Participants	Applicants	Participants
1985	76	23	15	11
1986	70	18	20	10
1987	82	32	32	10
1988	53	17	23	14
1989	39	15	13	4
1990	43	14	17	3
1991	42	13	8	5
1992	70	13	9	5
1993	60	13	6	2
1994	90	16	11	6

6. SRP FUNDING SOURCES

Funding sources for the 1994 SRP were the AFOSR-provided slots for the basic contract and laboratory funds. Funding sources by category for the 1994 SRP selected participants are shown here.

Table 4: 1994 SRP Associate Funding

FUNDING CATEGORY	SFRP	GSRP	HSAP
AFOSR Basic Allocation Funds	150	98 ^{*1}	121 ^{*2}
USAF Laboratory Funds	37	19	12
HBCU/MI By AFOSR (Using Procured Addn'l Funds)	5	0	0
TOTAL	192	117	133

*1 - 100 were selected, but two canceled too late to be replaced.

*2 - 125 were selected, but four canceled too late to be replaced.

7. COMPENSATION FOR PARTICIPANTS

Compensation for SRP participants, per five-day work week, is shown in this table.

Table 5: 1994 SRP Associate Compensation

PARTICIPANT CATEGORY	1991	1992	1993	1994
Faculty Members	\$690	\$718	\$740	\$740
Graduate Student (Master's Degree)	\$425	\$442	\$455	\$455
Graduate Student (Bachelor's Degree)	\$365	\$380	\$391	\$391
High School Student (First Year)	\$200	\$200	\$200	\$200
High School Student (Subsequent Years)	\$240	\$240	\$240	\$240

The program also offered associates whose homes were more than 50 miles from the laboratory an expense allowance (seven days per week) of \$50/day for faculty and \$37/day for graduate students.

Transportation to the laboratory at the beginning of their tour and back to their home destinations at the end was also reimbursed for these participants. Of the combined SFRP and GSRP associates, 58% (178 out of 309) claimed travel reimbursements at an average round-trip cost of \$860.

Faculty members were encouraged to visit their laboratories before their summer tour began. All costs of these orientation visits were reimbursed. Forty-one percent (78 out of 192) of faculty associates took orientation trips at an average cost of \$498. Many faculty associates noted on their evaluation forms that due to the late notice of acceptance into the 1994 SRP (caused by the late award in January 1994 of the contract) there wasn't enough time to attend an orientation visit prior to their tour start date. In 1993, 58 % of SFRP associates took orientation visits at an average cost of \$685.

Program participants submitted biweekly vouchers countersigned by their laboratory research focal point, and RDL issued paychecks so as to arrive in associates' hands two weeks later.

HSAP program participants were considered actual RDL employees, and their respective state and federal income tax and Social Security were withheld from their paychecks. By the nature of their independent research, SFRP and GSRP program participants were considered to be consultants or independent contractors. As such, SFRP and GSRP associates were responsible for their own income taxes, Social Security, and insurance.

8. CONTENTS OF THE 1994 REPORT

The complete set of reports for the 1994 SRP includes this program management report augmented by fifteen volumes of final research reports by the 1994 associates as indicated below:

Table 6: 1994 SRP Final Report Volume Assignments

LABORATORY	VOLUME		
	SFRP	GSRP	HSAP
Armstrong	2	7	12
Phillips	3	8	13
Rome	4	9	14
Wright	5A, 5B	10	15
AEDC, FJSRL, WHMC	6	11	16

AEDC = Arnold Engineering Development Center
FJSRL = Frank J. Seiler Research Laboratory
WHMC = Wilford Hall Medical Center

APPENDIX A – PROGRAM STATISTICAL SUMMARY

A. Colleges/Universities Represented

Selected SFRP and GSRP associates represent 158 different colleges, universities, and institutions.

B. States Represented

SFRP -Applicants came from 46 states plus Washington D.C. and Puerto Rico. Selectees represent 40 states.

GSRP - Applicants came from 46 states and Puerto Rico. Selectees represent 34 states.

HSAP - Applicants came from fifteen states. Selectees represent ten states.

C. Academic Disciplines Represented

The academic disciplines of the combined 192 SFRP associates are as follows:

Electrical Engineering	22.4%
Mechanical Engineering	14.0%
Physics: General, Nuclear & Plasma	12.2%
Chemistry & Chemical Engineering	11.2%
Mathematics & Statistics	8.1%
Psychology	7.0%
Computer Science	6.4%
Aerospace & Aeronautical Engineering	4.8%
Engineering Science	2.7%
Biology & Inorganic Chemistry	2.2%
Physics: Electro-Optics & Photonics	2.2%
Communication	1.6%
Industrial & Civil Engineering	1.6%
Physiology	1.1%
Polymer Science	1.1%
Education	0.5%
Pharmaceutics	0.5%
Veterinary Medicine	0.5%
TOTAL	100%

Table A-1. Total Participants

Number of Participants	
SFRP	192
GSRP	117
HSAP	133
TOTAL	442

Table A-2. Degrees Represented

Degrees Represented			
	SFRP	GSRP	TOTAL
Doctoral	189	0	189
Master's	3	47	50
Bachelor's	0	70	70
TOTAL	192	117	309

Table A-3. SFRP Academic Titles

Academic Titles	
Assistant Professor	74
Associate Professor	63
Professor	44
Instructor	5
Chairman	1
Visiting Professor	1
Visiting Assoc. Prof.	1
Research Associate	3
TOTAL	192

Table A-4. Source of Learning About SRP

SOURCE	SFRP		GSRP	
	Applicants	Selectees	Applicants	Selectees
Applied/participated in prior years	26 %	37 %	10 %	13 %
Colleague familiar with SRP	19 %	17 %	12 %	12 %
Brochure mailed to institution	32 %	18 %	19 %	12 %
Contact with Air Force laboratory	15 %	24 %	9 %	12 %
Faculty Advisor (GSRPs Only)	--	--	39 %	43 %
Other source	8 %	4 %	11 %	8 %
TOTAL	100 %	100 %	100 %	100 %

Table A-5. Ethnic Background of Applicants and Selectees

	SFRP		GSRP		HSAP	
	Applicants	Selectees	Applicants	Selectees	Applicants	Selectees
American Indian or Native Alaskan	0.2 %	0 %	1 %	0 %	0.4 %	0 %
Asian/Pacific Islander	30 %	20 %	6 %	8 %	7 %	10 %
Black	4 %	1.5 %	3 %	3 %	7 %	2 %
Hispanic	3 %	1.9 %	4 %	4.5 %	11 %	8 %
Caucasian	51 %	63 %	77 %	77 %	70 %	75 %
Preferred not to answer	12 %	14 %	9 %	7 %	4 %	5 %
TOTAL	100 %	100 %	100 %	100 %	99 %	100 %

Table A-6. Percentages of Selectees receiving their 1st, 2nd, or 3rd Choices of Directorate

	1st Choice	2nd Choice	3rd Choice	Other Than Their Choice
SFRP	70 %	7 %	3 %	20 %
GSRP	76 %	2 %	2 %	20 %

APPENDIX B – SRP EVALUATION RESPONSES

1. OVERVIEW

Evaluations were completed and returned to RDL by four groups at the completion of the SRP. The number of respondents in each group is shown below.

Table B-1. Total SRP Evaluations Received

Evaluation Group	Responses
SFRP & GSRPs	275
HSAPs	116
USAF Laboratory Focal Points	109
USAF Laboratory HSAP Mentors	54

All groups indicate near-unanimous enthusiasm for the SRP experience.

Typical comments from 1994 SRP associates are:

"[The SRP was an] excellent opportunity to work in state-of-the-art facility with top-notch people."

"[The SRP experience] enabled exposure to interesting scientific application problems; enhancement of knowledge and insight into 'real-world' problems."

"[The SRP] was a great opportunity for resourceful and independent faculty [members] from small colleges to obtain research credentials."

"The laboratory personnel I worked with are tremendous, both personally and scientifically. I cannot emphasize how wonderful they are."

"The one-on-one relationship with my mentor and the hands on research experience improved [my] understanding of physics in addition to improving my library research skills. Very valuable for [both] college and career!"

Typical comments from laboratory focal points and mentors are:

"This program [AFOSR - SFRP] has been a 'God Send' for us. Ties established with summer faculty have proven invaluable."

"Program was excellent from our perspective. So much was accomplished that new options became viable "

"This program managed to get around most of the red tape and 'BS' associated with most Air Force programs. Good Job!"

"Great program for high school students to be introduced to the research environment. Highly educational for others [at laboratory]."

"This is an excellent program to introduce students to technology and give them a feel for [science/engineering] career fields. I view any return benefit to the government to be 'icing on the cake' and have usually benefitted."

The summarized recommendations for program improvement from both associates and laboratory personnel are listed below (Note: basically the same as in previous years.)

- A. Better preparation on the labs' part prior to associates' arrival (i.e., office space, computer assets, clearly defined scope of work).
- B. Laboratory sponsor seminar presentations of work conducted by associates, and/or organized social functions for associates to collectively meet and share SRP experiences.
- C. Laboratory focal points collectively suggest more AFOSR allocated associate positions, so that more people may share in the experience.
- D. Associates collectively suggest higher stipends for SRP associates.
- E. Both HSAP Air Force laboratory mentors and associates would like the summer tour extended from the current 8 weeks to either 10 or 11 weeks; the groups state it takes 4-6 weeks just to get high school students up-to-speed on what's going on at laboratory. (Note: this same argument was used to raise the faculty and graduate student participation time a few years ago.)

2. 1994 USAF LABORATORY FOCAL POINT (LFP) EVALUATION RESPONSES

The summarized results listed below are from the 109 LFP evaluations received.

1. LFP evaluations received and associate preferences:

Table B-2. Air Force LFP Evaluation Responses (By Type)

Lab	Evals Recv'd	How Many Associates Would You Prefer To Get ?								(% Response)			
		SFRP				GSRP (w/Univ Professor)				GSRP (w/o Univ Professor)			
		0	1	2	3+	0	1	2	3+	0	1	2	3+
AEDC	10	30	50	0	20	50	40	0	10	40	60	0	0
AL	44	34	50	6	9	54	34	12	0	56	31	12	0
FJSRL	3	33	33	33	0	67	33	0	0	33	67	0	0
PL	14	28	43	28	0	57	21	21	0	71	28	0	0
RL	3	33	67	0	0	67	0	33	0	100	0	0	0
WHMC	1	0	0	100	0	0	100	0	0	0	100	0	0
WL	46	15	61	24	0	56	30	13	0	76	17	6	0
Total	121	25%	43%	27%	4%	50%	37%	11%	1%	54%	43%	3%	0%

LFP Evaluation Summary. The summarized responses, by laboratory, are listed on the following page. LFPs were asked to rate the following questions on a scale from 1 (below average) to 5 (above average).

2. LFPs involved in SRP associate application evaluation process:
 - a. Time available for evaluation of applications:
 - b. Adequacy of applications for selection process:
3. Value of orientation trips:
4. Length of research tour:
5.
 - a. Benefits of associate's work to laboratory:
 - b. Benefits of associate's work to Air Force:
6.
 - a. Enhancement of research qualifications for LFP and staff:
 - b. Enhancement of research qualifications for SFRP associate:
 - c. Enhancement of research qualifications for GSRP associate:
7.
 - a. Enhancement of knowledge for LFP and staff:
 - b. Enhancement of knowledge for SFRP associate:
 - c. Enhancement of knowledge for GSRP associate:
8. Value of Air Force and university links:
9. Potential for future collaboration:
10.
 - a. Your working relationship with SFRP:
 - b. Your working relationship with GSRP:
11. Expenditure of your time worthwhile:

(Continued on next page)

12. Quality of program literature for associate:
 13. a. Quality of RDL's communications with you:
 b. Quality of RDL's communications with associates:
 14. Overall assessment of SRP:

Laboratory Focal Point Responses to above questions							
	<i>AEDC</i>	<i>AL</i>	<i>FJSRL</i>	<i>PL</i>	<i>RL</i>	<i>WHMC</i>	<i>WL</i>
<i># Evals Recv'd</i>	10	32	3	14	3	1	46
<i>Question #</i>							
2	90 %	62 %	100 %	64 %	100 %	100 %	83 %
2a	3.5	3.5	4.7	4.4	4.0	4.0	3.7
2b	4.0	3.8	4.0	4.3	4.3	4.0	3.9
3	4.2	3.6	4.3	3.8	4.7	4.0	4.0
4	3.8	3.9	4.0	4.2	4.3	NO ENTRY	4.0
5a	4.1	4.4	4.7	4.9	4.3	3.0	4.6
5b	4.0	4.2	4.7	4.7	4.3	3.0	4.5
6a	3.6	4.1	3.7	4.5	4.3	3.0	4.1
6b	3.6	4.0	4.0	4.4	4.7	3.0	4.2
6c	3.3	4.2	4.0	4.5	4.5	3.0	4.2
7a	3.9	4.3	4.0	4.6	4.0	3.0	4.2
7b	4.1	4.3	4.3	4.6	4.7	3.0	4.3
7c	3.3	4.1	4.5	4.5	4.5	5.0	4.3
8	4.2	4.3	5.0	4.9	4.3	5.0	4.7
9	3.8	4.1	4.7	5.0	4.7	5.0	4.6
10a	4.6	4.5	5.0	4.9	4.7	5.0	4.7
10b	4.3	4.2	5.0	4.3	5.0	5.0	4.5
11	4.1	4.5	4.3	4.9	4.7	4.0	4.4
12	4.1	3.9	4.0	4.4	4.7	3.0	4.1
13a	3.8	2.9	4.0	4.0	4.7	3.0	3.6
13b	3.8	2.9	4.0	4.3	4.7	3.0	3.8
14	4.5	4.4	5.0	4.9	4.7	4.0	4.5

3. 1994 SFRP & GSRP EVALUATION RESPONSES

The summarized results listed below are from the 275 SFRP/GSRP evaluations received.

Associates were asked to rate the following questions on a scale from
1 (below average) to 5 (above average)

1. The match between the laboratories research and your field:	4.6
2. Your working relationship with your LFP:	4.8
3. Enhancement of your academic qualifications:	4.4
4. Enhancement of your research qualifications:	4.5
5. Lab readiness for you: LFP, task, plan:	4.3
6. Lab readiness for you: equipment, supplies, facilities:	4.1
7. Lab resources:	4.3
8. Lab research and administrative support:	4.5
9. Adequacy of brochure and associate handbook:	4.3
10. RDL communications with you:	4.3
11. Overall payment procedures:	3.8
12. Overall assessment of the SRP:	4.7
13. a. Would you apply again?	Yes: 85 %
b. Will you continue this or related research?	Yes: 95 %
14. Was length of your tour satisfactory?	Yes: 86 %
15. Percentage of associates who engaged in:	
a. Seminar presentation:	52 %
b. Technical meetings:	32 %
c. Social functions:	03 %
d. Other	01 %

16. Percentage of associates who experienced difficulties in:

- | | |
|---------------------|------|
| a. Finding housing: | 12 % |
| b. Check Cashing: | 03 % |

17. Where did you stay during your SRP tour?

- | | |
|----------------------|------|
| a. At Home: | 20 % |
| b. With Friend: | 06 % |
| c. On Local Economy: | 47 % |
| d. Base Quarters: | 10 % |

THIS SECTION FACULTY ONLY:

18. Were graduate students working with you? Yes: 23 %

19. Would you bring graduate students next year? Yes: 56 %

20. Value of orientation visit:

- | | |
|-----------------|------|
| Essential: | 29 % |
| Convenient: | 20 % |
| Not Worth Cost: | 01 % |
| Not Used: | 34 % |

THIS SECTION GRADUATE STUDENTS ONLY:

21. Who did you work with:

- | | |
|-----------------------|------|
| University Professor: | 18 % |
| Laboratory Scientist: | 54 % |

4. 1994 USAF LABORATORY HSAP MENTOR EVALUATION RESPONSES

The summarized results listed below are from the 54 mentor evaluations received.

1. Mentor apprentice preferences:

Table B-3. Air Force Mentor Responses

		How Many Apprentices Would You Prefer To Get ?			
		<i>HSAP Apprentices Preferred</i>			
<i>Laboratory</i>	<i># Evals Recv'd</i>	<i>0</i>	<i>1</i>	<i>2</i>	<i>3+</i>
AEDC	6	0	100	0	0
AL	17	29	47	6	18
PL	9	22	78	0	0
RL	4	25	75	0	0
WL	18	22	55	17	6
Total	54	20%	71%	5%	5%

Mentors were asked to rate the following questions on a scale from
1 (below average) to 5 (above average)

2. Mentors involved in SRP apprentice application evaluation process:
 - a. Time available for evaluation of applications:
 - b. Adequacy of applications for selection process:
3. Laboratory's preparation for apprentice:
4. Mentor's preparation for apprentice:
5. Length of research tour:
6. Benefits of apprentice's work to U.S. Air force:
7. Enhancement of academic qualifications for apprentice:
8. Enhancement of research skills for apprentice:
9. Value of U.S. Air Force/high school links:
10. Mentor's working relationship with apprentice:
11. Expenditure of mentor's time worthwhile:
12. Quality of program literature for apprentice:
13.
 - a. Quality of RDL's communications with mentors:
 - b. Quality of RDL's communication with apprentices:
14. Overall assessment of SRP:

	<i>AEDC</i>	<i>AL</i>	<i>PL</i>	<i>RL</i>	<i>WL</i>
<i># Evals Recv'd</i>	6	17	9	4	18
<i>Question #</i>					
2	100 %	76 %	56 %	75 %	61 %
2a	4.2	4.0	3.1	3.7	3.5
2b	4.0	4.5	4.0	4.0	3.8
3	4.3	3.8	3.9	3.8	3.8
4	4.5	3.7	3.4	4.2	3.9
5	3.5	4.1	3.1	3.7	3.6
6	4.3	3.9	4.0	4.0	4.2
7	4.0	4.4	4.3	4.2	3.9
8	4.7	4.4	4.4	4.2	4.0
9	4.7	4.2	3.7	4.5	4.0
10	4.7	4.5	4.4	4.5	4.2
11	4.8	4.3	4.0	4.5	4.1
12	4.2	4.1	4.1	4.8	3.4
13a	3.5	3.9	3.7	4.0	3.1
13b	4.0	4.1	3.4	4.0	3.5
14	4.3	4.5	3.8	4.5	4.1

5. 1994 HSAP EVALUATION RESPONSES

The summarized results listed below are from the 116 HSAP evaluations received.

HSAP apprentices were asked to rate the following questions on a scale from
1 (below average) to 5 (above average)

1. Match of lab research to you interest:	3.9
2. Apprentices working relationship with their mentor and other lab scientists:	4.6
3. Enhancement of your academic qualifications:	4.4
4. Enhancement of your research qualifications:	4.1
5. Lab readiness for you: mentor, task, work plan	3.7
6. Lab readiness for you: equipment supplies facilities	4.3
7. Lab resources: availability	4.3
8. Lab research and administrative support:	4.4
9. Adequacy of RDL's apprentice handbook and administrative materials:	4.0
10. Responsiveness of RDL's communications:	3.5
11. Overall payment procedures:	3.3
12. Overall assessment of SRP value to you:	4.5
13. Would you apply again next year?	Yes: 88%
14. Was length of SRP tour satisfactory?	Yes: 78%
15. Percentages of apprentices who engaged in:	
a. Seminar presentation:	48%
b. Technical meetings:	23%
c. Social functions:	18%

Design of Testing and Debugging Software for C31 NPE Board

W. Anthony Alford
Graduate Research Assistant
Department of Electrical and Computer Engineering

University of Tennessee Space Institute
Tullahoma, TN 37388

Final Report for:
Graduate Student Research Program
Arnold Engineering Development Center

Sponsored by:
Air Force Office of Scientific Research
Bolling Air Force Base, DC

and

Arnold Engineering Development Center

August 1994

Design of Testing and Debugging Software for C31 NPE Board

W. Anthony Alford
Graduate Research Assistant
Department of Electrical and Computer Engineering

Abstract

The design of diagnostic routines and a monitor program for the C31 NPE board is discussed. The operation of these programs are described, and their performance evaluated.

Design of Testing and Debugging Software for C31 NPE Board

W. Anthony Alford

Introduction

The C31 Numerical Processing Element (NPE) is a 160 Mflop parallel digital signal processing board that contains four Texas Instruments TMS320C31 digital signal processors (C31s). This board was designed by Sverdrup Technology for use in the Computer-Assisted Dynamic Data-Monitoring and -Analysis System (CADDMAS). Each processor on the board has its own memory banks, as well as shared memory; a buffered comport; a high-speed RS-422 serial link; and an input only RS-232 serial link. Since large quantities of these complex boards are to be used in the CADDMAS, it was necessary to create methods of checking newly produced boards, methods of debugging software designed to run on the board, and methods of downloading code to all processors in the system.

Problem

When new boards arrive from the manufacturer, they must be checked to verify functionality. The complexity of the boards requires an automated verification procedure to check the address and data lines for each memory bank and the comports. To solve this problem, a battery of diagnostic routines was designed and implemented.

Debugging code requires the ability to examine processor memory and registers. To accomplish this, a monitor program was designed. The monitor also includes ability to alter processor memory and registers, thus allowing download of code.

Methodology

To check memory data and address lines, the diagnostic routine writes a unique pattern to each memory location. After writing, it reads each location, comparing what is read with what was written. If the two values are different, the location of the lowest order bit in error is reported by flashing an LED on the board.

To check comports, several programs were designed. One program sends an incrementing pattern out the comport. Another reads the comport, checking for an incrementing pattern. These two programs, running on different processors, can verify a commlink. Another pair of programs transfer take turns sending data back and forth across a commlink, to verify token

transfers. Another program simply reads data from the comport and stores it in memory for later inspection.

The monitor program is designed to operate in a network of boards. The processors in the network are daisy-chained by attaching the transmit serial port of one to the receive serial port of the next. The ends of the chain are connected to a host computer. Although the C31 is a 32-bit processor, all data is transferred over the serial port in 16-bit words. 32-bit data is used, but is transferred over the network as two 16-bit words. The basic protocol is a C31 cannot transmit data until it receives data from its serial port. When it does receive data, it must transmit data on its serial port. Thus, every time the host sends data to the network, it receives data. Since the C31s cannot send data until they receive something, the host can control the data flow in the network.

The monitor program is invoked by the serial port receive interrupt. The C31s push all their registers onto their stacks. The monitor then begins initializing the network. To initialize the network, each C31 is assigned a unique ID number. Each C31 in the chain creates its ID by taking the first data word it receives over the serial port and adding 1 to it. It then passes its ID to the next C31 in the chain. The host starts by sending a 0 to the first C31. Thus, the first C31 is number 1. The last C31 in the chain will send its ID to the host, thereby indicating the number of C31s in the net.

After network initialization, the C31s are ready to accept commands. A command sequence consists of the following:

- (1) ID packet
- (2) command number
- (3) command arguments

The ID packet and command number are 16-bit data, while the command arguments are 32-bit.

An ID packet is a list of ID numbers, indicating which C31s are to respond to the command. The packet begins and ends with -1. The following is an ID packet containing ID numbers 3 and 5.

example:

```
FFFFh
0003h
0005h
FFFFh
```

If, instead of an ID packet, the C31 receives a 0, it acts as though it received its ID. This allows the host to send a command to all C31s in the network, without using each explicit ID.

After the ID packet comes the command number. If the C31 received its ID in the ID packet, or a 0 instead of an ID packet, it will process the command in execute mode. Otherwise, it will process the command in pass-through mode. The command number is used as an index in the appropriate look-up table, either execute or pass-through. In either case, the C31 will transmit the command number and the arguments out its serial port to the next C31 in the chain.

The valid monitor commands are:

- (1) Register dump
- (2) Block memory dump
- (3) Block memory load
- (4) Get address
- (5) Run
- (6) Exit monitor

After processing a command, the C31 waits for another command sequence. The following is a description of how the C31 processes each command.

Register Dump:

The register dump command has no arguments. In execute mode, the C31 reads the register values that were pushed onto the stack at entry to the monitor and sends them out the serial port one at a time. There are 36 register values on the stack, so the C31 must send 72 16-bit words. In pass-through mode, the C31 receives, then immediately transfers over the serial port, 72 16-bit words.

Block Memory Dump:

The block memory dump command has two arguments: the starting address and the block size. The starting address indicates the memory location of the first word in the block. The block size is the number of words the C31 dumps. In execute mode, the C31 reads from memory, beginning at the starting address, and transmits data out the serial port. In pass through mode, the C31 receives data from the serial port and immediately transmits the received data. However, it stores the block size, and keeps track of the number of words sent, so that it will know when to exit the command.

Block Memory Load:

The block memory load, as with memory dump, has two arguments: starting address and block size. After sending these arguments, the host will send the data for the C31 to load. The number of words it will send is the block size argument. In execute mode, the C31 receives the arguments from the serial port. It then receives the data and stores them in memory, beginning at the starting address. In pass through mode, the C31 receives and immediately transmits the data, keeping track of how many were sent, to know when to exit the command.

Get Address:

This command is used in conjunction with the Run command (see below). The host sends the address from which the target C31s are to begin running code. In execute mode, the C31 stores the address at a designated memory location, to be used later. In pass through mode, the C31 receives and immediately transmits the address.

Run:

In execute mode, the C31 loads the start address from memory (see Get Address command above) begins executing code at that location. There is no pass-through mode for this command. Note that if this command is not preceded at some point by the Get Address command, results may be unpredictable.

Exit:

In execute mode, the C31 exits the monitor program. There is no pass-through mode. It is usually desirable to issue this command to all C31s in the network, since the chain will be broken if at least one C31 exits the monitor.

Results

During my tour, our research group tested five NPE boards. Using the diagnostic routines, we detected and located faults in the construction of the boards. These included open traces in data and address line circuits. The comport diagnostic programs were used to detect faults on the boards and noise on the lines connecting the comports. Using these routines we found a shorted trace on one board. We also discovered ringing on the handshake lines, prompting us to terminate the lines.

The monitor was mainly used for downloading code to the several processors on the NPE board. This was done to test the flow of data through the various elements of the CADDMAS. The monitor was not used for debugging code, since most code had already tested. However, the monitor is capable of performing the basic debugging functions of memory and register dumps, and memory loads. The monitor was used to download the memory and comport diagnostic

routines, and to examine the results of these diagnostic which were stored in processor memory.

Conclusion

The diagnostic routines and monitor program that I developed during my tour are powerful tools that can aid in verifying both hardware and software for the CADDMAS. The diagnostics can quickly and accurately locate simple hardware faults, such as open traces. The monitor, when compared with commercial debuggers, is less flexible, but much more economical. It also has multi-processor capability, a feature lacking on most commercial debuggers available for the C31. This makes it an ideal tool for first cut debugging of software in a multi-processor system.

PERFORMANCE AND VALIDATION STUDIES OF THE
KIVA-II CODE FOR WIND TUNNEL SPRAY BAR DROPLET DISPERSION

Brian C. DeAngelis
Graduate Assistant
Department of Aeronautical and Astronautical Engineering

The University of Illinois at Urbana-Champaign
104 South Wright Street
Urbana, IL 61801-2997

Final Report for Graduate Student Research Program

Submitted to:
Arnold Engineering and Development Center
Arnold Air Force Base, TN

Sponsored by:
Air Force Office of Scientific Research
Bolling Air Force Base, Washington, D.C.

July 1994

PERFORMANCE AND VALIDATION STUDIES OF THE
KIVA-II CODE FOR WIND TUNNEL SPRAY BAR DROPLET DISPERSION

Brian C. DeAngelis
Graduate Assistant
Department of Aeronautical and Astronautical Engineering
The University of Illinois at Urbana-Champaign
Urbana, IL 61801-2997

ABSTRACT

A version of the KIVA-II flow code was first analyzed for performance improvements due to acceleration modifications and then compared with an experimental data set for validation. AEDC has sought a computational methodology for robust and accurate prediction of spray bar droplet dispersion for engine icing tests. Previous studies have determined that the most efficient computational methodology would involve a decoupled gas phase computation by the NPARC code, followed by a droplet and vapor computation by KIVA-II. In addition, KIVA-II would be modified to include local timestepping for both the vapor and particle computations to reduce CPU requirements. The present research involved the analysis of CPU time savings based on comparisons of liquid water content (LWC) over time between an accelerated and standard acceleration KIVA-II. These performance studies have shown a significant, yet varying degree of CPU time savings. In addition, a test case with a methanol spray was computed for comparisons with experimental results of an identical case. Initial studies of this validation case indicate a degree of computational accuracy in the vapor phase.

PERFORMANCE AND VALIDATION STUDIES OF THE KIVA-II CODE FOR WIND TUNNEL SPRAY BAR DROPLET DISPERSION

Brian C. DeAngelis

1. Introduction

This research was intended to analyze the effectiveness of a computational methodology developed in previous studies at AEDC and The University of Illinois at Urbana-Champaign (UIUC). Loth (1993) proposed a methodology for the computational modeling of wind tunnel spray bar droplet dispersion for the AEDC ASTF Test Cell C. This included the decoupling of the air gas phase from the water droplet and vapor phases based on dilute spray conditions. With this assumption, the air phase would be calculated using the NPARC code and the water phases would be calculated with a modified version of KIVA-II (Amsden, *et al.*, 1989). The modified KIVA-II, in addition to the removal of chemistry and air phase terms and the inclusion of a water thermochemistry library, would be modified to include convergence acceleration, being accomplished by local timestepping for the vapor diffusion and convection terms (Eulerian acceleration) and independent timestepping for the droplet terms (Lagrangian acceleration).

These acceleration modifications were completed during the previous academic year at UIUC. A simplified test case involving a single nozzle spraying evaporating and non-evaporating water droplets was studied. Following this, the optimum diffusion timestep, Δt , for minimum CPU requirements was studied.

Because validation studies had not been completed on the spray using the decoupled air and water, KIVA-II was tested using a version prior to acceleration modifications. In the absence of sufficient available data on water sprays, an experimental data set generated for a methanol spray was employed. All studies in this report were completed on a Cray Y-MP at UIUC.

2. Performance Testing

A key parameter of interest during engine icing tests is the liquid water content (LWC) (Bartlett, *et al.*, 1993). Steady state conditions in the computational environment are therefore based on convergence of LWC, which can be defined as follows:

$$LWC = \frac{M_p}{\Delta t \cdot A \cdot U_{air}} \quad (1)$$

where M_p is the mass of the particles which have fluxed through area A during time Δt .

A simple, nominally two-dimensional flow field was calculated by Dennis Lankford using NPARC. The computational grid is shown in Fig. 1. Upstream of the flow field is half of a spray bar which creates a shear layer between a wake and a high-speed free-stream. A spray nozzle was initialized immediately downstream of the spray bar face in the wake. Given an initial diffusion timestep Δt_i , KIVA-II was modified to keep this initial value constant throughout the entire calculation; i.e. the growth factor which determines Δt was set to 1.0. This was necessary because by including independent particle timestepping, the flux of particles is conserved per timestep and not necessarily per unit time. LWC was averaged over ten equally-spaced slices of the outflow plane (see Fig. 1) and over a certain number of timesteps in order to produce smoother profiles. Initially, Δt_i was set equal to 39.0 μs producing a convective subcycling number of 9 in the standard KIVA-II, one suggested operating condition (Amsden, *et al.*, 1989). Profiles of LWC were generated for an evaporating and non-evaporating case and are presented in Fig. 2. Note that the profiles shown are profiles for the area slice on the far end, downstream of the wake because this slice took the longest to converge and is thus the limiting case. As expected, the number of timesteps needed for convergence, n_{tc} , is significantly less than the accelerated case. Note that the converged LWC values are approximately 10% higher in the non-evaporating case, indicating that, in fact, evaporation is a necessary component in the KIVA-II calculations. Also note that the decrease in n_{tc} is greater in the non-evaporating case than in the evaporating case.

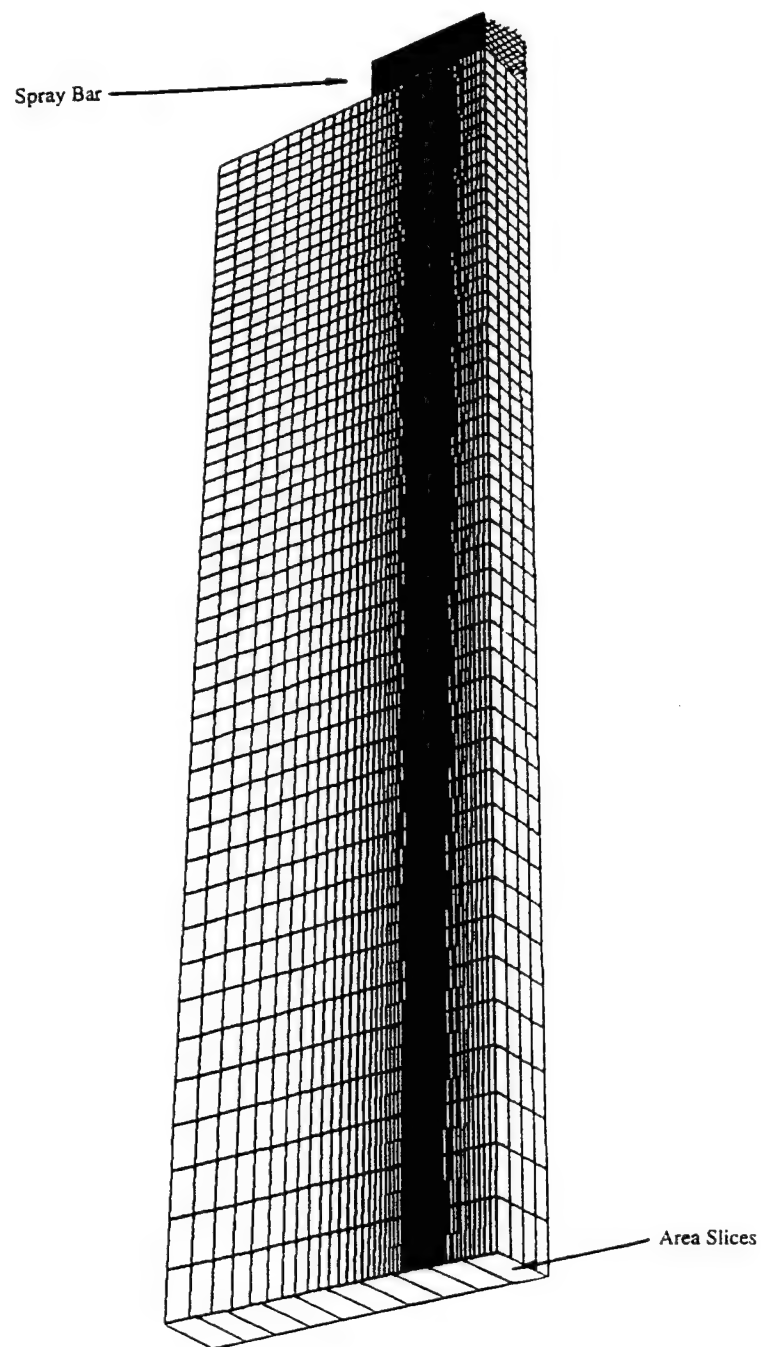


Fig. 1 Computational grid for performance studies

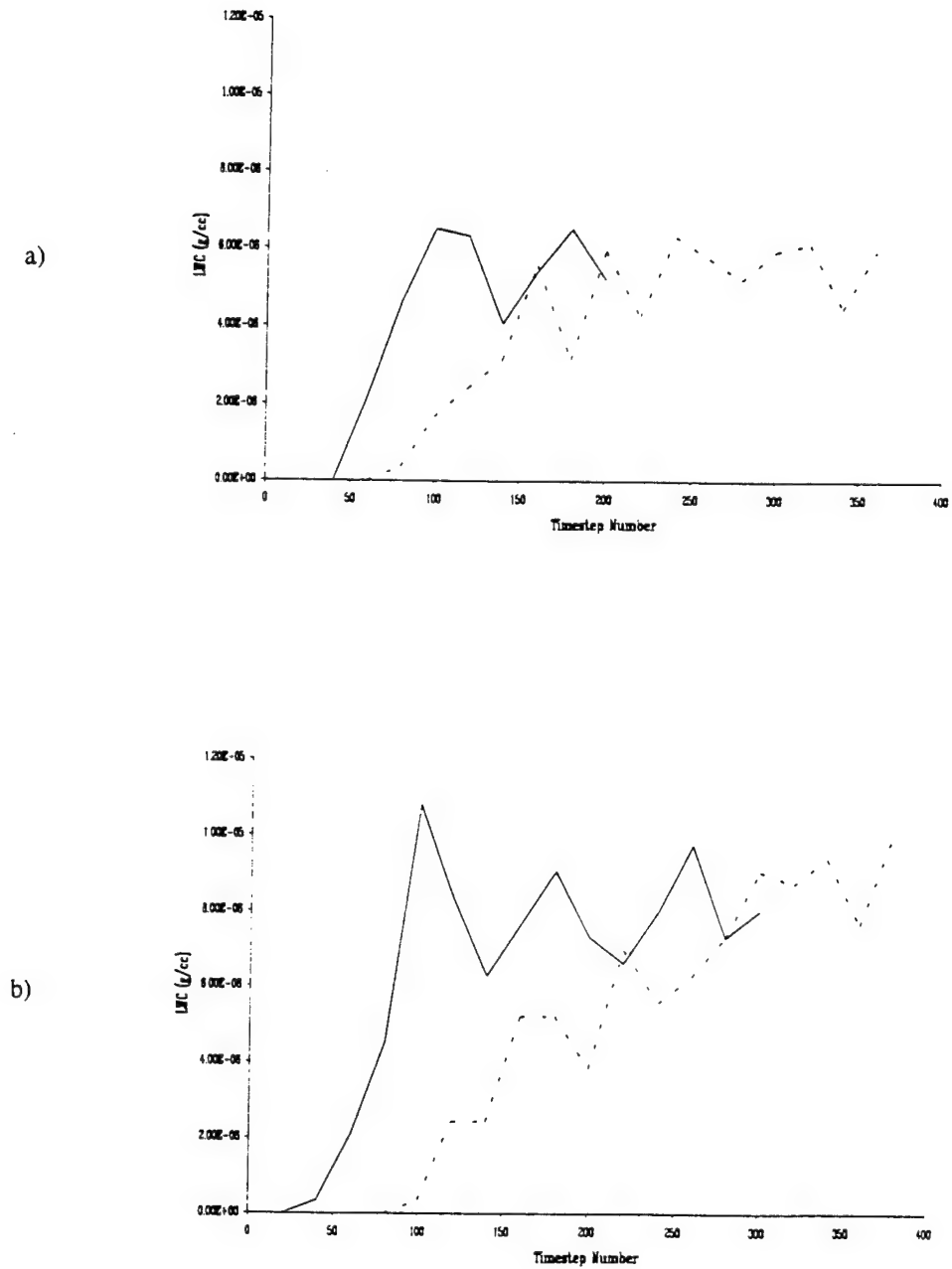


Fig. 2 LWC vs. Timestep Number with evaporation (a) and without evaporation (b). Solid lines indicate accelerated KIVA-II and broken lines indicate standard acceleration

Next, optimization of Δt_i was studied. First, the number of LWC profile slices was reduced to five, and the number of timesteps over which values were averaged was increased to produce even smoother profiles. Again, only the near-end slice was studied and several plots of LWC versus timestep number were produced. From these plots, the convergence timestep was visually extrapolated. In the case of the standard acceleration KIVA-II, time-accuracy required only one selection of n_{tc} which related to a total time to convergence, regardless of the value Δt_i . For the accelerated case, a new value of n_{tc} was determined for each case of Δt_i . For each case, the flows were recalculated to the corresponding value of timesteps n_{tc} and CPU time required, T_{cpu} , was recorded.

Figure 3 presents a plot of T_{cpu} versus Δt . The results for the standard acceleration case are consistent with expectations: as the number of convective subcycles is increased with increasing Δt , computational effort is reduced. This trend is followed in the full acceleration case for Δt_i greater than 60 μs . However, a maximum T_{cpu} is reached at approximately 60 μs , falling at greater and lesser values of Δt_i .

The behavior of the fully accelerated case seems to indicate that with the nominally two-dimensional grid and associated flow field used in this study, improvements due to Lagrangian acceleration may be flow field dependent. The trend seems to indicate that at Δt_i of approximately 60 μs , the turbulence correlation times, t_{turb} , for the most part, are no longer greater than the corresponding diffusion timestep. For Δt_i less than 60 μs , t_{turb} values were greater than Δt , allowing the particles to convect greater distances during each timestep. For Δt_i greater than 60 μs , very little Lagrangian acceleration can occur so that the only improvements in T_{cpu} are from the Eulerian acceleration.

Two other aspects of these performance calculations were noted. First, because convergence was based on LWC profiles and the flow field only allowed limited resolution, the vapor may have not reached steady state in the accelerated case for smaller values of Δt_i . With respect to vapor, the calculations remain somewhat time-accurate (i.e. vapor is not allowed to convect greater distances than originally); because values of n_{tc} were smaller in the accelerated case for small Δt_i , the vapor may not have been given enough time to fully converge. Second,

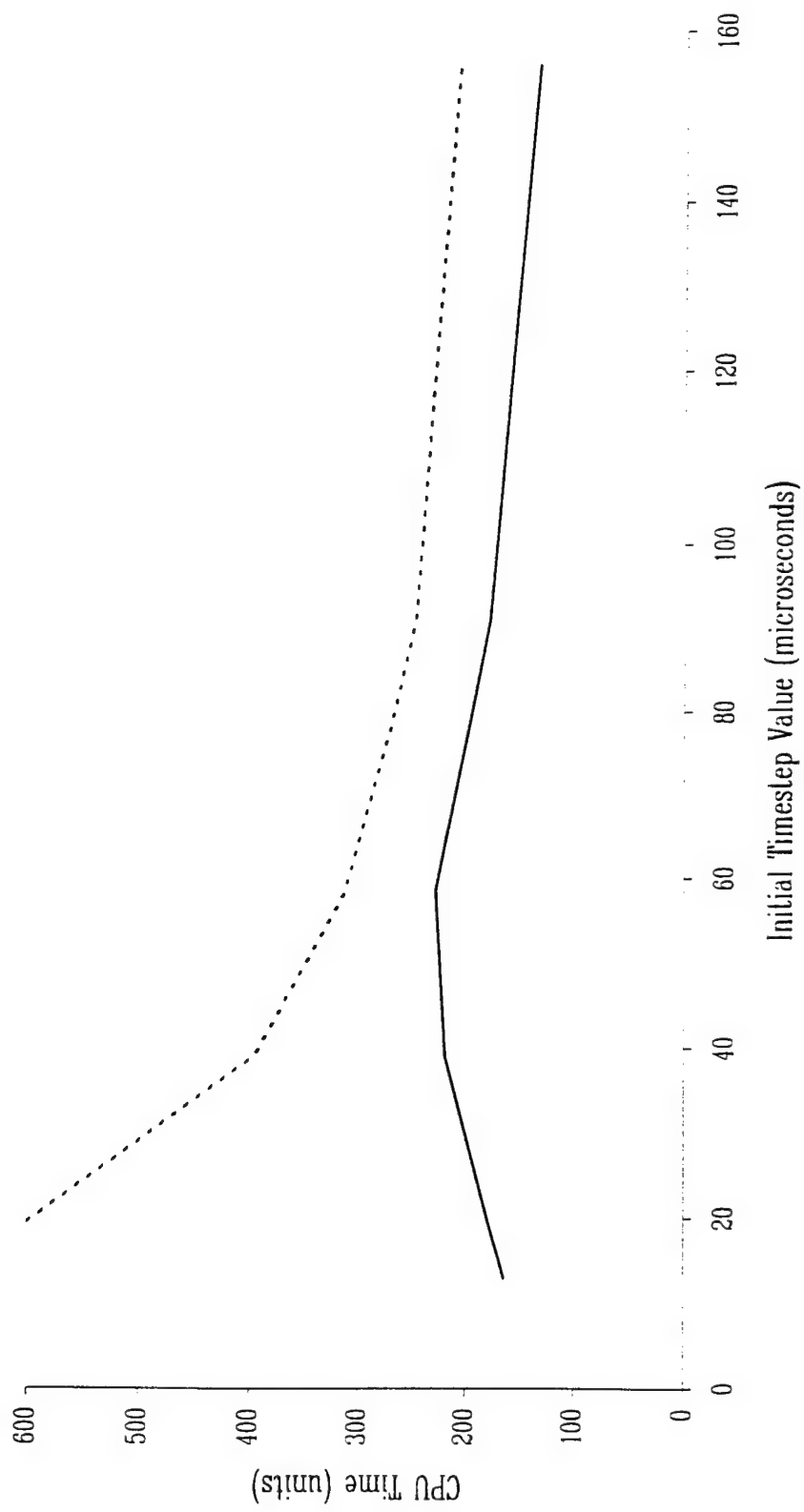


Fig. 3 CPU time needed for convergence versus Δt_i

at higher values of Δt_i , both versions of KIVA-II exhibited deteriorating accuracy in vapor calculations, again without affecting LWC profiles.

3. Validation Studies

For purposes of validating the droplet and vapor calculations of KIVA-II, an experimental database generated by McDonnell, *et al.* (1993a,b) was employed. The test case involved an air-assisted, non-swirling methanol spray injected downward into a cylinder with free stream air traveling downward at approximately 1 m/s. Both gas and droplet phase measurements were compiled.

To save computational effort, the air fluid properties were entered into KIVA-II based on measurements by McDonnell, *et al.* (1993a). Values for mean axial and radial velocities were linearly interpolated onto a nominally two-dimensional axi-symmetric grid. Grid spacing was selected to allow reasonable resolution throughout the flow (see Fig. 4). Density was assumed constant at 1.26 kg/m^3 and a temperature field was assumed based on observations made by Vince McDonnell (personal communication) associating methanol vapor concentrations to temperature. Turbulent kinetic energy, k , was computed using measurements of RMS turbulent velocity components. The last required quantity was turbulent dissipation, ε , which can be defined as the following (from notes by Dennis Lankford):

$$\varepsilon \approx \left\{ \left(\frac{\partial u}{\partial x} \right)^2 + \left(\frac{\partial v}{\partial y} \right)^2 + \left(\frac{\partial w}{\partial z} \right)^2 \right\} \quad (2)$$

where u , v and w are the turbulent velocities in the radial, azimuthal and axial directions, respectively. Since only RMS values of u and w were measured, Eq. 2 was altered:

$$\varepsilon \approx \left\{ \left(\frac{\Delta w}{\Delta z} \right)^2 + 2 \cdot \left(\frac{\Delta u}{\Delta x} \right)^2 \right\} \quad (3)$$

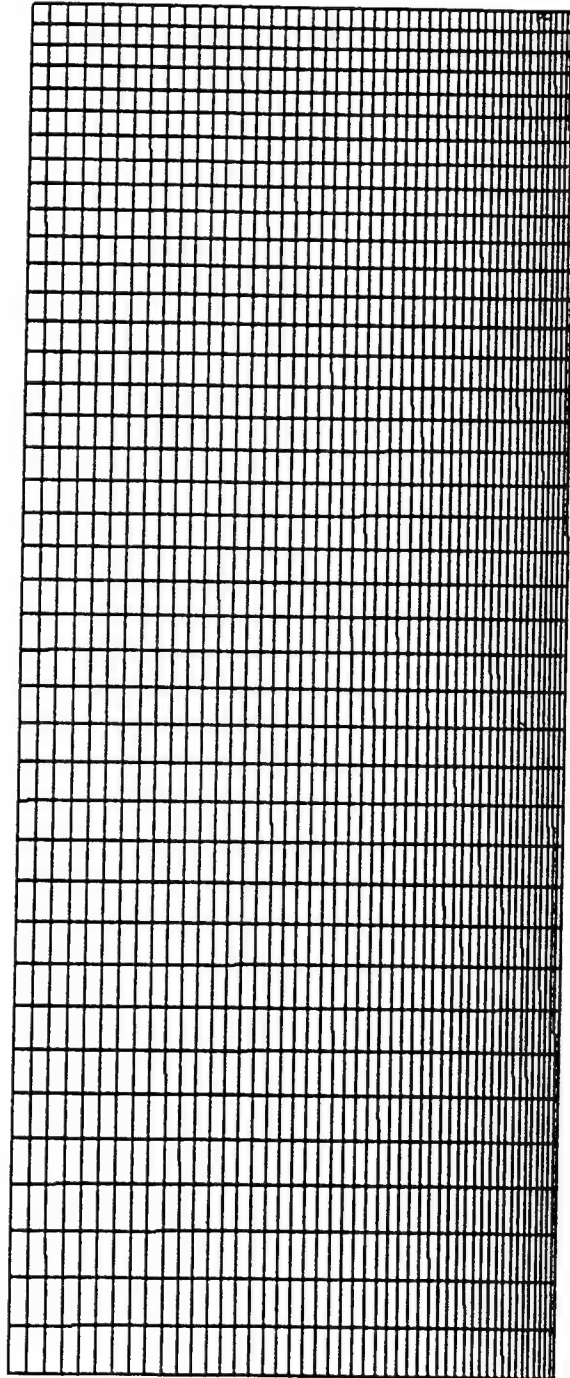


Fig. 4 Slice of computational grid for validation studies

assuming that the magnitude of the azimuthal velocity spatial derivative is approximately that of the radial component. Δw is then calculated as:

$$(\Delta w)^2 = (w_{k+1} - w_k)^2 = (w'_{k+1}^2 + w'_k{}^2 - 2 \cdot R_{11} \cdot w'_{k+1} \cdot w'_k) \quad (4)$$

where w' is the RMS value of w and R_{11} is a correlation coefficient given by Wygnanski and Fiedler (1969) for turbulent jet flows. The expression for this correlation factor was approximated as:

$$R_{11} \approx e^{(-20(\Delta z/z))} \quad (5)$$

Δu can be computed similarly using $R_{22} = R_{11}$.

Other assumptions about the flow were necessary to fill in data where none was provided. This included the $z = 0$ plane at the face of the nozzle port. Here, a parabolic axial velocity profile with a maximum value of 62.5 m/s (the bulk velocity at the nozzle tip) along the centerline, falling to near zero velocity at the nozzle block face. Other values including the RMS turbulent velocities were linearly extrapolated from the nearest measurement location. Because KIVA-II does not contain a methanol thermochemistry library, one was included from values and formulas given in Vargaftik (1975) and Reid (1977). In addition, KIVA-II was modified to ignore all particles that are injected outside the computational domain since the injector would be placed behind the flowfield along the axial centerline.

The spray was then initialized and the flow computed. A solid-cone spray half-angle of 17° (measured from a photograph from the experiment) and other parameters were set consistent with the experimental conditions. Δt_i was set at 6.5 μs , which was determined to be an acceptable value based on stability concerns. The flow was then computed to 7000 timesteps. At this point, the vapor had yet to reach steady state, but a reasonable profile had been generated as in Fig. 5. In this figure, the vapor concentration profile measured by

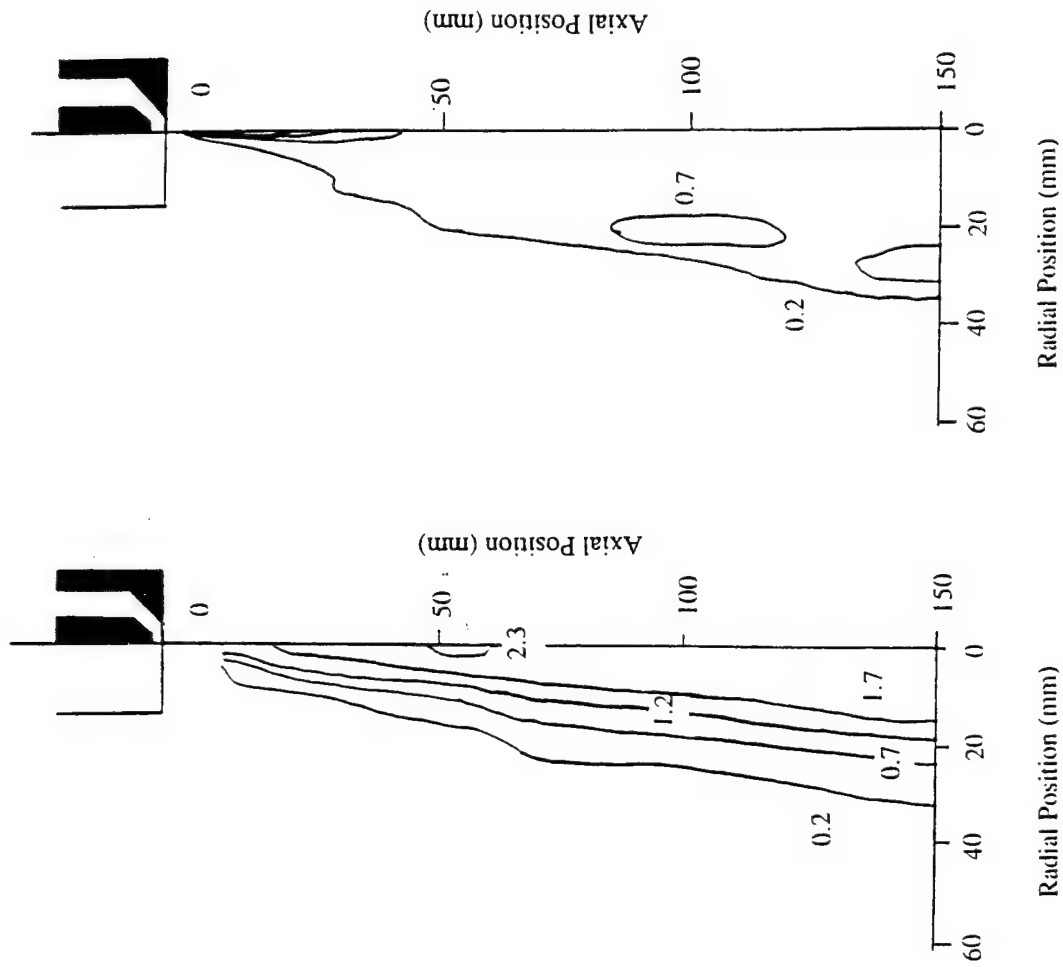


Fig. 5 Molar percent concentrations of methanol (IHC) from McDonnell (a) and KIVA-II (b)

McDonnell, *et al.* (1993a) is shown next to the KIVA-II calculation. The minimum vapor contours are extremely similar, though the contours of greater vapor concentrations have not fully developed.

4. Conclusions and Future Work

Work completed over the summer has provided insight into the performance capabilities of the KIVA-II code both in its standard and accelerated form. Because the performance studies were completed using a single operating condition over a small domain, the results can only show qualitative trends. In addition, many of the initial conditions that were specified for the validation case spray were assumed for lack of more detailed experimental conditions. A better understanding of the flow physics must be obtained to make more realistic assumptions.

Performance and validation studies will continue in a broader scope. In the case of performance, more detailed studies of LWC convergence will provide better knowledge about the extent to which the evaporation calculations must proceed. Possibly, the convection of vapor may be eliminated after a certain distance downstream of the injector, allowing more efficient calculations. Validation studies will continue with improved initial condition specifications on the methanol spray case to compare droplet volume fluxes, sizes and velocities. In addition, larger scale validation studies will be completed on actual wind tunnel LWC profiles.

DEVELOPMENT OF A MONITOR FOR A MULTI-PROCESSOR NETWORK

H. David Helsley, Jr
Graduate Research Assistant
Department of Electrical and Computer Engineering
dhelsley@sparc2000.utsi.edu

University of Tennessee Space Institute
B. H. Goethart Parkway
Columbia, Tennessee 37388

Final Report for:
Graduate Student Research Program
Arnold Engineering Development Center

Sponsored by:
Air Force Office of Scientific Research
Bolling Air Force Base, DC

and

Arnold Engineering Development Center

August, 1994

DEVELOPMENT OF A MONITOR FOR A MULTI-PROCESSOR NETWORK

H. David Helsley, Jr
Graduate Research Assistant
Department of Electrical and Computer Engineering
University of Tennessee Space Institute

Abstract

In the course of the development of a new multi-processor C31 (Texas Instruments TMS320C31) computer board, it became increasingly necessary to find ways to communicate with the processors on the board without the use of a JTAG-standard emulator pod (which can be expensive), and without having to constantly reprogram EPROMs every time a program change is needed. It was decided that a daisy-chain loop connecting the host IBM-compatible PC to a network of C31s was the most direct, and simplest way to accomplish this goal. Since each C31 has exactly one serial communication input and one output, wiring the monitor system was simply a matter of connecting serial outputs to serial inputs and connecting the ends of the loop to the IBM PC. A computer program was then developed to interface with all of the C31s in the loop so that at any time, the user could access registers, look at memory locations, and download code or data to any of the processors in the loop. The reader may find several ideas which may be employed in developing his or her own JTAG-independent monitor programs for use with a multi-processor computer system.

DEVELOPMENT OF A MONITOR FOR A MULTI-PROCESSOR NETWORK

H. David Helsley, Jr

Introduction

A new computer board with four Texas Instruments TMS320C31 microprocessors was developed and recently built. It became necessary to create some of the building blocks which would be used in the future for software development. Some of these building blocks include: a way to download code, a way to retrieve a block of memory, the ability to look at the registers, look at different flags (FIFOs and Dual-Port Memory Interrupts), and turn the processor loose by executing code from a specified address. In addition, all of these operations must be possible for any of the processors being examined at any time. It was decided that the best way to accomplish this would be to use the serial input/output ports for the C31s in a daisy-chain formation. With this configuration, it is absolutely necessary for all commands to originate from the IBM PC and to end at the IBM PC, so that every processor in the network knows exactly what is happening at each instant. With this philosophy in mind, a program was written by the author (in "C") to interface with the network of C31s in order to provide the building blocks for later software development on this multi-processor board.

Low-Level Methodology

This section will go through the basic functions implemented by the C31s and describe the method which was used to do it. For most of the commands to the C31s, a value of -1 was sent through the chain, followed by all ID numbers to whom the command refers, followed by another -1. Then, the command number would be sent, followed by any arguments the command might require (like starting address or block size). This is the basis for the entire monitor program.

The first order of business is initialization of the system. This is accomplished in the following way: the IBM PC sends the value "0" to the first C31. Once data is received in the serial input port register, an interrupt is generated and the monitor program begins (assuming the interrupt is enabled at

the time). Each C31 reads the value it receives, increments it, keeps it as its own ID number, and then sends the incremented value out its serial port. If all of the serial links are connected properly, the IBM PC should receive a number equal to the number of C31s in the loop. This number is stored in a global variable for reference throughout the program. The C31 system is now initialized and ready to receive commands from the IBM PC.

Now, we need a command structure. The structure we used is relatively simple, reserving most of the complexity for the IBM PC program. The commands are (at the C31 end):

- 1 - Send Registers (from stack)
- 2 - Block Memory Send
- 3 - Block Memory Receive
- 4 - Get Starting Address (for program execution)
- 5 - Go (from starting address specified in #4)
- 6 - Exit (return to where C31 was before interrupt)
- 7 - Send Processor Type

Command #7 was needed so that the IBM PC could tell which processor (out of four) this particular C31 was on the computer board. This type value is displayed on the screen below the Active C31 Number.

Looking at the values of the registers was an interesting feature of the C31 Monitor program. These values were pushed onto the stack once the C31 entered the "Debug Mode" after initialization. Command #1 causes the C31 to simply send the values straight from the C31s stack to the IBM PC. The IBM then interprets the information from the C31 and displays it in a form that is familiar to the user.

There is something which needs to be said about data transfers from the C31 to the IBM PC. All data transfers need to originate from the IBM, so any retrieval of data must come as a result of a "go ahead and send" command from the IBM. This way, any processors not involved directly in the data transfer can become a "wire" and just pass data through. Therefore, what would generally happen is the IBM would send an arbitrary value ("0" was as good as any), and the only C31 processor in the chain which was authorized to change that value was the C31 to whom the command was directed. All non-active processors would keep track of block sizes and the number of words transferred, so that

they could get in on the next command. The "Send Registers" (#1) and "Block Memory Send" (#2) commands operated under these guidelines.

Data transfers from the IBM to the C31 require similar handshaking. In order to make sure all of the C31s in the chain knew what was going on at every instant, when the IBM sent data to the C31, the C31 would send the data back out unchanged as an acknowledge. In this way, multiple processors in the loop are able to "latch on" to data as it goes by. Whether or not they do is dependent upon the ID numbers which were sent before the command to perform a "Block Memory Receive" (#3).

"Get Starting Address" (#4) is simply a platform for specifying the starting address for program execution once the C31 exits Debug Mode via "Go" (#5). In this case, after forwarding the global "GO" command to the next C31 in the chain, the stack pointer is restored to where it was before entering debug mode, (registers are not restored) and the C31 branches to the address specified by command #4. The "Exit" command (#6), however, will restore the registers to their previous values and return from the interrupt in the normal fashion. Note that in all cases, the "Exit / Go" commands are forwarded to the next C31 in the chain, so that all of the C31s can exit at the proper time.

C31 MONITOR USER'S MANUAL

Main Menu

This section will describe the general operation of each of the menu items contained in the IBM PC side of the monitor program. When the program is first executed, the main menu with three options is displayed. Command #1 (Initialize) will initiate the daisy-chain initialization procedure described in the "Low-Level Methodology" section. If the user is unable to initialize the daisy-chain system, he/she can check the LEDs associated with each of the processors in the chain. Any processors with their LED lights on are in the debug mode, and generally one can find the problem by checking the first processor in the chain with its LED off. Command #2 (Troubleshooting Tips) will display a blue screen which gives some tips on some things to try when the system will not initialize. Command #3 (Quit) will return the user to DOS.

The Active C31

Once the system is initialized, the Debug Mode Menu is displayed. Under the title in blue is the ID number of the current Active C31, followed by the number of C31s in the daisy-chain system and the Active C31s type (A, B, C, or D) according to its orientation on the board. Any of the commands which refer to only one processor (all commands except Boot, Broadcast and Exit) will be directed at the Active C31. If you wish to change the Active C31, you may do so by selecting Command #7 (New Active C31). The program will prompt the user for the new Active C31 ID Number, and once received, checks to make sure the ID number specified is valid.

Register Examination

The command at the top of the menu is the Register Dump (#1) Command. Selecting this option will bring the user to a screen which shows the values of all of the C31s registers, as they were before the Monitor interrupted program execution. By default, all of the registers are displayed in hexadecimal format. If the user wishes to see the registers in Floating-Point or Integer formats, he/she may press "F" followed by the desired format. All extended-precision and auxiliary registers will be displayed in the selected format. The other registers (Status Register, Interrupt Enable, Repeat Count, etc.) are not very interesting in the other formats, so they remain in hexadecimal format. If the user wishes to make a change to one or more of the registers, he/she may select (C)hange Registers by typing "C". The user will be prompted for the register to change, and the value to change it to. This value must entered be in hexadecimal format! Attempting to type in a floating point number will produce unpredictable results! Once all changes have been made, the user may (W)rite the changes to the C31s stack by selecting "W". Pressing the ENTER key alone or typing "Q" will bring the user back to the main menu.

Block Memory Read

Command #2 will allow the user to examine a block of memory as the C31 sees it in its memory space. The author was able to get blocks of up to 13,000 words (3500h) to load successfully into memory. Once the user types the starting address and block size to read from the C31, the IBM PC begins reading

the data. When it is finished, the display changes to reflect the contents of the memory block requested. On the left in red text is the address of the first word on that particular row, followed by four words. To find the contents of a particular address, look for the address closest to but not greater than the address you are looking for, and then count from left to right. The user may scroll through the data by using the Up and Down arrow keys, Page Up, Page Down, Home and End. Once again, the user has the option to change the format of the data as it is displayed on the screen by typing 'F', followed by the desired format. When finished, the user can select (D)one to go to the next menu.

At this time, the monitor program advances to another menu which allows the user to save the block of data which is currently residing in memory to disk, see the block again, or quit. When saving the data, the monitor program prompts the user for the filename to save it under, and then saves the data in the hexadecimal format with the starting address first, followed by the block size, and then the data itself. This format is compatible with the file format which is used to send a block of data to a C31 (which is described next).

Block Memory Send

This main menu option essentially does the opposite of Block Memory Read, but in a different order. When Block Memory Send is selected, the monitor program prompts the user for the name of the file which contains the data block to send to the Active C31. It then loads the starting address, block size, and actual data into memory and brings the user to a menu. At this time, the user may examine the data which has just been loaded into memory, change the starting address to something other than what was specified in the file, actually send the data out to the Active C31, or quit. A good exercise for testing a processor's memory space is to send a data block to a particular address by using Block Memory Send, and then attempt to read the data block back by using Block Memory Read.

Run From Address

If the user wishes for one particular C31 to begin running from a certain address, this is where it can happen. It may be that a program was downloaded

to the C31 by way of option #5 (Download EMP File), or an extremely simple program was downloaded by using Block Memory Send. Whatever the circumstances, selecting this option will cause the monitor to ask for a starting address to run from, and then the monitor will turn all of the processors loose with the Active C31 running from the address specified. Simply pressing RETURN will return the user to the Main Menu.

Download EMP File

The EMP (EproM Programmer) file format was chosen for downloading code to the C31s. The data is in hexadecimal, byte-reversed format similar to what one would find in an EPROM if the processor reads from the least significant byte to the most significant byte. The data is arranged in blocks beginning with the starting address, followed by the block size, and the data itself. Note that this format is very similar to the file format used for Block Memory Read and Block Memory Send. In fact, the same routines that are used for sending blocks of data across the link are used for this command. Regardless, this option will allow the user to download an EMP file's contents to the Active C31 and then will give the user the option to either run from the program's starting address or return to the Main Menu. If the user wants to download code to more than one C31 in the chain, a network configuration should be used under the Boot Network option.

Examine Flags

The C31 board developed by the author and his team contains several memory-mapped flags including Dual-Port Memory mailbox flags and Input/Output First-In First-Out Buffer (FIFO) flags. It was decided it would be "nice" if there was an option in the monitor which would read all of those flags and display them in an easy-to-read fashion. This option does just that. If the user wishes to examine the status of the C31 board's flags, this is the selection to make.

Select Active C31

The C31 Monitor allows the user to work extensively with any of the C31s in the daisy-chain loop at any time. If the user wants to work with another C31,

select this option, followed by the number of the desired C31. Once a valid ID number has been entered, the display is modified to reflect the change. The user may now use the device-specific options on the new Active C31.

Broadcast Block

This is a special option which allows the user to send one block of memory to a number of C31s. Broadcast Block begins with asking for the data file name, and once loaded, another menu is displayed. This menu allows the user to look at the data block in memory, change the starting address, send the block to the C31s, quit, and one other option that is not present in Block Memory Send -- specify recipients. To toggle who receives the data and who doesn't, the user selects this option and a screen is displayed which shows the current recipient status. The default is ALL C31s, but if, for example, the user does not want C31 #2 to receive the data, he/she may type '2' to eliminate C31 #2 from the list. The list is updated every time an option is toggled, and when finished, the user should type '0'. Once everything is set correctly with the data block correctly loaded, the starting address correctly set, and the recipients correctly specified, the user may send the block to all of the recipients simultaneously.

Boot Network

With prior specification of a configuration file, the network of C31s can be booted by using this option. The configuration file contains the following information: on the first line is the number of C31s that are in the network that the configuration file is for, followed by the first ID number, then the file name, then the second ID number and the second file name, etc. An example of a configuration file might look like this:

```
4
1, 4
emp\diaga2.emp
2
emp\diagb2.emp
3
emp\diagc2.emp
```

In this particular boot configuration, processors #1 and #4 will receive the contents of "emp\diaga2.emp", processor #2 will get "emp\diagb2.emp", and processor #3 will receive "emp\diagc2.emp".

The Boot Network menu is fairly self-explanatory. First, load the configuration file into memory by selecting option #1 (Load Configuration). Then, examine the configuration as it loaded into memory to make sure everything is right through option #2. Finally, boot the network with option #3. There's a chicken exit through option #4, which will return the user to the debug menu.

Command Line Booting

A feature of the C31 Monitor is the automatic booting sequence. C31MON can be executed with the name of the configuration file as a command line argument. The monitor will enter an auto-boot sequence where it initializes the system, loads the code according to the configuration file, and turns the system loose all in one shot. It may be advisable to load the configuration file manually first to make sure the program has interpreted it correctly. Once it has been confirmed as being correct, the auto-boot sequence can be called upon to boot the entire network from a DOS batch file or from the C:> prompt. If the system does not boot correctly with the auto-boot sequencer, check to make sure the filenames are correct and the pathnames will lead the monitor to the right file. Also check the wiring to be sure that what was specified as processor #1 is actually processor #1, and so on.

Exiting the Monitor

There are two ways to exit the main Debug Menu and they are "Abandon" and "Exit". If the user wants the system to return to the way it was (with the exception of the LEDs on the board), type 'X'. All registers will be restored to the way they were (unless they were changed under Register Dump), and program execution will resume where it left off when it was interrupted. If someone pushed the reset button when they shouldn't have and the C31s are no longer in Debug Mode, the "Abandon" option is always available. Abandon does nothing on the links, does not restore registers, and does not restore execution. This

saves the user from having to look at error messages when the monitor tries to execute an exit sequence when the C31s are not ready for it.

Conclusion

The design of a JTAG-independent multi-processor monitor system was described in detail. Also, a manual describing the general operation of the monitor system was presented. Since the successful writing of this program and its implementation, the C31 Monitor has been used extensively in finding hardware and software errors on new computer boards as they come in from the manufacturer. It has been an excellent tool for debugging purposes. Ideas for possible expansion include adding the capability of single-stepping through disassembled code, memory maps, and the examination of a particular program's global variables in memory space.

PARALLELIZATION OF CHIMERA UTILIZING PVM

Chris W. Humphres
Graduate Student
Department of Electrical Engineering

University of Alabama
Box 870286
Tuscaloosa, AL 35487-0286

Final Report for:
Graduate Student Research Program
Arnold Engineering Development Center

Sponsored by:
Air Force Office of Scientific Research
Bolling Air Force Base
Washington DC

August 1994

PARALLELIZATION OF CHIMERA UTILIZING PVM

Chris W. Humphres
Graduate Student
Department of Electrical Engineering
University of Alabama

Abstract

The parallelization of the Computational Fluid Dynamics chimera based flow solver XAIR through the utilization of Parallel Virtual Machine software is described. The required modifications are discussed in a four step process. Efficiency results indicate an almost linear speedup and limited communication overhead for a near perfect test case.

PARALLELIZATION OF CHIMERA UTILIZING PVM

Chris W. Humphres

Introduction

In recent years, the increased computational size and CPU time required for the solution of computational fluid dynamics (CFD) problems combined with the high cost of vectorized computers has led to the need for faster and more cost effective computing. The primary application of a CFD program is to calculate aerodynamic flow separation. This need to complete large-scale CFD projects by specified deadlines has led to an increased interest in the parallel utilization of networked heterogenous computers. One software package currently available for the interconnection of heterogenous computers for parallel processing is Parallel Virtual Machine (PVM) [1].

Methodology

Chimera is a methodology employed by some CFD flow solvers. The basic outline of chimera consists of domain decomposition with overset grids and interpolation at grid boundaries. The parallelization of the chimera based XAIR, a baseline CFD program developed at Arnold Engineering Development Center (AEDC) involved several steps. The first step in the parallelization process was the design of an overall structure for the parallel implementation of XAIR. The next step involved implementation of a pre/post-processor and modification of XAIR for efficient input, output, and communication operations. The third step was the actual implementation of PVM. The final step consisted of error control and cleanup.

The original design structure for the parallel XAIR was based on the chimera domain decomposition approach combined with a three-tiered hierarchy [3]. Domain decomposition methods create sub-domains (e.g., a grid) and boundaries. An overset approach is used at the boundaries. Values within each sub-domain are advanced one time step. After each advancement, the values on the boundaries must be updated before the next advancement because the boundary of one sub-domain is contained in another sub-domain. The update of boundary

values consists of interpolation between the two sub-domain boundaries. An illustration of domain decomposition is shown in Figure 1.

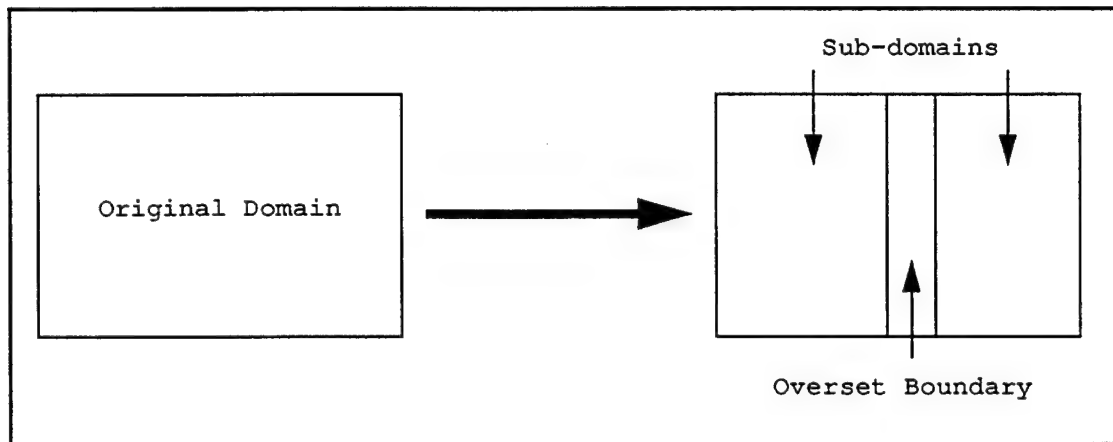


Figure 1. Domain Decomposition.

The requirements for the parallel XAIR consisted of the ability to:

1. Run large problems on computers with small memory.
2. Manage geometric complexity through the use of less complex parts.
3. Facilitate relative motion among the geometric parts.
4. Interchange geometric parts among aircraft.
5. Use multiple solvers.
6. Increase speed to meet deadlines.

The first four requirements were handled by domain decomposition and were also requirements for the original XAIR. The last two were handled by the three-tiered parallel hierarchy shown in Figure 2.

The ability to use multiple solvers was necessary for problems where one sub-domain may require one solver and another sub-domain may require a different solver, for example, if structured and unstructured grids were used simultaneously. In this design, the cluster controller is in charge of transferring input files to the appropriate hosts, starting host controllers on each host, providing start up information to the host controllers, accepting output from the flow solvers, performing needed computations to generate new

input files, and passing new input files to the host controllers. The host controllers start the needed flow solvers, pass the flow solvers information on the sub-domain to be advanced, and receive and store new input files from the cluster controller. The flow solvers receive sub-domain information from the host controllers, advance the solution one time step, and send the results to the cluster controller. The PVM code was kept as independent as possible from the flow solver code to allow the use of multiple solvers. This separation was also needed because the PVM code and the solver code are maintained by separate communities.

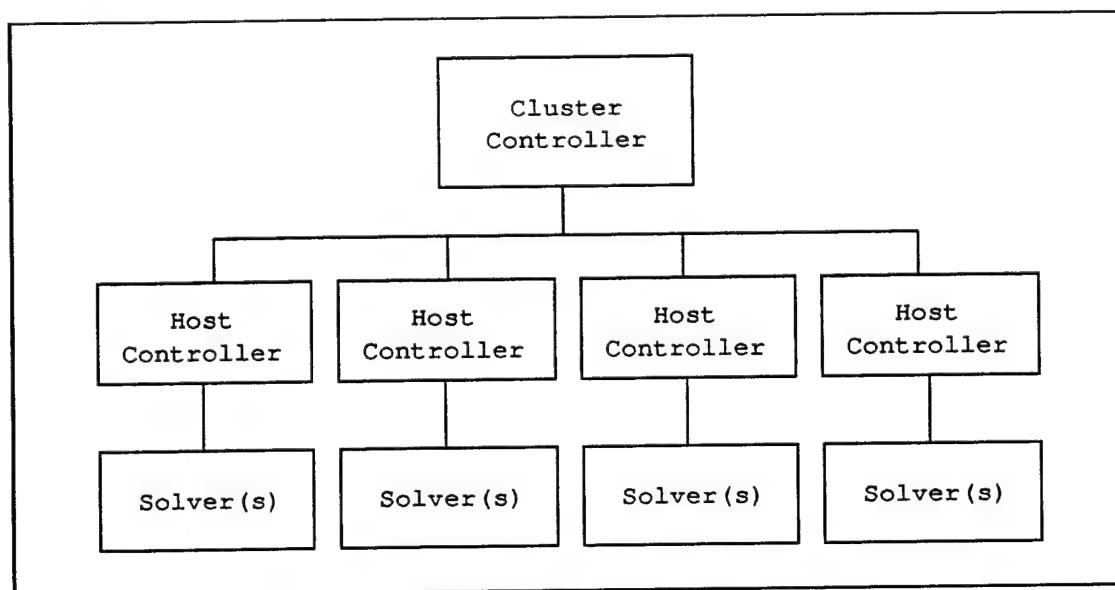


Figure 2. Three-Tiered Parallel Hierarchy.

The next step involved implementation of a pre/post-processor and modification of XAIR for efficient input, output, and communication operations. The purpose of the pre/post-processor was to allow users familiar with the original XAIR to use the parallel XAIR without additional training. The preprocessor parses the original input files into sub-domain input files or grid files (e.g. grida = sub-domain a, gridb = sub-domain b,...). The postprocessor is used to generate output files for graphical analysis. By parsing the input files into grid files, only grid files which will be processed on a particular host must be transferred to that host.

The original XAIR was written with both Fortran and C I/O. Since testing has proven the C programming language to be a more efficient means for I/O [3], all I/O within the parallel solver was changed to C. In addition, the I/O format was converted to work with a set of individual files per grid. Currently, two versions of the parallel XAIR code exist. One version utilizes C reads and writes for I/O, while the other version utilizes memory mapping. Memory mapping copies the first page of a memory object on disk to the memory space of the process. Page size is usually 512 bytes but varies from system to system. Once a file is mapped, pointers to various objects within the file can be established. Memory mapping reduces the amount of memory required because only those pages of memory which are referenced are brought into memory. Initial testing of memory mapping on Silicon Graphics and SUN workstations indicated an improvement in speed over C reads and writes due to a reduction in buffering. However, testing on DEC's AXP 3000/800 workstations produced the opposite result.

Two disadvantages of memory mapping exist. First, memory mapping is dependent on paging and virtual memory and is not compatible with machines without virtual memory (e.g. CRAY). Second, some architectures with virtual memory do not yet fully support memory mapping techniques. Therefore, the decision was made to allow two versions of the code to exist, one with C reads and writes and one with memory mapping, until further research can be completed.

The third step involved the utilization of PVM to produce a parallel XAIR. PVM allows a user-defined collection of serial, parallel, and vector computers to work as one large distributed-memory computer. PVM uses TCP and UDP Internet protocols for communication between processes and provides two options for routing, as shown in Figure 3. First, PVM allows direct TCP connections between processes if requested and available. Otherwise, PVM routes process communication through PVM daemons with UDP used for daemon-to-daemon communication and TCP used for process-to-daemon and daemon-to-process communication. The PVM daemon is a background process which serves as a

message router and controller. PVM also performs External Data Representation (XDR) encoding of data for compatibility across architectures with different data formats.

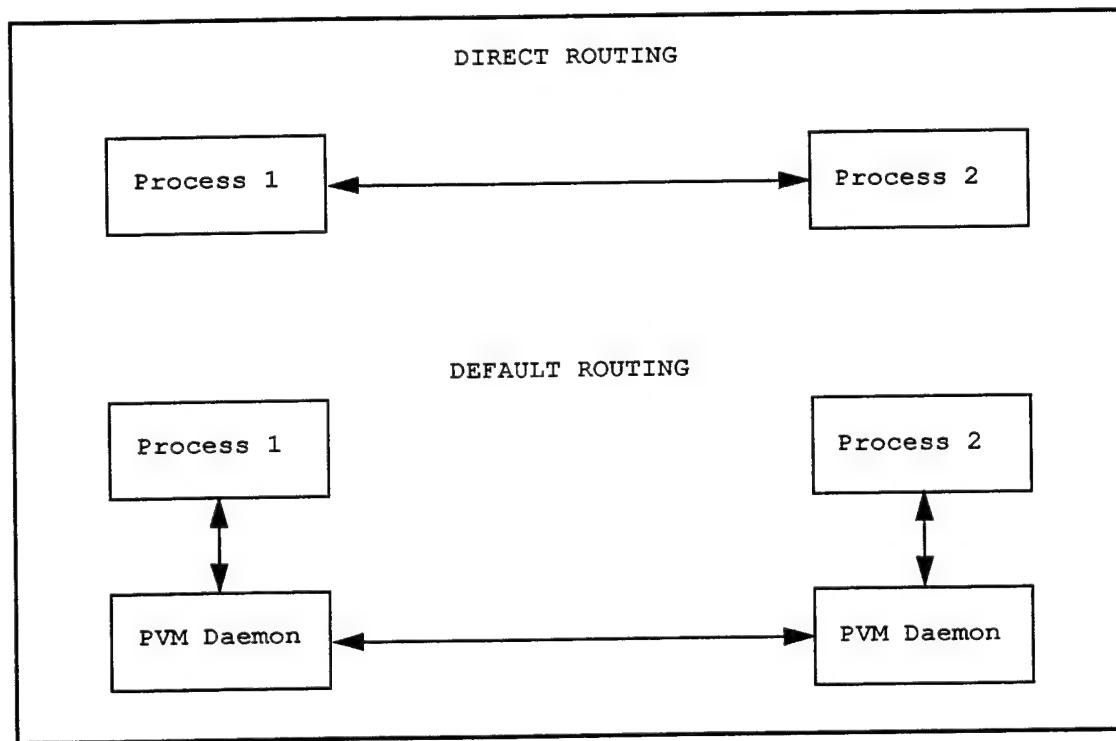


Figure 3. PVM Routing Options.

PVM functions were used to start up processes on the hosts, to transfer files to the appropriate hosts, and to allow communication between the host controller, cluster controller, and flow solver. Through the use of PVM in the parallel XAIR, the user can specify the host and solver to be used with each sub-domain as well as the number of solvers and sub-domains per host. Specifying what hosts advances a particular sub-domain offers two advantages. First, flow solvers which are highly vectorized may be placed on vector computers. Second, sub-domains with the greatest computational requirement may be placed on computers with the greatest computing power.

The final step was implementation of error control and cleanup. Due to the possibility of an uncontrollable error causing a process to fail (e.g.,

disk full, host failure, network failure,...), some type of error control and cleanup is needed. Signals and signal handlers were chosen for this task. Signals inform processes of the occurrence of asynchronous events and may be sent by other processes or by the operating system. Signal handlers are basically subroutines which are executed upon a signal detection.

The abort and alarm signals were chosen and a signal handler established. The abort signal was used to notify other processes of a failure resulting from errors which the program could detect through error checking. For example, if a disk was full, a write to disk would fail and be detected. When a failure was detected, the signal handler would use PVM to send abort signals to all other known processes before exiting. If a host controller detected a signal and the controller was not on the cluster controller processor, the host controller would also remove all files which had been transferred to that host before exiting. The alarm signal was added to detect errors when a failing process was unable to send a signal (e.g. host crash). The time to wait before the alarm goes off is specified by the user. Each time step, the alarm timer of every process is reset to the user specified time. If the alarm reset does not occur within the specified period of time, the alarm goes off and the signal handler is called.

Results

Initial testing of the parallel XAIR was performed on a four node cluster of DEC AXP 3000/800 processors interconnected by a Gigaswitch. The original test case consisted of four sub-domains labeled "grida", "gridb", "gridc", and "gridd". Each grid consisted of 54,000 points, but dimensions in each computational direction varied. Timing was performed with the C shell time function. This function is a measure of wall clock time only and variances did occur due to processor and network load variations.

Table 1 and Table 2 show the comparison of the original XAIR with the parallel XAIR on one, two, three, and four processors. Efficiency in the tables is calculated as the time/step/grid of the original XAIR divided by the time/

step/grid of the parallel XAIR. Efficiency results from Table 1 show the communication cost between processes for the one processor case was less than one percent because of PVM's ability to take advantage of communication within a host. The addition of other hosts minimally increased communication costs due to the high speed Gigaswitch connection. Accordingly, the two processor case should have a lower efficiency than the one processor case. With two processors, two out of the four grids must be transferred across the network to double the processing power. On the other hand, with four processors, only three out of the four grids must be transferred while processing power is quadrupled. Therefore, the four processor case should provide a higher efficiency than the two processor case. However, the 92.6% efficiency shown for the two processor case is probably too low and may be attributable to CPU usage by other users. Unfortunately, time restrictions prevented conclusive proof of this conjecture.

	Original XAIR	Parallel XAIR 1 Processor	Parallel XAIR 2 Processors	Parallel XAIR 4 Processors
Time Steps	425	425	425	425
Total Time (hrs:min:sec)	4:53:42	4:55:47	2:38:42	1:15:06
s/step/grid	10.37	10.44	11.2	10.6
s/step/grid/proc	10.37	10.44	5.6	2.65
Percent Efficiency	100	99.3	92.6	97.8

Table 1.

The three processor case was added to Table 2 to illustrate maximum speedup is dependent on the host which takes the longest to advance all of its sub-domains. With three processors and four grids, two of the processors will be wasted while the other one advances its second grid. Therefore, the maximum efficiency should be 66.7%. In light of this, the 65.5% actual efficiency is quite good.

	Parallel XAIR 2 Processors	Parallel XAIR 2 Processors	Parallel XAIR 3 Processors	Parallel XAIR 4 Processors
Time Steps	150	75	75	75
Total Time (min:sec)	53:33	26:53	26:26	13:43
s/step/grid	10.71	10.75	15.84	10.71
s/step/grid/proc	5.36	5.38	5.28	2.74
Percent Efficiency	96.8	96.5	65.5	94.5

Table 2.

An initial start-up cost for transferring files to other hosts was calculated with the following assumptions:

1. Time to transfer each grid is equivalent.
2. Computation time is proportional to the number of time steps to advance.

From the above assumptions, the following equation can be derived:

$$\tau_0 = (\beta \tau_2 - \tau_1) / (\beta - 1)$$

where: τ_0 = start-up time

τ_1 = total time 1

τ_2 = total time 2

β = computation time 1 / computation time 2

\approx time steps 1 / time steps 2

For two processors, the evaluation of the 75 and 150 time step cases yielded a start-up time of 6.4 seconds per grid transferred.

Conclusions

This paper presents the implementation details of the parallelization of the chimera based flow solver XAIR. The use of domain decomposition allowed a straightforward parallel implementation of XAIR without major changes to the original code. The parallel XAIR operated efficiently under the test cases presented.

This research provides a basis from which further research and improvements may begin. The ability to calculate moving mesh and turbulence models are a must for this software to become a part of a productive CFD solution. Further research may also be directed into I/O techniques such as memory mapping. Additionally, future portability must be maintained as the Message Passing Interface Standard is implemented for parallel communication.

References

- [1] Geist, A., Beguelin, A., Dongarra, J., Jiang, W., Manchek, R., and Sunderam, V., "PVM 3 User's Guide and Reference Manual," ORNL/TM-12187, May 1994.

- [3] Benek, J., Dietz, W., Evans, S., Hoffman, P., Suhs, N., and Thomson, W., "A Domain Decomposition Approach for Applying PVM to Navier-Stokes and Other Time-Dependent Problems," PVM User Group Conference, May 19-20, 1994.

PREDICTION OF THE PERFORMANCE OF
A 7-STAGE AXIAL-FLOW COMPRESSOR
WITH WATER INGESTION
USING A SINGLE-PHASE MODEL

Curtis S. Mashburn
Graduate Student
Department of Aerospace Engineering

University of Tennessee Space Institute
B.H. Goethert Highway
Tullahoma, Tennessee 37388

Final Report for:
Graduate Student Research Program
Arnold Engineering Development Center

Sponsored by:
Arnold Engineering Development Center
Arnold AFB, Tullahoma, Tennessee
and
Sverdrup Technology, Inc.
AEDC Group
Arnold AFB, Tullahoma, Tennessee
and
Air Force Office of Scientific Research
Bolling AFB, Washington, DC.

August 1994

PREDICTION OF THE PERFORMANCE OF
A 7-STAGE AXIAL-FLOW COMPRESSOR
WITH WATER INGESTION
USING A SINGLE-PHASE MODEL

Curtis S. Mashburn
Graduate Student
Department of Aerospace Engineering
University of Tennessee Space Institute

Abstract

A single-phase analytical model has been developed to predict the performance of an axial-flow compressor with liquid water ingestion. Performance of a generic 7-stage axial compressor operating at three corrected rotation speeds, three corrected mass flow rates, and five mixture compositions was predicted using the model. The effects of liquid water ingestion upon power absorption, total pressure, static pressure, total temperature, and static temperature were predicted. The direction of the performance trends predicted by the model were found to agree with the direction of the performance trends obtained by S.N.B. Murthy; however, the magnitudes of the predicted performance trends could not be directly compared with Murthy's predicted performance trends due to differences in model output parameters between this model and Murthy's model. ² This model predicts much higher evaporation rates than Murthy's model. Murthy's model predicts little evaporation of water, while this model predicts complete evaporation of water for the same mass fractions of liquid water.

PREDICTION OF THE PERFORMANCE OF
A 7-STAGE AXIAL-FLOW COMPRESSOR
WITH WATER INGESTION
USING A SINGLE-PHASE MODEL

Curtis S. Mashburn

Introduction

The first step in understanding the effects of water ingestion on an aircraft gas turbine engine, is to understand the effects of water ingestion on the axial-flow compressor. A search of open literature on the subject revealed that S.N.B. Murthy has extensively studied this phenomenon and produced a complex two-phase model to predict the performance of a fan and compressor and has incorporated this model into a transient engine model.¹ The purpose of this study was to see if a much simpler model could be produced that would predict similar performance trends to those predicted by Murthy for an axial-flow compressor.² It was chosen to use a steady-state, single-phase, constant-radius, isentropic, stage-stacking model. The performance characteristics predicted by this model for a 7-stage axial compressor are presented and discussed.

Analytical Model

The analytical model is a steady-state, single-phase, constant-radius, isentropic, stage-stacking model. The model treats the mixture of air, water-vapor, and liquid water as an ideal-gas continuum. This is done by mass averaging the individual component properties of constant pressure specific heat, and specific gas constant, to obtain mixture properties of constant pressure specific heat and specific gas constant. These mixture properties are used to calculate the ratio of specific heats for the mixture which is equal to the constant pressure specific heat of the mixture divided by the difference between the mixture constant pressure specific heat and the mixture specific gas constant. These properties describe an idealized composition of the mixture which can change in every blade row since evaporation, condensation, and vaporization are allowed to occur.

For this isentropic model, the relative total pressure of the mixture is constant across a blade row. In order to conserve energy, the relative total enthalpy of the mixture is constant across a blade row. Since the relative total

enthalpy of the mixture per unit mass is defined as the product of the constant pressure specific heat of the mixture and the relative total temperature of the mixture, the relative total temperature of the mixture across a blade row will only be constant if the constant pressure specific heat of the mixture is constant across a blade row. The constant pressure specific heat will change across a blade row if the composition of the mixture changes. The composition of the mixture can change due to evaporation, condensation, or vaporization in the blade row.

The model assumes that α_1 , the rotor inlet air angle, which is the same as α_3 , the stator exit air angle from the previous blade row, is constant, and is equal to the design value, as is β_2 , the relative exit air angle from the rotor.³ This implies that the exit deviation angles for the blade rows are fixed at the design values for the off-design calculations because, the stator blade angles are also assumed constant and fixed at the design values. Because of these assumptions, flow turning is increased at lower rotation speeds because, the blade inlet air angles are smaller, but the exit air angles are held constant. This increased flow turning produces increased blade row diffusion factors, which lead to unrealistically high performance at some off-design conditions.

The determination of mixture composition is based on the relative humidity which is assumed to be held at 100% in each blade row if possible.⁴ If there is not enough liquid water in the blade row to hold the relative humidity at 100%, then all of the liquid water that is available in the blade row is assumed to evaporate. Also, all the liquid water in the blade row is assumed to vaporize if the static temperature of the mixture at the entrance to the blade row is greater than the boiling temperature for water at the inlet static pressure of the mixture.

Model Predictions and Analysis

The modeled compressor was a 7-stage, constant mean-line design compressor fitted with an isentropic bell mouth inlet. The bell mouth inlet had an inlet area of 4.7983 m^2 , and an exit area of 0.1206 m^2 . The mean radius of the compressor was 0.1697 meters. The design rotation speed and mass flow of the compressor were 15000.15 rpms, and 20.00 kg/s respectively. The compressor did not have inlet guide vanes. The design point simulated

flight conditions at the inlet were Mach 0.01, and sea level, standard day, static temperature and static pressure.

The design point parameters for the compressor are shown in Table 1.

The model was used to predict the performance of the compressor for 45 cases. Three corrected rotation speeds 15000, 13500, and 12000 rpms, at three corrected mass flows 20.00, 18.00, and 16.00 kg/s, at four mass fractions of liquid water 0.00, 0.05, 0.10, 0.15, and dry air. For the four cases with liquid water ingestion, the inlet relative humidity was 100%. The following 18 figures show compressor power absorption verses stage, mass flow of liquid, total temperature, total pressure, static temperature, and static pressure verses station, for the three corrected rotation speeds. The compressor station descriptions are explained in Table 2. In the figures, the first term in the legend for each curve is the corrected mixture mass flow (MDOTC), and the second term is the initial mass fraction of liquid water (MFL). In the simulation, some of the possible simulation point combinations would not run to the end of the simulation. The figures show the data points for each combination that were obtained before the simulation stopped. The simulation would stop when the solution to the conservation equations across a blade row could not be found.

Through all of the figures, some trends are apparent. (1) The difference between the curves for dry air and saturated air is negligible. (2) The number of blade rows that could be simulated before the program stopped, decreased, with increasing mass fraction of liquid water, with increasing corrected mass flow, and with increasing corrected rotation speed. (3) As the corrected rotation speed decreases from the design corrected speed, the curves begin to spread out. This spreading is due to the constant stator angle settings assumed in the simulation. All of the figures show one or more curves that have a large oscillation in magnitude. Those curves do not follow the general pattern of the other curves. In all of those oscillating cases, the compressor was evaporating and condensing large amounts of water in an oscillating pattern. It was determined, that this was caused by the simulation converging on an alternate mixture composition that satisfied the conservation equations.

Figures 1, 2, and 3 show the compressor power absorption in each stage for a corrected rotation speed of 12000, 13500, and 15000 rpms, respectively. The compressor power absorption is the difference between the total enthalpy at the exit of the rotor row and the total enthalpy at the inlet of the rotor row. The three figures show that the power absorption decreases, as the corrected rotation speed decreases, as the mass fraction of liquid water increases, and as the corrected mass flow increases. When the power absorption is negative, the rotor exit total enthalpy is less than the rotor inlet total enthalpy. This means that the stage is producing power and acting like a turbine stage.

Figures 4, 5, and 6 show the mass flow of liquid water at each station of the compressor for a corrected rotation speed of 12000, 13500, and 15000 rpms, respectively. The three figures show that the rate of evaporation increases with increasing corrected rotation speed. When the curves have a positive slope, water is condensing, and when the curves have a negative slope, water is evaporating. These figures dramatically show the oscillating evaporation and condensation cycles for some of the curves.

Figures 7, 8, and 9 show the total temperature of the mixture at each station of the compressor for a corrected rotation speed of 12000, 13500, and 15000 rpms, respectively. The three figures show that the total temperature increases, as the corrected rotation speed increases, as the corrected mass flow rate decreases, and as the initial mass fraction of liquid water decreases. In the figures, when the total temperature is constant across a stator row, the composition of the flow does not change across the stator row. When the curve corresponding to a stator row has a non-zero slope, the mixture composition is changing across the stator row. A positive slope indicates that water is evaporating in the stator row, while a negative slope indicates that water is condensing in the stator row. In the initial stages the total temperatures are higher for the cases that have higher initial mass fractions of liquid water, but in the later stages the total temperatures are higher for the cases that have lower initial mass fractions of liquid water.

Figures 10, 11, and 12 show the total pressure of the mixture at each station of the compressor for a corrected rotation speed of 12000, 13500, and 15000 rpms, respectively. The three figures show that the total pressure increases, as the corrected rotation speed increases, as the corrected mass flow decreases, and as the initial mass fraction of liquid decreases.

Figures 13, 14, and 15 show the static temperature of the mixture at each station of the compressor for a corrected rotation speed of 12000, 13500, and 15000 rpms, respectively. The figures for the static temperature are similar to the figures for the total temperature. The same trends were observed.

Figures 16, 17, and 18 show the static pressure of the mixture at each station of the compressor for a corrected rotation speed of 12000, 13500, and 15000 rpms, respectively. The figures for the static pressure are similar to the figures for the total pressure. The same trends were observed.

Conclusions

The model predicts that the power absorption increases with increased corrected rotation speed, decreased initial mass fraction of liquid, and decreased corrected mass flow. The evaporation rate increases with increased rotation speed. The compressor can handle greater mass fractions of liquid water at lower corrected mass flows and at lower corrected rotation speeds. The overall compressor mixture total temperature decreases as the corrected rotation speed decreases, as the corrected mass flow rate increases, and as the mass fraction of liquid increases. The mixture static temperature follows the same trend as the mixture total temperature. The overall compressor mixture total pressure decreases as the corrected rotation speed decreases, as the corrected mass flow rate increases, and as the mass fraction of liquid increases. The mixture static pressure follows the same trend as the mixture total pressure. The model predicted that the compressor performance, when operated with dry air, and when operated with initially saturated air, was essentially the same. The above trends agree in direction with the trends reported by S.N.B. Murthy.² Although, the trends agree in direction with Murthy's, this model has not been verified, and is known to predict unrealistically high performance for some of the off-design cases. The oscillating cycles of

evaporation and condensation for some of the curves was caused by a deficiency in the model that allowed the model to converge on an alternate mixture composition, that satisfied the conservation equations. The erratic behavior of the curves at off-design corrected rotation speeds was due to another deficiency in the model, which assumed that the stator blade angles were constant, and that the blade row exit air angles were constant.

References

1. Haykin, T. and Murthy, S.N.B., "Transient Engine Performance with Water Ingestion," *J. Propulsion and Power* Jan.-Feb., 1988.
2. Tsuchiya, T. and Murthy, S.N.B. "Water Ingestion into Jet Engine Axial Compressors," AIAA Paper No. 82-0196, Jan. 1983.
3. Cohen, H., Rogers, C.F.C., and Saravanamuttoo, H.I.H., *Gas Turbine Theory*, John Wiley & Sons, Inc., New York, NY, 1991.
4. Van Wylen, Gordon J., and Sonntag, Richard E., *Fundamentals of Classical Thermodynamics*, John Wiley & Sons, Inc., New York, NY, 1986.

Table 1. 7-Stage Axial-Flow Design Point Parameters ³

STAGE	1	2	3	4	5	6	7
CA2 (m/s)	135.59	133.03	135.93	132.63	130.21	128.08	124.22
CW2 (m/s)	76.27	123.76	168.57	167.24	166.66	166.71	162.11
ALPHA2 (deg)	29.36	42.93	51.12	51.59	52.00	52.47	52.54
BETA2 (deg)	54.53	47.03	35.79	36.83	37.50	37.94	40.06
AREA2 (m²)	0.1123	0.0965	0.0825	0.0705	0.0606	0.0525	0.0465
CA3 (m/s)	145.17	139.77	135.90	133.10	131.19	128.24	123.59
CW3 (m/s)	28.38	76.30	74.19	72.66	71.61	70.01	67.16
ALPHA3 (deg)	11.06	28.63	28.63	28.63	28.63	28.63	28.52
BETA3 (deg)	58.64	53.70	54.76	55.53	56.06	56.88	58.21
AREA3 (m²)	0.1039	0.0891	0.0759	0.0650	0.0560	0.0489	0.0439

Table 2. Compressor Station Descriptions

Station	Description	Station	Description	Station	Description
-1	Bell mouth Inlet	3	Stage 3 Rotor Inlet	6	Stage 6 Rotor Inlet
0	IGV Inlet	3.5	Stage 3 Stator Inlet	6.5	Stage 6 Stator Inlet
1	Stage 1 Rotor Inlet	4	Stage 4 Rotor Inlet	7	Stage 7 Rotor Inlet
1.5	Stage 1 Stator Inlet	4.5	Stage 4 Stator Inlet	7.5	Stage 7 Stator Inlet
2	Stage 2 Rotor Inlet	5	Stage 5 Rotor Inlet	8	Stage 7 Stator Exit
2.5	Stage 2 Stator Inlet	5.5	Stage 5 Stator Inlet		

Figure 1. Power Absorption vs. Stage for a Corrected Rotation Speed of 12000 rpm

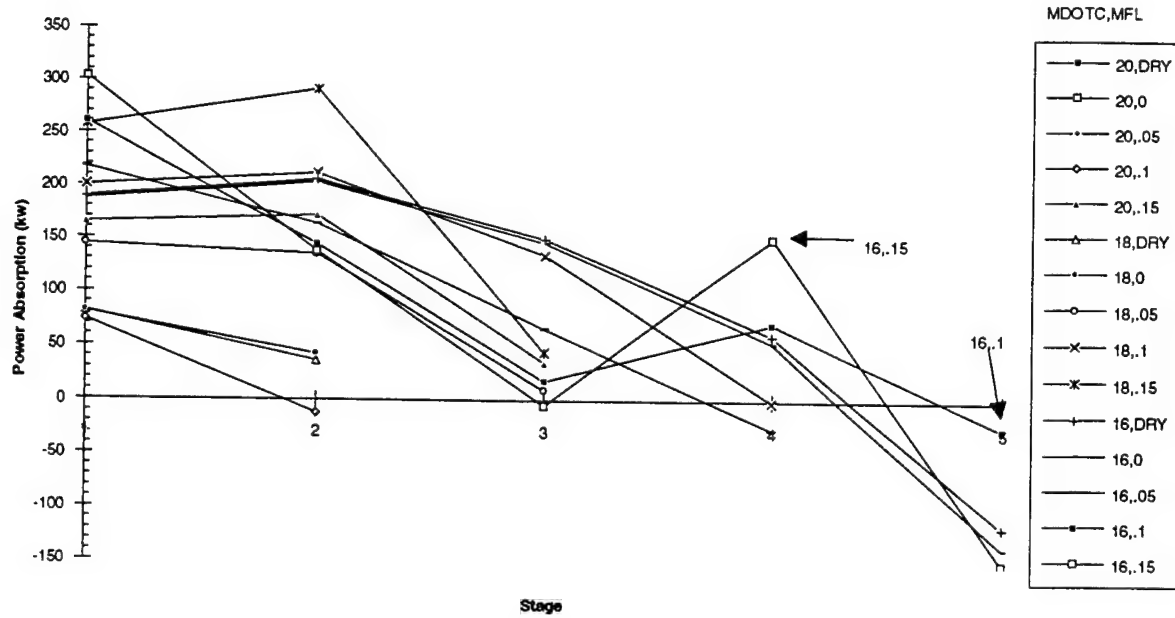


Figure 2. Power Absorption vs. Stage for a Corrected Rotation Speed of 13500 rpm

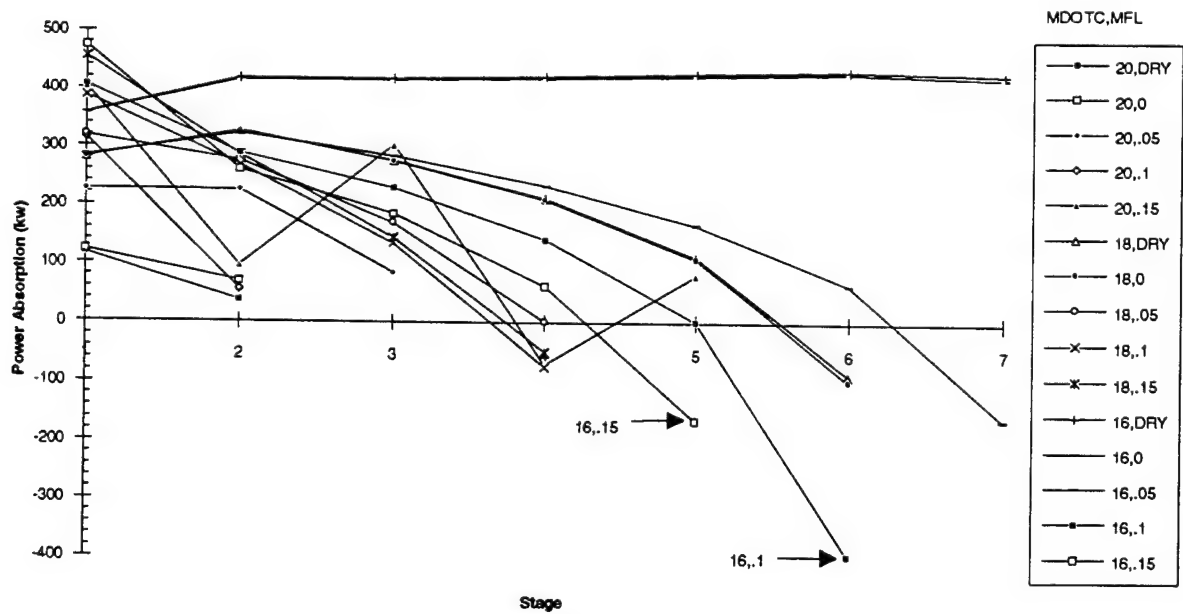


Figure 3. Power Absorption vs. Stage for a Corrected Rotation Speed of 15000 rpm

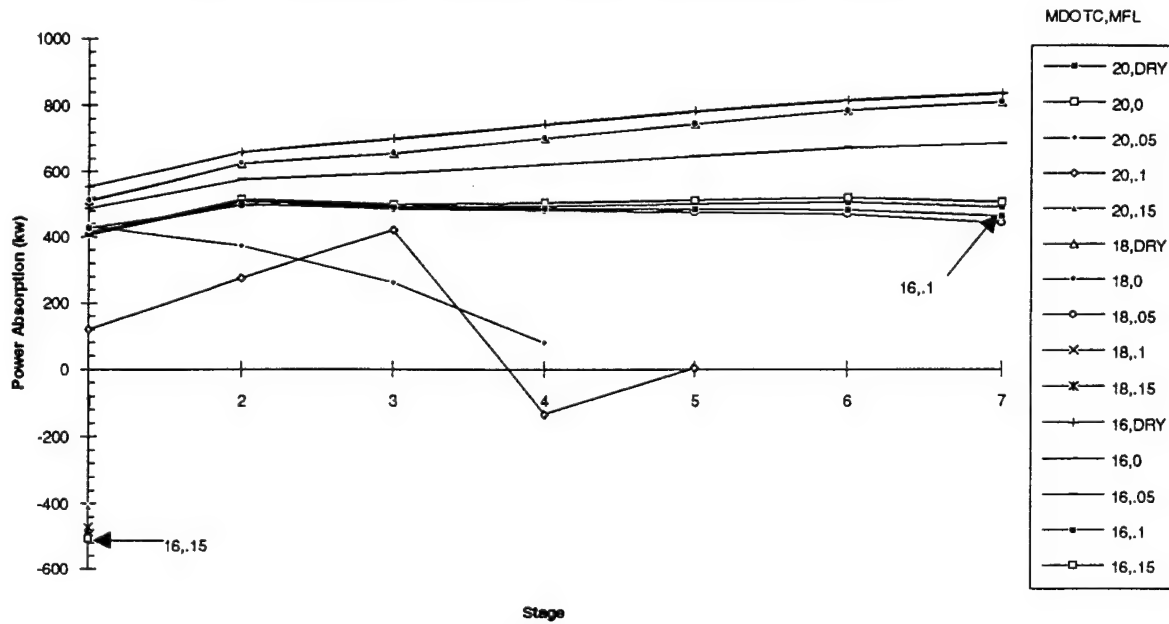


Figure 4. Mass Flow of Liquid Water vs. Station for a Corrected Rotation Speed of 12000 rpm

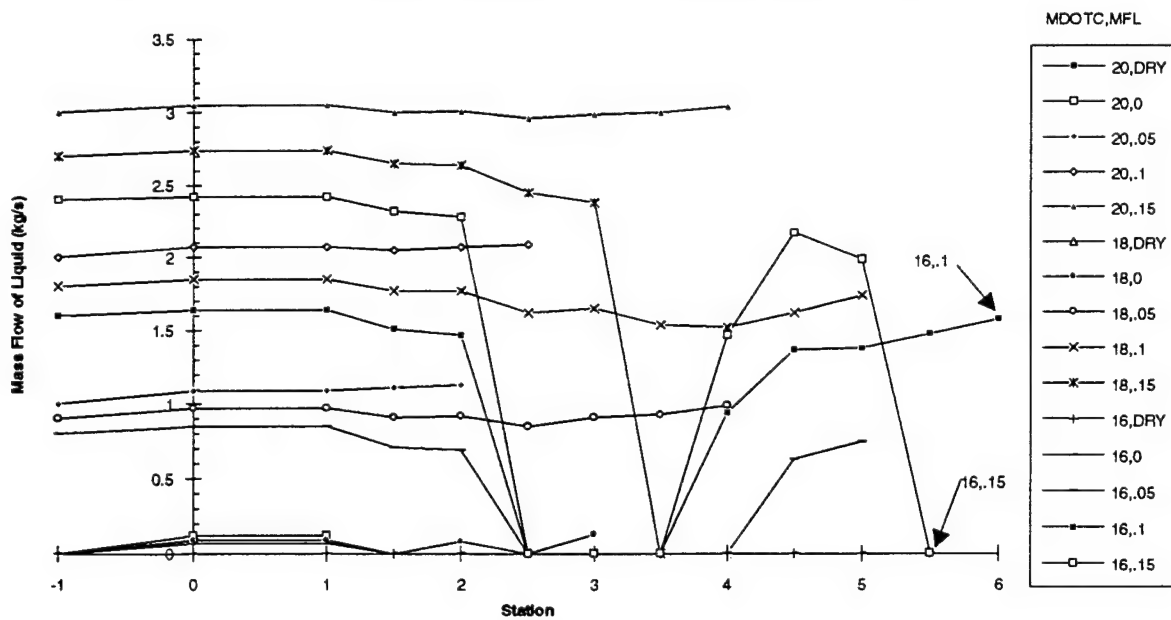


Figure 5. Mass Flow of Liquid Water vs. Station for a Corrected Rotation Speed of 13500 rpm

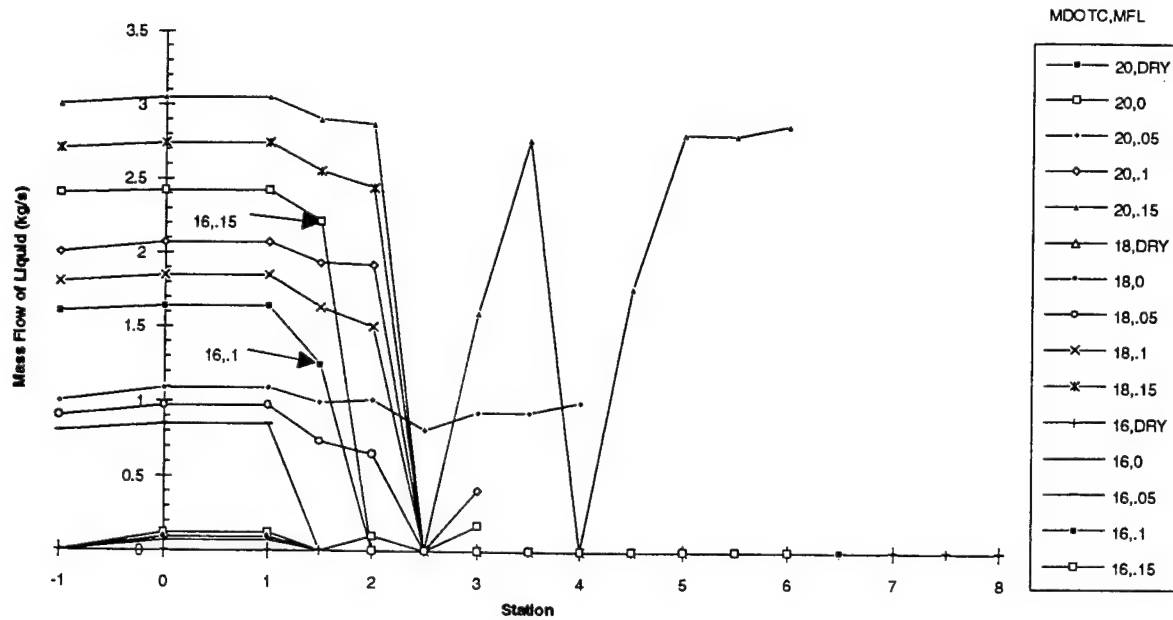


Figure 6. Mass Flow of Liquid Water vs. Station for a Corrected Rotation Speed of 15000 rpm

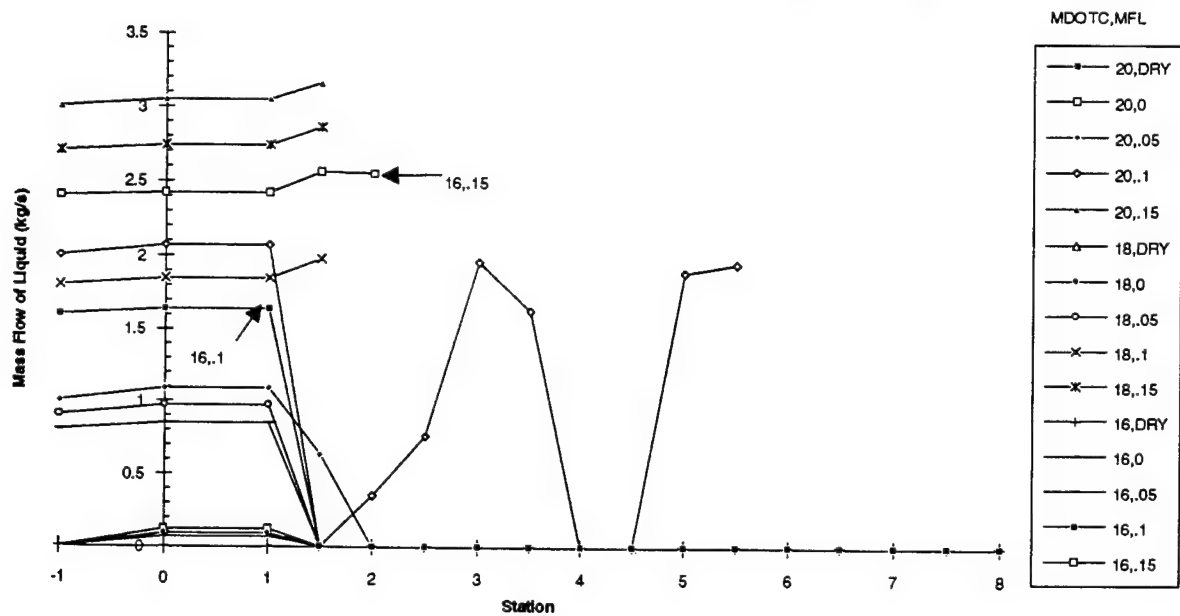


Figure 7. Total Temperature vs. Station for a Corrected Rotation Speed of 12000 rpm

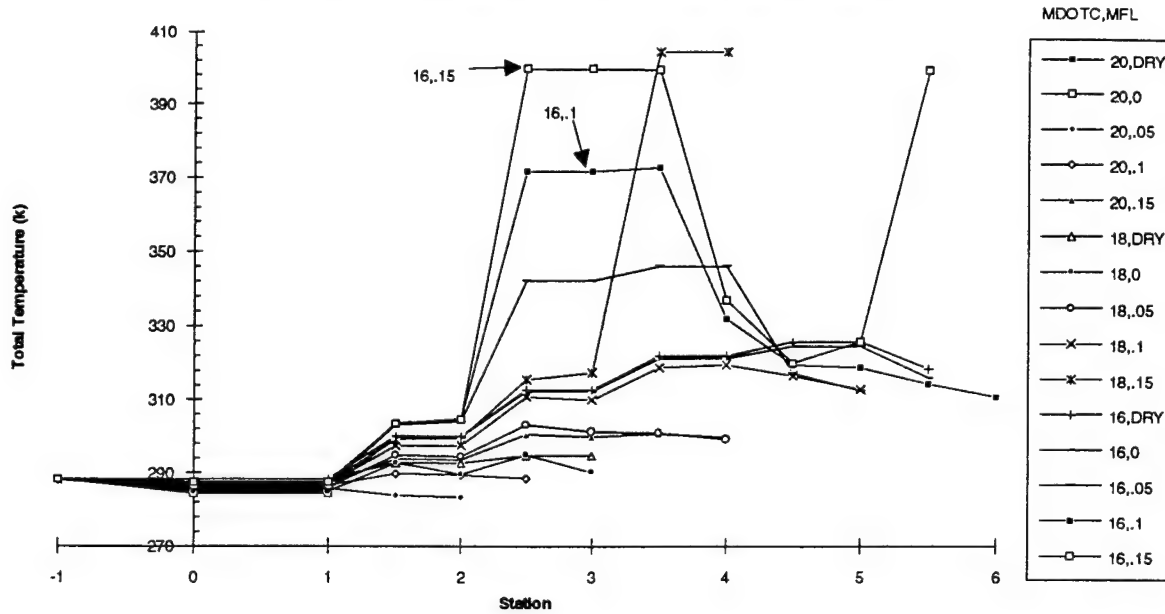


Figure 8. Total Temperature vs. Station for a Corrected Rotation Speed of 13500 rpm

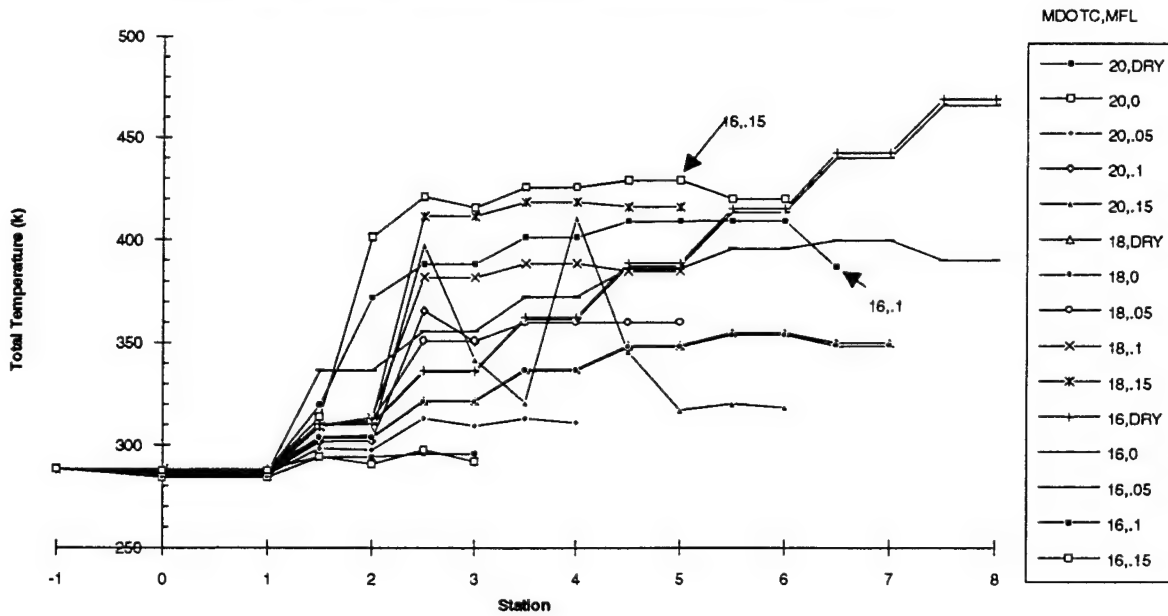


Figure 9. Total Temperature vs. Station for a Corrected Rotation Speed of 15000 rpm

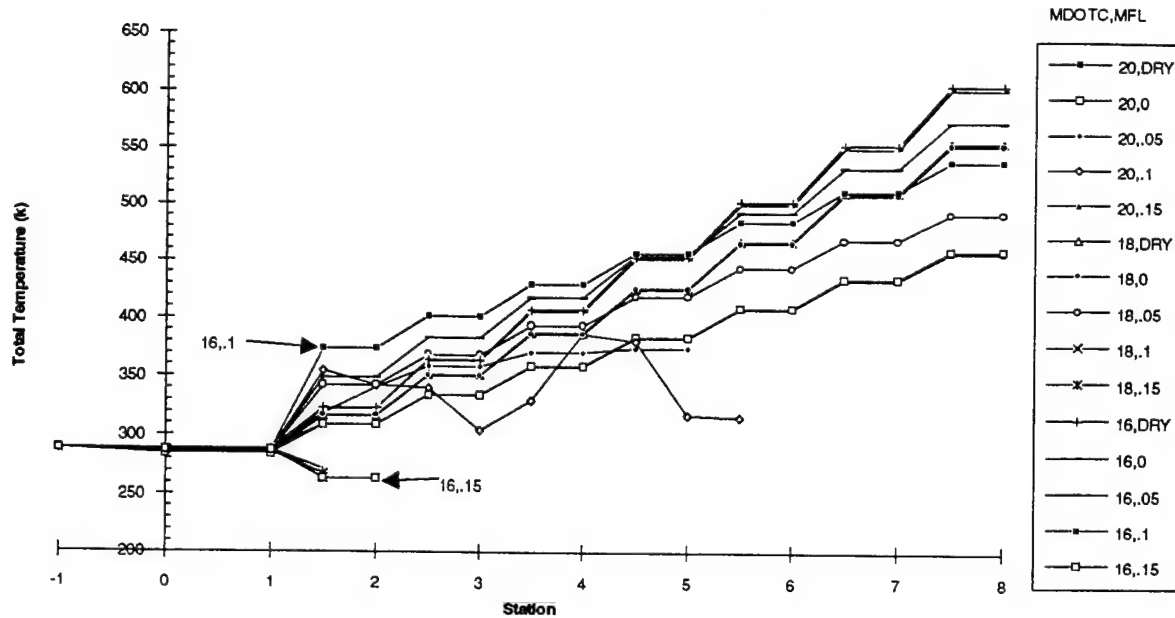


Figure 10. Total Pressure vs. Station for a Corrected Rotation Speed of 12000 rpm

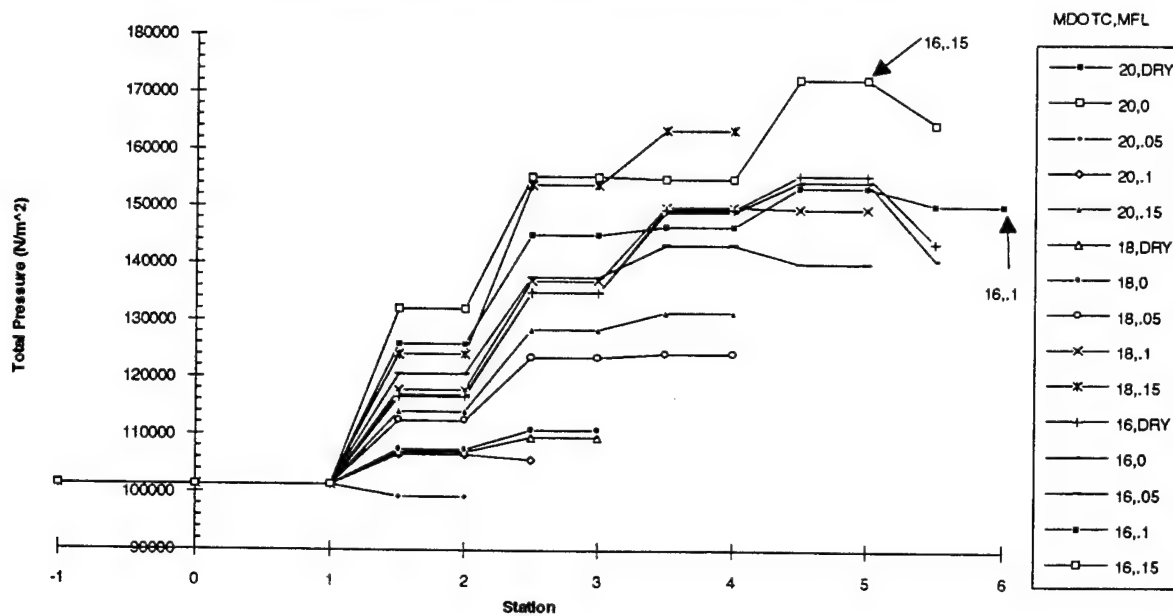


Figure 11. Total Pressure vs. Station for a Corrected Rotation Speed of 13500 rpm

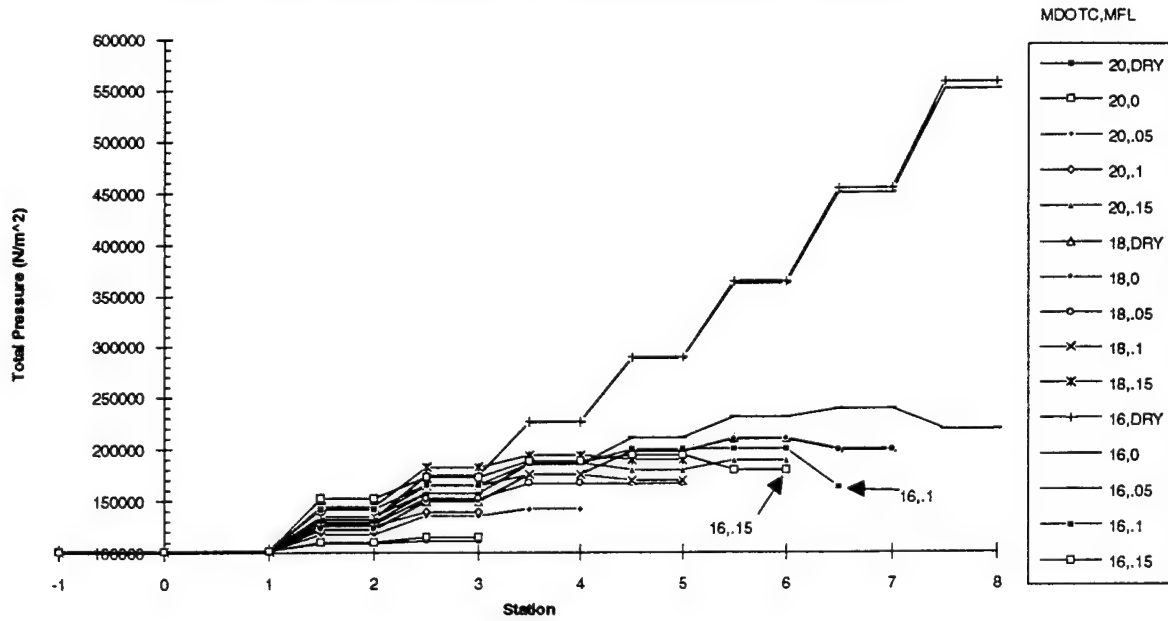
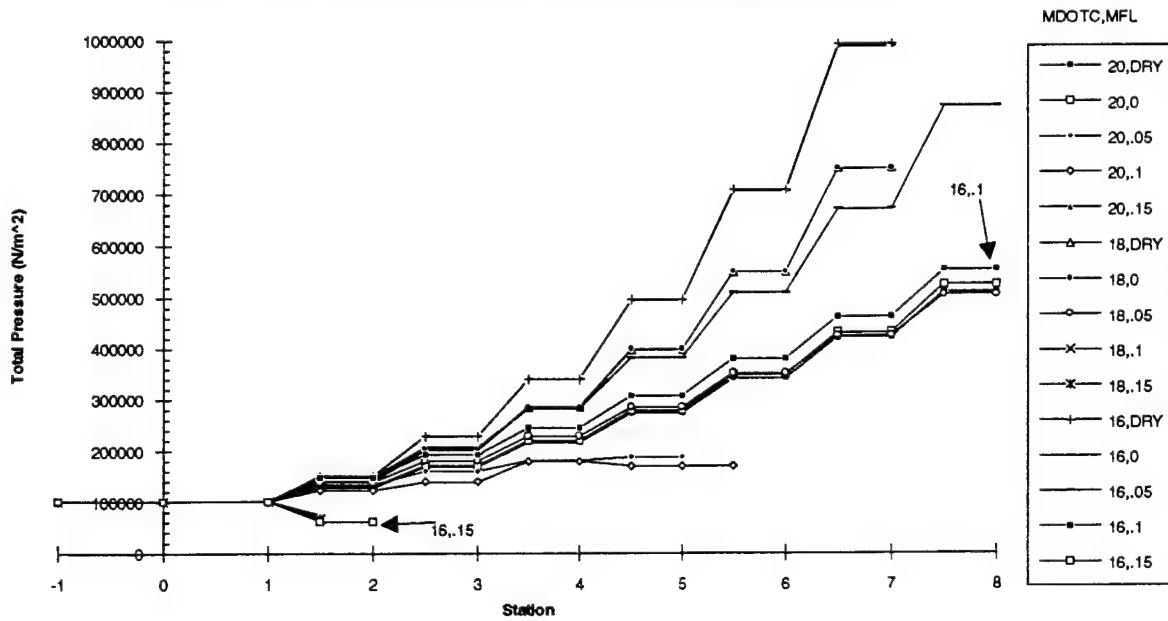


Figure 12. Total Pressure vs. Station for a Corrected Rotation Speed of 15000 rpm



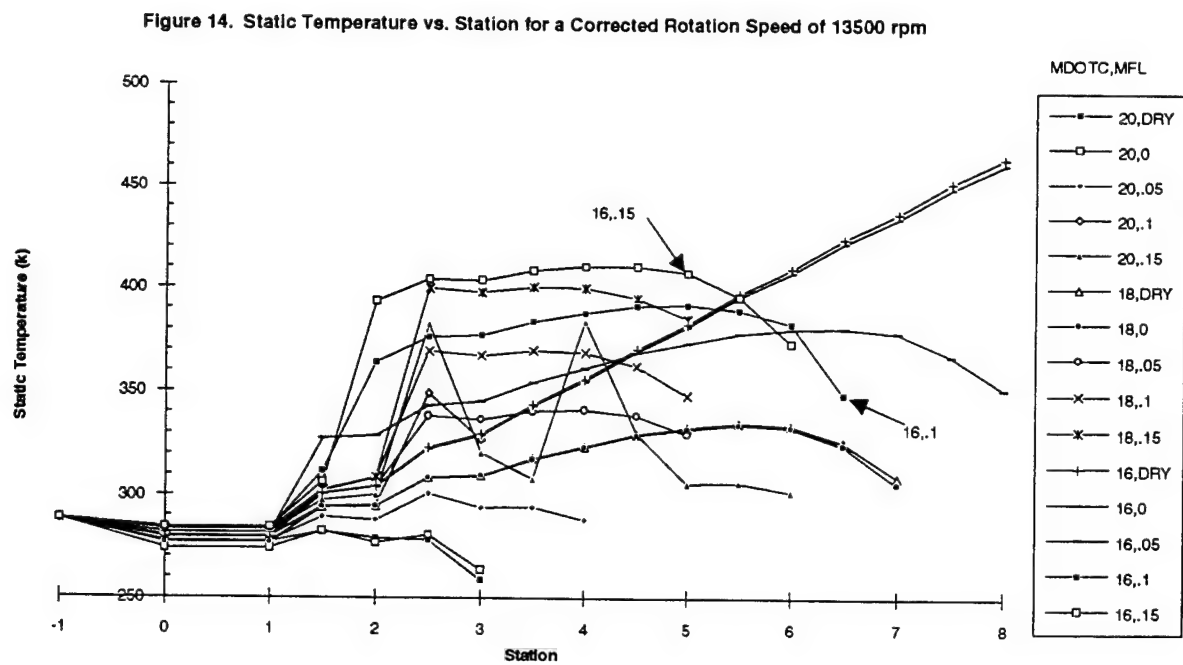
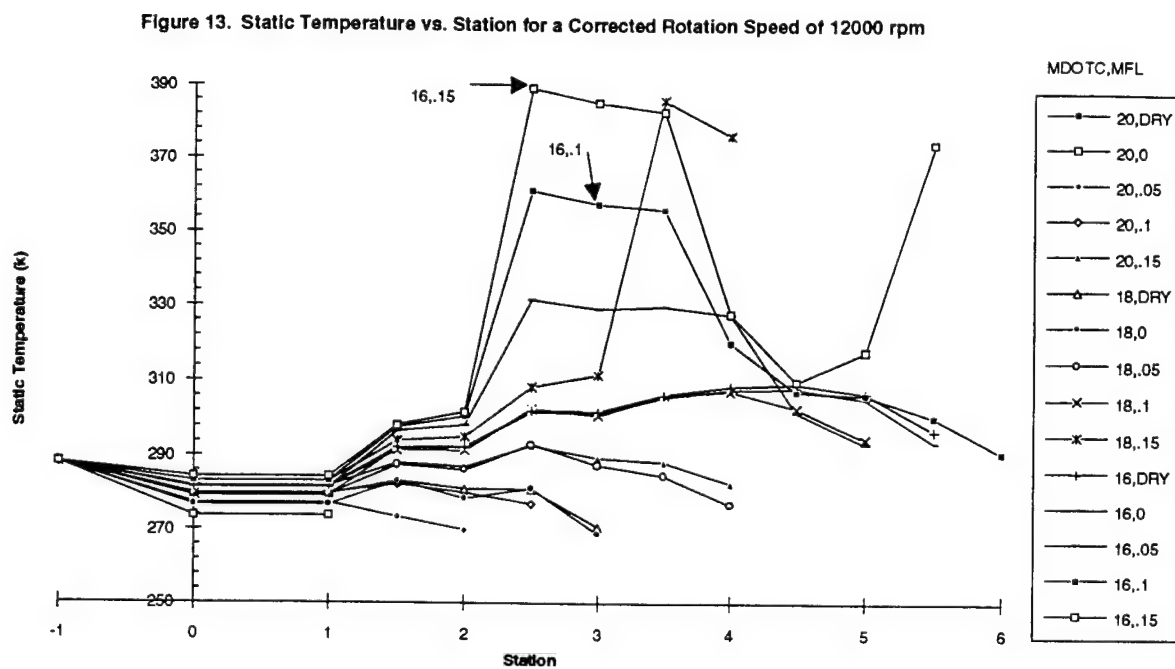


Figure 15. Static Temperature vs. Station for a Corrected Rotation Speed of 15000 rpm

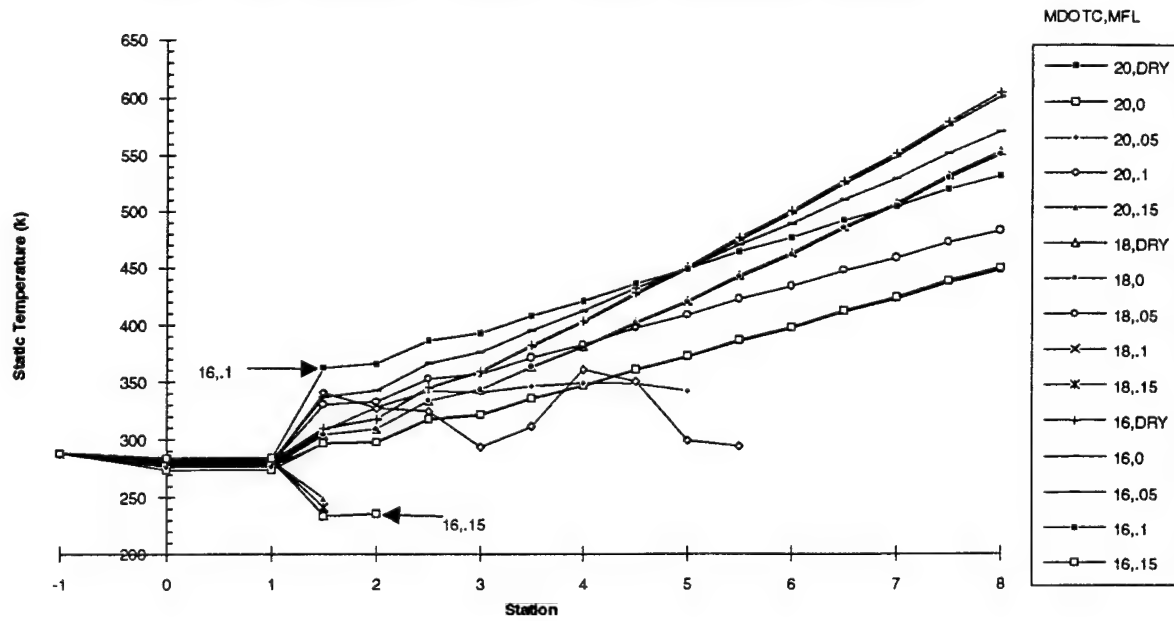


Figure 16. Static Pressure vs. Station for a Corrected Rotation Speed of 12000 rpm

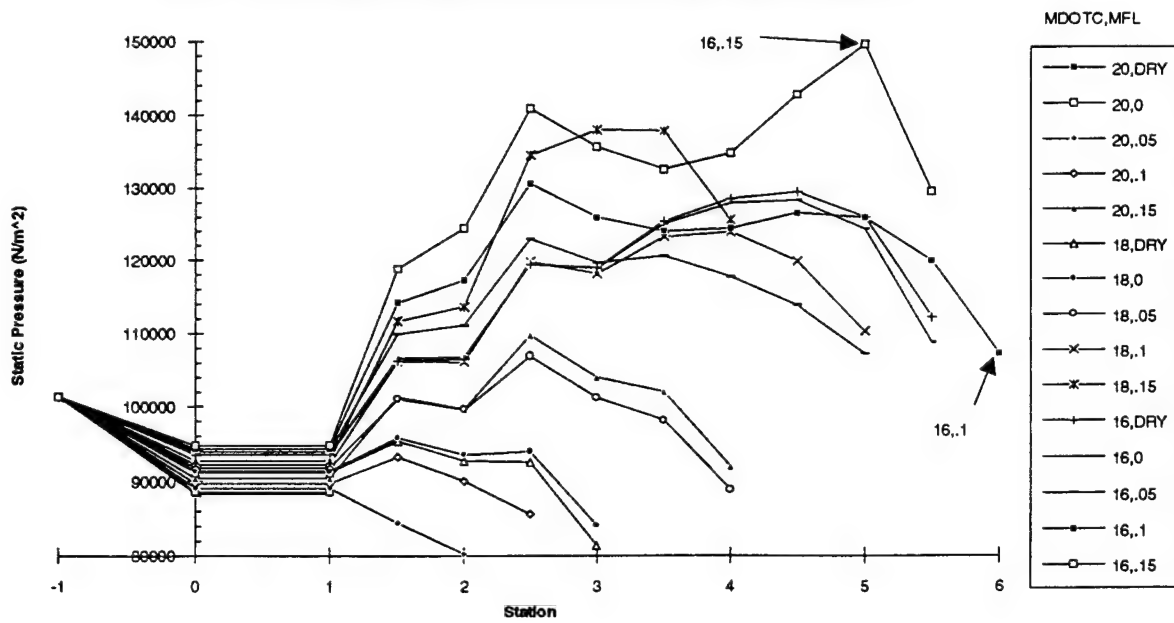


Figure 17. Static Pressure vs. Station for a Corrected Rotation Speed of 13500 rpm

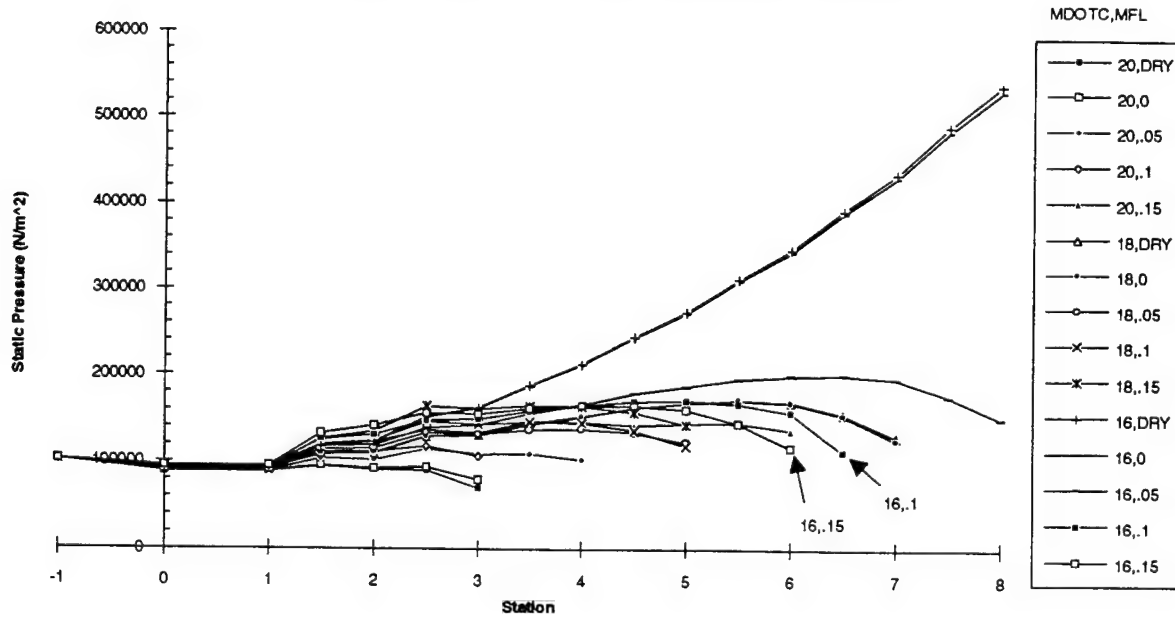
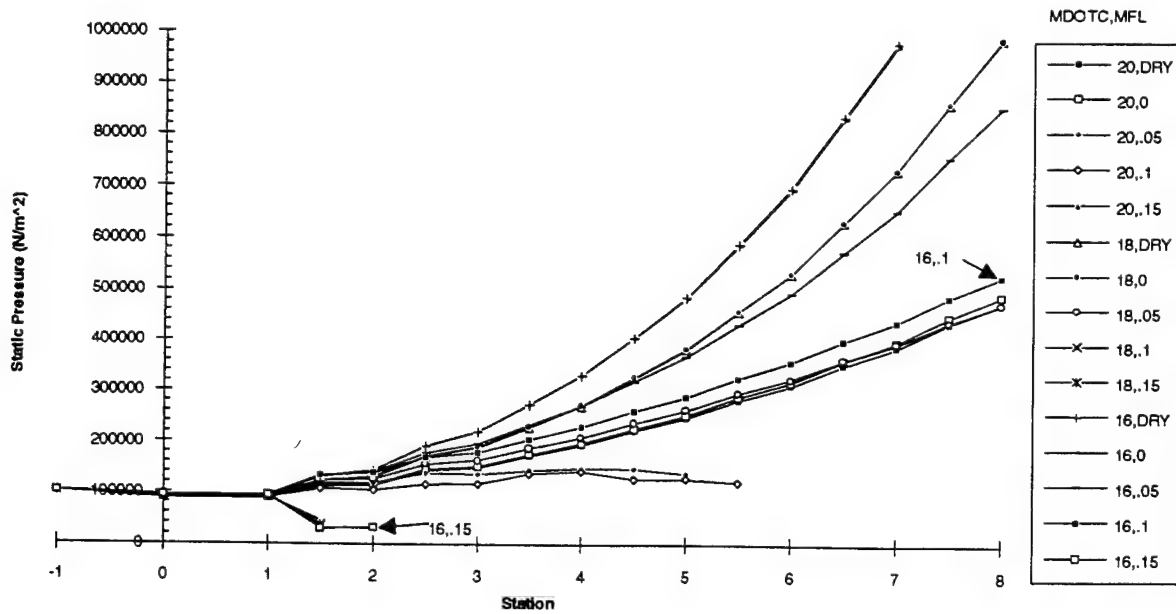


Figure 18. Static Pressure vs. Station for a Corrected Rotation Speed of 15000 rpm



**A COMPARISON OF
HYPERSONIC TEST FACILITIES**

**William Scott Meredith
Graduate Research Assistant
Department of Aerospace and Mechanical Engineering**

**University of Tennessee Space Institute
411 B. H. Goethert Pkwy
Tullahoma, Tn 37388**

**Final Report for:
Graduate Student Research Program
Arnold Engineering Development Center**

**Sponsored by:
Air Force Office of Scientific Research
Bolling Air Force Base, DC**

and

Arnold Engineering Development Center

August 1994

A COMPARISON OF HYPERSONIC TEST FACILITIES

**William Scott Meredith
Graduate Research Assistant
Department of Aerospace and Mechanical Engineering
University of Tennessee Space Institute**

Abstract

This paper is a study of hypersonic test facilities which utilizes research information to compare AEDC test units in the Von Karman Gas Dynamics Facility with other similar hypersonic and supersonic test facilities. AEDC's APTU is compared with the 8-Foot High Temperature Tunnel at NASA's Langley Research Center; Tunnel A at AEDC is compared with the Unitary Plan Wind Tunnel at Langley and with Vought's High Speed Wind Tunnel at Dallas, Texas; Tunnels B and C at AEDC are compared with Tunnel 9 at the Naval Surface Warfare Center.

A COMPARISON OF HYPERSONIC TEST FACILITIES

William Scott Meredith

Introduction

Hypersonic testing is important in the development of aerospace planes, reentry vehicles, and missiles. Therefore, knowledge of available test facilities and their capabilities is of utmost importance. Hypersonic/Supersonic test units in the Von Karman Gas Dynamics Facility at Arnold Engineering Development Center (the Aerodynamic Propulsion Test Unit, Tunnel A, Tunnel B, and Tunnel C) are studied and then compared with similar test facilities. The Aerodynamic Propulsion Test Unit (APTU) is compared to NASA's Langley's 8 -Foot High Temperature Tunnel, Tunnel A is compared with Langley's Unitary Plan Wind Tunnel and Vought's High Speed Wind Tunnel in Dallas, Texas, and Tunnels B and C are compared with Tunnel 9 at the Naval Surface Warfare Center.

APTU

The Aerodynamic Propulsion Test Unit (APTU) at Arnold Engineering Development Center (AEDC) (Figure 1) is a vitiated blown wind tunnel which is suited to perform aerothermal testing of relatively large components and vehicles including full-scale tactical missiles. It also can perform tests of air-breathing propulsion systems such as ram/scram jets. APTU's test cell is 16 feet in diameter, and it has free jet nozzles with exit diameters ranging from 32 to 38 inches and with Mach numbers ranging from 2.2 to 4.1. APTU has an oxygen replenished system which replaces the oxygen consumed by the isobutane-fueled vitiated air heater. It is capable of performing true-temperature-aerodynamic, high-temperature-materials and propulsion tests.

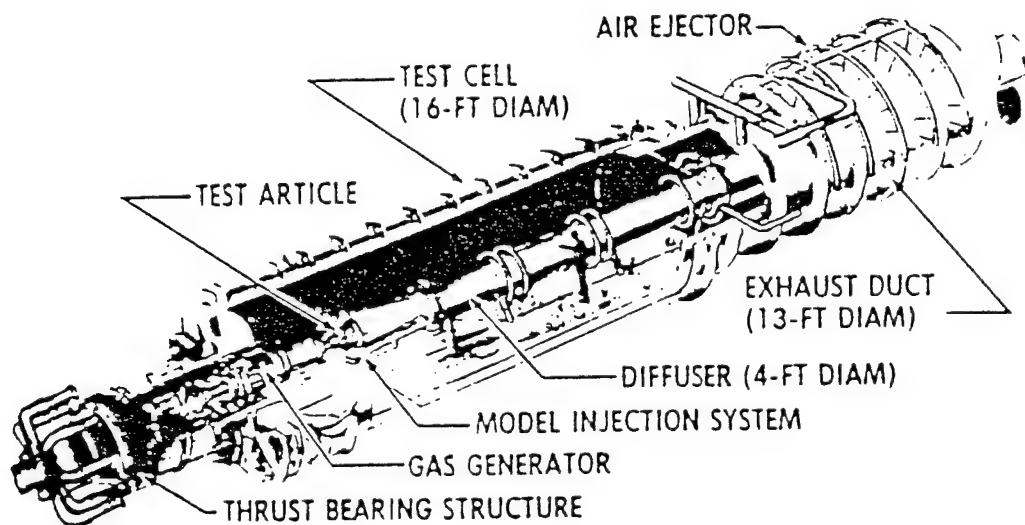


Figure 1 APTU Wind Tunnel at AEDC

8-Foot High Temperature

The 8-Foot High Temperature Tunnel (8' HTT) at NASA's Langley Research Center (LaRC) is a blowdown vitiated air facility. It has primarily been used in aerothermal and thermo-structures testing. Recently an oxygen-enrichment capability has been added which allows propulsion testing to be conducted. The up-grade also added Mach 4 and Mach 5 capabilities to its previous Mach 7 capability. All of the 8' HTT free-jet nozzles have exit diameters of 8 feet. The newly added oxygen enrichment system limits the simulation to higher altitudes because it has a lower operating pressure (2,290 psia) than the tunnel's maximum total combustor pressure (4,000 psia).

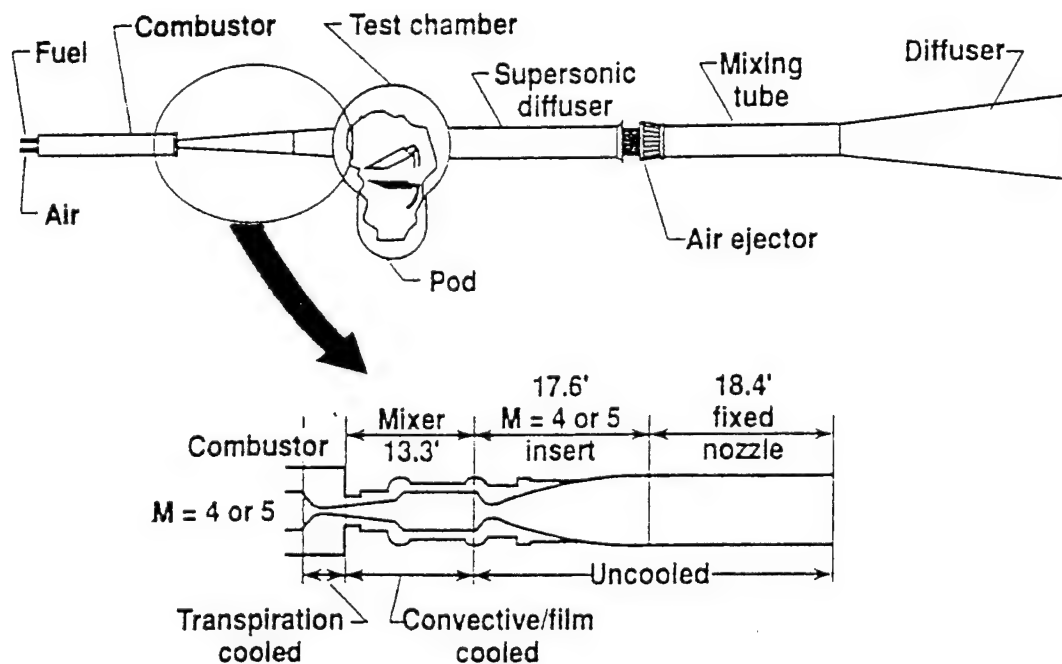


Figure 2 Schematic of Langley's 8' HTT with different nozzle capabilities (From Ref. 2)

Comparison

For propulsion testing, APTU simulates lower altitudes and lower Mach numbers than the 8-Foot High Temperature Tunnel, as seen in Figure 3. Therefore, these two test facilities complement each other's propulsion test capabilities.

For aerothermal-structure testing, the 8-Foot High Temperature Tunnel has definite advantages over APTU. Current APTU configurations limit it to a stagnation pressure of 300 psia and stagnation temperature of 2000°R compared to the 8' HTT's stagnation pressure of 4000 psia and stagnation temperature of 4000°R. With this greater driving potential, the 8' HTT has a three-times greater peak heat flux. However, at peak conditions the 8' HTT can only

run for approximately one second while APTU's maximum run time at peak conditions is 180 seconds. APTU does have hardware on hand which could close this gap by raising its stagnation pressure to 2800 psia and stagnation temperature to 4700°R while providing longer run times.

A summary of the operating capabilities of APTU and the 8'HTT can be seen in Table I.

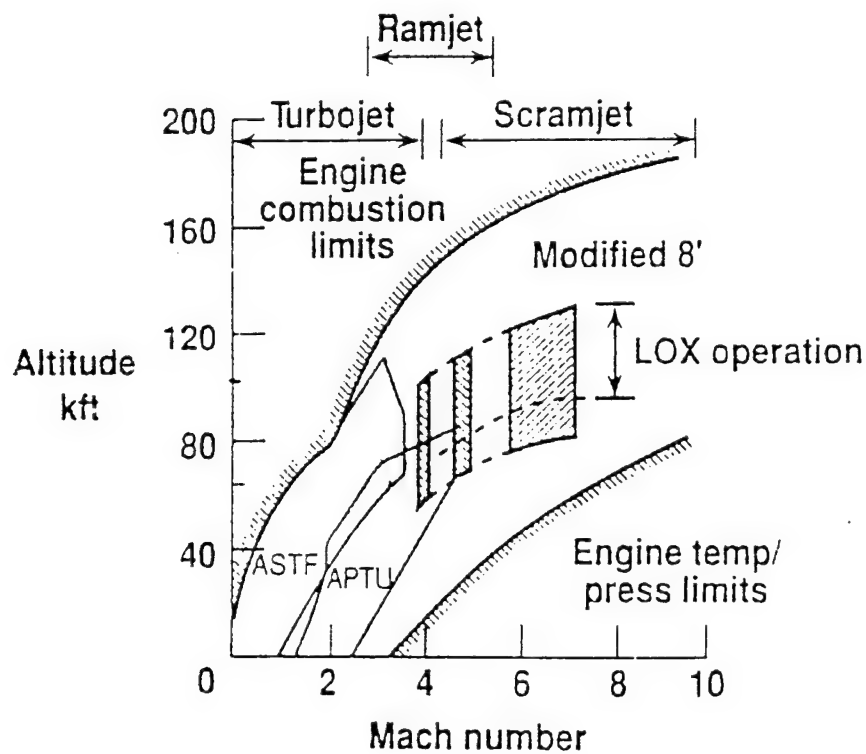


Figure 3 Operational envelopes for air-breathing propulsion test facilities (From Ref. 2)

Table I Comparison of Operating Capability of APTU and 8' HTT

	APTU	8' HTT
Mach numbers	2.2, 2.55, 2.72, 3.5, 4.1	4, 5, 7
Total Pressure (psia)	20 - 300	50 - 4000
Total Temperature (°R)	700 - 2000	1200 - 4000
Run Time (Sec.)	180 - 720	1 - 340
Reynolds number per foot	1×10^6 to 18×10^6	0.3×10^6 to 11×10^6
Altitude (Kft)	0 - 80	60 - 130

Tunnel A

AEDC's Tunnel A is a closed-circuit, continuous-flow, variable density supersonic wind tunnel. It has a Mach number range of 1.5 to 5.5 made possible by the variable area nozzle. The test section is 40 inches by 40 inches. This tunnel is utilized to obtain an aerodynamic data base required for the development of supersonic flight vehicles.

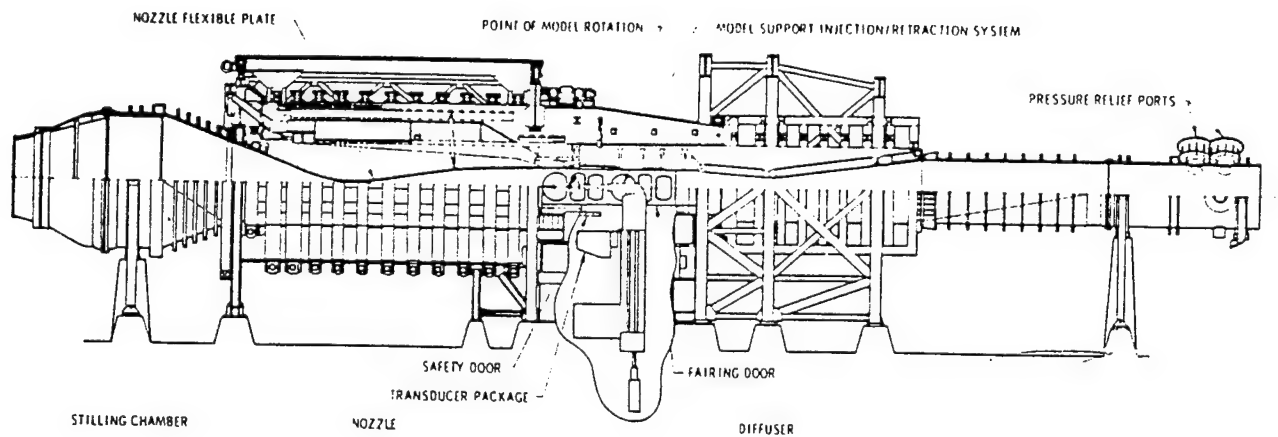


Figure 4 Tunnel A at AEDC

Unitary Plan Wind Tunnel

The Unitary Plan Wind Tunnel (UPWT) at Langley Research Center (LaRC) is a closed-circuit supersonic wind tunnel with two test sections. Both test sections measure 4 feet by 4 feet. The low Mach number test section has a range from 1.47 to 2.86, and the higher Mach number test section has a range from 2.29 to 4.63. The variation in Mach numbers is accomplished by sliding block-type nozzles. This tunnel is used to gather aerodynamic research data.

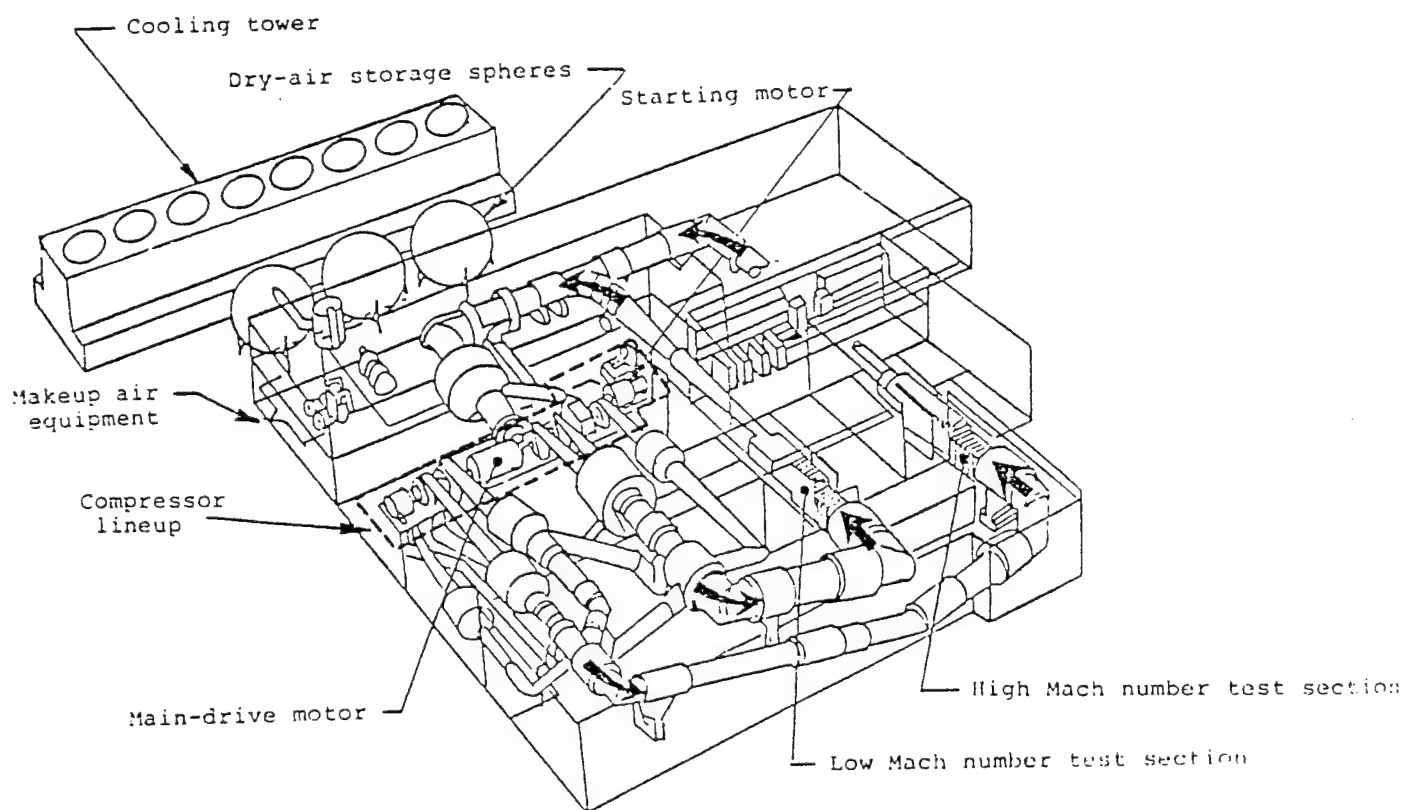


Figure 5 **Schematic of the Unitary Plan Wind Tunnel (From Ref. 4)**

Vought's High Speed Wind Tunnel

Vought's High Speed Wind Tunnel (HSWT) in Dallas, Texas, is a blowdown-to-atmosphere trisonic wind tunnel with a variable nozzle that allows the Mach number to be varied from 0.4 to 5. The air storage capability is 40,000 cubic feet at 600 psi, and the nominal storage temperature is 100 F° (Ref. 5).

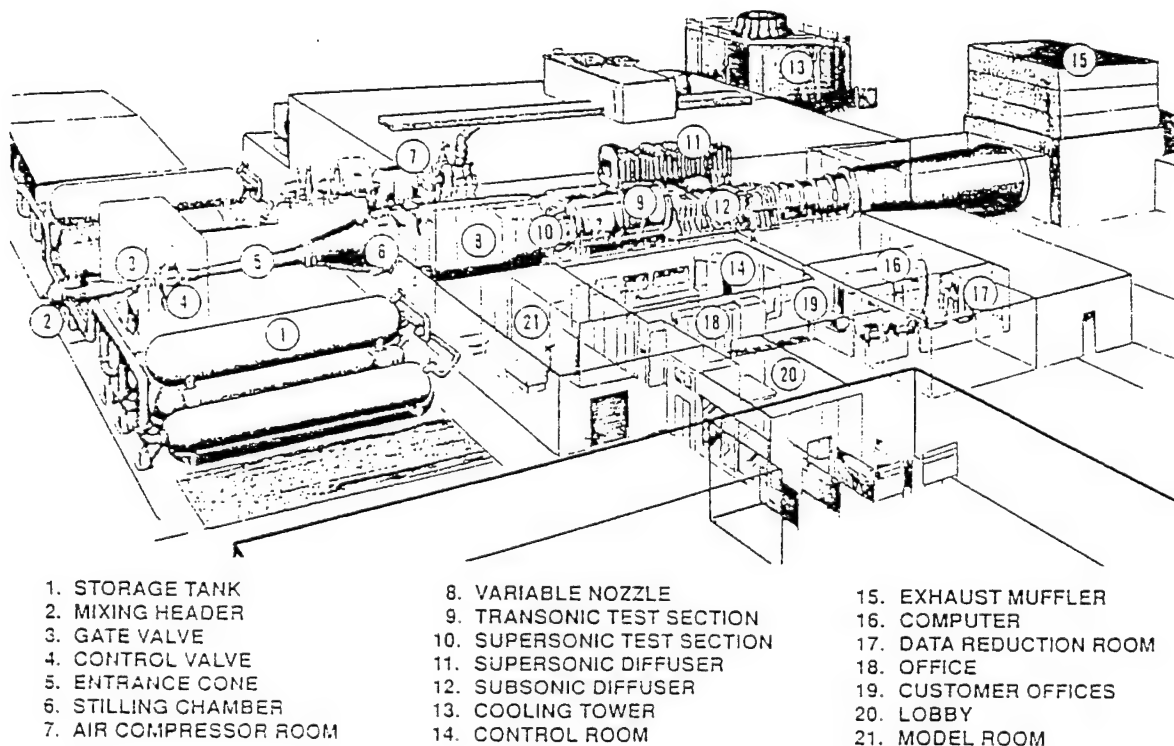


Figure 6 Vought's High Speed Wind Tunnel (From Ref. 5)

Comparison

Tunnel A and UPWT have nearly equivalent performance capabilities. The only substantial difference is that Tunnel A has a higher maximum Mach number capability.

Vought can achieve a significantly higher Reynolds number and dynamic pressure, but because it is a blowdown facility, it has a short run time. For tests with a large matrix of runs (greater than 1400 runs for standard six component force tests), Tunnel A test cost is typically less than test cost at Vought. For more modest test programs, Vought can provide

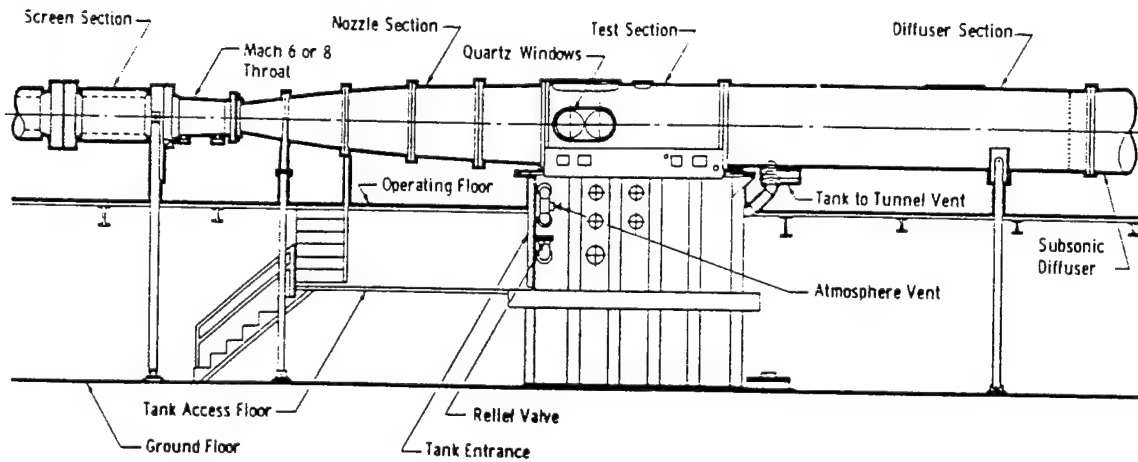
significant advantages in both facility performance and reduced cost. Table II shows the operating capabilities for these three wind tunnels

Table II Comparison of the operating capabilities for Tunnel A, UPWT and Vought's HSWT

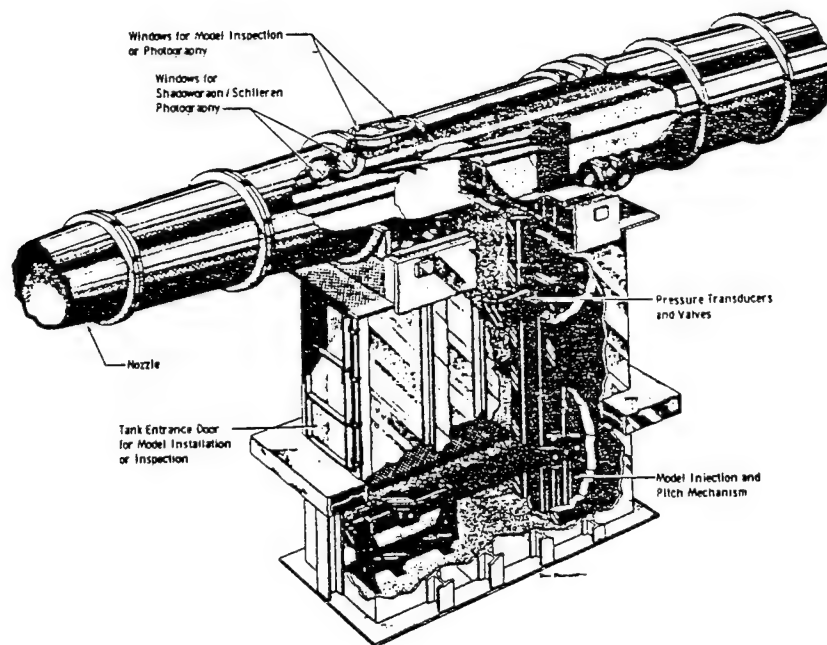
	Tunnel A	UP WT		Vought's HSWT
		Test Section 1	Test Section 2	
Mach numbers	1.5 - 5.5	1.47 - 2.86	2.29 - 4.63	0.4 - 5.0
Total Pressure (psia)	1.5 - 200	3.0 - 57	3.0 - 150	20 - 368
Total Temperature (°R)	530 - 750	560 - 760	560 - 760	540 - 620
Type	Continuous	Continuous	Continuous	Blowdown
Reynolds number per foot	0.3×10^6 to 9.2×10^6	0.5×10^6 to 12.2×10^6	0.5×10^6 to 9.5×10^6	2×10^6 to 38×10^6
Dynamic Pressure (psf)	53 - 1780	90 - 2670	90 - 1710	400 - 5000

Tunnels B and C

AEDC's Tunnels B and C are the only closed circuit continuous flow hypersonic wind tunnels in operation. The test section diameter for both tunnels is 50 inches. The nozzle exit diameter for B and C are 50 inches except for the Mach 4 and Mach 8 free jet nozzles for Tunnel C, which are 25 inches. Tunnel B has a Mach 6 and a Mach 8 nozzle, and the fifty-inch nozzle in Tunnel C is a Mach 10 nozzle. These tunnels are high-productivity for performing aerodynamic and aerothermal testing.



(a) Tunnel Assembly



(b) Test Section

Figure 7 AEDC Tunnel B (From Ref. 6)

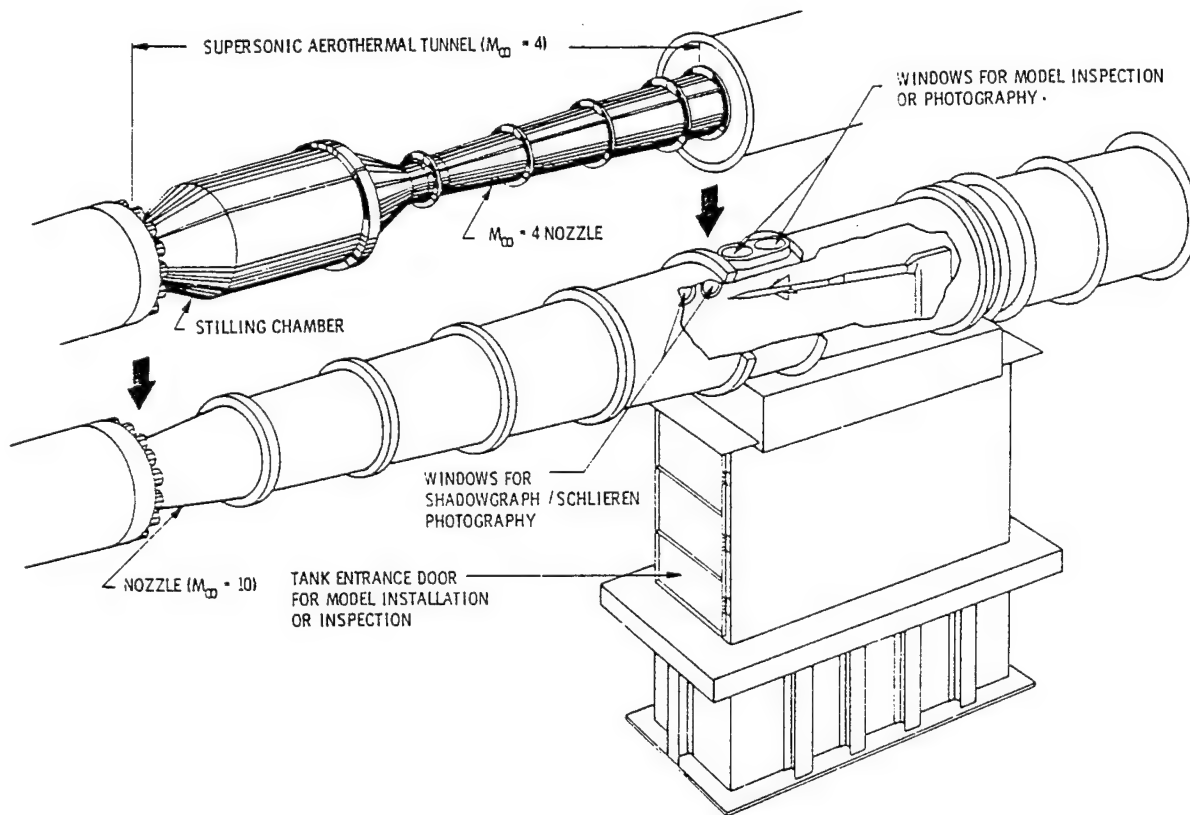


Figure 8 Tunnel C at AEDC (Mach 4 and Mach 10 Nozzles) (From Ref. 6)

Tunnel 9

Tunnel 9 at the Naval Surface Warfare Center (NSWC) is a blowdown to vacuum wind tunnel that uses nitrogen as the working gas. The Mach 10, 14, and 16.5 nozzles for Tunnel 9 have 5 ft. diameter exits. The Mach 7 Thermal/Structural Facility's nozzle has an 11 inch diameter exit, and the Mach 8 nozzle has a 33-inch-diameter exit. This tunnel is used for aerothermal and aerodynamic testing.

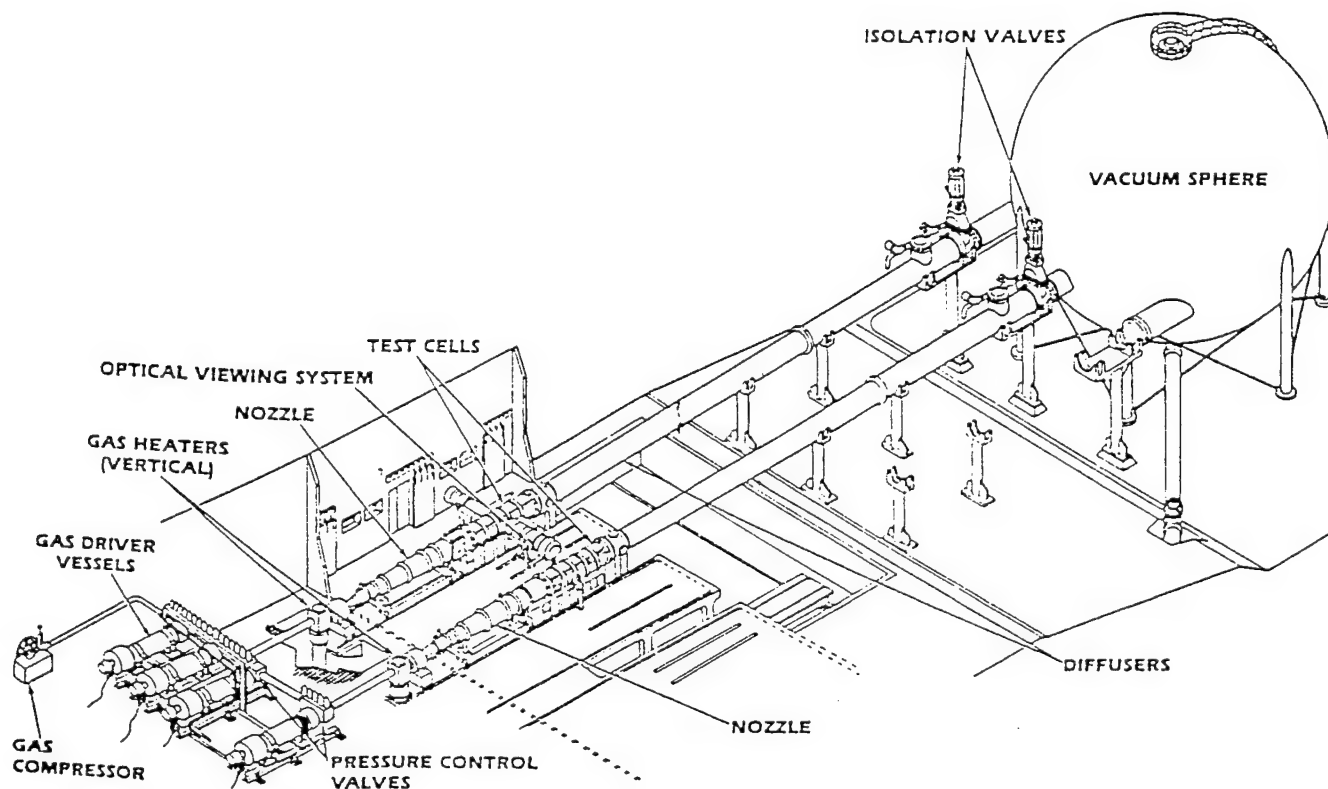


Figure 9 NWSC Hypervelocity Wind Tunnel No. 9 (From Ref. 5)

Comparison

Tunnel 9 has high performance capacities but a short run time. Because of Tunnels B and C's continuous run capabilities, they can gather substantial amounts of test data. As a result, Tunnels B/C and Tunnel 9 complement each other. The large volume of data required for building an aerodynamic data base for hypersonic vehicle design can be obtained most cost efficiently in Tunnels B/C. Typically, a small subset of the aero data base is also obtained in Tunnel 9 to examine incremental effects of higher Reynolds numbers. The capabilities for Tunnels B and C and for Tunnel 9 are shown in Table III.

Table III Comparison of the Operating Capabilities for Tunnel B, Tunnel C, and Tunnel 9

	Tunnel B	Tunnel C	Tunnel 9
Mach numbers	6, 8	4, 8, 10	7, 8, 10, 14, 16.5
Total Pressure (psia)	20 - 900	20 - 2,000	100 - 21,000
Total Temperature (°R)	700 - 1,350	700 - 1,900	1560 - 3460
Run Time (Sec.)	Continuous	Continuous	0.2 - 6
Reynolds number per foot	0.3×10^6 to 4.7×10^6	0.3×10^6 to 8.1×10^6	$.072 \times 10^6$ to 56×10^6

Conclusion

All the tunnels discussed in this study (APTU, the 8-Foot High Temperature Tunnel, Tunnel A, the Unitary Plan Tunnel, Vought's High Speed Wind Tunnel, Tunnels B and C, and Tunnel 9) have unique characteristics and are capable of contributing useful data. In general, the AEDC facilities (APTU, Tunnels A, B, and C) are higher productivity wind tunnels which cost effectively provide large amounts of data needed in the development of hypersonic systems.

References

Deletti

1. ~~2.~~

Resbush, D. E., Puster, R. L., Kelly, H. K., "Modification to the Langley 8-Foot High Temperature Tunnel for Hypersonic Propulsion Testing" AIAA Paper No. 87-1887, July 1987.

Deletti 3

2. ~~4.~~

Jackson, C. M., Corlett, W. A., *Description and Calibration of Langley Unitary Plan Wind Tunnel*, NASA TP 1905, November 1981.

3. ~~5.~~

Penaranda, F. E., Freda, M. S., *Aeronautical Facilities Catalogue. Volume 1: Wind Tunnels*, NASA RP-1132, January 1985.

4. ~~6.~~

Matthews, R. K., *Supersonic/Hypersonic Wind Tunnel Testing*, Presented Whorick, J. M., at The Aerospace Ground Test Facilities Short Course given UTSL.

5. ~~7.~~

Lafferty, J. F., Marren, D. E., "NSWC Hypervelocity Tunnel 9 Upgrade to Produce Flight Duplication at Mach 7 For Use in Endo-Atmospheric Interceptor Testing" AIAA Paper no. 94-2494, June 1994.

A MODEL BASED REAL TIME IMAGE
PROCESSING SYSTEM

Michael S. Moore
PhD. Candidate
Department of Computer and Electrical Engineering

Vanderbilt University
400 24th Ave. S.
Nashville, TN 37235-1824

Final Report for:
Graduate Student Program
Arnold Engineering Development Center

Sponsored by:
Air Force Office of Scientific Research
Bolling Air Force Base, Washington, D.C.

September 1994

A MODEL BASED REAL TIME IMAGE PROCESSING SYSTEM

Michael S. Moore
PhD. Candidate
Department of Electrical Engineering
Vanderbilt University

Abstract

This report presents the results of the 1994 AFOSR-RDL Summer Research Program. A system was developed which uses model based techniques to create real time data parallel implementations of image processing algorithms. The system, called PCT (Pipeline Cut Through) achieves real time execution by automatically parallelizing the algorithms and scaling the solution to the level of parallelism needed to reach the target data rate. The PCT system has been shown to be fully programmable and scalable, two features provided by the modeling concept. The hardware platform of the PCT system is an interconnected network of TI TMS320C40 DSPs. The current prototype is capable of performing an arbitrary length pipeline of user defined computations on 512×480 , $8 \frac{\text{bit}}{\text{pixel}}$ frames at the target rate of 30 frames per second¹, given that enough C40s are available in the hardware architecture. While performing an edge detection application, a large system containing 41 C40s was benchmarked at 440Mflops sustained (counting only useful computations). However, smaller systems (on the order of 6 processors) have also been shown to be efficient and useful for applications such as screech detection. Due to the use of model based techniques, the system can be scaled up or down by simply removing or adding C40s to the hardware architecture, and the software application can be reconfigured by merely changing the models. PCT has been tested extensively, and is expected to be used in a turbine engine test later this year.

¹ The digitization resolution (width and height of the digitized frames), the data depth (bits per pixel), and the frame rate are adjustable. However, $512 \times 480 \times 30 = 7.3 \frac{\text{Mbytes}}{\text{sec}}$ is the highest data rate yet achieved due merely to the limitations of the C40 communication link. Future plans include increasing this maximum data rate by a factor of nearly 5, to at least $35 \frac{\text{Mbytes}}{\text{sec}}$ by using multiple data paths.

Introduction

At Arnold Engineering Development Center, there is a need for a real time image processing system for both on-line video support during turbine engine tests and expedient off-line reduction of video test data. An example application for which this system is needed is for detecting "screech" in turbine engines. Screech is a phenomenon which occurs in the final stages of a turbine engine and can be tied to fluctuations in the efficiency of the engine. If detected and recorded, the screech data can be used by the turbine engine designers to fine tune the design for efficiency. Since screech is an extremely high speed event (it can last for as little as $\frac{1}{60}$ sec), it is very difficult to detect visually on line. In the past, the turbine engine designers concerned with screech have had to make video recordings of the test and later analyze the video off line. This off line analysis is time consuming and can hinder the usefulness of the data. Using a real time imaging system, screech can be detected on line during the test, potentially both adding to the test capabilities and reducing the required test time.

AEDC currently owns a real time image processor made by Quantex, which in the past has proven very useful. However, the system is inoperable and not economically serviceable. A replacement real time imaging system with at least the capabilities of the Quantex is needed in order to provide on and off line test support such as screech detection and data reduction.

In this paper, I discuss a new C40 based real time image processing system called PCT (Pipeline Cut Through), which was developed during the 1994 AFOSR-RDL Summer Research Program. The system is capable of performing any of the operations available on the Quantex PMAC, including convolution. In addition, the system is completely programmable and scalable, and requires no specialized image processing hardware except for a C40 frame grabber (A/D) module and a display (D/A) module. Thus, virtually any image processing algorithm can be executed in real time, given that enough hardware is available.

The system provides a programming interface/framework which allows the user to create customized image processing algorithms by writing standard C subroutines². The PCT library automatically builds a large grained data parallel implementation of the algorithm, which can be executed on a network of C40s. The resolution of the parallel processing issues (data distribution/combining, inter-processor communication, synchronization, etc.) is completely transparent to the user, who is then free to concentrate on the image processing algorithmic specific issues.

A high level modeling environment acts as the system level interface. The user provides a simple textual model, which includes the following information: (1) what computations will be done (2) how many processors are required for the target performance (3) in what way the data should be distributed among the processors (eg. on entire image per processor or groups of rows per processor). Based on the information in the model, the PCT model interpreter automatically

² The subroutines must conform to the assumptions of the PCT system, which are discussed later in the text.

creates a parallel software implementation and allocates it to the available hardware, resulting in a parallel run time system with the target performance. Through use of the modeling concept, the PCT system effectively masks the complexity of the system from the user, allowing him/her to create customized real time image processing applications without dealing with the real time issues.

What is Real Time?

In this paper, the term *real time* means that the system grabs (A/D), computes, and displays (D/A) the video data at the same rate that it is produced by the input device (eg. camera, laser disk, etc.). Of course, the input device's frame rate, the spatial resolution (width and height of digitized image in pixels), and the pixel depth (number of bits per pixel) can vary. Since each of these factors directly affects the actual data rate, this definition requires further clarification. We are assuming the following in our definition of *real time*:

- the input device generates $30 \frac{\text{frames}}{\text{sec}}$
- the digitizer grabs 512x480 images
- the data is $8 \frac{\text{bits}}{\text{pixel}}$

Using these assumptions, we can calculate an actual data rate which corresponds to our definition of real time.

$$\text{rate} = 512 \times 480 \times 30 = 7.3728 \frac{\text{Mbytes}}{\text{second}} \quad (1)$$

The Quantex Image Processor

The Quantex real time image processing system uses specialized hardware modules called PMACs (Processor, Memory, Accumulator). A PMAC can perform various simple real time computations, which are listed below. The system also contains one special module which can perform real time convolution with various fixed kernels (eg. low and high pass filters). Several PMACs can be chained together to form more complex computational networks. The PMAC is capable of the following types of computation at real time rates:

- look-up table
- integration
- averaging
- differencing
- fixed kernel convolution (special PMAC)

- low pass filter
- high pass filter

The Quantex approach of building specialized hardware to handle the algorithms most commonly used in real time image processing is an economical one, especially if the application does not warrant any non standard techniques. The Quantex system has been proven useful at AEDC for such applications as noise reduction and off line screech detection, both of which use standard techniques. However, since the Quantex uses specialized hardware, its capabilities are fixed and limited by the type and amount of hardware available with the system. It is not programmable or scalable: two qualities which are highly desirable. Programmability would allow the user to experiment with non-standard techniques and design specialized algorithms for particular applications. Scalability would provide the capabilities to parallelize experimental algorithms to achieve real time, and to increase the length of the computational pipeline.

The PCT C40 Image Processing System

The PCT C40 image processing system is a model based environment which allows the user to easily create specialized real time image processing applications without any image processing specific hardware. Model based software synthesis has been shown to be useful for managing the complexity of high-performance reactive systems [2]. The approach is to represent application specific knowledge in formal multi-aspect models. Model interpreters which are specific to the target system are used to "compile" the knowledge contained in the models. The interpreters automatically synthesize and integrate the target system components. A standard model based system has 4 components:

- A Modeling Building Environment
- A Model Database
- Model Interpreters
- An execution Environment

Since real time image processing is by nature a problem which requires both high computational performance and interactivity, it is an ideal application domain for model based software synthesis[4]. Though the PCT system architecture is very simple, as will be shown in the discussion, it does follow the standard model based architecture. The modeling paradigm is textual and quite simple, so the model building environment is your favorite text editor, and the model database consists of the resulting text files. The PCT model interpreter is a stand-alone C program, and the execution environment is provided by the PCT support library.

The PCT C40 real time image processing system consists of the following elements (see figure):

- A program model builder (text editor)

- An automatic hardware model builder (TICK [1])
- The PCT model interpreter
- The PCT run-time system
 - Application Program (Algorithm) Modules
 - PCT communication library
 - PCT program support services
- A network of TMS320C40 DSPs

This section will describe the following details of the system:

- How Pipeline Cut Through works
- The PCT modeling paradigm
- The PCT programming interface
- Hardware requirements of the PCT system

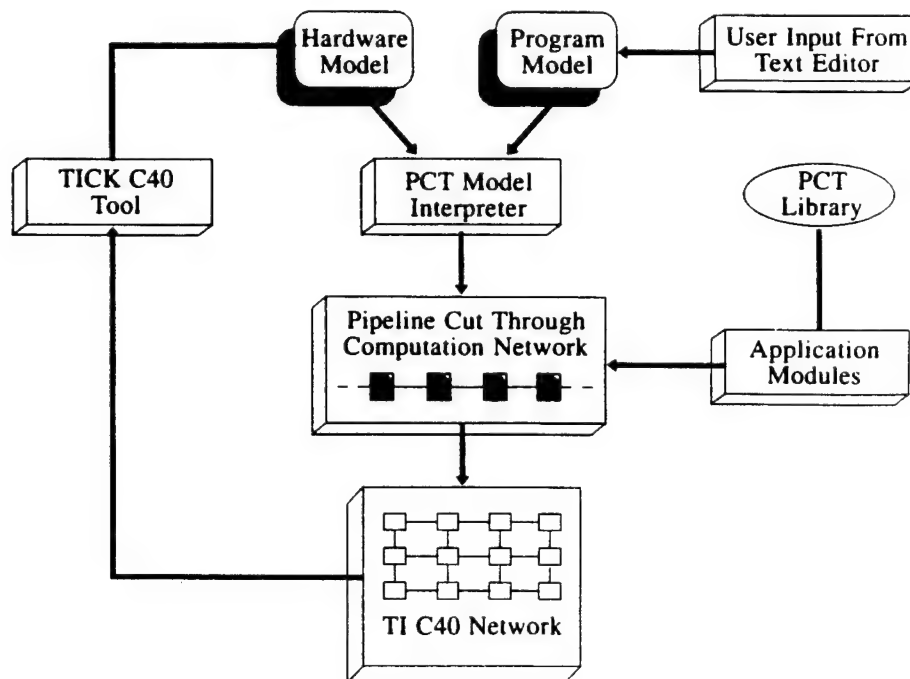


Figure 1: The PCT System Architecture

What is Pipeline Cut Through?

In this section, I discuss how the PCT communications system works. This requires some general background on data parallelism and the TMS320C40.

Data Parallelism

The PCT system achieves real time by using *data parallelism*. Data parallelism is a scheme of partitioning, or *splitting*, the input data in some way and distributing the partitions to several processors. The processors perform the same algorithm concurrently, each operating on its input data, thus affecting a speedup in the computation. The results of the computations are then combined, or *merged*, to form the collective output. This technique is sometimes referred to as *farming*, or the *split and merge* paradigm [4]. Since most image processing algorithms employ simple, regular computations across the entire image, it seems natural that image processing would be an application domain well suited for data parallelism [5]. In fact, it has been shown [6] that split and merge parallelism is applicable to a large group of the commonly used image processing algorithms called *neighborhood operators*³. The issues that must be solved to create a data parallel algorithm include (1) in what way will the data be partitioned? (2) how are the partitions going to be distributed to the processors? (3) how will the results be re-combined?

The Pipeline Cut Through Scheme

Pipeline Cut Through (PCT) is a data parallelization scheme we have developed for the C40 which forms a computational pipeline of several processors working on the same problem. PCT resolves the communication issues and allows image processing algorithms to be parallelized automatically. The application specific code does not change in any way. PCT takes advantage of the DMA (direct memory access) co-processors and the communication ports of the C40. Since the C40 DMA engines are autonomous, communications and computation can be done concurrently, effectively removing communications overhead. The DMAs can be programmed to initialize themselves automatically without CPU intervention. This is called *DMA chaining* (see "Fun With Link Pointers" [7]). What the PCT system does is program the DMA co-processors via circular linked lists of DMA control structures. The DMAs are synchronized with the CPU and each other via interrupt routines. This setup causes the input and output DMAs to act together in a way that can be described by a synchronous state machine. The key to the PCT scheme is this communication state machine. The basic states of the communication system are:

- **recv/send**

Receive the next input image from the input comm port and send the most recent output image to the output comm port (at the same time).

³A *neighborhood operator* is an algorithm which computes a pixel's output value from the input values of the pixels within a fixed sized neighborhood. Examples are 2D convolution, adaptive histogram equalization, etc.

$N = 3$ No overlap of I/O and Compute

	proc0	proc1	proc2
state $n\%3$	recv send	compute forward	compute forward
state $(n+1)\%3$	compute forward	recv send	compute forward
state $(n+2)\%3$	compute forward	compute forward	recv send

Figure 2: The PCT States (no I/O and compute overlap)

- forward, or cut through

Forward an image from the input comm port directly to the output comm port. In this state, the node is effectively a wire. Data cuts through the node. This state is repeated $N - 1$ times, where N is the number of processors in the pipeline. Then PCT automatically re-initializes itself to the recv/send state and waits for the restart signal from the CPU.

Only one processor in the pipeline can be in the recv/send state at one time. All others will be forwarding. Thus, the processor which is in the recv/send state is effectively connected directly to the input and output of the pipeline. The position of this “active” processor inside the pipeline will circulate inside the pipeline in increasing node order⁴. Since the DMA engines operate independently of the CPU, the CPU is free to perform computations during either the forward states or both the recv/send and the forward states. Note that if the computation is overlapped with the recv/send state, then the input and output images must be double buffered to insure data consistency. For this reason, the PCT library performs a check and automatically double buffers if the “-M” switch is set (see the description of the PCT command line arguments). The CPU is programmed with an infinite loop which (1) waits until the new input image has arrived (2) performs the computation (a user defined algorithm), then (3) signals that the output image is ready to be sent out. An important feature of the PCT scheme is that outside of the computational pipeline the ordering and length of the data stream do not change. The parallelism is totally invisible to the rest of the system. The PCT scheme has been implemented in C and packaged into a library, to which the application code interfaces with a one time function call: “_pct_run(void &algorithm())” (see example in the PCT

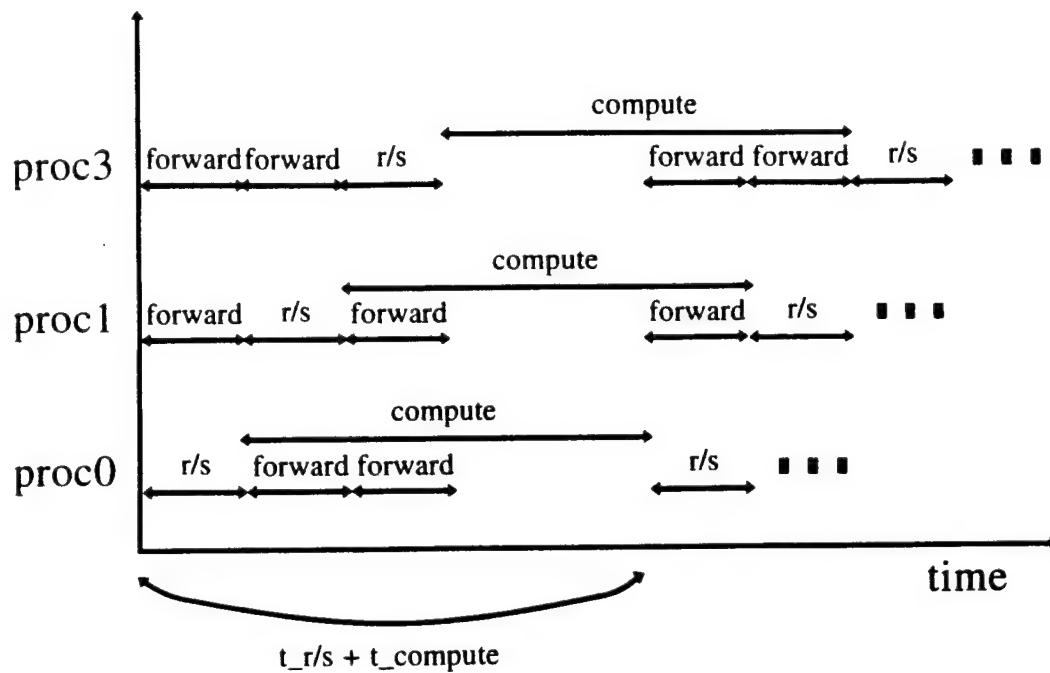


Figure 3: The PCT Timing Diagram (no I/O and compute overlap)

Programming Interface section).

To further understand how the PCT system works, refer to figures 2, 3, 4, and 5. Figure 2 shows the states of a 3 node PCT pipeline in the case where the communication and computation are not overlapped. Figure 4 shows the same system with I/O and computation overlap. Notice that due to double buffering, the system in Figure 4 has twice as many communication states as the one in Figure 2. Figures 3 and 5 are timing diagrams for the systems in Figures 2 and 4, respectively.

Performance Calculations

In this section I will formulate predictive models for the performance gains due to parallelization in the PCT system. There are two interesting performance measurements which will be discussed:

- throughput
the frame rate, usually measured in frames per second
- latency
the amount of time that it takes a particular frame to move through the computational pipeline

I will show that for a given benchmarked algorithm, it is simple to find the number of processors required to achieve the target throughput (real time frame rate). Also, I will discuss latency and show how to reduce it.

⁴The prototype hardware has a software programmable led for each C40. I can turn it on when the processor is in the recv/send mode, so you can see the circulation pattern. It's really pretty cool to watch, sort of like a lava lamp...

N = 3 With overlap of I/O and Compute

	proc0	proc1	proc2
state $n\%3$	recv send compute0	compute1 forward	compute1 forward
state $(n+1)\%3$	compute0 forward	recv send compute0	compute1 forward
state $(n+2)\%3$	compute0 forward	compute0 forward	recv send compute0
state $(n+3)\%3$	recv send compute1	compute0 forward	compute0 forward
state $(n+4)\%3$	compute1 forward	recv send compute1	compute0 forward
state $(n+5)\%3$	compute1 forward	compute1 forward	recv send compute1

There are 6 states because of the forced double buffering!

Figure 4: The PCT States With Overlap of I/O and Compute

Suppose that the execution time required for an algorithm to compute one entire frame is $t_{compute}$, and that the time required to receive and send an image is $t_{r/s}$. (See figures 3 and 5). It is assumed that $t_{compute} > t_{r/s}$. Note that $t_{r/s}$ should be the period it takes the input device to produce a frame, so $\frac{1}{t_{r/s}} =$ the target system frame rate. If there are N processors in the computational pipeline there are two cases for the system throughput:

- I/O and compute NOT overlapped

In this case N frames will exit the pipeline every $t_{compute} + t_{r/s}$ seconds (see figure 3). Thus

$$throughput = \left(\frac{N}{t_{compute} + t_{r/s}} \right) \quad (2)$$

Setting $throughput = target_rate$ to find the number of processors necessary for the target rate (N_{rt}), we get

$$\frac{N_{rt}}{t_{compute} + t_{r/s}} = \frac{1}{t_{r/s}} \quad (3)$$

$$N_{rt} = \frac{t_{compute}}{t_{r/s}} + 1 \quad (4)$$

- I/O and compute ARE overlapped

In this case N frames will exit the pipeline every $t_{compute}$ seconds (see figure 5). Thus

$$throughput = \left(\frac{N}{t_{compute}} \right) \quad (5)$$

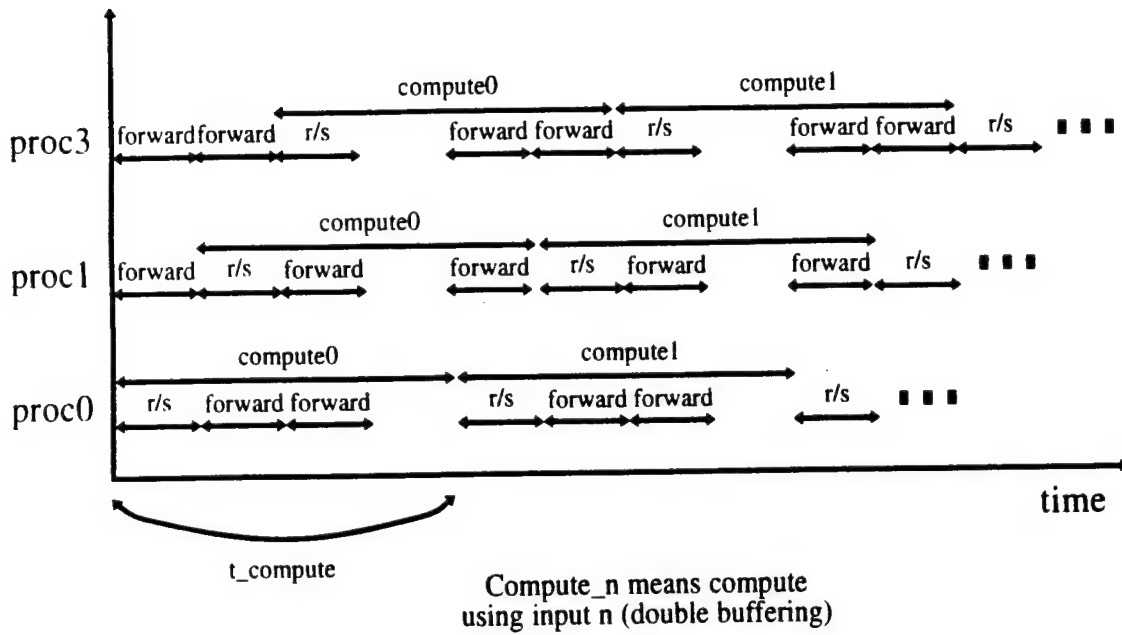


Figure 5: The PCT Timing Diagram with Overlap of I/O and Compute

Setting $throughput = target_rate$ to find the number of processors necessary for the target rate with I/O and compute overlap (N_{rto}), we get

$$N_{rto} = \frac{t_{compute}}{t_{r/s}} \quad (6)$$

Thus, a user who develops a new algorithm which he/she wants to scale to the target throughput must do the following:

1. find the target frame period (eg. 1/30)
2. benchmark the algorithm on one processor (find $t_{compute}$)
3. calculate the number of processors needed using either equation 4 or 6.
4. specify this number in the model (see the section on the PCT modeling paradigm).

The other performance consideration is latency. The assumption made is that each processor performs the computation on its local *image*. The term *image* can have two possible meanings as it is used here. Which meaning applies depends on the type of data splitting that is being used.

- (TIME_SPLIT)

If the image sequence is being split at frame borders, or split in the time dimension, then an entire frame will be processed by each node. In this case, *image* means an entire frame. There are two sub-cases for the latency. Refer to figures 3 and 5.

- I/O and computation are NOT overlapped

$$latency_{ts} = t_{r/s} + t_{compute} \quad (7)$$

- I/O and communication ARE overlapped

$$latency_{tso} = 2 * t_{compute} \quad (8)$$

The factor of 2 is because of the double buffering.

Where $t_{compute}$ is the execution time of the algorithm for an entire image on one processor.

- (SPATIAL_SPLIT)

If the data is being partitioned by rows, or split in space, then only a piece an entire frame will be processed by each node. In this case, an image is some number of rows. The exact dimensions of the local image can be retrieved from the PCT library by calling the functions `_pct_get_local_imw()`, `_pct_get_local_imh()`, and `_pct_get_local_ims()` (these are described in the PCT programming interface section). The computation and communication times will be proportionately smaller due to the decreased local image size. Again, there are two sub-cases for the latency. Refer to figures 3 and 5 and remember that one frame will be distributed over the N processors in the computational pipeline.

- I/O and computation are NOT overlapped

$$latency_{ss} = \frac{t_{r/s} + t_{compute}}{N} \quad (9)$$

When $N = N_{rt}$

$$latency_{ssmin} = t_{r/s} \quad (10)$$

- I/O and communication ARE overlapped

$$latency_{sso} = \frac{2 * t_{compute}}{N} \quad (11)$$

When $N = N_{rto}$

$$latency_{ssomin} = 2 * t_{r/s} \quad (12)$$

Thus, in order to minimize the latency and maximize the throughput at the same time, the user should set up the model as follows:

1. do not overlap of I/O and computation (no “-M” switch)
2. set the splitting mode to SPATIAL_SPLIT
3. set $N = N_{rt}$

This setup will produce a system with the target frame rate and a 1 frame latency (for each computational pipeline used).

The PCT Modeling Paradigm

The PCT modeling paradigm includes two types of models: program and hardware models. A model interpreter synthesizes a parallel run time network from these models. The models and the interpreter are described below.

The PCT Program Model

The program model is the user's interface to the system software configuration. The program model is a very simple text file written by the user, and can be created using any text editor. It consists of a sequential list of lines, each containing the name of an application program module with its command line arguments. The target system performance (throughput and latency) is controlled in the model by the allocating the appropriate number of processors to each task (see the description below of the command line arguments). Also embedded in the program model are parameters which control of the type of parallelism used.

The command line arguments in the model consist of two types.

- An argument preceded by a single "-" (eg. "-N5") is parsed by the PCT library and controls some low-level feature of the communications system.
- An argument preceded by a double "--" (eg. "--l1.5) is parsed by the user module and controls some feature of the application program. An example program model is shown below.

```
grab.dwn
lut.dwn -N1 -S --l1.5
lap3x3.dwn -N5
lut.dwn -N1 -S --tl128
disp.dwn
```

The system resulting from this model will digitize (grab) frames from a live video source using a frame grabber, perform a lookup table operation with a logarithmic table, base=1.5 (--l1.5), compute the 3x3 laplacian, threshold the image to values above 128 (lut.dwn ... --tl128), and display the result as analog video. This sequence of operations will detect edges in the scene.

Meanings of the PCT Command Line Arguments

There are several command line arguments which control the low-level features of the PCT communication system. Each is listed below with a descriptions its function.

- "-N?"

? is the number of processors which will be used in this particular operation. The number of processors needed to achieve real-time for a particular module is highly dependent on the algorithm, and is determined by simply benchmarking the algorithm on one processor and calculating the speedup needed for the target throughput. For example, the lap3x3.dwn (computes a 3x3 laplacian) module is capable of computing about 3 frames/second on one processor. Thus, in order to achieve 30 frames/second, 10 processors are needed. (Note that in the example above only 5 processors are allocated to the laplacian, which is not enough for it to achieve real time. The example model will compute $3 * 5 = 15$ frames/second.) The model interpreter checks that the total number of processors specified in the software model is not greater than the actual number of processors available (in the hardware model). If it is, the interpreter generates an error message and exits so you can fix the model. For example, we can see that the program model example given above specifies a total of $1 + 5 + 1 = 7$ C40s (not counting the grabber and display modules). If fewer are available, the software model must be modified, which will result in lower performance.

- "-S" or "-T"

This argument specifies whether the image data will be "split" in Space (one piece of an image per processor), or in Time (one entire image per processor). "-T" is the default.

- "-M"

This argument controls whether the I/O operations (receiving and sending images) will be overlapped with the processing operation. If "-M" is specified, then these operations will not be overlapped. The default is to overlap I/O and compute, which requires double buffering of the input and output, which will automatically be provided for by the PCT library.

- "-I?" and "-O?"

The user can control the number of previous input and output states which will be available to the processing algorithm. If the command line has -In, then the algorithm will have access to the last $n-1$ input buffers ($in_k, in_{k-1}, in_{k-2}, \dots, in_{k-n+2}$), unless "-M" was specified. In the case where "-M" is specified, the algorithm will have access to n input buffers ($in_k, in_{k-1}, in_{k-2}, \dots, in_{k-n+1}$) because the I/O and processing are not overlapped. To clarify this, suppose that I wrote an algorithm which was going to calculate the current output (out_k) based on the current input (in_k) and the previous 3 inputs ($in_{k-1}, in_{k-2}, and in_{k-3}$). Suppose also that the I/O and computation will be overlapped (no "-M" option). In order for this to be possible, I must include "-I5" in the command line string of the appropriate line of the model. Note that the number of input or output states which can be saved is bounded above by the number of image buffers that can be allocated. The smaller the available memory and larger the image data, the fewer states can be saved.

The PCT Hardware Model

The hardware model is a textual representation of the C40 network. It is generated automatically using the TICK C40 detection/loader tool written by Ben Abbott of Vanderbilt University[1]. The only time that the hardware model is regenerated is when the hardware architecture has changed (eg. if processors or links were added/removed). The user need only know the name of the current hardware model file so it can be specified to the model interpreter. An example hardware model is shown below. It specifies 9 processors, including the frame grabber (#1) and the display module (#9).

#	TYPE	MHz	LINK0	LINK1	LINK2	LINK3	LINK4	LINK5	GMEM	LMEM	FMEM
1	000B0001-000B	40	2:3	2:4	3:5	HOST	0Kb	4096Kb	8Kb
2	00010002-000A	40	3:3	1:0	1:1	3:2	4096Kb	4096Kb	8Kb
3	00010002-000A	40	4:4	...	2:5	2:0	...	1:2	4096Kb	4096Kb	8Kb
4	00120104-0001	40	5:5	5:0	3:0	6:2	4096Kb	4096Kb	8Kb
5	00120104-0001	40	4:3	...	7:5	7:0	...	4:2	4096Kb	4096Kb	8Kb
6	00120104-0001	40	7:3	...	4:5	...	8:0	7:2	4096Kb	4096Kb	8Kb
7	00120104-0001	40	5:3	...	6:5	6:0	...	5:2	4096Kb	4096Kb	8Kb
8	00120104-0001	40	6:4	9:0	...	9:2	4096Kb	4096Kb	8Kb
9	000B0002-000A	40	8:3	...	8:5	0Kb	4096Kb	8Kb

The PCT Model Interpreter

The PCT model interpreter is a C program which builds the executable parallel system based on the program and hardware models. The interpreter executes the following procedure:

1. Find a connected sequence of processors in the hardware model starting with the frame grabber board, ending at the display board, and crossing every processor exactly once (A Hamiltonian path, in Graph Theoretic terms [3]). If a Hamiltonian path does not exist, then return the longest path starting with the grabber and ending with the display module.
2. Interpret the program model and create a parallel software network to perform the computations at the target data rate.
3. Check to ensure that there is enough hardware to solve the problem. If not, inform the user that modifications must be made to either the program or hardware model.
4. Allocate the tasks in the software network to the processors in the hardware network along the Hamiltonian path.
5. Save the processing network information using the TICK boot file format (see [1]).
6. Boot the network using TICK. The system will begin execution automatically.

An example TICK boot file is shown below which corresponds to the program model and hardware model examples given above.

```
; This file was generated by the PCT (Pipeline Cut-Through)
; model interpreter
0 1 0 grab.dwn -p1
1 2 1 lut.dwn -N1 -S --l1.5 -n0 -i4 -o0
2 3 0 lap3x3.dwn -N5 -n0 -i3 -o0
3 4 0 lap3x3.dwn -N5 -n1 -i4 -o2
4 5 2 lap3x3.dwn -N5 -n2 -i5 -o2
5 7 2 lap3x3.dwn -N5 -n3 -i5 -o2
7 6 2 lap3x3.dwn -N5 -n4 -i5 -o4
6 8 4 lut.dwn -N1 -S --tl128 -n0 -i0 -o3
8 9 3 disp.dwn -p0
```

The PCT Programming Interface

The true flexibility of the PCT system is its programmability. The user can easily add capabilities to the system without worrying about communication or synchronization. All that is required is a normal serial C subroutine, and a small C main program.

Assumptions of the PCT Programming Interface

The PCT system makes several assumptions about the application process, so the application subroutine must follow a few guidelines. Otherwise, the routine is normal C code. The assumptions and guidelines are outlined below.

- The application program is assumed to produce one output image from one input image of the same size. This assumption allows the PCT system to take advantage of the simplicity of the pipeline structure.
- Any memory allocations will be done with calls to the PCT memory management functions, and no memory will be freed.

Programming Guidelines

Several key services are available from the PCT system. These following types of services are available to the application program. (1) memory management (2) retrieval of information pertinent to the local computation (3) retrieval of past input and output states (4) byte access

- Memory management
 - `_pct_obuf_alloc(size)`

- `_pct_locbuf_alloc(size)`
- `_pct_glbbuf_alloc(size)`

These routines allocate *size* bytes in on-chip, local-bus, and global-bus memory. Do not try to free any memory, and do not call `malloc!!!`

- Retrieving Network Information

- `_pct_get_nodes()`
- `_pct_get_node_num()`

These functions are used to retrieve information about the computational pipeline in which the local processor lies. For example, if 5 processors are computing an operation, then the first one in the laplacian computational pipeline would be told *nodes* = 5 and *node_num* = 0.

- Retrieving Data Size Information from PCT

- `_pct_get_local_imw()`
- `_pct_get_local_imh()`
- `_pct_get_local_ims()`
- `_pct_get_equal_imh()`
- `_pct_get_equal_ims()`

The `_pct_get_local_im?()` functions should be used to set the local image dimensions instead of using the `IMW`, `IMH`, and `IMS` macros in `pct.h`, because if spatial splitting is used, the local image will not be full size. Note that the image height is in terms of rows, but the image width and size are in terms of bytes ($\text{imw} = \frac{\text{columns}}{4}$). The `_pct_get_equal_imh()` and `_pct_get_equal_ims()` functions are needed for the following reason. Suppose that an image with 480 rows is distributed by rows across 7 processors. Since 480 is not divisible by 7, the 7 processors cannot be allocated equal numbers of rows. The PCT communication system deals with this problem by allocating $\frac{480}{7} = 68$ (integer division) rows to the first 6 processors, and $\frac{480}{7} + 480\%7 = 72$ rows to the last processor. This inequality can cause a loss in efficiency, since the 7th processor will take longer than the first 6 due to its larger data set. To curb this effect, it is quite sensible to only compute the first $\frac{480}{7}$ rows on the last processor also, because the remaining 4 rows are at the bottom of the image, and their not being computed will probably cause no problem. Thus, the two functions `_pct_get_equal_imh()` and `_pct_get_equal_ims()` are provided, and can be called in place of `_pct_get_local_imh()` and `_pct_get_local_ims()`.

- Retrieving Past I/O States

- `_pct_get_input(delays)`

– `_pct_get_output(delays)`

These functions can be used to retrieve past input and output buffers, if they are available (See the -I and -O argument descriptions above). “Delays” is the number of delay states requested. (eg. `_pct_get_input(1)` returns a pointer to the image that was used as the input last time the function ran). Note that if sequence splitting is used, that `_pct_get_input(1)` will not return the image which was grabbed immediately before the current input. It will return the image that was used as the input last time the function ran, which was grabbed *nodes* states before the current input (see the description of the PCT communication scheme). Thus, the user should be wary and use spatial splitting (see the “-S” switch described above) whenever previous states of the input or output are required in a computation.

- Byte Access

– `PACK_BYTES(b3,b2,b1,b0)`

– `GET_BYTE(long,pos)`

The C40 C130 compiler does not provide byte access. I have included macros in `pct.h` for retrieving a byte from a 4-byte word, and packing 4 bytes into a word.

Example Application Program

Below is an example application program which averages the current input frame with the previous input frame. This example executes at just under 15 frames per second on one processor.

```
/**
    tavg2 averages the current input with the previous input.
***/
#include "pct.h"
#define MASK=0xfefefefe;
void tavg2(image ip,image op)
{
    register long i,len=_pct_get_equal_ims();
    unsigned long *old_ip=_pct_get_input(1);
    for(i = 0; i < len; i++)
        op[i] = ((ip[i]&MASK)>>1)+((old_ip[i]&MASK)>>1);
}
int main(int argc, char* argv[])
{
    _pct_run(argc,argv,&tavg2);
}
```

Hardware Requirements of the PCT System

The PCT system assumes the following about the hardware:

- The hardware consists of a connected network of TI TMS320C40 DSPs, and must be detectable by TICK [1].
- At least one C40 is capable of digitizing images (A/D) from a standard analog video source or otherwise obtaining digital images from a device (eg. a laser disk) at the desired frame rate.
- At least one C40 is capable of displaying images (D/A) in a standard video format or outputting the digital data to a device (eg. a real time digital storage device) at the desired frame rate.
- A path exists from the input C40 to the output C40 through C40 links.
- The intermediate nodes (along the path) have adequate memory for the operations which will be performed on them. The PCT system is small, so most of the memory is taken up by image buffers. Most operations can be executed on a C40 with 512Kbytes on each the global and the local bus. However, if several states of the input or output buffers are required by the operations (see the “-I” argument in the discussion of the PCT command line switches), then more memory may be required. The prototype uses 2Megx2Meg TIMS (TI Modules).

Future Improvements to the PCT System

Plans for future improvement to the PCT image processing system include the following:

- The Pipeline Cut Through scheme will soon be modified to support multiple parallel data paths. This modification will provide a factor of 5 increase in the maximum data rate achievable with a network of C40s, raising it to about $35 \frac{\text{bytes}}{\text{sec}}$.
- The frame grabber software will be modified to support “field mode”, which will effectively increase the frame production rate to $60 \frac{\text{frames}}{\text{sec}}$.
- An interactive graphical user interface is under development. The user will be able to make adjustments to some algorithmic parameters (eg. the convolution kernel, the shape of the lookup table, the threshold value) interactively as the system runs.
- The modeling paradigm will be expanded to include (1) explicit performance information about the algorithms which will be used (2) explicit declaration of the performance goals (throughput and latency). This added information will be used to further automate the system.
- The application example library will be further developed.

- The feasibility of a model level and a program level interface to the popular image processing package Khoros will be explored. It seems possible to automatically produce real time versions of select algorithms from the Khoros library. Then Khoros dataflows could be “converted” to real time PCT dataflows.

The result of these improvements will be a very easy to use, high performance, graphically interactive real time image processing system.

ACKNOWLEDGMENTS

I would like to acknowledge the United States Air Force for making it possible for me to perform this research. The AFOSR summer research program has been an enriching and rewarding experience. I would also like to acknowledge Ben Abbott, Ted Bapty, and Csaba Biegl, who helped with the development of the PCT system.

References:

- [1] B. Abbott and A. Ledeczi: “TICK: TI TMS320C40 Utility Program”, Proceedings of the International Conference on Signal Processing Applications and Technology, Oct. 1994 [in press].
- [2] B. Abbott, T. Bapty, C. Biegl, G. Karsai, and J. Sztipanovits: “Model-Based Software Synthesis,” IEEE Software, May 1993.
- [3] J.A. Bondy and U.S.R. Murty: “Graph Theory with Applications”, North-Holland, New York, 1976.
- [4] M.S. Moore, G. Karsai, and J. Sztipanovits: “Model-Based Programming for Parallel Image Processing”, Proceedings of the First IEEE International Conference on Image Processing (ICIP), Nov. 1994 [in press].
- [5] J. Sztipanovits, B. Abbott, and C. Biegl: “Programming Environment for Parallel Image Processing,” Report Prepared for Sverdrup Technology, Inc., September, 1992.
- [6] M. S. Moore: “A Programming Environment for Parallel Image Processing: Progress Report”, Report Prepared for Sverdrup Technology, Inc., 31 January 1993.
- [7] Texas Instruments: “TMS320C4x User’s Guide”, Texas Instruments, May 1991.

ANALYSIS AND COMPARISON OF THE PERFORMANCE/LIFE COMBUSTION
AND THE ROCKET COMBUSTION INTERACTIVE DESIGN COMPUTER MODELS

David T. Pratt
Graduate Student
Department of Mechanical and Aerospace Engineering

University of Tennessee Space Institute
B. H. Goethert Parkway
Tullahoma, TN 37388-8897

Final Report For:
Graduate Student Research Program
Arnold Engineering Development Center

Sponsored By:
Air Force Office of Scientific Research
Bolling Air Force Base, DC

and

Arnold Engineering Development Center

September 1994

ANALYSIS AND COMPARISON OF THE PERFORMANCE/LIFE COMBUSTION
AND THE ROCKET COMBUSTION INTERACTIVE DESIGN COMPUTER MODELS

David T. Pratt
Graduate Student
Department of Mechanical and Aerospace Engineering
University of Tennessee Space Institute

Abstract

The Performance/Life Combustion (PLC) and the Rocket Combustion Interactive Design (ROCCID) computer models were analyzed and compared. The purpose of the present research was to determine which model was better suited for modification to better describe the fluid mechanics that influence combustion chamber performance. Although ROCCID incorporates more physical processes into its model than PLC, its highly simplified combustion chamber performance calculations are primarily used to evaluate the stability of the combustion chamber while PLC is applicable to multiple injector configurations. Therefore, PLC was selected for refinement. The result will be a model that simultaneously evaluates the conservation equations and allows the area of each grid cell to change, with the constraint that pressure is constant at any axial location.

ANALYSIS AND COMPARISON OF THE PERFORMANCE/LIFE COMBUSTION AND THE ROCKET COMBUSTION INTERACTIVE DESIGN COMPUTER MODELS

David T. Pratt

Introduction

The present research stems from a need to model rocket chamber performance accurately and economically. Although there are many existing computer programs that model rocket combustion, most are either too simplistic or too complex for the user's current application. This project involved an analysis and comparison of the Performance/Life Combustion (PLC) and the Rocket Combustion Interactive Design (ROCCID) computer models. PLC was originally developed to evaluate the energy release efficiency and wall mixture ratio distribution within the Space Shuttle Main Engine. It was later modified by a student at The University of Tennessee Space Institute to allow for improved modeling of complex injector patterns. ROCCID was developed by combining existing performance and combustion stability models into one extensive program that can (1) analyze the performance and stability of existing rocket combustion chambers or (2) design stable and efficient rocket combustion chambers. PLC was originally thought to be the sub module of ROCCID responsible for steady state combustion calculations, but examination of a ROCCID development report (3) revealed that PLC was not recommended for use in ROCCID's steady state performance calculations. Although PLC was adapted for use in ROCCID to model atomization of shear coaxial and swirl coaxial injectors, PLC performance calculations became questionable and a more in-depth analysis of both programs was performed. The performance calculations are primarily associated with the fluid mechanics of the combustion chamber flow. Therefore, this study focused on chamber flow dynamics.

ROCCID Logic

ROCCID calculates propellant mixing efficiency using a two zone, four streamtube model (4). There is no interaction between the two zones (Figure 1), the core and the barrier,

which accommodate different injector types (4). The core and baffle element flows are mixed in the core zone, while the barrier and fuel film/cavity cooling elements are mixed in the barrier zone (4). The barrier zone consists of the annular region encompassing the core zone. Each zone is separated into two streamtubes of mixture ratio above and below the zone's mean mixture ratio (4). The overall Rupe mixing efficiency and the local vapor mixture ratio determine the streamtubes' mixture ratio and mass fraction (4). The streamtubes's C^* and Specific Impulse (ISP) are determined using the vapor mixture ratio of the streamtubes at the chamber throat (4). Throat C^* and ISP are used to determine the delivered C^* , C^* efficiency, and ISP-based energy release efficiency by mass weighting the individual streamtube contributions and correcting for any mass defect resulting from incomplete vaporization (4).

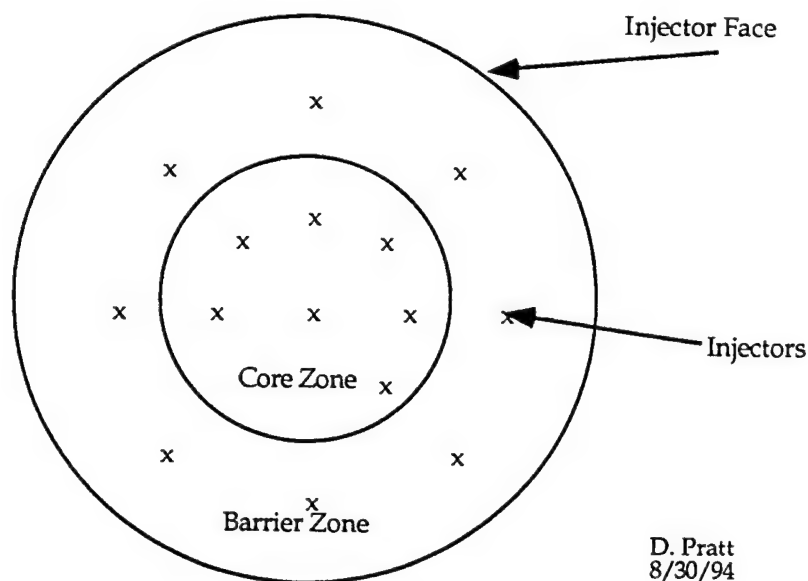


Figure 1 Core-Barrier Zones

PLC Logic

The chamber flow dynamics in PLC are modeled assuming flow in the near face region is in discrete injector stream tubes, while flow in the remainder of the chamber is modeled as finite elements or 'cells' (1). PLC distributes the vapor mass to grid cells from injector stream

tubes after the summation of stream tube areas completely fill the chamber cross-section (Fig 2). The grid cell area is converted into an equivalent circular area (2). The summation of the circular area radius and stream tube radius is compared to the distance from the center of the stream tube to the center of the circular area (2). If the distance between centers is less than the sum of radii, then the stream tube touches that grid cell (2). If the stream tube radius is greater than the distance between centers, all the mass from that stream tube is added to that cell (2). If the distance between centers is greater than the stream tube radius, half the vapor mass is added to that cell (2). The percentage of vapor mass in each cell is then compared to the actual mass in the flow. When the flow reaches the throat, the vapor mixture ratio is used to calculate C^* in each cell and the values are summed using a weighting factor. The summation of C^* values is used to calculate the energy release efficiency, which is used in turn to calculate the mixing efficiency.

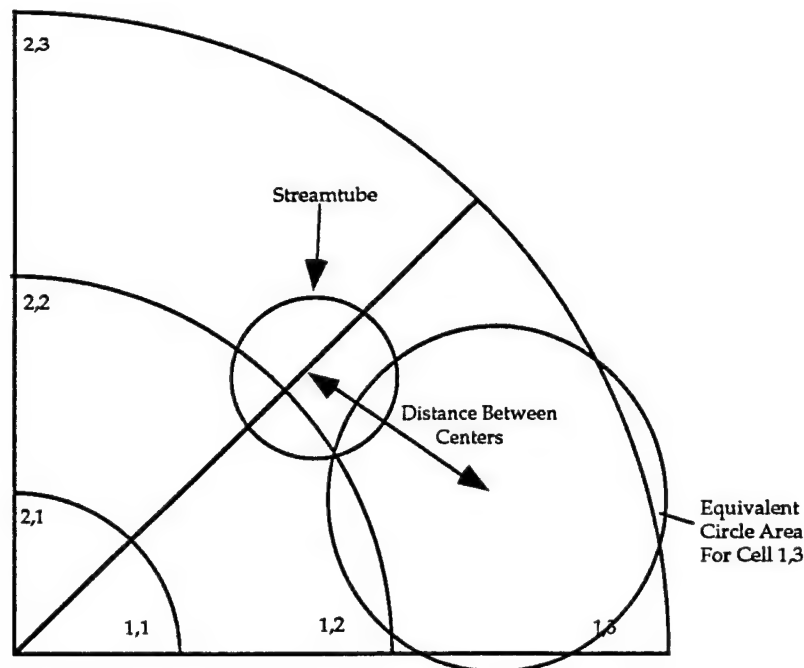


Figure 2 Streamtube Overlap Geometry

D. Pratt
8/29/94

Uncertainties Associated With PLC

Each of these programs involve simplifying assumptions in modeling the flow through the combustion chamber, but PLC does not include many processes that are fundamental to the physics of the flow. The following are assumptions made in the development of PLC:

- Conservation of momentum is ignored with respect to the droplet drag calculations; the droplets apply no drag forces to the gases that are accelerating them (2).
- Conservation of mass is ignored in the mass distribution process; the mass added to the cells was greater than the mass injected into the flow.
- The pressure is assumed constant and equal to the nominal chamber pressure throughout the cylindrical portion of the chamber.
- Droplets are assumed to move as a uniformly distributed ring surrounding the axis of the injection element from which they emanated (4).
- Flow calculations are based on the assumption of choked flow at the throat, but the assumption's validity is never checked (1).

Research in progress by the author will address all the above oversimplifications.

Selection of a Model for Further Research

Although ROCCID incorporates more physical processes into its model than PLC, it's two zone, four streamtube combustion chamber performance calculations are primarily used to evaluate the stability of the combustion chamber. Also, ROCCID is not currently configured to model complex injector patterns. Although PLC has many simplifications associated with its performance calculations, it can easily incorporate elaborate injector patterns. Therefore, PLC was selected for future research involving improved chamber flow modeling and mass distribution.

REFERENCES

1. Muss, J. A., Nguyen, T.V. and C.W. Johnson, User's Manual for Rocket Combustion Interactive Design (ROCCID) and Analysis Program, Volume II - Appendixes A-K; NASA CR-187110, May 1991.
2. O'Brien, Nancy D. "Effect of Liquid Coaxial Fuel Injector Distributions on Combustion Efficiency" Thesis. U of Tennessee Space Institute, 1993.
3. Pieper, Jerry L. and Richard E. Walker, LOX/Hydrocarbon Rocket Engine Analytical Design Methodology Development and Validation, NASA CR-191058, May 1993.
4. Muss, J. A., Nguyen, T.V. and C.W. Johnson, User's Manual for Rocket Combustion Interactive Design (ROCCID) and Analysis Program, Volume I - User's Manual; NASA CR-187109, May 1991.
5. Bernstein, A., Heiser, W. H. and C. Hevenor, "Compound-Compressible Nozzle Flow," Journal of Applied Mechanics September 1967: 548-554.

APPLICATION OF VORTICITY CONFINEMENT
TO A DELTA WING

David B. Underhill
Graduate Research Assistant
Department of Engineering Science & Mechanics

University of Tennessee Space Institute
B.H. Goethert Pkwy
Tullahoma, TN 37388

Final Report for:
Graduate Student Research Program
Arnold Engineering and Development Center

Sponsored by:
Air Force Office of Scientific Research
Bolling Air Force Base, DC

and

Arnold Engineering and Development Center

August 1994

APPLICATION OF VORTICITY CONFINEMENT TO A DELTA WING

David B. Underhill
Graduate Research Assistant
Department of Engineering Science & Mechanics
University of Tennessee Space Institute

Abstract

The computation of high angle of attack flow over a 75° delta wing was studied. At high angles of attack a flow phenomena of vortex bursting occurs, which is of great engineering concern. The efficient numerical modelling of such a flow field has proven to be difficult, and new methods must be explored to measure their feasibility of calculating such flows. The 'Vorticity Confinement' method was added to an existing flow solver to evaluate its performance. For this evaluation, experimental, adaptive grid, non-confined, and confined results are compared. The results indicate an improvement with regards to preventing excessive diffusion of vorticity, but no improvement with regards to the flow solvers ability to enhance vortex bursting. Due to the relatively short period of time allocated for this study, such results are preliminary at best.

APPLICATION OF VORTICITY CONFINEMENT TO A DELTA WING

David B. Underhill

Introduction

The numerical simulation of vortical flows is of growing concern. Vortices generated by an aircraft help determine the flight characteristics of the aircraft itself, and any other aircraft that may come in contact with these vortices. Of particular concern is vortex bursting, which has an effect on the generating aircraft. A vortex burst occurs in the presence of a strong adverse pressure field, such as those encountered over a delta wing at high angles of attack. This vortex burst results in a wildly fluctuating flow field, which can reduce the life expectancy of aircraft components and reduce the predictability of aircraft response to maneuvers. It is desirable to develop a numerical model that can predict such bursting without making the complexity of the simulation too difficult, that it cannot be achieved easily with present day computing capacity.

Methodology

The 'Vorticity Confinement' method presented by Steinhoff and Underhill{1} is mated to the 'XAIR' code supplied by CALSPAN INC. for this project. The 'XAIR' code is a variation of the Beam and Warming flow solver. For simplicity the Euler equations were chosen to model the flow field. The Euler equations in vector form:

$$\partial_t \vec{Q} + \partial_\xi \vec{F} + \partial_\eta \vec{G} + \partial_\zeta \vec{H} = 0$$

where

$$\vec{Q} = \frac{1}{J} \begin{pmatrix} \rho \\ \rho u \\ \rho v \\ \rho w \\ e \end{pmatrix} \quad \vec{F} = \frac{1}{J} \begin{pmatrix} \rho U \\ \rho u U + \xi_x P \\ \rho v U + \xi_y P \\ \rho w U + \xi_z P \\ (e + P) U \end{pmatrix}$$

and

$$U = u \xi_x + v \xi_y + w \xi_z$$

similarly for G and H.

The 'Vorticity Confinement' modifies the Euler equations by adding an additional term to the Euler equations. The modified Euler equations:

$$\partial_t \bar{Q} + \partial_t \bar{F} + \partial_\eta \bar{G} + \partial_\zeta \bar{H} + \epsilon \bar{K} = 0$$

where

$$\bar{K} = \frac{1}{J} \begin{pmatrix} 0 \\ \rho k_1 \\ \rho k_2 \\ \rho k_3 \\ 0 \end{pmatrix}$$

k_1, k_2, k_3 are the i,j,k components of

$$\frac{\nabla a}{|\nabla a|} \times \bar{\omega}$$

and

$$a = - |\bar{\omega}|$$

For programming ease a fractional step method is utilized, such that the original Euler equations are solved, then an additional step is taken to solve for the confinement terms. The confinement step:

$$\partial_t \bar{Q} + \epsilon \bar{K} = 0$$

This method also leaves the original algorithm in the 'XAIR' code intact, with only minor alterations in the controlling subroutines to allow for calling the 'Confine' subroutine. The 'Confine' subroutine employs cell weighting presented by Steinhoff, et al.(2), which convects vorticity in the direction of the local maximum of the gradient of vorticity, which is in the opposite direction of the vorticity diffusion. The confinement terms are calculated on grid points, and then averaged onto grid cell centers. The values at the cell centers are now transferred back to the grid points such that the grid points with higher than average values of 'a' receive a weighted value, and grid points with lower than average values of 'a' receive no confinement weighted from that cell center.

The procedure for arriving at a solution is as follows. First the 'XAIR' code is run without confinement until it arrives at a converged solution, which for this project took 8,000 to 10,000 time steps. After it is converged,

the 'Confine' subroutine is now called, and 'XAIR' is run in the fractional step mode. This portion took between 500 and 1,000 time steps to reach the converged confined solution. This method of first converging the unconfined solution was used to save time. It was seen that 'Confine' subroutine increased the run time by 40% for the 'XAIR' code, but it was also determined that approximately the same solution was reached if 'Confine' was called during the entire run. This method resulted in only a 2 to 4 percent increase in the total run time, rather than the 40% previously mentioned.

The flow conditions solved were air flow over a flat 75° delta wing similar to the one used by Modiano{3}. The Mach number used was 0.3, to make the compressibility effects negligible. The outer boundaries were held fixed at freestream velocity. This boundary approximation is allowable given the great distance of the boundary to the body, which is about 3 chord lengths. Slip boundary conditions were imposed on the body. At the outflow boundary, simple extrapolation was used. Two different grids were used, first a medium grid which had $71 \times 57 \times 71$ points in the axial, circumferential, and radial directions, and a coarse grid which had $43 \times 31 \times 36$ points. The terms medium and coarse are used in comparison to the grids used by Ekaterinaris and Schiff{4}. In reference 4 the fine grid contained $112 \times 105 \times 70$ grid points. Several runs were made on each grid at differing fixed angles of attack. These angles of attack were chosen in order to make a direct comparison to previously published works by experts in the field.

The value of epsilon was chosen so as not to cause any adverse effects upon the stability of the solution. This value is the maximum recommended for this solution, and lower values of epsilon were also used.

Numerical Results

Looking at the vorticity distribution, the 'Confine' subroutine made improvements in the solution over the delta wing. Above the body at 0.9 chord length on the medium grid at 20.5° angle of attack, the maximum vorticity increased from 0.0015 to 0.0018, a 20 percent increase. The coarseness of both grids in the wake section led to great amounts of diffusion and far superior performance from the 'Confine' subroutine. For the medium grid at an angle of attack of 32.0° , at only one chord length behind the wing, the maximum vorticity was increased from 0.0028 to 0.0062, more than a 100 percent increase. This improvement can be seen in the Vorticity Magnitude contour plots in figure 1.

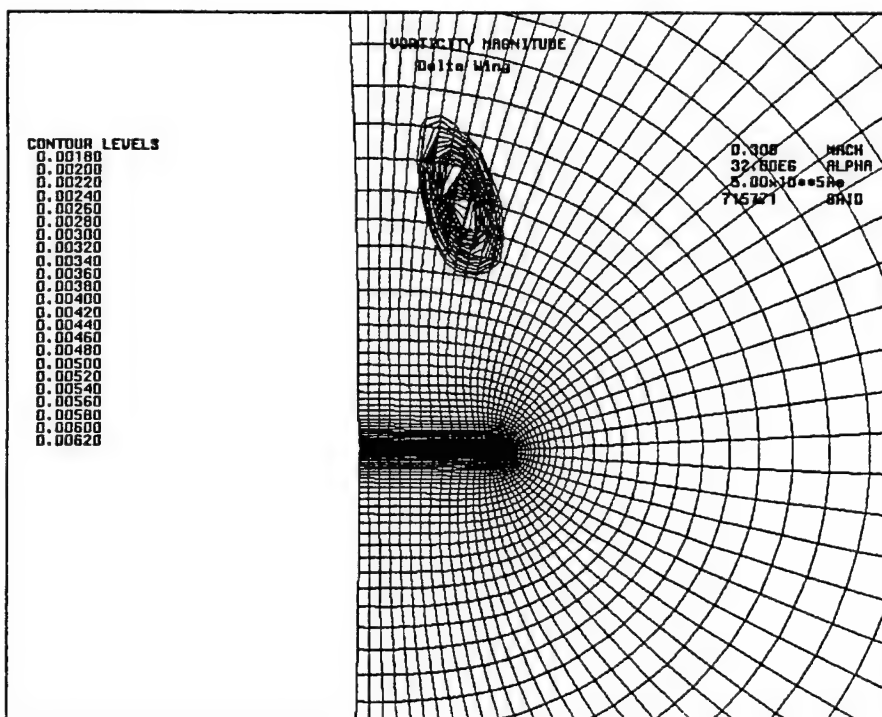
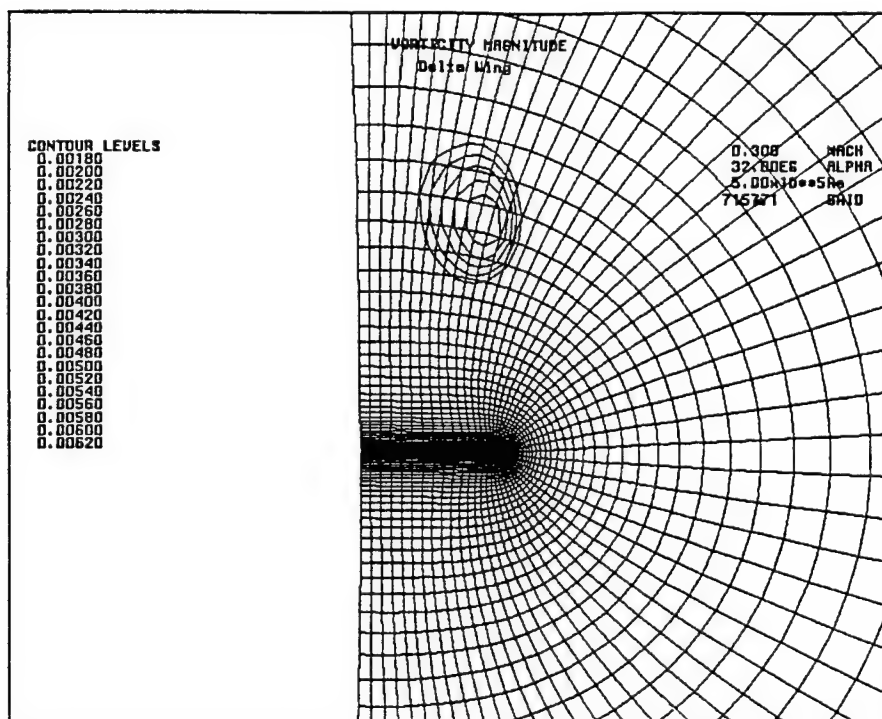


Figure 1: Vorticity magnitude contours. Top, the unconfined solution, and bottom, the confined solution.

In the comparison of normal force and pitching moment coefficients, two sources of data were used. They are the experimental (Exp) results of Jarrah{5} for normal forces and Hummel and Srinivasan{6} for pitching moments, the fixed grid finite element (Coarse) and adaptive mesh (Adapted) results both from Modiano{3}. The results are also tabulated by angle of attack (Alpha), grid mesh size utilized by 'XAIR' computations (Grid), and by confinement coefficient (Epsilon). In table 1, the unconfined results (Xair), have consistently lower normal force coefficients than the Adapted solution, with the Adapted solution results being closer to the experimental results. The Confined solution results were generally the same in the Alpha = 20.5° case in which bursting did not occur, however in the cases where vortex bursting did occur, there was a general increase in the normal force coefficients. This increase compares well with both the Adapted and Exp results.

Alpha	Grid	Exp	Coarse	Adapted	Xair	Confine	Epsilon
20.5	71x57x71	0.92	0.773	0.86	0.824	0.821	5.00E-08
32.0	71x57x71	1.45	1.35	1.49	1.26	1.31	5.00E-08
20.5	71x57x71	0.92	0.773	0.86	0.824	0.821	1.00E-07
32.0	71x57x71	1.45	1.35	1.49	1.26	1.33	1.00E-07
0.0	43x31x36	0.05	-0.076	--	-0.071	--	--
20.5	43x31x36	0.92	0.773	0.86	0.76	0.764	5.00E-08
32.0	43x31x36	1.45	1.35	1.49-1.55	1.31	1.36	5.00E-08
38.0	43x31x36	1.40	1.53-1.59	1.32-1.50	1.32	1.47	5.00E-08
52.0	43x31x36	1.36	1.76-1.81	1.21-1.26	1.08	1.34	5.00E-08

Table 1: Coefficients of normal force

In Table 2, the calculations of pitching moment coefficients, the Adapted solutions were consistently high when compared to Exp. The Confine solutions also increase the moments beyond that of the Exp results. This is also true for Xair in the coarse grid calculations, but not in the medium grid results. Higher angle of attack runs need to be made to determine if the medium grid Xair results remain low. It should also be noted that the vortex burst is an unsteady flow and the moment will actually oscillate. Due to the relatively short period of time allotted for this study, complete results were not obtained in the cases with bursting.

For the coarse grid, vortex bursting did not occur when and where experimental results indicate. In the experimental results, bursting occurred at Alpha = 32.0°, but in the coarse grid calculations, bursting did not occur until Alpha = 38.0°. The burst also occurred further back on the delta wing than experimentally predicted for the

coarse grid. With this information, it is concluded that the coarse grid did not have a sufficient number of grid points. It was also observed that the confinement did not lead to earlier breakdown of the vortex, but instead it was shown that a value of epsilon that is too large can hinder breakdown. In computations completed on the medium grid it was seen that the confined and the unconfined solutions had the same location of the vortex burst. Further, it was seen that burst location did not change when epsilon was varied.

Alpha	Grid	Exp	Coarse	Adapted	Xair	Confine	Epsilon
20.5	71x57x71	0.098	0.112	0.126	0.110	0.108	5.00E-08
32.0	71x57x71	0.12	0.161	0.153	0.111	0.126	5.00E-08
20.5	71x57x71	0.098	0.112	0.126	0.110	0.128	1.00E-07
32.0	71x57x71	0.12	0.161	0.153	0.111	0.137	1.00E-07
0.0	43x31x36	0.0	0.0	--	0.0	--	--
20.5	43x31x36	0.098	0.112	0.126	0.0973	0.0987	5.00E-08
32.0	43x31x36	0.12	0.161	0.153	0.146	0.162	5.00E-08
38.0	43x31x36	0.11	0.210	0.131	0.134	0.183	5.00E-08
52.0	43x31x36	--	0.282	0.317	0.183	0.206	5.00E-08

Table 2: Coefficients of pitching moments

Conclusion

Computational results have been presented for subsonic flow over a delta wing. The 'Vorticity Confinement' method was added to the existing 'XAIR' flow solver in hope of improving its vortical dynamics, with the simple addition of a single subroutine. The 'Confine' subroutine was added to the flow solver by utilizing a fractional step formulation. With this approach, virtually any flow solver can coexist with 'Vorticity Confinement.' It was shown that the 'Confine' subroutine improved the solution in highly diffusive grid regions such as the wake region of the delta wing. It was also shown that with the formulation used for this study, the confinement neither hindered nor encouraged vortex bursting. Future research needs to be directed towards new formulations of the 'Confinement Method' that can enhance vortex bursting even on extremely coarse grids.

References

- {1} J. Steinhoff and D. Underhill, "Modification of the Euler Equations for 'Vorticity Confinement': Application to the Computation of Interacting Vortex Rings," Physics of Fluids, Vol. 6, 2738 (1994)
- {2} J. Steinhoff, T. Mersch, and F. Decker, "Computation of Incompressible Flow over Delta Wings Using Vorticity Confinement," AIAA Paper 94-0646 (1994).
- {3} D. Modiano, "Adaptive Mesh Euler Equation Computation of Vortex Breakdown in Delta Wing Flow," Phd. Dissertation, MIT, 1993.
- {4} J. Ekaterinaris and L. Schiff, "Vortical Flows over Delta Wings and Numerical Prediction of Vortex Breakdown," AIAA Paper 90-0102 (1990).
- {5} M. Jarrah, "Unsteady Aerodynamics of Delta Wings Performing Maneuvers to High Angle of Attack," Phd Dissertation, Stanford, 1988.
- {6} D. Hummel and P. Srinivasan, "Vortex Breakdown Effects on the Low-Speed Aerodynamic Characteristics of Slender Delta Wings in Symmetrical Flow," Royal Aeronautical Society Journal, Vol. 71, 319, (1967).

**A THEORETICAL STUDY OF LITHIUM AND
MOLTEN SALT GRAPHITE-INTERCALATES**

**Christian S. Bahn
Graduate Student
Department of Chemistry & Geochemistry**

**Colorado School of Mines
Golden, CO 80401**

**Final Report for:
Graduate Summer Research Program
Frank J. Seiler Research Laboratory**

**Sponsored by:
Air Force Office of Scientific Research
Bolling Air Force Base, DC**

and

Frank J. Seiler Research Laboratory

September 1994

A THEORETICAL STUDY OF LITHIUM AND MOLTEN SALT GRAPHITE-INTERCALATES

Christian S. Bahn
Graduate Student
Department of Chemistry & Geochemistry
Colorado School of Mines

Abstract

A theoretical study was performed to design a method for predicting intercalation behavior of room temperature molten salts into a graphite lattice. The molten salt examined was 1-ethyl-3-methylimidazolium tetrafluoroborate (EMI-BF₄). The graphite sheet system was modeled on a workstation using MOPAC 93 to observe potential structural changes in the graphite and/or the molten salt following an intercalation process as well as any molecular orbital interactions between the graphite and the salt. The modeling of the graphite sheets used the much studied lithium intercalated graphite (LIG) as a benchmark. The results indicate that the complex graphite system can be modeled simply and effectively using semiempirical methods to study the intercalation-deintercalation behavior of ions.

Introduction

Batteries using graphite for both the anode and cathode have been studied recently as an alternative to those using transition-metal oxide electrodes¹. Graphite provides some key advantages over the transition metal oxides, particularly in the areas of cost and environmental safety. This dual graphite electrode set up is known as a dual intercalating molten electrolyte (DIME) system¹, where the molten electrolyte is a room temperature molten salt. The molten salts currently being looked at by electrochemists are 1-ethyl-3-methylimidazolium (EMI^+) and 1,2-dimethyl-3-propylimidazolium as the cations and BF_4^- or AlCl_4^- as the anions. A battery configuration with these molten salts has the salt acting as both electrolyte and intercalate for both anode and cathode. The interactions taking place between the graphite and the constituents of the salt during intercalation is relatively unknown. The effects of interest include the molecular orbital interactions, electron transfer, and structural changes of the ions and the graphite sheets. Molecular modeling of the graphite-molten salt system can give some insight to the changes that occur during the intercalation process. To model this complex system effectively, one must create a representative example of the graphite, maximizing the view of the ions to an infinite sheet, and minimizing computational resources required for reasonable results. The most cost effective method to accomplish these objectives is to use a semiempirical computational approach, for which MOPAC 93² was utilized.

Method

All calculations were performed on a SUN SparcStation2 using MOPAC 93 and the PM3 Hamiltonian³ unless otherwise mentioned. The initial process in this study was the benchmarking of a graphitic system to known values, to include the bond lengths and the sheet spacing. The two forms of graphite concerned are pure graphite in a staggered arrangement (Figure 1) and lithium

Figure 1

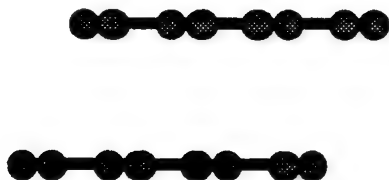
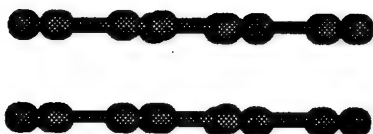


Figure 2



intercalated graphite in an eclipsed AA arrangement (Figure 2). For the purpose of modeling the graphite, graphite-like molecules were used (benzene, coronene, etc.). The sheets were constrained to be planar and parallel to each other. All the bond distances and angles were optimized to maintain D_{6h} symmetry.

Results and Discussion

The first attempts at modeling intercalation involved placing a single lithium ion above and centered over a benzene ring (Figure 3) or a coronene ring (Figure 4). In both of these cases, the ion remained centered during the optimization but moved too far above the ring (2.35 Å) to be considered a good representation of intercalation. A question arose as to the ability of MOPAC to optimize a cation ion centered on a π -cloud if the ion did not begin the optimization in that location. A trial was performed on coronene with a lithium ion placed above the ring at a 1 Å lateral offset from the center that was allowed to optimize. The distance from the ring was set at 2.35 Å and constrained. MOPAC successfully optimized the ion to be centered above the ring. However, in order to properly model an intercalated ion, two layers of rings are needed to form an upper and lower layer of graphite.

Figure 3

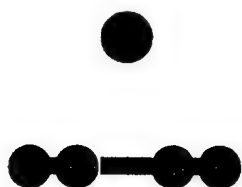


Figure 4

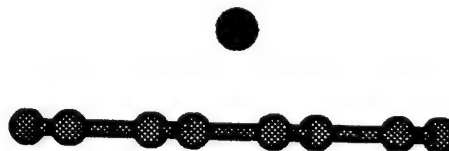
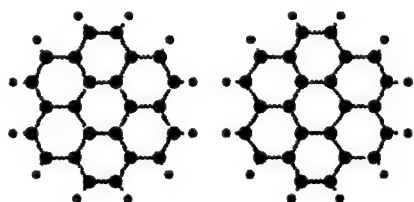


Figure 5



was chosen rather than benzene layers as the model for intercalation since the larger size of the coronene would be better suited for later studies on the organic molecules. A calculation of two coronene rings centered above one another and allowing only the sheet distance to optimize yielded unreasonable results when compared to graphite. The rings had a tendency to optimize far beyond the known d-spacing of 3.39 \AA and ended up with a 12 \AA separation. Allowing the rings to slip laterally during the optimization yielded a side by side structure (Figure 6). The forces which give solid graphite its

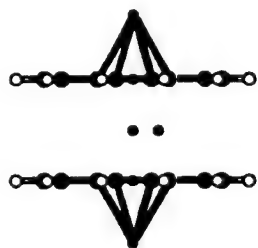
Figure 6



structure were clearly not accounted for in this model. A possible explanation for this behavior is that programs such as MOPAC assume a gas phase system with isolated molecules rather than a solid or crystalline phase. The intermolecular forces which are present in a solid are not parameterized within the program, therefore, some type of artificial restoring force is required to simulate the solid state.

One approach for simulating graphite sheets as they would exist in a solid is to place a restorative force on the sheets to mimic the pressure felt from the many layers beyond the two used in the calculation. This restorative force was established by placing a 2- sparkle, a doubly negative

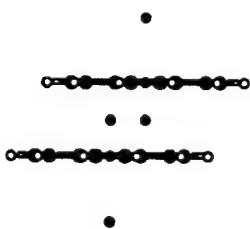
Figure 7



point charge, on either side of the entire system a fixed distance from the center (Figure 7). The initial set of calculations used the eclipsed form of graphite and found that the sparkle-to-center distance should be set at 4.55 \AA to bring the two sheets to a 3.39 \AA spacing. This arrangement, however, gives a false picture of graphite in its natural form, which is known to be the staggered AB configuration. Using this AB structure in

the model (Figure 8), the sparkle-to-center distance increased to 4.70 Å. The increase in the sparkle-to-center distance is an important result because it shows that MOPAC is correctly interpreting the π -cloud interactions between the graphite sheets. There is less repulsion in the staggered

Figure 8



arrangement of the sheets, thus it is a lower energy arrangement which agrees with the known natural structure. For MOPAC to see a difference between the two structures is very significant since the sheets go from staggered to eclipsed during the intercalation process. One set of calculations that was performed, but not reported in detail, used capped bonds in place of terminal hydrogens on the coronene

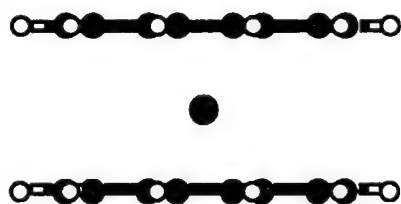
molecules. Capped bonds are an optional "element" available in MOPAC. They are designed to meet valency requirements in the chemical environment of the molecule without acquiring a net charge. A capped bond will behave like a monovalent atom that is capable of changing its electronegativity to achieve a zero charge^{2,3}. Theoretically, the capped bonds used in place of hydrogens should more accurately portray an infinite sheet of graphite. Results were mixed, but generally showed little deviation from the hydrogen terminated systems. Systems incorporating reaction coordinates may find the capped bonds more useful. All results reported in this study used hydrogen terminated bonds.

While the modeling of the graphite sheets is a significant accomplishment and an important step, it is not the focus of this study. The need to understand intercalated systems for molten salts is the primary focus, but first some standard must be established with a known system. To benchmark these intercalated graphite systems, lithium intercalated graphite (LIG) was chosen because of the vast amount of experimental data collected in recent years. LIG exists with many different degrees of saturation of lithium within the graphite⁵, with each different degree known as a stage. First stage LIG is the most saturated form and has the general formula LiC_6 , and will be used for this

study. The initial calculations were performed without the charged sparkles to see if the simpler models would simulate the same behavior as the pressured models of graphite had done previously.

The first effort at LIG was conducted with one lithium ion between two coronene sheets (Figure 9). The addition of the lithium ion allows some of the electron density in the π -cloud to be transferred to the ion, decreasing the electron repulsion between sheets. Optimization of this

Figure 9



intercalated system resulted in a sheet separation of 4.56 Å, which is a 22% error when compared to the X-ray diffraction (XRD) value of 3.74 Å for first-stage lithium intercalated graphite⁵. This error is considered too great for any type of quantitative analysis, but is acceptable for qualitative modeling.

An attempt was made to reduce sheet spacing by placing a total of three lithium ions between the sheets, possibly having the effect of lowering the electron density further, and reducing sheet-sheet repulsion. The lithium ions were arranged in a triangular pattern sitting in the center of alternating six-membered rings on the outside portion of the coronene ring (Figure 10). The optimization gave poor results, as the lithium ions migrated outside of the carbon portion of the ring system completely (Figure 11). This appears to be a direct result of the lithium ions not seeing an infinite sheet of

Figure 10

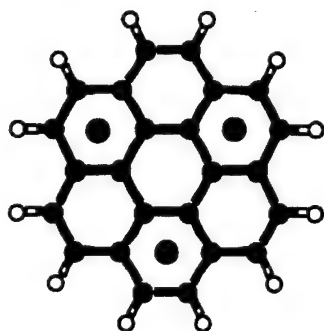
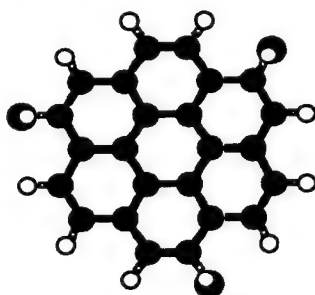


Figure 11



graphite. The terminal hydrogens have a tendency to lose electron density to the ring causing a charge imbalance within the carbon network. This imbalance of charge is responsible for pushing the lithiums toward the outside of the ring system.

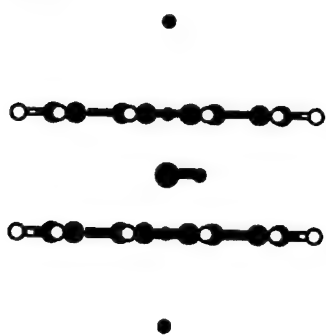
Because this imbalance of charge is caused by the edge of the graphite sheet model, it will be referred to as an edge effect. In order to utilize more lithiums in the intercalated system, a larger

series of rings will need to be used. A test performed to observe the nature of the interaction between the lithium and the graphite was to replace the lithium ion with a positively charged sparkle, a point charge of +1, and observe the behavior of the sheets. The calculation with the sparkle gave a 9.8 Å spacing, suggesting that the lithium-graphite system is stabilized by wavefunction interaction and not just by electrostatics. This test is also the first evidence that MOPAC is capable of correctly interpreting the nature of molecular orbital interactions taking place between a cation and graphite during the intercalation process. However, to look at these interactions properly, the two-layer model for graphite utilizing the pressure centers must be used in order to better portray the conditions found within solid graphite

It became clear that the benchmarking of LIG would require the utilization of sparkles in the same manner as they had been for non-intercalated graphite. First stage LIG was simulated by using an eclipsed coronene model with a -2 sparkle fixed on either side of the coronene molecules.

The sparkles were fixed at the 4.70 Å distance found to portray precisely the graphite system. There

Figure 12



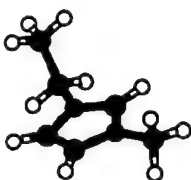
was a lithium ion centered on the coronenes and directly between the two sheets (Figure 12). The eclipsed model was chosen for conservation of computational resources. It is known experimentally that LIG is in an eclipsed AA arrangement⁵ and this starting point spares the calculation from having to make the conversion from staggered to eclipsed. The results from this calculation showed a 3.739 Å sheet spacing, which is essentially identical to the XRD value of 3.74 Å⁵. The

accuracy with which MOPAC modeled the LIG system using the sparkle distances for non-intercalated graphite is very encouraging. These results strongly suggest that similar modeling of intercalated organics should provide reasonable predictions of the system's characteristics.

The first organic cation modeled as an intercalate was the EMI⁺ cation. Experimentally, EMI⁺ is a favorable candidate for use in batteries¹, but repeated cycling leads to severe exfoliation of

the graphite electrode. The belief is that exfoliation is caused by excessive c-axis "breathing" (perpendicular to the sheets) by the graphite lattice during intercalation-deintercalation. Modeling of the intercalated species should give some insight as to why the exfoliation occurs to such a large

Figure 13

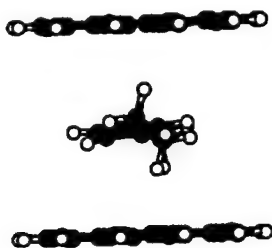


degree. Before modeling the EMI⁺ as an intercalate, it was first modeled and optimized alone (Figure 13) so that comparisons could be made between the intercalated and the non-intercalated molecule. In order to be sure that a stable geometry was achieved, a harmonic vibrational analysis was performed on the optimized molecules. This analysis yields the infrared

frequencies for the molecule. Should any imaginary frequencies result, the molecule is not at a stable point and a manual geometry adjustment followed by reoptimization will need to be done. EMI⁺ was found to be stable with the ethyl group perpendicular to the plane of the ring and the methyl group rotated so that one hydrogen is perpendicular to the ring and on the same side as the ethyl group. Using the same methodology as for the lithium ion trials, the calculations for the intercalated cation were performed with and without the -2 sparkles. The main purpose for doing so is to provide more data for predictions of XRD and IR results.

When the EMI⁺ was placed between the two sheets in the non-pressured model, the graphite and the cation underwent some interesting changes. The graphite expanded its d-spacing to 8.01 Å, (Figure 14). This expansion of nearly 250% agrees with the exfoliation behavior found experimentally. However, based on the separation behavior of the graphite sheet model with the lithium ion and no

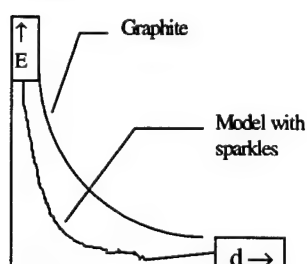
Figure 14



sparkles, this d-spacing is most likely too large. The cation optimized with the ethyl group rotating 52° from perpendicular, one of the methylene hydrogens in the plane of the ring, and the other methylene hydrogen pointing at a graphite sheet. The three closest hydrogens to either graphite sheet were all approximately 2.55 Å from a sheet. The trials with the EMI⁺ cation intercalate and the external pressure centers show a

variation from the above results. The most important change occurs in the graphite sheet spacing which decreases to 5.18 Å. Pronounced structural changes in the EMI⁺ cation are also seen from the optimization. The imidazole ring system arranged itself to be parallel to the graphite sheets, pointing out possible π -system interactions, and the ethyl group on the EMI⁺ rotated so as to be in the plane with the ring. Much of this particular calculation must be taken with suspicion since the optimization was not able to reach a stable geometry. A prolonged optimization showed that the

Figure 15



cation will slip from between the graphite sheets. This is most likely due to edge effects. Again, a larger sheet model for the graphite will need to be employed. It is also possible that the use of the sparkles at their 4.70 Å distance will not work properly for large organic cations which force the graphite sheets beyond some point. Figure 15 shows how the repulsion vs. distance graph may appear for both normal graphite

and the sparkles. Because of the difficulties encountered with the sparkle model, a vibrational analysis was not performed on this structure.

Harmonic vibrational analyses were done on the intercalated cation with no sparkles and the non-intercalated cation to look at the changes in the ion's C-H stretching frequencies. The results for this particular model are questionable because of the possible edge effects on the ethyl group, and subsequent shifting of the cation within the graphite lattice. The calculation revealed that the greatest change took place with the hydrogens on the methylene carbon. The hydrogen which turned to point at a sheet became the primary contributor to a frequency that displayed a 68 cm⁻¹ drop going from non-intercalated to intercalated. The other hydrogen on that carbon showed a 20 cm⁻¹ drop in frequency (Table 1).

Table 1: Methylene Hydrogen Frequencies and Percentage of Contribution		
Non-intercalated		
	2926.05 cm ⁻¹	2986.03 cm ⁻¹
C7 - H15	46.8%	51.2%
C7 - H16	50.4%	47.2%
Intercalated		
	2858.69 cm ⁻¹	2966.62 cm ⁻¹
C79 - H87	85.9%	9.6%
C79 - H88	11.7%	88.5%

Table 2: Ring Hydrogen Frequencies and Percentage of Contribution		
Non-intercalated		
	3056.54 cm ⁻¹	3072.85 cm ⁻¹
C3 - H13	44.0%	47.5%
C5 - H14	49.1%	42.8%
Intercalated		
	3065.79 cm ⁻¹	3081.87 cm ⁻¹
C75 - H85	48.2%	43.8%
C77 - H86	45.1%	46.9%

An unexpected observation is that the hydrogens attached to the ring atoms showed virtually no change in frequency (Table 2). This could be a sign that there is little or no π - π interactions between the π -cloud of the imidazolium ring and the π -clouds on the graphite sheets at this large d-spacing. A charge comparison between the intercalated and non-intercalated cation shows little difference in net charge on individual atoms. This verifies that in this arrangement there is very little charge transfer taking place, which is another possible indicator of no interactions between the different ring systems in this configuration. One piece of information from the optimization that is difficult to interpret involves a slippage of the cation, forming an ABA type arrangement with the graphite. There are two major possibilities for this effect. The first is that the ethyl group was too close to the edge of the coronene to see an infinite sheet. Edge effects could come into play here and cause the imidazolium to migrate to the outside. The other possibility is that there are some sort of π -cloud effects between the imidazolium and the graphite that gives a staggered ABA natural graphite-like structure. Further study with a larger graphite model will be necessary to discover what is occurring in this instance.

Experience with EMI⁺ shows that a graphite model with at least one more outside layer of rings will be required for qualitatively modeling intercalated DMPI⁺. It is likely that even for the next larger model, DMPI⁺ will experience similar edge effect problems as the EMI⁺ cation. Creation of this larger sheet system dramatically increases the total number of atoms in the system, which dramatically increases the CPU time required for the various calculations. The larger graphite system was modeled and an optimization was attempted. Even without an intercalated organic, the full optimization was judged to be time prohibitive for this study. Later examination of these intercalated systems may focus on these larger sheets. Non-optimized versions of the graphite and two separate isomers of DMPI⁺ as intercalates were modeled for graphical purposes. The isolated cations have been optimized for comparison with future studies.

Comparison to Previous Work

One of the most significant features of this set of calculations is the size of the system used. Previous attempts at studying LIG were performed using *ab initio* techniques on substantially smaller systems. Other differences involve looking at the charge transfer taking place between the lithium and the graphite. Most studies have concerned themselves with the intercalation of a lithium atom losing its 2s electron to the graphite π -cloud, whereas here the lithium ion has already been stripped of this electron before intercalation. The intercalated atom is claimed to gain the entirety of a +1 charge in the *ab initio* studies, however intercalation of a +1 ion using semiempirical methods shows a partial gain of electron density by the lithium ion from the graphite sheets.

Conclusions

This study has found that an effective model for graphite in a non-intercalated or intercalated structure can be established using a representative large system and semiempirical techniques. Based upon

the results for non-intercalated and lithium intercalated forms of graphite, it is feasible to examine the actual intercalation process of individual ions using other more advanced features of MOPAC. We have also found that to look at larger organic cations, i.e. for molten salt systems, a graphite-like ring system will need to be constructed so that the outermost layer of rings extend beyond the outer perimeter of the cation by at least one layer. One boundary layer appears to be enough to make the intercalate behave as if it were in an infinite lattice.

Acknowledgments

I would like to thank the Air Force Office of Scientific Research and the Frank J. Seiler Research Laboratory for sponsoring this research. Special thanks go to Captain Walter Lauderdale and Dr. Richard Carlin for their valuable assistance and guidance during the course of this research effort. Thanks must also go to the rest of the staff at FJSRL for the camaraderie and pleasant working environment that made the summer a very positive experience.

¹ Richard T. Carlin, Hugh C. De Long, Joan Fuller, Paul C. Trulove, *J. Electrochem Soc.*, **141**, L73(1994)

² MOPAC 93, ©Fujitsu Inc.

³ J. J. P. Stewart, *J. Comp. Chem.*, **10**, 209(1989)

⁴ F. Albert Cotton, Geoffrey Wilkinson, *Advanced Inorganic Chemistry*, 4 ed., p. 357, 1980

⁵ M. Stanley Whittingham, Allan J. Jacobson, *Intercalation Chemistry*, p. 20, 27, 31, 1982

Theoretical Investigations of the NLO properties of substituted Acetylenes

Antonio M. Ferreira

Department of Chemistry

University of Memphis

Memphis, Tennessee 38152

e-mail: amferreira@msuvx2.memphis.edu

Final Report for:
Graduate Student Research Program
Frank J. Seiler Research Laboratory

Sponsored by:
Air Force Office of Scientific Research
Bolling Air Force Base, DC

and

Frank J. Seiler Research Laboratory
United States Air Force Academy

October 1994

Theoretical Investigations of the NLO properties of substituted Acetylenes

Antonio M. Ferreira

Abstract: The Nonlinear Optical (NLO) properties of a series of substituted acetylenes have been studied from a theoretical perspective. Calculations of the polarizability and the first and second hyperpolarizabilities have been carried out using an *ab initio* Time-dependent Hartree-Fock (TDHF) approach with several basis sets in order to evaluate the computational methods involved as well as substituent effects on a class of relatively simple molecules.

Theoretical Investigations of the NLO properties of substituted Acetylenes

Antonio M. Ferreira

Introduction:

The properties of nonlinear optical materials are of great interest for a variety of scientific and engineering applications. Much of the current research is geared primarily toward the field of photonics and associated technologies. As an emerging technology, photonics provides a great driving force for both applied and basic research in the field of nonlinear optics (NLO). The advent of lasers has provided a readily available source of coherent light at suitable intensities for the observation of NLO phenomena in a variety of materials and a good deal of experimental data has been accumulated regarding NLO properties and phenomena in a wide variety of chemical systems. In addition, much basic research is directed toward the NLO process at the molecular level as well as with bulk media. The attempt to understand the nature of NLO phenomena and the molecular basis for such properties is of central importance to the field.

Currently, there is a fair amount of experimental data concerning the NLO properties of many materials ranging from inorganic compounds, such as liquid crystals, to organic systems containing large, delocalized π -electron systems. From a theoretical standpoint, there is a need to understand the basis of NLO phenomena in these materials for use as a predictive tool. One of the current goals for theory is the ability to identify feasible NLO materials in an effort to conserve time and resources at the experimental level. Theory has yet to devise widely applicable predictive tools which are useful to the experimentalist or non-theoretician in the identification of potentially useful materials.

The long term goal of the current research is to develop a fairly simple model for use in such predictions. Substituents, crystal defects, dipole moments, and other molecular properties all play an important role in determining the nature of the NLO response of a material. The effect of substituents has been chosen for the current investigation as an area where theory may be able to provide some insight into the effect of substituent groups on the NLO response of materials.

There is some theoretical evidence which suggests that a linear relationship exists between the static and frequency dependent properties of substituted organic systems.¹ Current evidence suggests that frequency dependent properties such as second harmonic generation (SHG), third harmonic generation (THG), optical

¹ W. J. Lauderdale Unpublished results.

rectification (OR) and others appear to be a linear function of substituent group and the associated static property. It is hypothesized that a free energy type of relationship can be derived to predict frequency dependent properties for substituted systems based on calculated static values. The goal is to derive a predictive method similar to the well-known Hammett linear free energy relationship. If such a relationship can be found there is the potential for a widely applicable predictor for use in NLO material selection.

Another consideration is the size of the basis set required to obtain acceptable results in such NLO calculations. Basis sets as small as STO-3G and as large as the Sadlej² basis have been used for such calculations. The dilemma is to identify a computational method which satisfies the required accuracy while keeping calculation times to a minimum. The current investigation hopes to provide some insight into this second question as well.

Methods:

The current calculations were performed using the GAMESS³ quantum chemistry package as modified by Henry A. Kurtz.⁴ This method employs an iterative solution for the Time-dependent Hartree-Fock (TDHF) approach to the NLO problem. In short, TDHF theory derives from an analytic set of solutions to the time-dependent electronic response of a material to incident electromagnetic radiation. These solutions are then converted to frequency domain solutions by means of a Fourier series.⁵ This method provides us with an analytic solution to the problem that is well suited to *ab initio* methods.

The primary difficulty in the TDHF calculations described in this report stems from the theoretical description of the NLO phenomenon. In order to accurately model the NLO response of materials it is necessary to include diffuse *p*- and *d*-orbitals in the basis sets. The necessity of large basis sets is a direct result of the need to describe the polarization response of the electrons. This leads to large basis sets on even the smallest atoms in an attempt to completely describe the orbital space which interacts with the incident radiation. As a result, calculation times are greatly increased and quickly become prohibitive for large systems.

One solution to this problem is to employ parallel computation methods to reduce the wall-clock time required for the calculations. Two architectures were used to this end, a cluster of 18 SPARC-2 workstations using the tcgmsg message passing system⁶ and a CM-5 distributed memory parallel super computer. In each case, the distributed memory model is employed for calculations.

² Andrzej Sadlej *Czechoslovak Chem. Comm.* **1988**, **53**, 1995.

³ M. W. Schmidt; K. K. Baldridge; J. A. Boatz; J. H. Jensen; S. Koseki; N. M. Matsunaga; M. S. Gordon; K. A. Nguyen; S. Su; T. L. Windus; S. T. Elbert *J. Comp. Chem.* **1993**, **14**, 1347.

⁴ Department of Chemistry, University of Memphis, Memphis, TN 38152. *e-mail*: kurtzh@msuvx2.memphis.edu

⁵ There are several excellent texts which describe the TDHF derivations, such as *Quantum Mechanics in Chemistry* (Schatz and Ratner) and *Nonlinear Optics* (Boyd).

⁶ R. J. Harrison *Int. J. Quantum Chem.* **1991**, **40**, 847.

In choosing a suitable set of related materials, two considerations were paramount: (1) It was necessary for the materials to possess a significant amount of redundancy in structure so that substituent effects could be isolated and (2) The compounds selected for study had to be of a reasonable size due to time constraints and available computer resources. With these two considerations in mind, a series of substituted acetylenes of the form $X-C\equiv C-Y$ was chosen where X and Y were members of the set {H-, F-, CN-, NH₂-, NH₂[†]-, NO₂-}. The actual set of compounds used for the calculations was HCCH, FCCH, FCCNH₂[†], FCCNH₂, CNCCH, CNCCNH₂[†], CNCCNH₂, NH₂CCH[†], NH₂CCH, NH₂CCNH₂[†], NH₂CCNH₂, and NO₂CCH. (The NH₂[†] group was taken to be the planar form of the NH₂- substituent.) The choice offers the advantage that the substituent effects are the primary source of variation in the NLO properties since only a carbon-carbon triple-bond is present in each of the structures. An added advantage for this choice of compounds is the possibility for future study of related systems. For instance, the diacetylenes and triacetylenes can be studied as well to establish trends in substituent effects on the NLO response of materials.

The geometries were determined using Dunning's correlation consistent polarized Valence Double Zeta (cc-pVDZ) basis set.⁷ As a first approximation, a quick molecular mechanics optimization was carried out with the CHEM-3D⁸ program. The Cartesian coordinates from this result were then used for the input to the GAMESS package for the quantum mechanical geometry optimization. In order to ensure that calculated structures were true stationary points (or transition states in the case of the NH₂[†]- groups) the analytic hessian was calculated at the equilibrium geometry. A vibrational analysis was performed to determine the number of imaginary frequencies inherent to the structure. A single imaginary mode was taken to indicate a transition state structure whereas structures possessing only real-valued vibrational modes were considered to be local minima or stationary points.

Once the geometries were determined at the cc-pVDZ basis set, these structures were used for all of the calculations of the TDHF properties. The properties which were calculated for these compounds were the second harmonic generation (SHG), optical rectification (OR), and electro-optic Pockels effect (EOPE) for the first hyperpolarizability (β) and third harmonic generation (THG), DC electric field induced second harmonic generation (DC-EFISHG), intensity dependent refractive index (IDRI), and optical Kerr effect (OKE) for the second hyperpolarizability (γ). Each of these properties was calculated at the same geometry for four basis sets. The relative size of each of these basis sets is given below:

Basis Set	Approximate size
STO-3G	210G
cc-pVDZ	321G*
cc-pVDZ+	431G*
Sadlej	532G**

⁷ T. H. Dunning, Jr. *J. Chem. Phys.* **1989**, **90**, 1007.

⁸ *CSC Chem3D Plus*TM; Cambridge Scientific Computing, Inc. © 1992.

From the comparison of approximate sizes we see that from the STO-3G to the cc-pVDZ we add $1s$, $1p$, and $1d$ function to the basis set. Similarly, the cc-pVDZ to cc-pVDZ+ represents the addition of a single p function and the cc-pVDZ+ to Sadlej represents the addition of $1s$, $1p$, and $1d$. This allows us to evaluate the importance of the extra p and d functions in the computational results. All of the basis sets except for the STO-3G were input into GAMESS manually to allow greater control over the number and description of the basis functions.

Results:

Unfortunately, space restrictions prevent the inclusion of the complete results obtained for each of the basis sets implemented in this study. However, there are plans to publish the complete results of this study in a peer-reviewed journal at a later date. Included below are two sets of data which are representative of the results obtained in this study as a whole. The first two tables contain the results for acetylene and fluoroacetylene using each of the basis sets included in this study (STO-3G, cc-pVDZ, cc-pVDZ+, and Sadlej). Tables 3, 4, and 5 contain the data obtained for the STO-3G basis set on each of the twelve compounds studied. The similarities between the qualitative behavior of the results allow us to omit the data for the larger basis sets without a significant loss of content.

In examining the data contained in the first two tables we see that qualitative trends in the data are preserved though the magnitude of the calculated effect varies significantly as a function of basis set. For acetylene, the β values are omitted since are all equal to zero. This is expected since acetylene is a symmetric molecule with no permanent dipole moment.

HCCH	STO-3G	cc-pVDZ	cc-pVDZ+	Sadlej
(γ) THG	21.8347	151.1535	3836.5481	6782.2153
(γ) DC-EFISHG	20.8650	142.2332	3262.5620	5918.8765
(γ) IDRI	20.5530	139.4201	3098.9778	5668.3508
(γ) OKE	20.2351	136.6339	2946.4351	5430.8868

Table 1: TDHF data for acetylene. (β values are omitted since all are zero.) All values are in atomic units

FCCH	STO-3G	cc-pVDZ	cc-pVDZ+	Sadlej
(β) SHG	44.3512	145.5127	296.6656	349.7869
(β) OR	43.9193	143.1985	283.6264	333.3016
(β) EOPE	43.9193	143.1986	283.6264	333.3016
(γ) THG	47.9175	206.3317	3045.4771	5462.7897
(γ) DC-EFISHG	46.0323	192.1749	2596.6183	4771.0730
(γ) IDRI	45.4295	187.8042	2469.5277	4571.5502
(γ) OKE	44.4295	183.5112	2351.9183	4383.3459

Table 2: TDHF data for fluoroacetylene. All values are in atomic units.

The statistics for the seven properties we are concerned with exhibit the previously observed linear behavior with respect to varying substituent groups. The R^2 values from a linear regression analysis of the results for the calculated properties are very close to unity: SHG (0.99988), OR (0.99999), EOPE (0.99999), THG (0.99938), DC-EFISHG (0.99966), IDRI (0.99970), and OKE (0.99972). In addition, the y -intercepts for each of the regression analyses are within 1-2% of zero with slopes ranging from about 1.01 to 1.17.

	α			
	0.00000	0.04282	0.08565	0.12847
HCCH	7.3496	7.3758	7.4556	7.5930
FCCH	7.6369	7.6641	7.7471	7.8899
FCCNH ₂ [†]	11.9177	11.9660	12.1136	12.3696
FCCNH ₂	11.9174	11.9656	12.1132	12.3692
CNCCH	15.6234	15.7137	15.9945	16.4914
CNCCNH ₂ [†]	21.7782	21.9255	22.3852	23.2115
CNCCNH ₂	21.7779	21.9252	22.3849	23.2112
NH ₂ CCH [†]	11.5810	11.6282	11.7725	12.0229
NH ₂ CCH	11.5908	11.6383	11.7834	12.0353
NH ₂ CCNH ₂ [†]	15.8977	15.9672	16.1804	16.5519
NH ₂ CCNH ₂	16.4351	16.5094	16.7374	17.1363
NO ₂ CCH	16.6621	16.7961	17.2263	18.0603

Table 3: Calculated α values for STO-3G basis set. All values are given in atomic units.

	β			
	Static	SHG	OR	EOPE
HCCH	0.0000	0.0000	0.0000	0.0000
FCCH	43.7062	44.3512	43.9193	43.9193
FCCNH ₂ [†]	38.9335	41.2683	39.6922	39.6922
FCCNH ₂	38.9282	41.2626	39.6968	39.6868
CNCCH	26.7818	29.5249	27.7283	27.6725
CNCCNH ₂ [†]	441.0790	472.0981	451.0582	451.0308
CNCCNH ₂	441.0751	472.0933	451.0539	451.0266
NH ₂ CCH [†]	96.2620	99.6916	97.3814	97.3814
NH ₂ CCH	97.2169	100.7246	98.3613	98.3613
NH ₂ CCNH ₂ [†]	0.0000	0.0000	0.0000	0.0000
NH ₂ CCNH ₂	77.3463	79.8100	78.1486	78.1486
NO ₂ CCH	53.4862	52.0903	53.0105	53.0105

Table 4: Calculated β values for STO-3G basis set. All values are given in atomic units.

γ		
	Static	THG
HCCH	19.9284	21.8347
FCCH	44.2257	47.9175
FCCNH ₂ [†]	160.1580	176.6134
FCCNH ₂	160.1461	176.5995
CNCCH	353.8096	399.9044
CNCCNH ₂ [†]	1063.5735	1226.9006
CNCCNH ₂	1036.5676	1226.8732
NH ₂ CCH [†]	125.3350	138.5928
NH ₂ CCH	127.3532	140.9633
NH ₂ CCNH ₂ [†]	285.9844	315.9970
NH ₂ CCNH ₂	342.9471	382.5103
NO ₂ CCH	280.3456	336.4735

γ			
	DC-EFISHG	IDRI	OKE
HCCH	20.8650	20.5530	20.2351
FCCH	46.0323	45.4295	44.8155
FCCNH ₂ [†]	168.1156	165.4292	162.7419
FCCNH ₂	168.1027	165.4167	162.7297
CNCCH	375.8267	368.2032	360.9138
CNCCNH ₂ [†]	1125.6173	1094.8816	1064.9270
CNCCNH ₂	1125.5928	1094.8581	1064.9042
NH ₂ CCH [†]	131.7444	129.5763	127.4178
NH ₂ CCH	133.9288	131.7039	129.4891
NH ₂ CCNH ₂ [†]	300.4541	295.5341	290.6876
NH ₂ CCNH ₂	361.9206	355.4513	349.0934
NO ₂ CCH	306.7892	297.9277	288.6349

Table 5: Calculated γ values for STO-3G basis set. All values are given in atomic units.

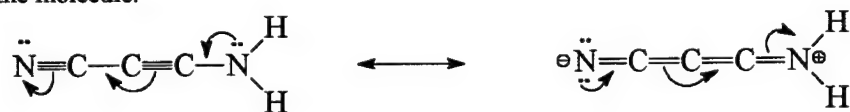
Discussion:

There are two important trends in the results obtained here. The first is that the qualitative behavior of the results is consistent regardless of the basis set. This basis set independence is interesting, but not necessarily useful. The quantitative inaccuracy of the results is a hindrance when attempting an in-depth study of a series of compounds. Additionally, though this particular set of compounds exhibits basis set independence, it must be remembered that these are relatively simple systems. It is quite possible that when dealing with large, complicated structures the effect of basis set would become far more important. With this set of substituted acetylenes, we are dealing with a set of fairly short-range interactions responsible for the NLO response of the material. In a larger system, say a small polymer, the smaller basis sets may seriously underestimate the NLO response of the material caused by longer-range or highly delocalized interactions.

It is clear from the data obtained from these calculations that there exists a linear relationship between the static and frequency dependent properties for any given compound. The data in Tables 3, 4, and 5 demonstrates this as well as the graphs included at the end of this report. What is unclear is whether there is an appropriate scaling factor which may be applied in the general case to save calculation time. The results suggest that for a single frequency with the compounds under consideration that a factor of slightly greater than 1 is appropriate, though clearly there is insufficient data to make any serious suggestion of such a scaling factor. If a scaling factor could be found to relate the static and frequency dependent properties of a material, then calculation times for any compound could be drastically reduced making computational study more widely applicable. In fact, the calculation of the static values represents only about 20-40% of the total calculation time depending on the molecule and basis set. Clearly these preliminary results warrant further study.

The primary long-term goal of this study is to develop a widely applicable method for predicting the NLO response of a material. In general, it is known that delocalized systems and multiply bonded complexes provide the necessary physical characteristics to observe the desired NLO responses. The goal is to quantitate the difference between various substituent groups on a common framework. We may consider the substituents in this study in terms of donor and acceptor character and order their contributions in terms of their electron donor or acceptor capabilities. This seems reasonable in light of the data. The compound with the best donor-acceptor pair of substituents (CNCCNH₂) has the largest NLO response and the compound with the least donor-acceptor character (acetylene) has the smallest NLO response. We also find that the donor-acceptor combination is very important. The data shows an increased NLO response with the addition of a single donor or acceptor substituent, but the coupling of an electron donor with an electron acceptor greatly increases the overall response of the material.

If we consider the Hammett σ values for these substituents we find that although the Hammett values provide a good preliminary indicator, they do not accurately describe the phenomenon as a whole. The problem is that there are clearly other effects important to the process. As an excellent example of these other phenomena we can consider the structure of cyanoiminoacetylene. This structure is interesting in its own right in addition to providing some useful insights into the kinds of effects which need to be considered. With the resonance structures shown below there is an increased ability to delocalize the electrons in the π system which allows for greater polarizability in the molecule.



Clearly the other compounds under consideration do not have this great a resonance capability and we can hypothesize that it is the combination of this resonance with the donor-acceptor character which gives rise to the large NLO response observed in both the β and γ calculations. In order to develop a good predictor for NLO properties in such organic systems based on substituent contributions a measure of both the donor-acceptor character and the resonance ability of the substituents is required.

One possible solution is the use of the σ^+ values proposed by Brown and Okamoto⁹ which measure the Hammett-like effect of substituents on the stabilization of positively charged systems. Similarly, the σ^- values could be used since these deal with electron rich systems. Yet another possibility is to use the F and R values proposed by Swain and Lupton¹⁰ which separate the field (F) and resonance (R) contributions to the Hammett σ values for a given substituent. There is obviously a need for further study into the importance of the dipole and resonance effects of the substituent groups on the NLO response of the system. However, it is evident from the data that a relationship does exist between these two fundamental properties and the NLO response of the material. An intuitive analysis of the data leads to the conclusion that a larger permanent dipole and a better resonance ability will greatly enhance the NLO response, what remains is to determine the relative importance of each effect with respect to the overall response of the material.

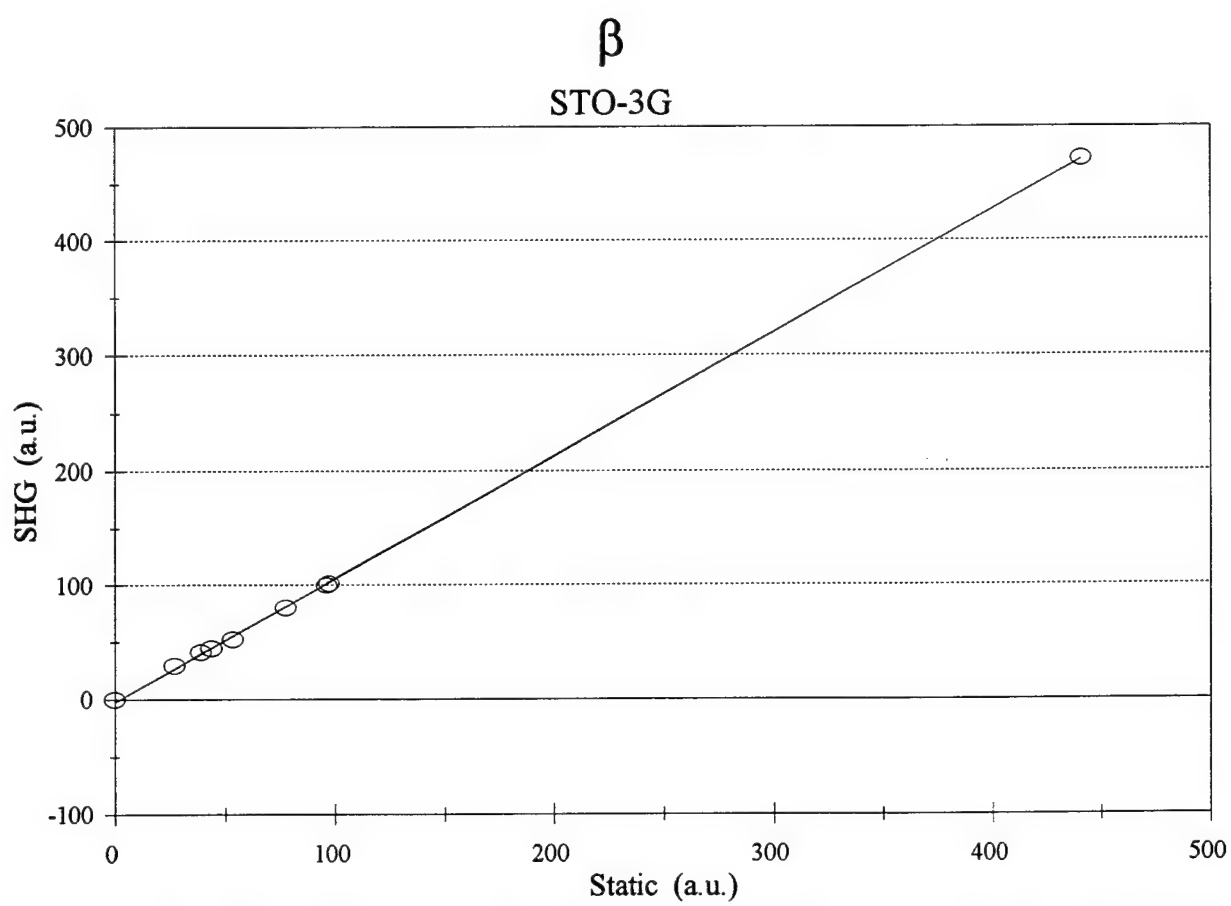
The effect of basis set on the calculation results is another consideration addressed by this study. The important trends in the data can be seen in Tables 1 and 2. It is observed that the changes from STO-3G to cc-pVDZ and from cc-pVDZ to cc-pVDZ+ each bring about significant changes in both total magnitude and relative magnitudes in all of the results. The important feature is that the relative difference between the calculated magnitudes of various effects changes as we increase the size of the basis set. However, the cc-pVDZ+ to Sadlej transition shows that relative difference between values ceases to change significantly with this change while the magnitude of these values does change significantly. This is a fairly important result in that it, perhaps, points to a trend that could be significant in the related studies discussed. If the difference between values remains the same

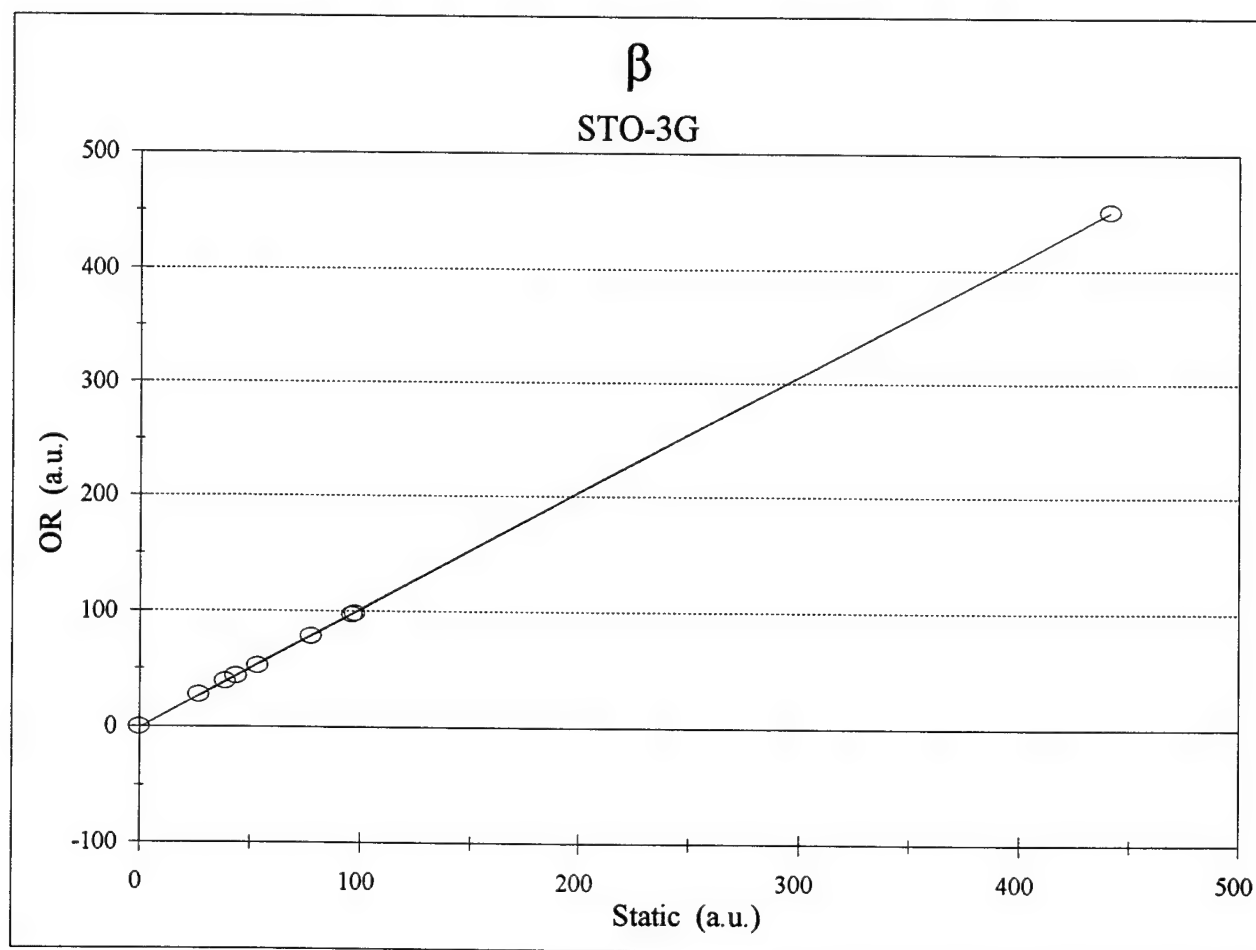
⁹ H. C. Brown and Y. Okamoto *J. Amer. Chem. Soc.* **1958**, **80**, 4979.

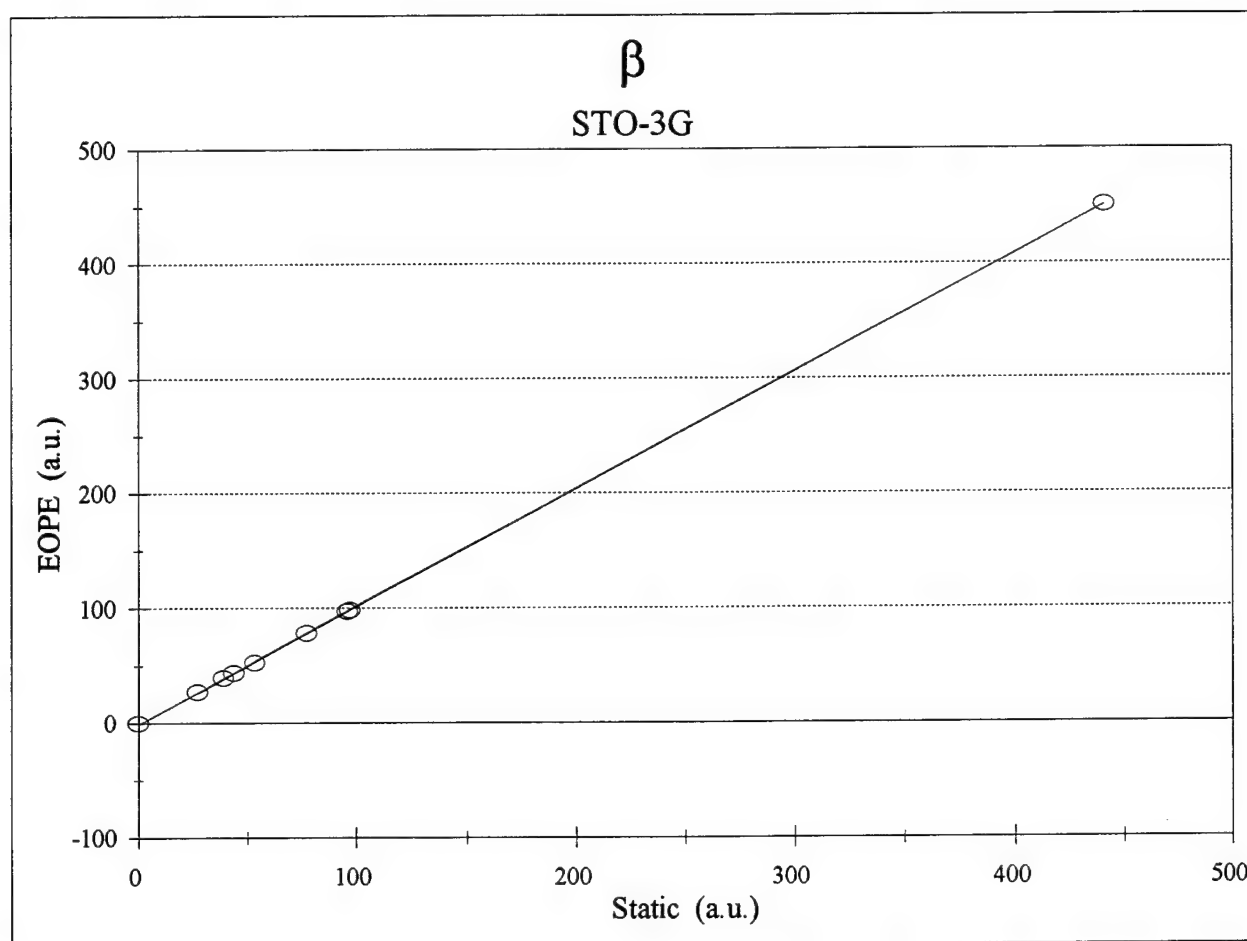
¹⁰ C. G. Swain and E. C. Lupton, Jr. *J. Amer. Chem. Soc.* **1958**, **80**, 4979.

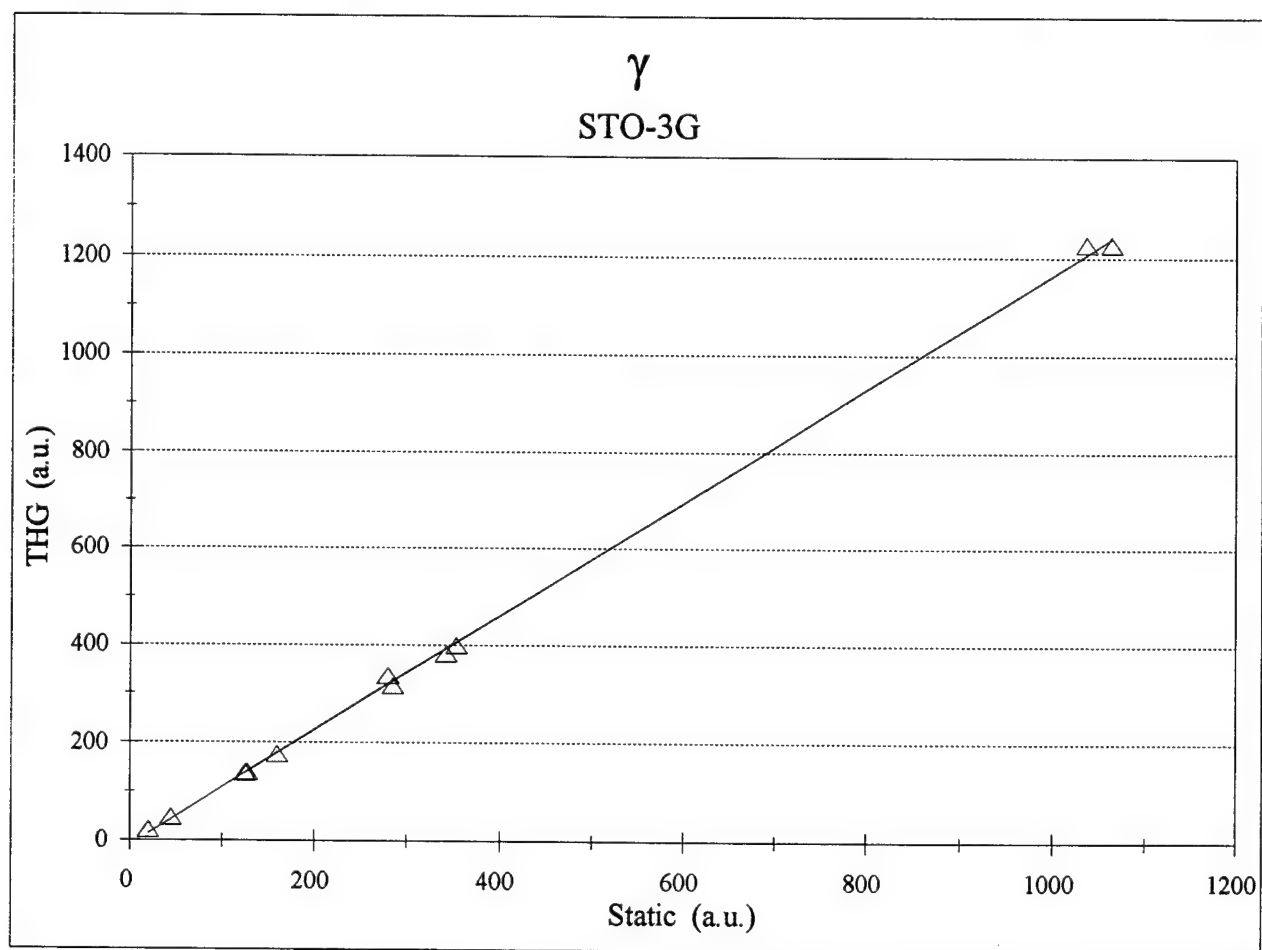
while the total magnitude changes, it may be possible to estimate most accurate numbers with a significantly more time-efficient calculation without sacrifice of the quantitative relationship between effects.

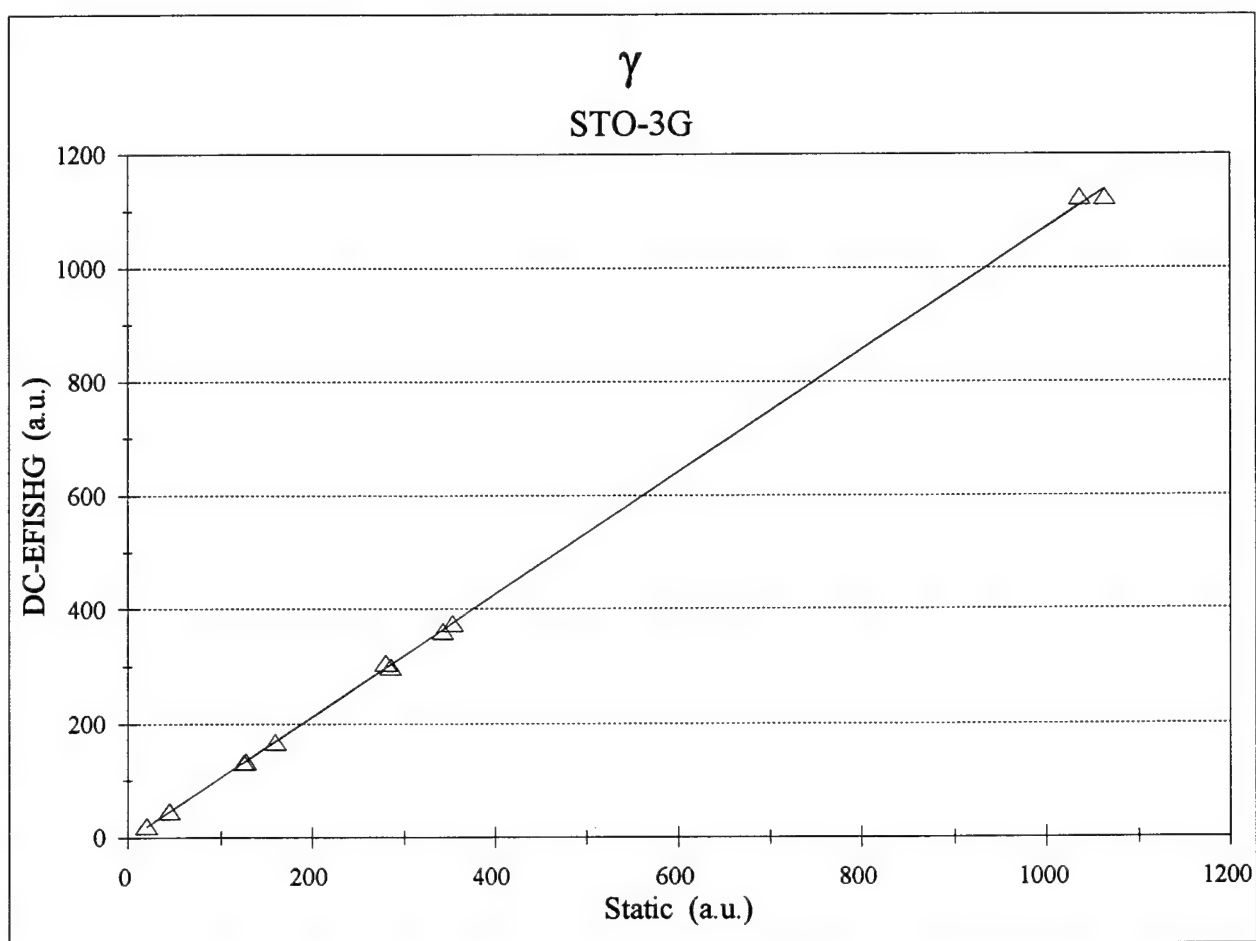
The need for further study is evident from the results of this singular investigation. Work is currently being carried out with the di- and tri-acetylenes as well as substituted aromatic systems. However, the influence of substituents in each of these classes of compounds needs to be independently determined before the long-term goal of a widely applicable method for screening organic compounds can be reached. Fortunately, the excellent correlations observed and the linear relationships present in the data do provide a great deal of optimism for the achievement of the long-term goals of the current effort. The basis set dependence is also promising. If further study reveals similar trends in basis set dependence of the values another possible avenue for reducing calculation times may be available thus making the computational screening of NLO materials more widely applicable.

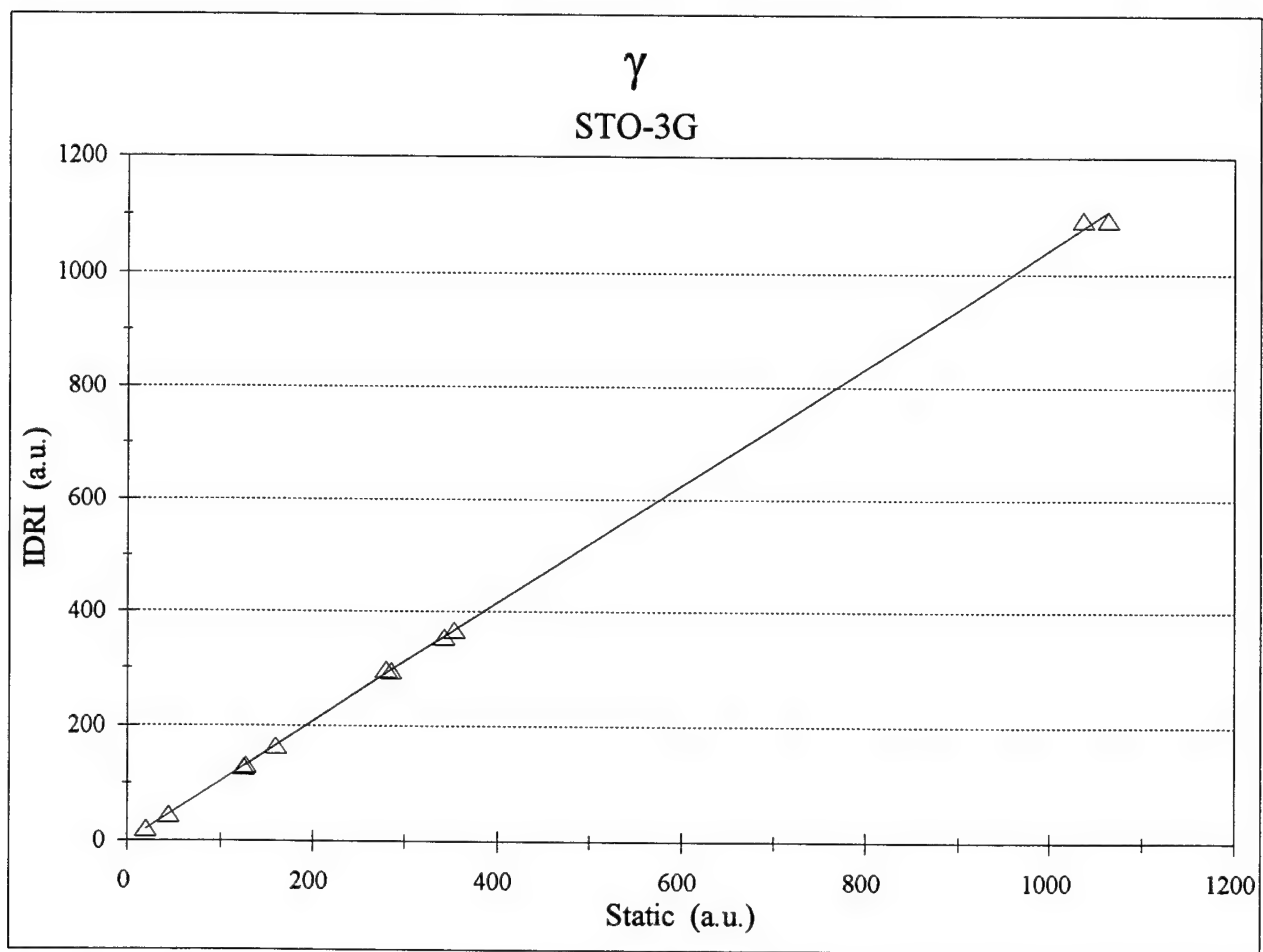


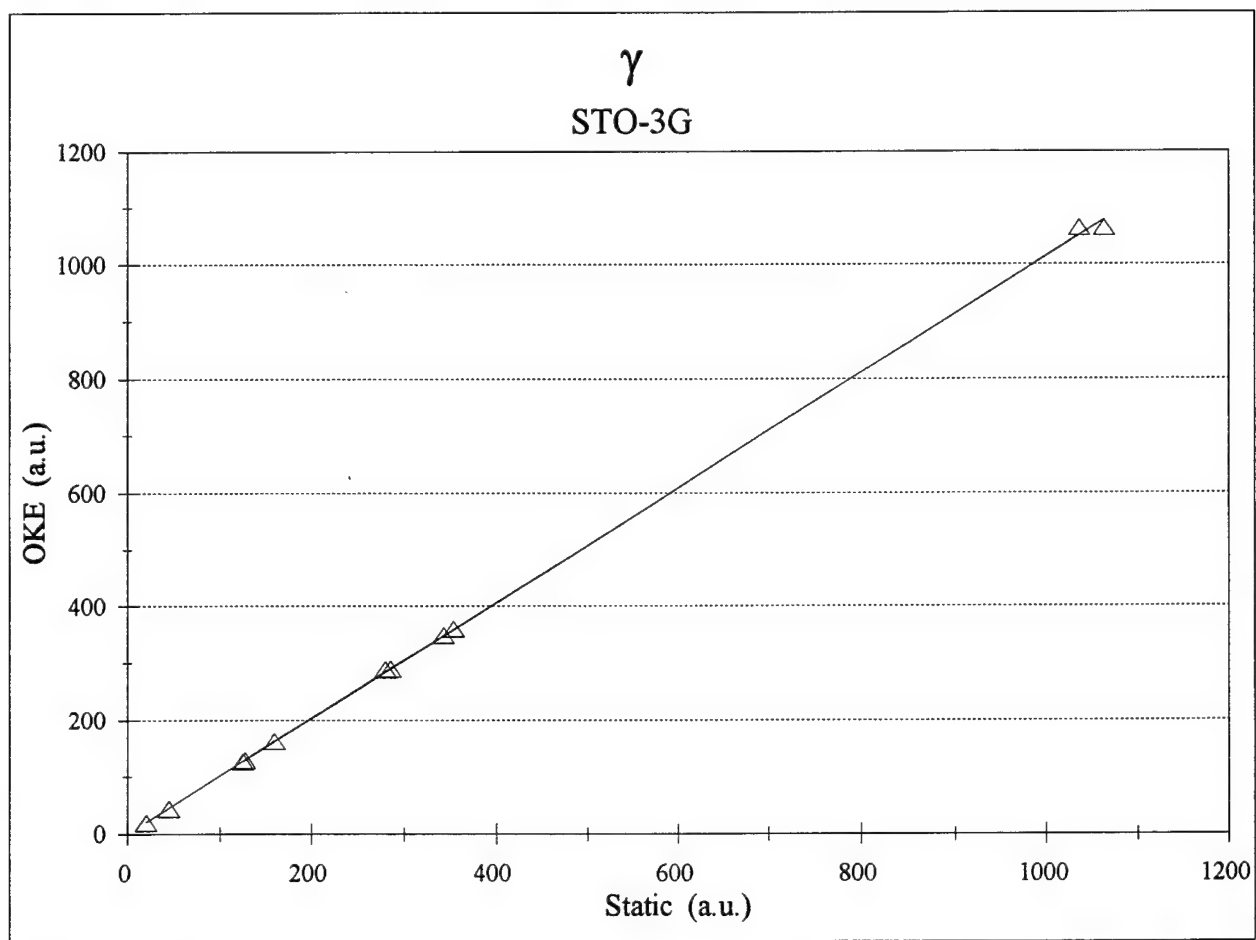












INVESTIGATIONS OF CARBON MATERIALS IN ALKALI METAL BUFFERED
CHLOROALUMINATE MOLTEN SALTS

Joan Fuller
Graduate Student
Department of Chemistry

University of Alabama
Chemistry Department
Tuscaloosa, Al 35487

Final Report for:
Graduate Student Research Program
Frank J. Seiler Research Laboratory

Sponsored by:
Air Force of Scientific Research
Bolling Air Force Base, Washington, D.C.

September 1994

INVESTIGATIONS OF CARBON MATERIALS IN ALKALI METAL BUFFERED CHLOROALUMINATE MOLTEN SALTS

Joan Fuller
Graduate Student
Department of Chemistry
University of Alabama

Abstract

This project involved the electrochemical investigations of carbon electrodes in buffered room temperature molten salts composed of AlCl_3 , 1-ethyl-3-methylimidazolium chloride (EMIC), and an alkali metal chloride, MCl ($\text{M}=\text{Li}, \text{Na}, \text{K}$). The EMIC/ AlCl_3 / MCl molten salt has several unique properties which makes it a promising candidate for battery electrolytes, including a wide electrochemical window, high inherent conductivity, negligible vapor pressure, high thermal stability, high alkali metal cation concentration, and low alkali metal cation solvation energies. By intercalating the desired alkali metal into a graphite electrode the problems commonly associated with elemental alkali metal anodes are avoided and thus the efficiency and safety of the battery are improved. Carbons investigated in these melts included Glassy Carbon, Graphite Rod, and Graphite Sheet.

Introduction into Room Temperature Chloroaluminate Melt

Lithium rocking chair batteries employing a lithium/carbon intercalation anode and a transition metal oxide intercalation cathode have captured a significant portion of battery research throughout the world.¹ The intercalation of lithium into a carbon matrix provides a more stable and safer means for lithium utilization than an elemental lithium anode.¹ The room-temperature molten salts composed of AlCl_3 , 1-ethyl-3-methylimidazolium chloride (EMIC), and an alkali metal chloride, particularly LiCl and NaCl , have recently been employed as electrolytes for alkali metal electrochemical investigations.²⁻⁵ These melts have several unique properties which make them good candidates for battery electrolytes, including a wide electrochemical window, high inherent conductivity, negligible vapor pressure, high thermal stability, high alkali metal cation concentration, and low alkali metal cation solvation energies.²⁻⁵ In particular, the low solvation energy for Li^+ in these melts, 78 kJ mole^{-1} less than in water,⁵ may promote facile anodic and cathodic electrochemical intercalation reactions. Although it is possible to reduce and anodize elemental lithium and sodium in these melts under certain conditions, their stability is very limited due to reaction with the organic cation, EMI^+ .²⁻⁴ Therefore, to stabilize the reduced alkali metal in these melts, it is a logical extension of previous melt investigations and rocking chair technology to examine the electrochemistry of alkali metals at graphite or carbon intercalation electrodes. We wish to report here the initial investigation of alkali metal electrochemistry at carbon electrodes in these molten salt electrolytes.

Experimental

Alkali metal chloride buffered melts, $\text{AlCl}_3\text{:EMIC:MCl}$, were prepared as previously described.³ All voltammetric experiments were performed using an EG&G PARC model 273 Potentiostat/Galvanostat controlled with the EG&G PARC 270 software package. The working electrode was either a high purity, spectroscopic grade

graphite rod with a 3 mm diameter (Union Carbide) or a pressed, high purity, graphite sheet (Aldrich). Both the graphite rod and the graphite sheet was pretreated by drying at 400 °C for several hours in air and cooling under vacuum in the dry box antechamber. The glassy carbon working electrode was a 3 mm diameter disk electrode sealed in Kel-F (Bioanalytical Systems). The reference electrode consisted of an Al wire immersed in a 1.5:1.0 AlCl_3 :EMIC melt contained in a separate fritted glass tube. The counter electrode was an Al wire dipped into a portion of the analyte melt contained in a 3 mm OD, D-porosity gas dispersion tube (Ace Glass). All experiments were performed in a Vacuum Atmosphere Dry Box under He with an $\text{O}_2 + \text{H}_2\text{O}$ concentration of < 5 ppm.

Lithium Chloride System

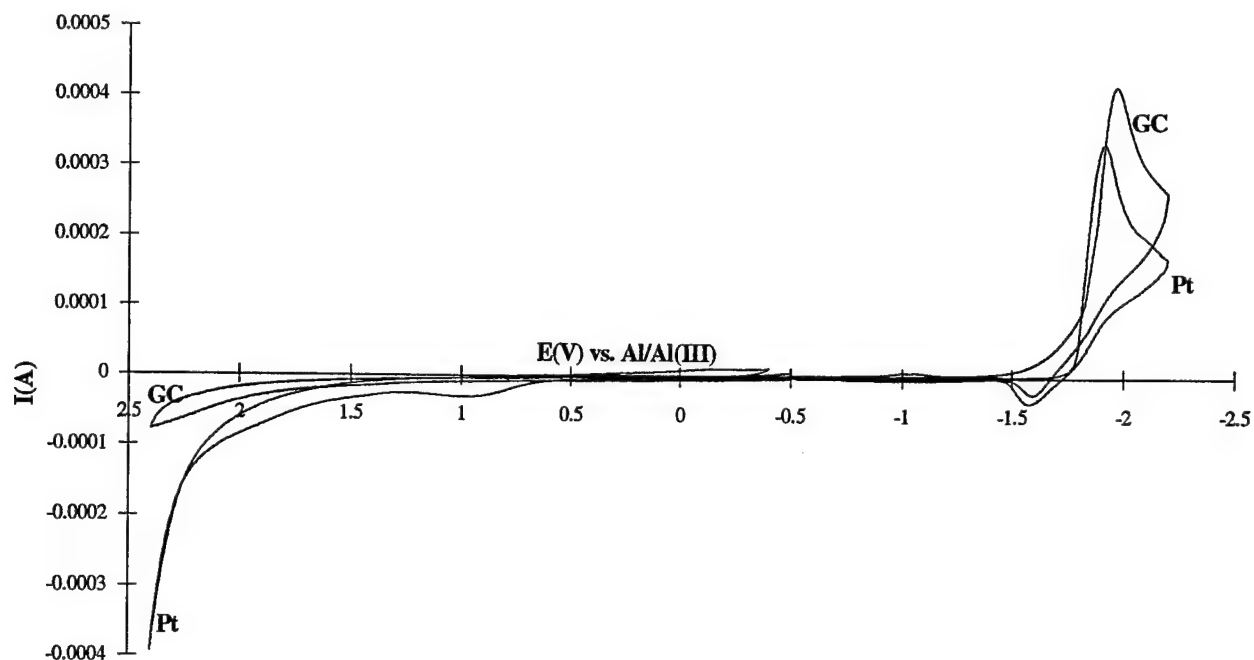


Figure 1. Cyclic voltammograms at platinum and glassy carbon electrodes. Scan rate is 25 mV/sec.

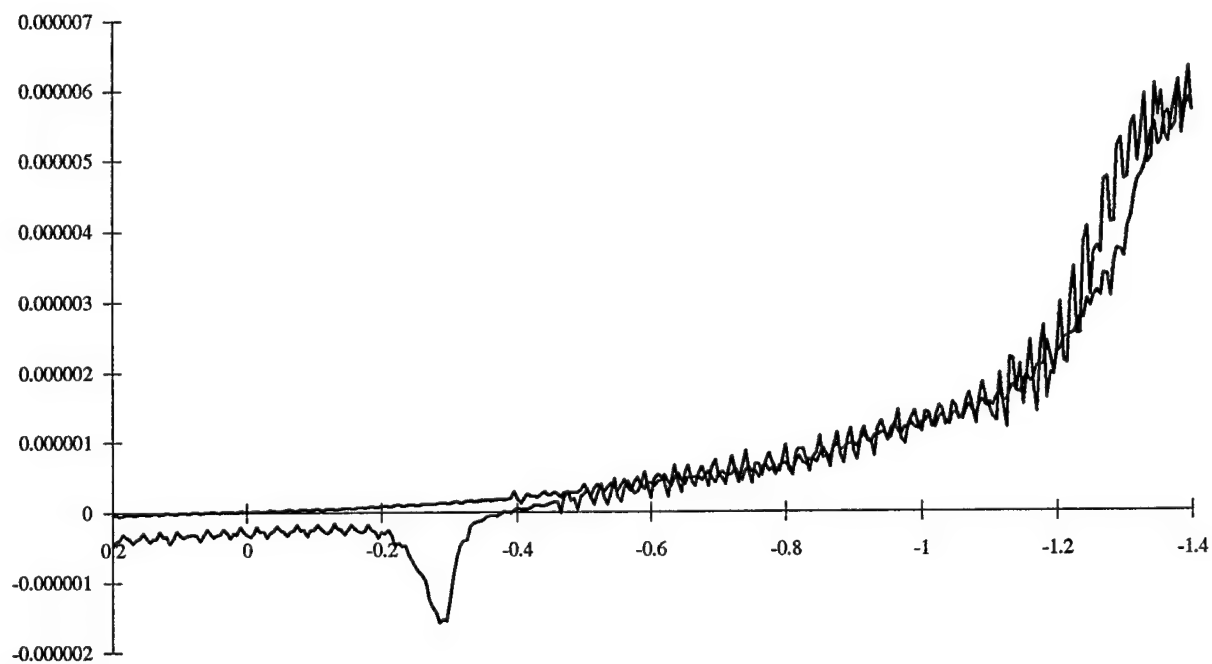


Figure 2. Glassy carbon cyclic voltammogram at 1mv/sec.

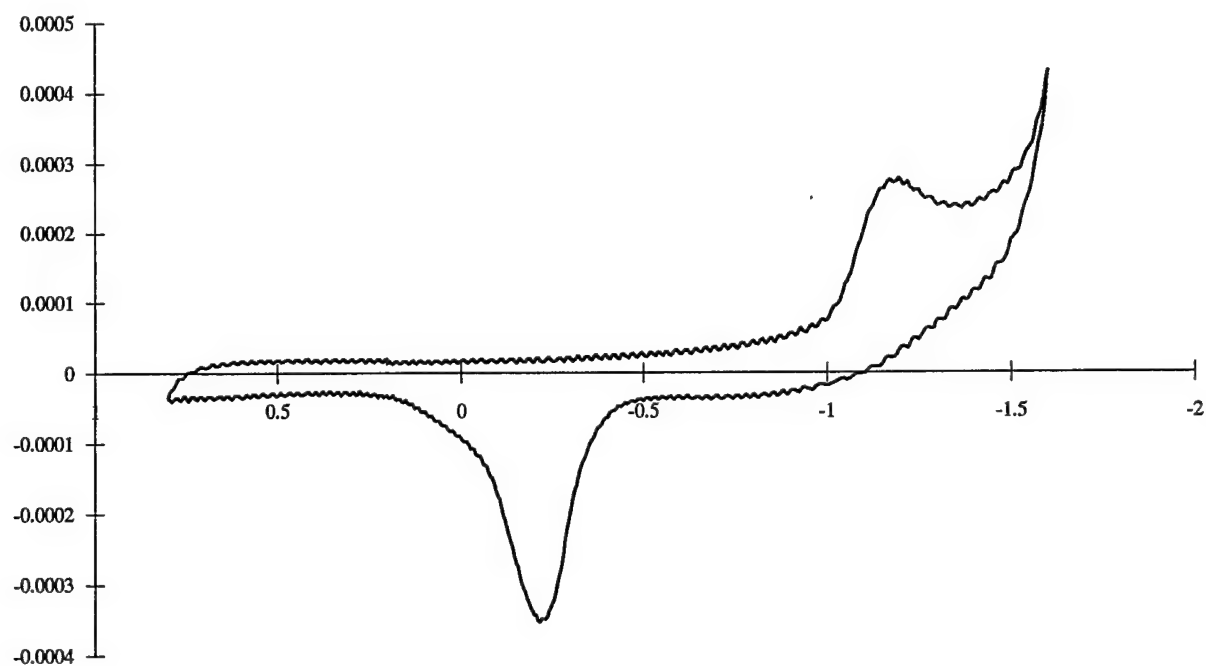


Figure 3. Graphite sheet cyclic voltammogram at 1mv/sec.

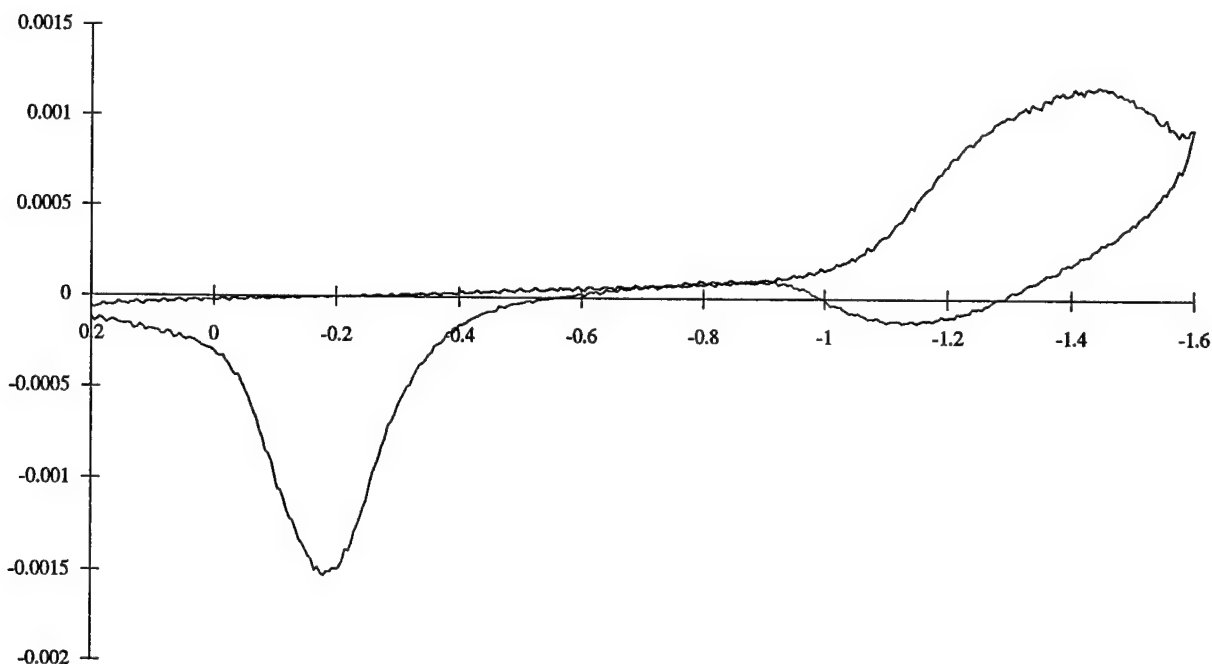


Figure 4. Graphite rod cyclic voltammogram at 1mv/sec.

Figures 2 - 4 clearly show a reduction wave and an corresponding oxidation wave following scan reversal; these were initially assigned to lithium intercalation and deintercalation processes at the graphitic electrodes.⁶ However, recent XPS evidence using a nickel electrode indicates a "aluminum-lithium" alloy is deposited at the potentials where the lithium-graphite intercalation process was originally assigned.⁷ We now believe the reduction and oxidation processes observed in Figures 2 - 4 are due to deposition and stripping, respectively, of this new "aluminum-lithium" alloy. The electrochemical behavior of this "aluminum-alloy" is complicated by co-precipitation of LiCl and reaction of the alloy with trace oxygen, forming an orthorhombic perovskite aluminum oxide phase. This deposition process is still under investigation and will be reported in a separate work.

Sodium Chloride System

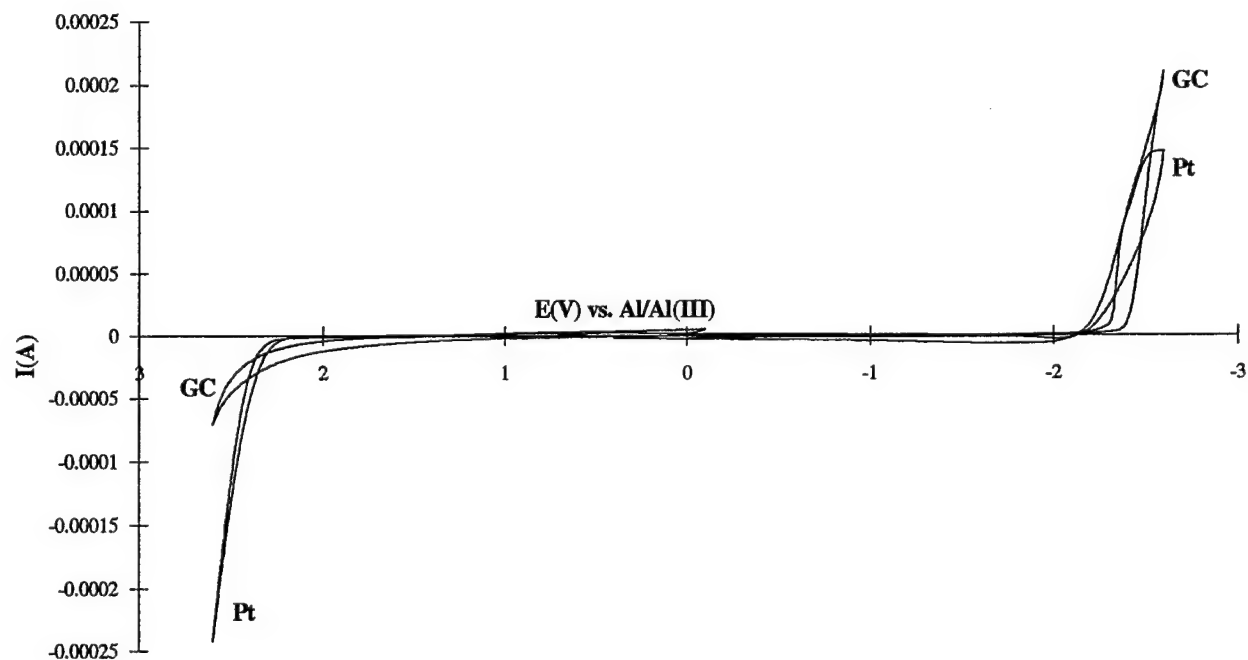


Figure 5. Cyclic voltammograms at platinum and glassy carbon electrodes. Scan rate is 25 mv/sec.

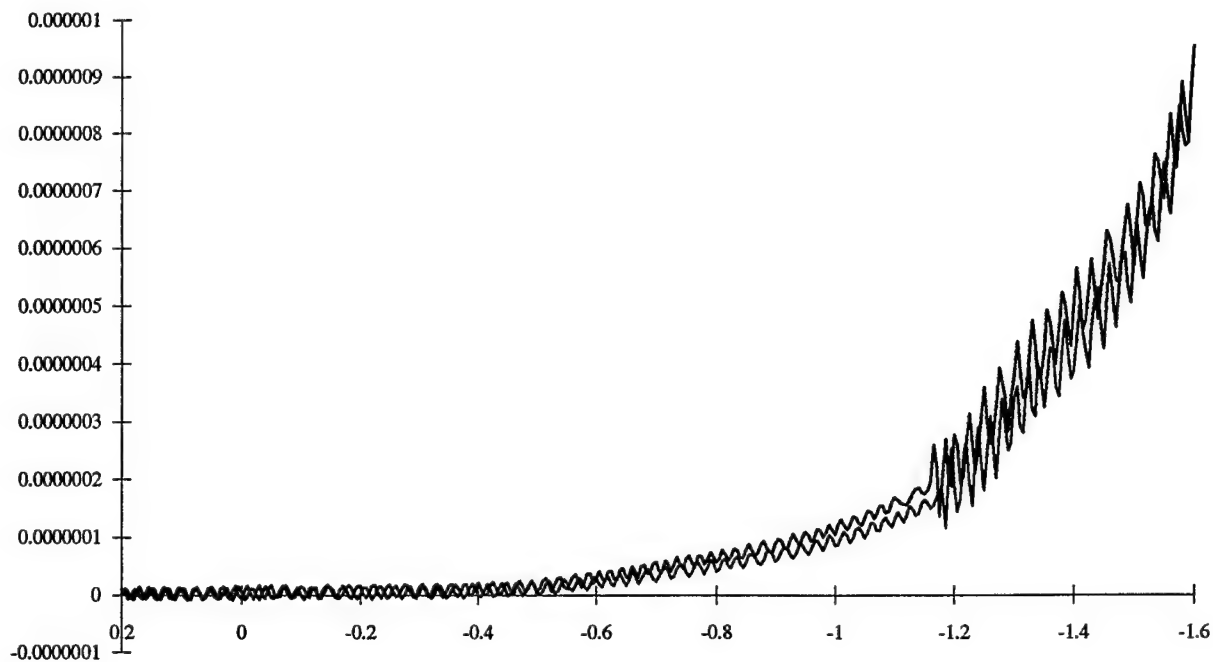


Figure 6. Glassy carbon cyclic voltammogram at 1mv/sec.

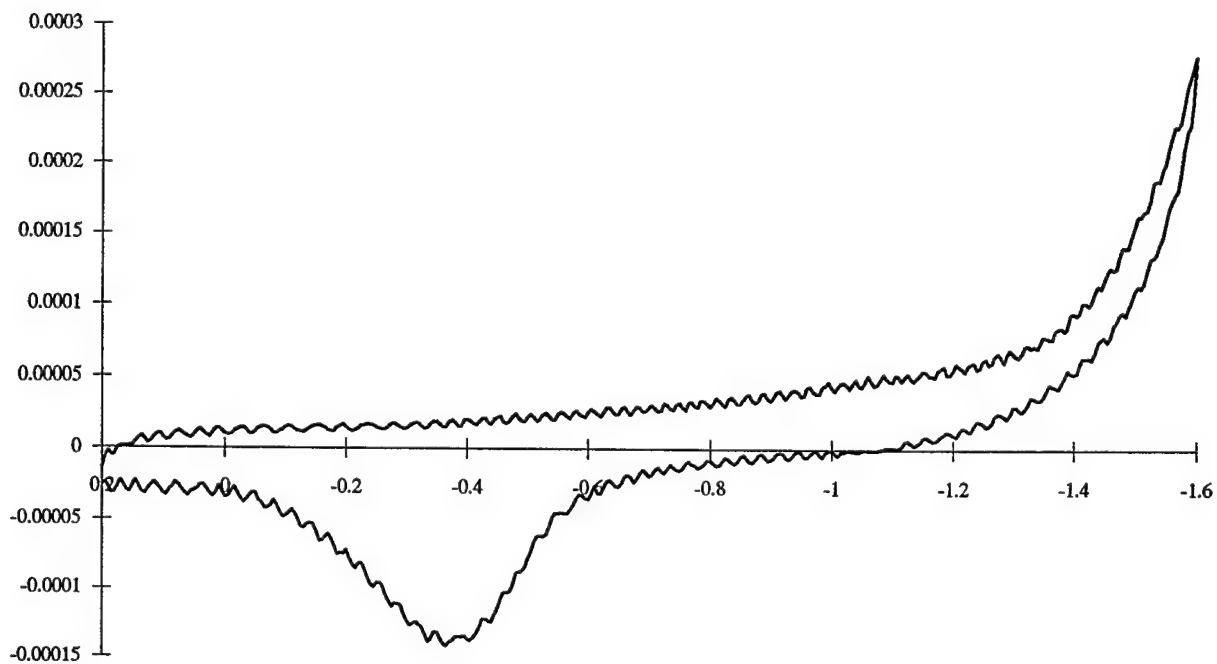


Figure 7. Graphite sheet cyclic voltammogram at 1mv/sec.

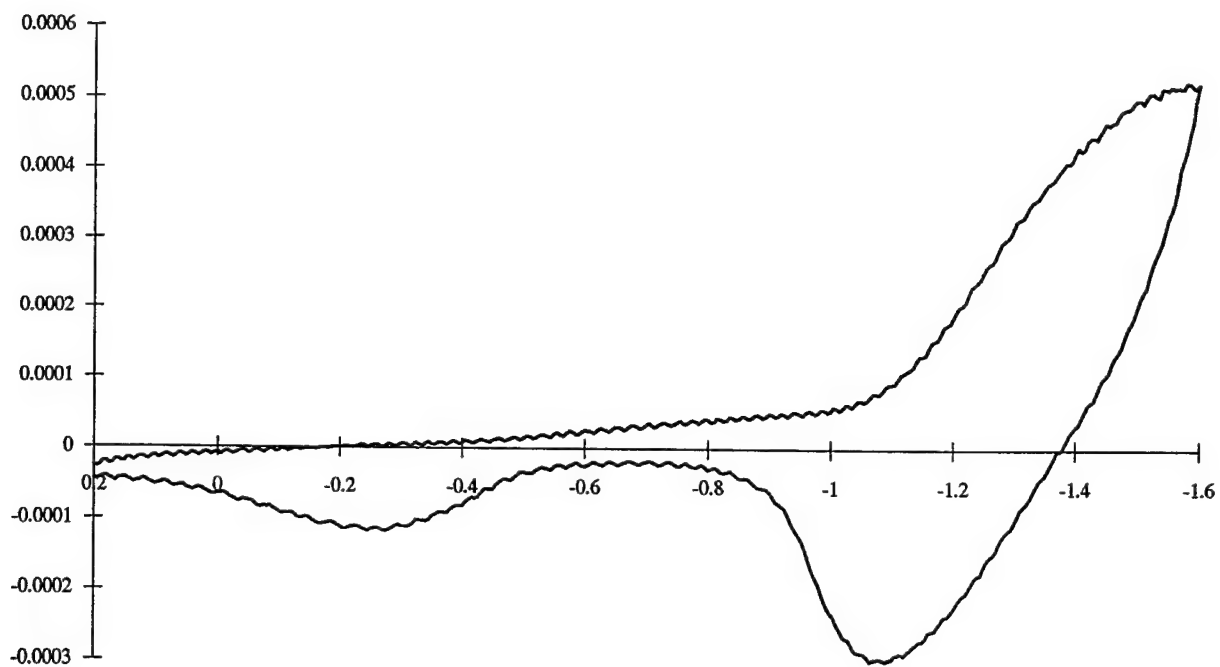


Figure 8. Graphite rod cyclic voltammogram at 1mv/sec.

The sodium system is similar in some ways to the lithium system. The same reduction and oxidation processes are still present, but only at the graphitic electrodes and at the glassy carbon electrode. It is possible that an "aluminum-sodium" alloy is formed in a manner similar to the "aluminum-lithium" alloy; however, no low temperature "aluminum-sodium" alloys are known. It is interesting to note that the thermodynamic reduction potential of an "aluminum-sodium" solid solution phase should be approximately the same as that for an "aluminum-lithium" solid solution phase due to the similarities in the reduction potentials for the elemental lithium and sodium in these melts.³ This system is also undergoing a more thorough study to determine the composition of the material deposited at -1.1V.

Potassium Chloride System

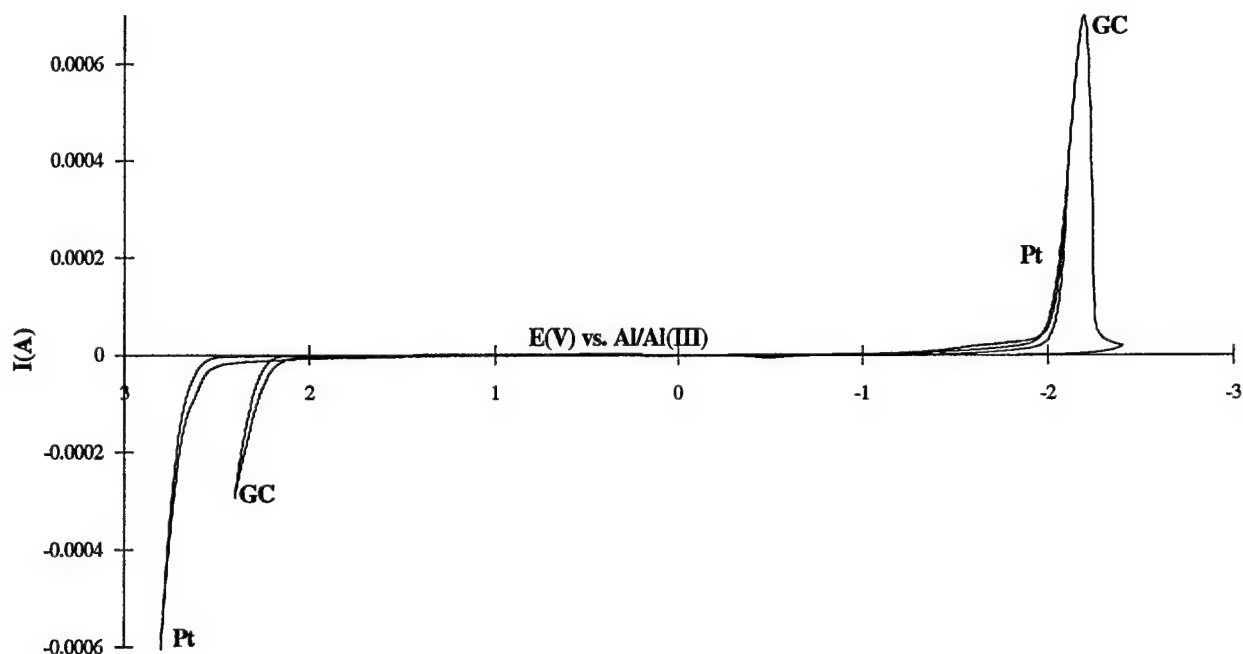


Figure 9. Cyclic voltammograms at platinum and glassy carbon electrodes. Scan rate is 25 mv/sec.

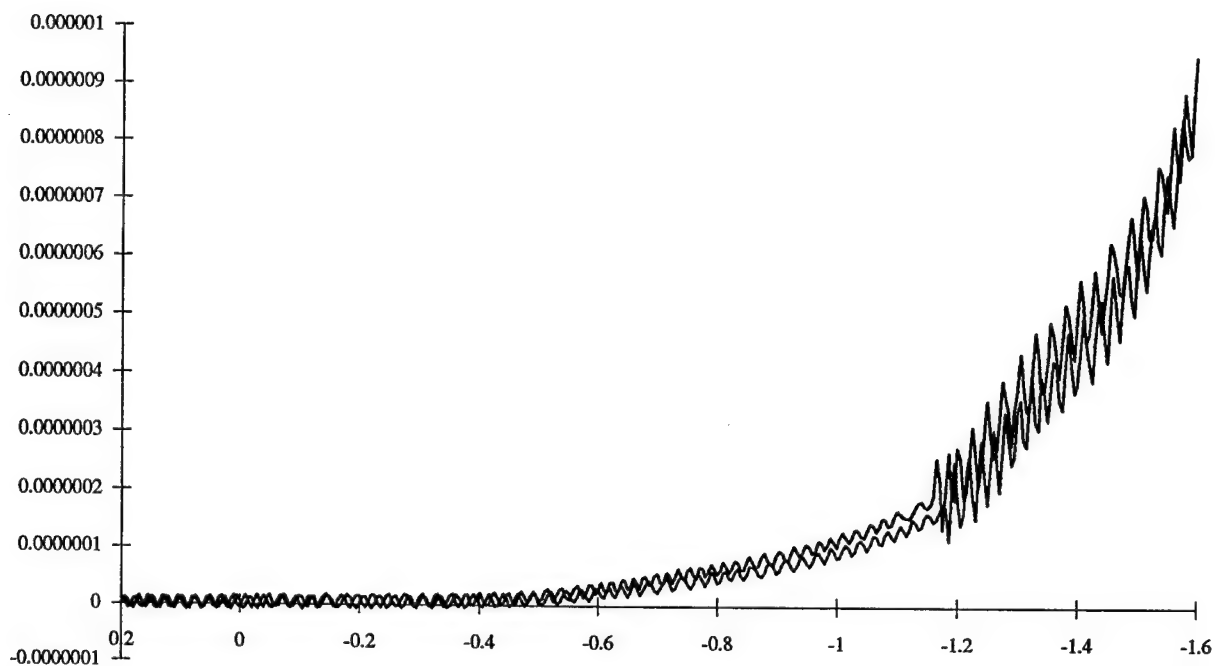


Figure 10. Glassy carbon cyclic voltammogram at 1mv/sec.

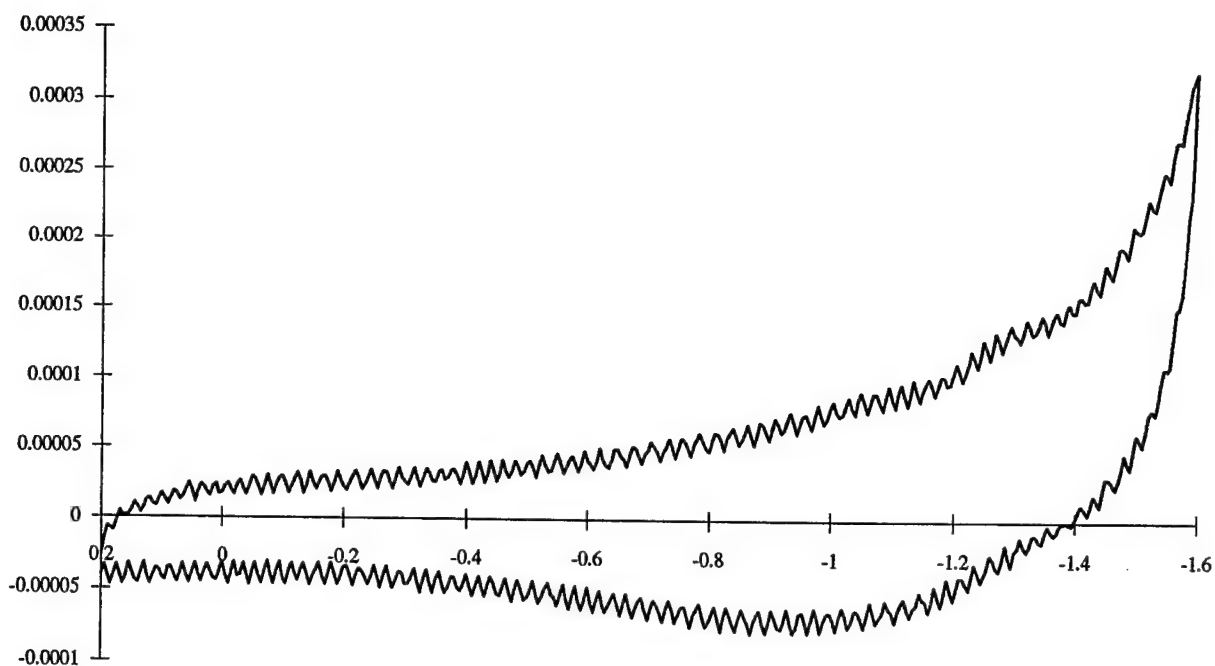


Figure 11. Graphite sheet cyclic voltammogram at 1mv/sec.

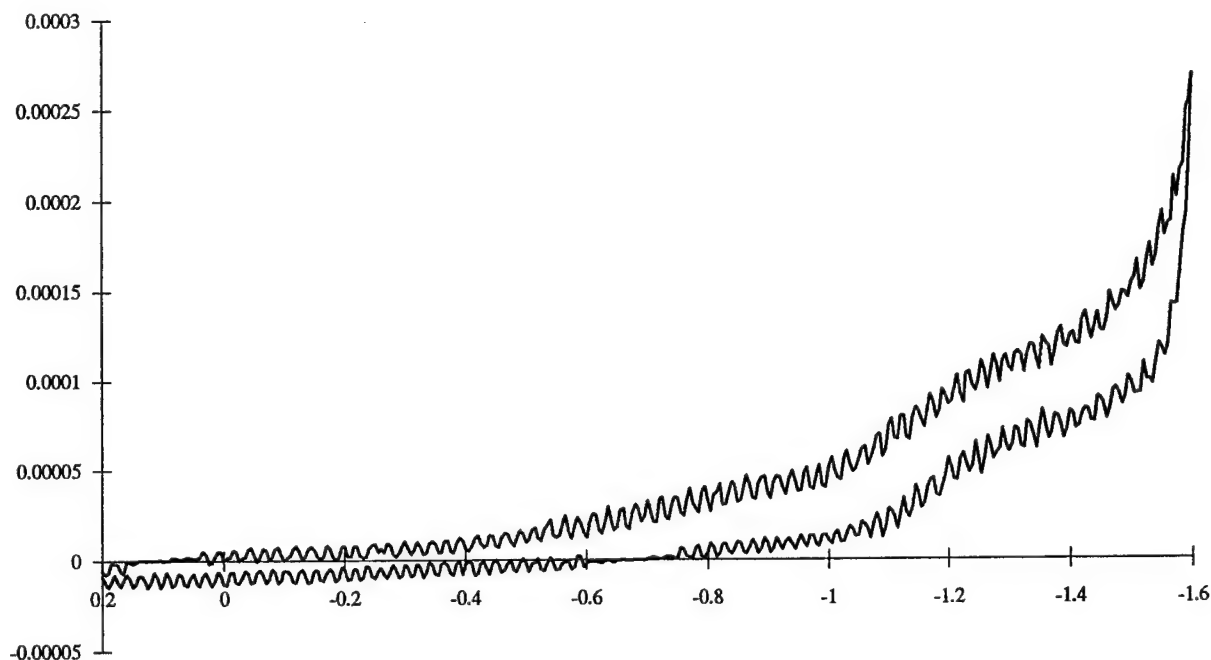


Figure 12. Graphite rod cyclic voltammogram at 1mv/sec.

The potassium system showed no indications of the reduction or oxidation processes found in the lithium and sodium melts. It is therefore possible that the KCl buffered melt could be used as a true buffer for the EMI/ AlCl_3 melts.

Conclusion

This investigation of the electrochemistry of alkali metals at graphite has led to an interesting discovery and an unfortunate dilemma. The discovery is that the electrochemical process originally assigned as a lithium-graphite intercalation process appears to be instead the electrochemical deposition and stripping of an "aluminum-lithium" alloy phase. A similar alloy electrodeposition and stripping is found in the sodium melt. The dilemma is that this alloy formation may hamper the application of these

buffered neutral melts in certain battery applications, particularly with regard to intercalation anodes. However, the formation of these alloy phases may have many applications and will therefore be the subject of more extensive investigations.

References

1. J. M. Tarascon and D. Guyomard, *Electrochimica Acta*, **38**, 1221 (1992).
2. R. T. Carlin and C. Scordilis-Kelley, Proceedings of the Ninth International Symposium on Molten Salts, The Electrochemical Society, Pennington, N. J., 1993.
3. C. Scordilis-Kelley and R. T. Carlin, *J. Electrochem. Soc.*, **140**, 1606 (1993).
4. T. L. Riechel and J. S. Wilkes, *J. Electrochem. Soc.*, **139**, 977 (1992).
5. C. Scordilis, J. Fuller, R. T. Carlin, and J. S. Wilkes, *J. Electrochem. Soc.*, **139**, 694 (1992).
6. R. T. Carlin, J. Fuller, and M. Hedenskoog, *J. Electrochem. Soc.*, **141**, L21 (1994).
7. R. T. Carlin and K. Kuhn, work in progress.

EFFECTS OF TEMPERATURE ON VARIOUS HEMATOLOGICAL PARAMETERS

Ramachandra Tummala
University of Alabama-Birmingham School of Medicine
Birmingham, AL 35294

Final Report for:
Summer Graduate Student Research Program
Clinical Investigation Directorate
Wilford Hall Medical Center
Lackland AFB, San Antonio, TX

Sponsored by:
Air Force Office of Scientific Research
Bolling Air Force Base, DC

and

Wilford Hall Medical Center

September 1994

Effects of Temperature on Various Hematological Parameters

Ramachandra Tummala, University of Alabama-Birmingham School of Medicine
and Faculty Co-Investigator, W. Drost-Hansen, Department of Chemistry,
University of Miami

ABSTRACT

Using human blood samples, we have determined the effects of temperature on the following hematological parameters: Erythrocyte Sedimentation Rate (ESR), Mean Red Cell Volumes (MCV), Mean Platelet Volumes (MPV), and the sodium/potassium ratio in the plasma of heat-treated whole blood. As described in reports from previous years, ESR data obtained over the range from about 30 °C and up to approximately 52 °C show distinct, abrupt, and frequently dramatic changes near 45 °C, and somewhat similar changes are observed at this temperature in the measured volume properties (MCV and MPV) and ion-distribution data. The temperature range from 44 ° to 46 °C is known to be a critical temperature range for all mammals and birds and is indeed the upper thermal limit for such organisms. As stressed in our earlier reports, the dramatic effects on cell physiology near 45 °C undoubtedly reflect the transition at the third vicinal water thermal transition temperature ($T_{k=3}$), which is known to affect a large number of parameters of the cell-associated water [see papers by Drost-Hansen et al.]. Some measurements of the same parameters have also been made at lower temperatures, for instance from 8 ° to 25 °C and from 20 ° to 37 °C. Some indications of anomalies at 15 ° and 30 °C have been seen (corresponding to the lower, critical thermal transition temperatures for vicinal water, $T_{k=1}$ and $T_{k=2}$), but the anomalies at these temperatures are far less pronounced than the 45 °C anomaly. To insure the best resolution practical, measurements have been made over the different temperature intervals at increments of 0.6 ° to 0.9 °C using our Temperature Gradient Incubator (TGI or "Polythermostat"), which allows for simultaneous measurements at thirty different, constant temperatures. Earlier, we have proposed that the distinct changes near 45 °C ($T_{k=3}$) may play an important role in hyperthermia treatment of malignancies. While the findings in the current study do not prove this supposition, the data are consistent with this proposal: dramatic changes appear to take place at this critical temperature in such parameters as the ESR (probably reflecting reduced red cell aggregation and/or rheological changes in the blood, likely related to vicinal hydration changes of the proteins present), and/or intracellular ion or solvent activities, and possibly changes in the stability of critical membrane-associated proteins or enzyme activities. Such changes may indeed preferentially affect the thermal stability of malignant cells compared to normal cells if the relative abundance of vicinal water in malignant cells differs from that of normal cells. The latter proposition is likely true as it is well-known that malignant cells have notably elevated water contents compared to healthy cells. The excess water of the malignant cells more closely resembles "bulk water" (solvent) than vicinal.

INTRODUCTION

The Erythrocyte Sedimentation Rate (ESR) has a long and distinguished history as one of clinical medicine's most frequently used diagnostic indicators and in spite of its lack of specificity and the advent of highly sophisticated electronic Hematology Counters the test continues to be in common use. A great deal of research has been reported on various aspects of the fundamental processes underlying the ESR yet our understanding of the aggregation and sedimentation processes remains notably incomplete and in fact unsatisfactory. The present study was initiated about five years ago in an effort to contribute towards a more complete description of the ESR in terms of the underlying adsorption phenomena, transport processes, biochemistry and basic cell physiology. In this connection we have stressed the response of the ESR to temperature: a subject not frequently dealt with in the literature.

In the Clinical Laboratory the ESR is usually determined at room temperature [taken to be 25 °C in USA but probably closer to ca. 20 °C in other locations, say Northern Europe, and likely higher than 25 °C in many tropical, Third World Countries]. We have previously advocated that it may be useful, on a routine basis, to determine the ESR at two (or more) different temperatures, such as to obtain a temperature coefficient (i.e. $d[\text{ESR}]/dt$). We continue to explore the possibility that such a temperature coefficient may contain valuable diagnostic information and in view of the ease and low cost of the ESR measurements such an approach may be well worth the extra effort. The great drawback of such measurements at this time is the lack of any historical data for the temperature coefficient but considering the temperature data obtained in the present study, including the enormous variability in the effects of temperature on the ESR, it is highly probable that $d[\text{ESR}]/dt$ does indeed contain some important information. In view of the fact that the temperature coefficient is a differential quantity it is conceivable that it does not depend on some of the variables known to affect the ESR itself such as age of the patient or obesity.

EXPERIMENTAL PROCEDURES

As in previous years under the aegis of the AFOSR Summer Faculty Research Program, ESR data have been obtained using Wintrobe tubes. The blood (usually 50 ml) was obtained from human volunteers by antecubital venipuncture. Unless otherwise stated, the blood was drawn in plastic syringes (60 ml capacity) to which had been added 1.0 ml 0.25 molar sodium EDTA solution as anticoagulant. Depending on the experiment the blood samples were either stored at room temperature before using, or, if measurements at higher temperatures were planned, at 36 °- 37 °C. Usually the blood was used within one hour after collection. Routine Hematology characterization was made on all blood samples immediately after collection using the Baker 9000 Hematology Counter. Such characterization of the blood was also made at the end of each series of ESR determinations; thus, in general 30 complete sets of blood characteristics were determined after completion of exposure of the blood samples to the various temperatures in the Temperature Gradient Incubator (TGI). In previous years we have demonstrated that after exposure to the various temperatures the observed volume changes of both erythrocytes and platelets remain nearly exactly unchanged for at least two hours (and

frequently longer) after removal of the blood samples from the TGI. Thus the relatively slight delay between removing the tubes from the TGI and the time the 30 samples could be run on the Hematology Counter is not likely to introduce spurious variations.

As in previous years we have used Wintrobe tubes exclusively for the ESR determinations; the reason for the choice of the Wintrobe tubes is purely by convenience: Westergren tubes do not fit into the constrained geometry of the sample wells in the TGI. With practice, each Wintrobe tube could be filled with blood [using a Pasteur pipette] in about 20 - 30 sec, and the entire range of sample wells in the TGI filled in about 10 to 15 minutes. Readings of the sediment heights was subsequently performed at the same rate as the charging of the TGI bar and the entire experiment therefore constitutes essentially truly simultaneous measurements. With experience it is possible to read [or rather, to estimate] the sediment height to within (0.1 to) 0.2 mm insuring excellent precision (note the extremely small scatter in the ESR data shown in the Data Section of this Report).

The Temperature Gradient Incubator (TGI or "Polythermostat") has been described in previous Reports; a brief summary is given in the Appendix. The TGI provides 30 different, constant temperatures; the temperature constancy in any given run (over two - three hours) is within 0.1 °C in each well - and sometimes notably better. The temperature gradient was obtained from readings using five or six different thermometers in different wells along the bar, using the second set of wells for the controls. The temperature readings were used on the computer to provide a least square best fit over the entire bar, usually to a second degree polynomial and frequently with extremely good correlation coefficients ($R = 0.999+$). The difference in temperature between adjacent wells may readily be varied. In nearly all the runs described in this Report the temperature difference between samples has been 0.6 ° to 0.9 °C, thus providing excellent resolution in the temperature dependence of the different variables.

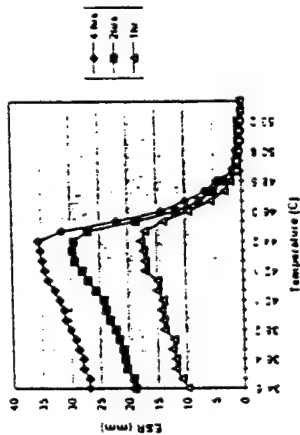
A number of sodium and potassium analyses were made on blood plasma after incubation of the whole blood for varying length of time. The ion analysis was made with a clinical ion-analyzer, based on ion-selective membranes. As most of the determinations were made on samples which were nearly identical except for their thermal history it is assumed that errors in absolute ion concentrations essentially cancel out. The samples were most often taken from the Wintrobe tubes after an ESR series of measurements. The Wintrobe tubes were spun down at _____ RPM for 10 minutes and the supernatant plasma removed with Pasteur pipettes and transferred to 1 ml sample vials for the measurement of the ion concentrations. In most all cases sodium, potassium and chloride ion concentrations were determined. Corrections were made to the sodium ion concentration to allow for the sodium added as anticoagulant (Na_4EDTA).

Dilutions: In some cases the whole blood was diluted using "Lactated Ringer's Solution", manufactured by Baxter; nominal (calculated) osmolarity: 273 mOsmol/liter, to which had been added 2.0 ml 0.25 Molar Na_4EDTA per 100 ml lactated Ringer.

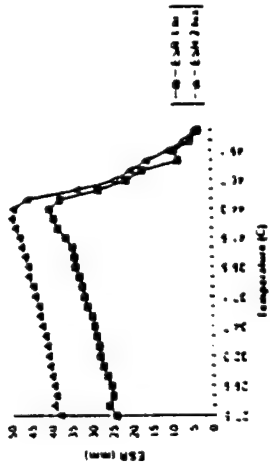
FIGURES 1-8

See Table at the end of this report for summary of time of incubation, type of experiment, donor code, age of donor and Hematocrit (Hct).

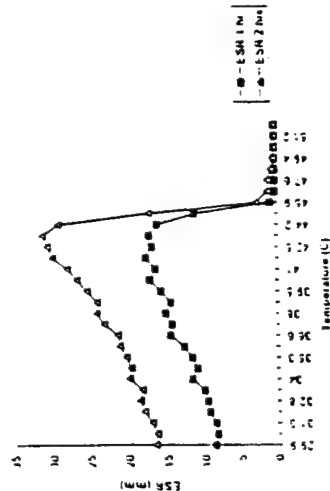
ESR vs. Temperature at Various Time Intervals



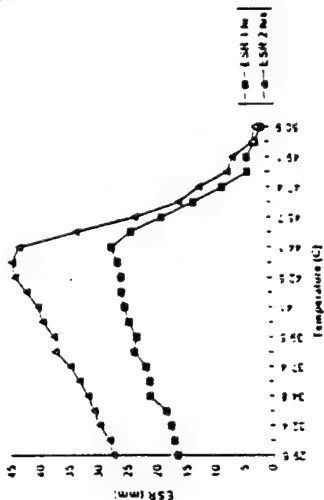
ESR vs. Temperature for Various Time Intervals



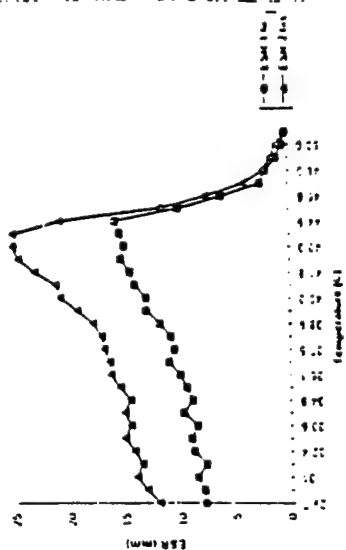
ESR vs. Temperature for Various Time Intervals



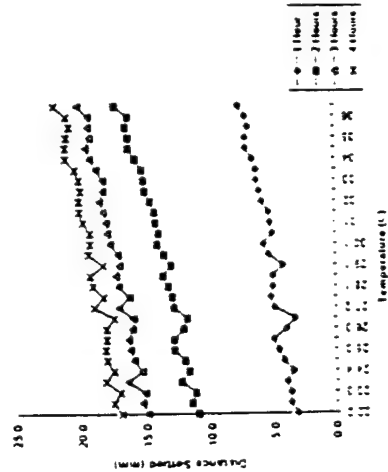
ESR vs. Temperature for Various Time Intervals



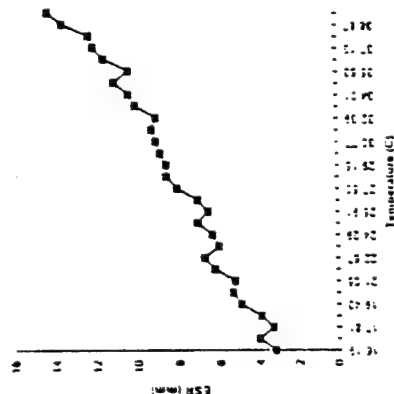
ESR vs. Temperature for Various Time Intervals



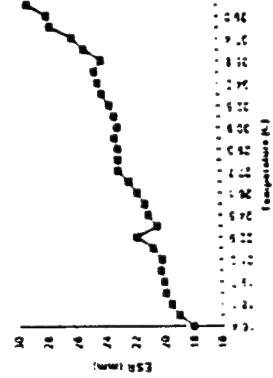
Distance Settled vs Temperature for Various Time Intervals



ESR vs. Temperature after 1 hr in TGI

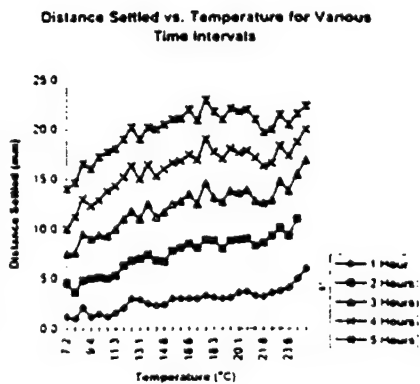


ESR vs. Temperature after 4 hours in TGI

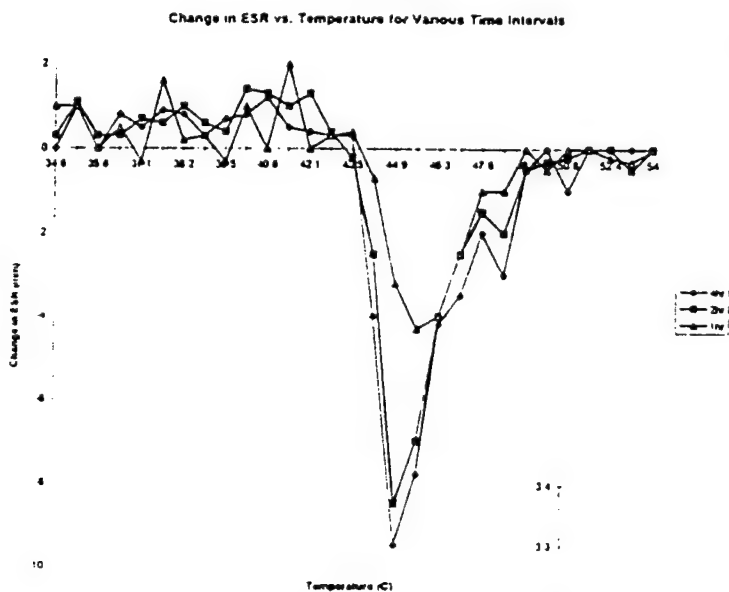


EXPERIMENTAL RESULTS [SELECTED, TYPICAL DATA]

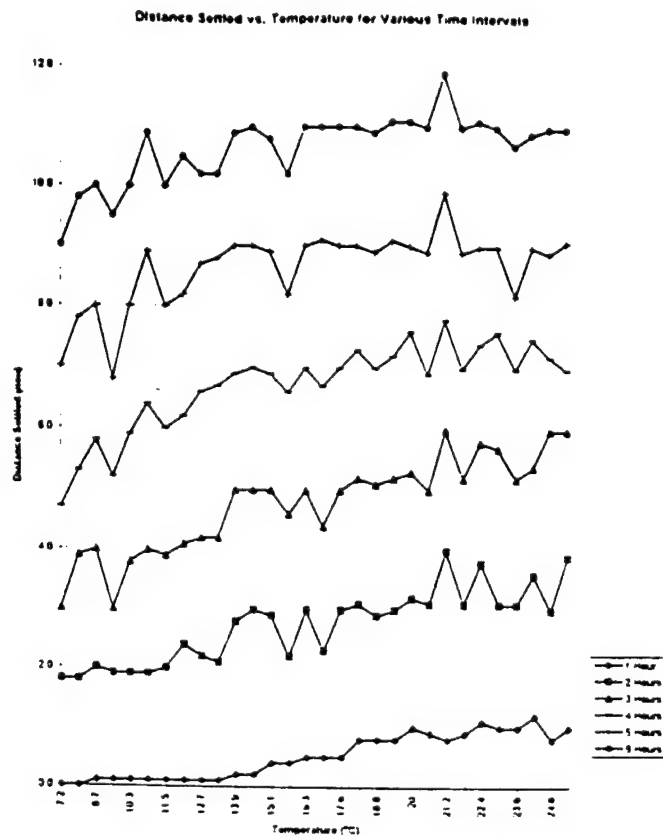
FIGURES 9 - 12



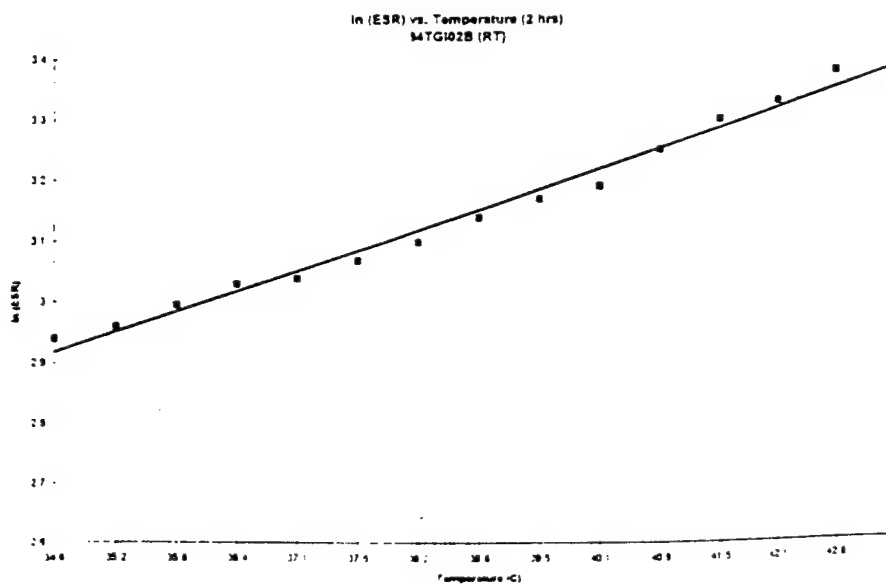
Change in ESR vs. Temperature for Various Time Intervals
94TG102B (RT)



Distance Settled vs. Temperature for Various Time Intervals
94TG119B (BD)

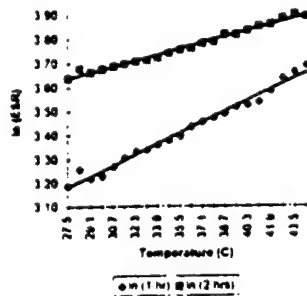


In (ESR) vs Temperature after Two Hours

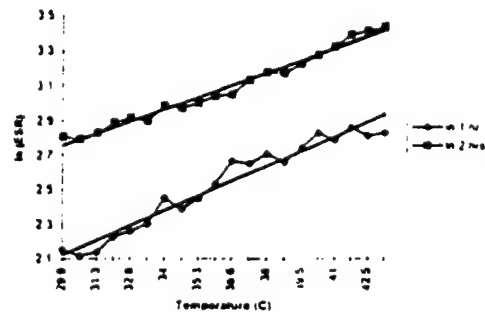


FIGURES 13 - 20

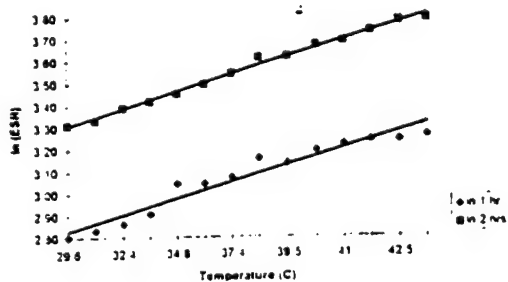
In (ESR) vs. Temperature for Various Time Intervals



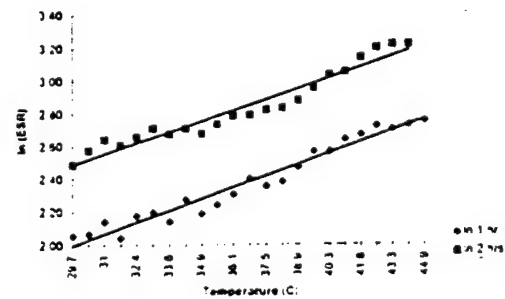
ln(ESR) vs. Temperature for Various Time Intervals



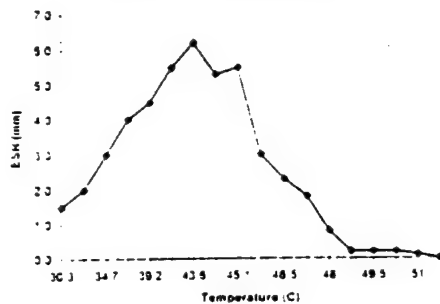
In (ESR) vs. Temperature for Various Time Intervals



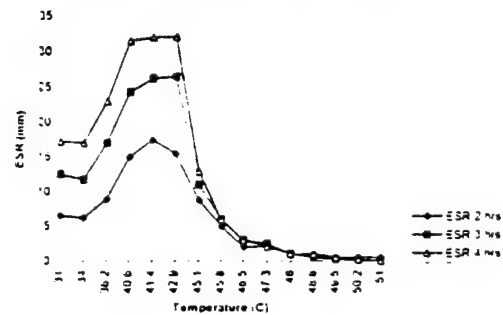
In (ESR) vs. Temperature for Various Time Intervals



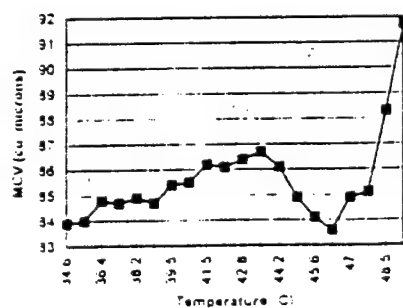
ESR vs. Temperature after 1 hour



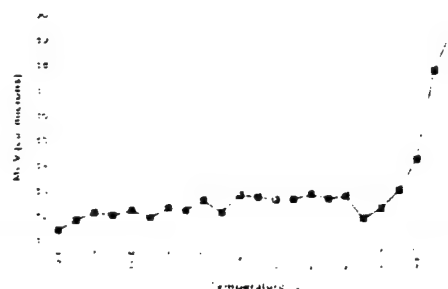
ESR vs. Temperature for Various Time Intervals



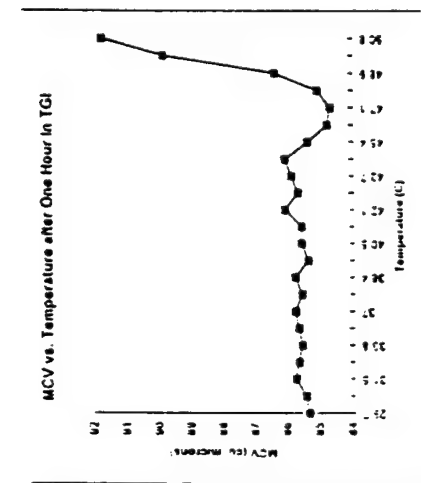
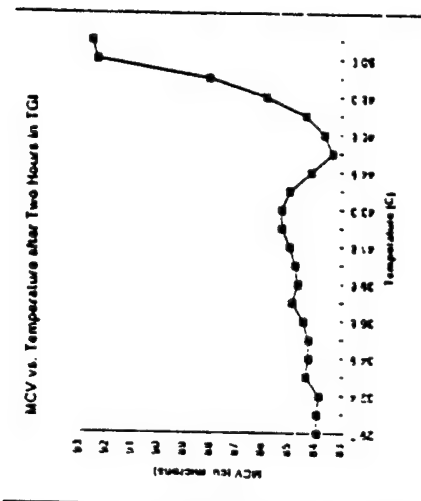
MCV vs. Temperature After Four Hours in TGI



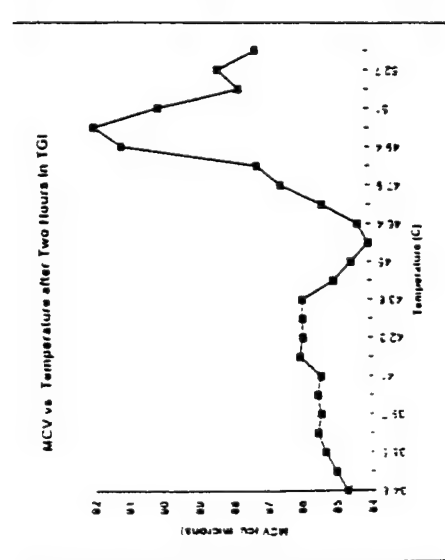
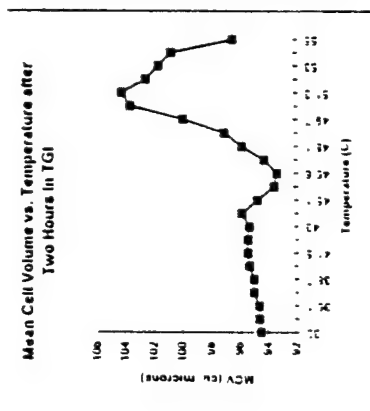
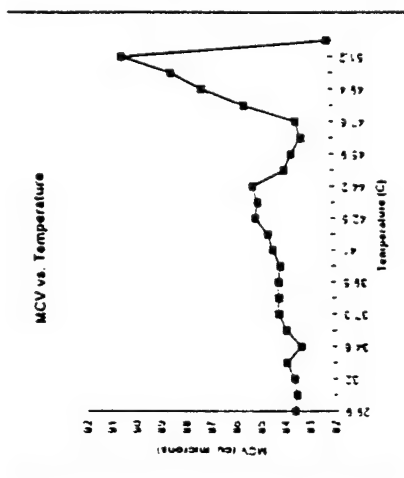
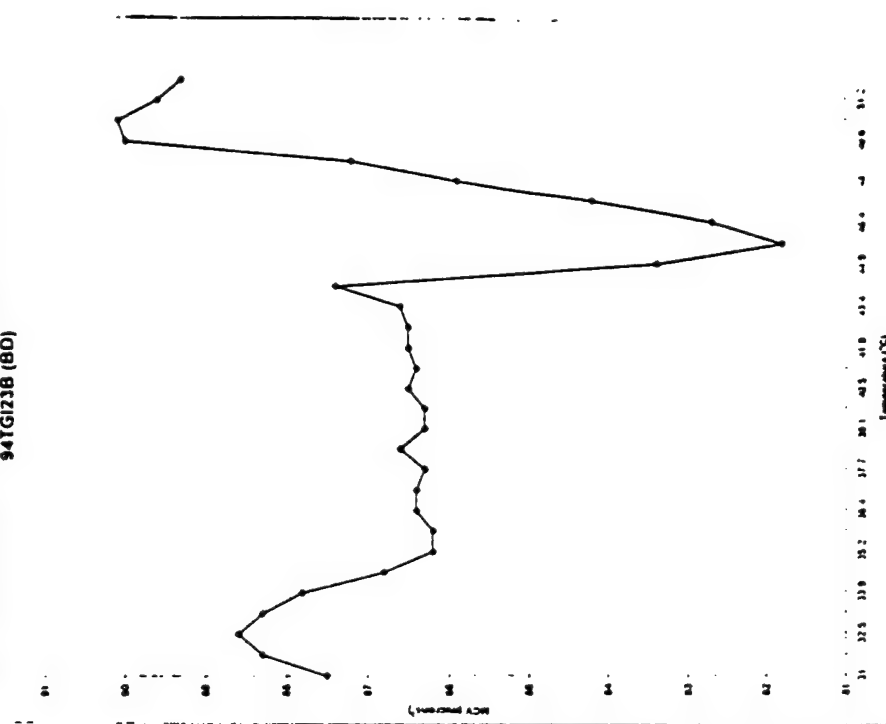
MCV vs. Temperature after Two Hours in TGI



FIGURES 21 - 26

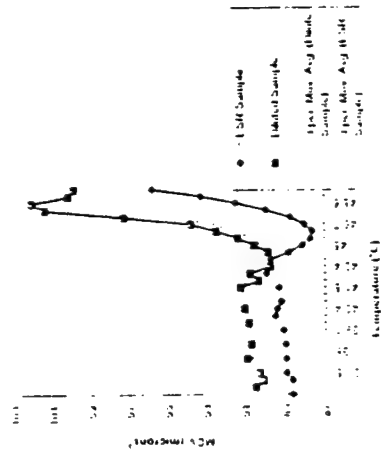


MCV of ESR Samples vs. Temperature after Three Hours in TGI
94TGI238 (BD)

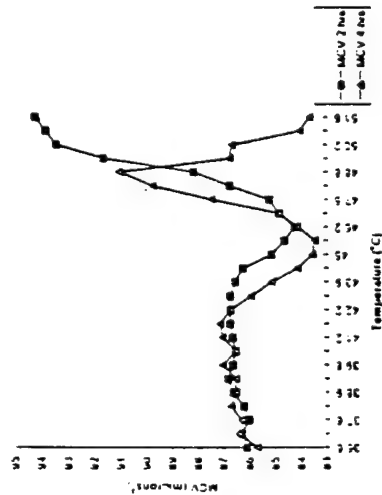


FIGURES 27 - 33

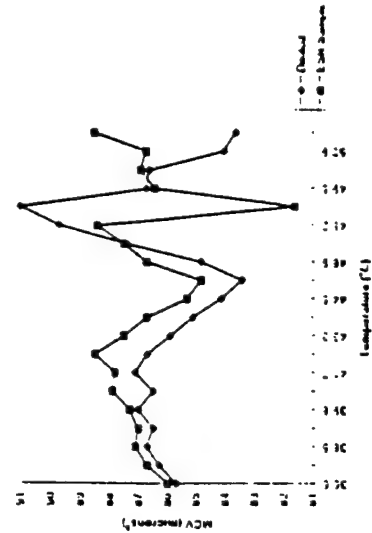
MCV vs. Temperature after 2 Hours in TGI



MCV vs. Temperature for Various Time Intervals



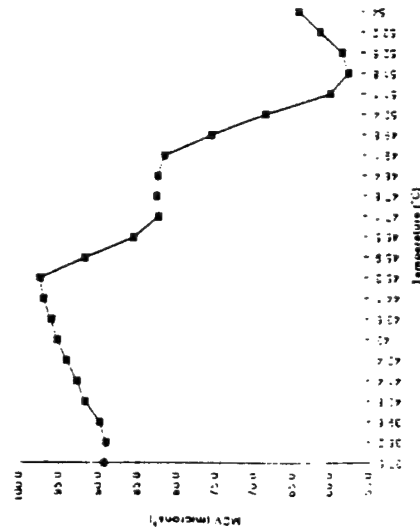
MCV vs. Temperature after Four Hours in TGI



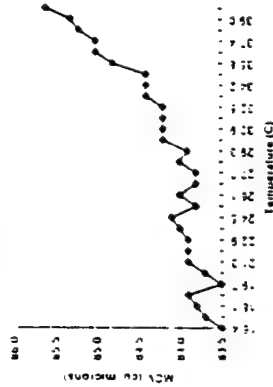
MCV of ESR Samples vs. Temperature after Six Hours in TGI
94TGI22B (RP)

MCV of ESR Samples vs. Temperature after Six Hours in TGI

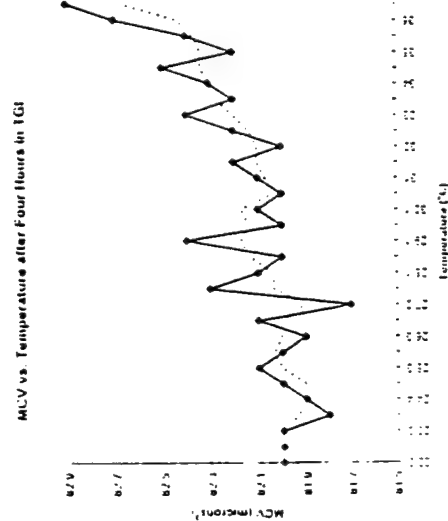
MCV vs. Temperature after 22 Hours in TGI



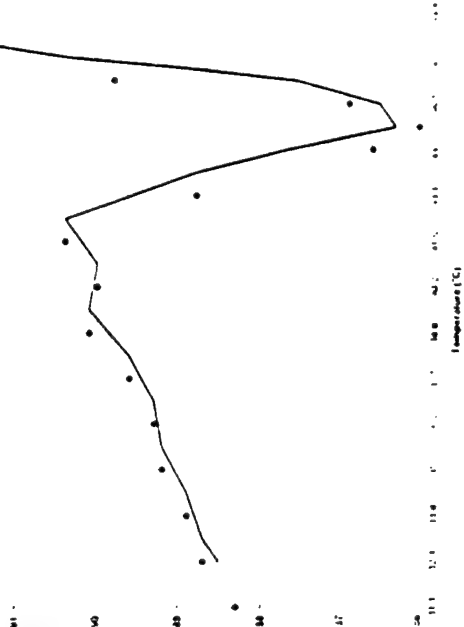
MCV vs. Temperature after 4 Hours in TGI



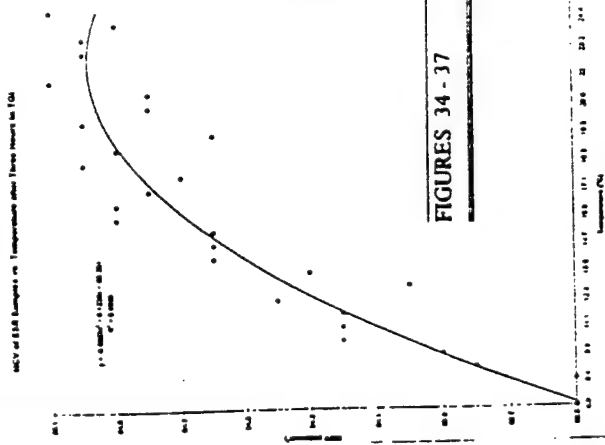
MCV vs. Temperature after Four Hours in TGI



MCV vs. Temperature after Four Hours in TGI

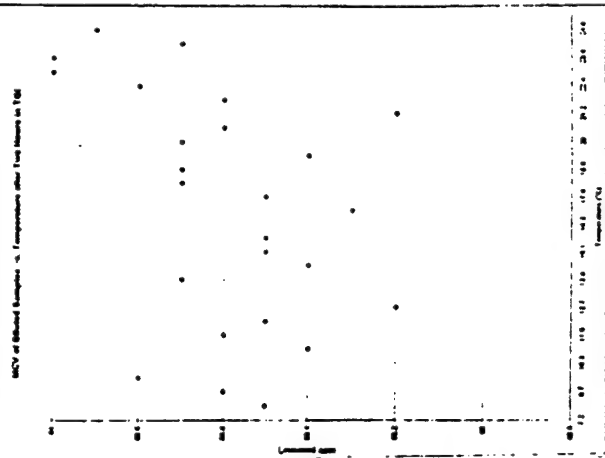


MCV of ESR Samples vs. Temperature after Three Hours in TGI
94TGI08 (RT)

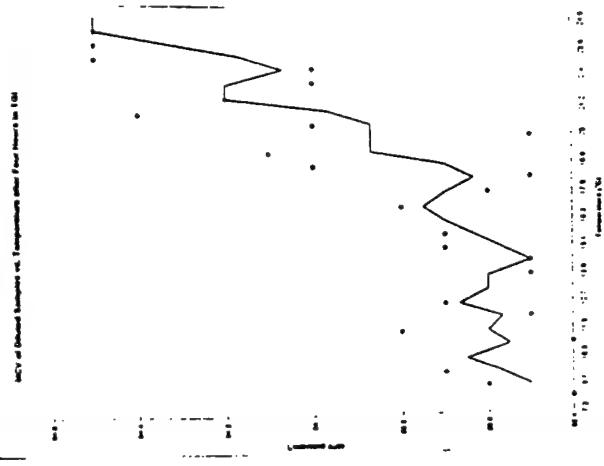


FIGURES 34 - 37

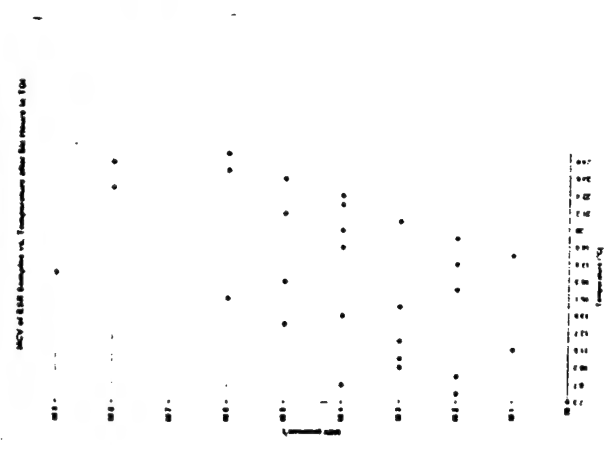
MCV of Diluted Samples vs. Temperature after Two Hours in TGI
94TGI08 (BD)



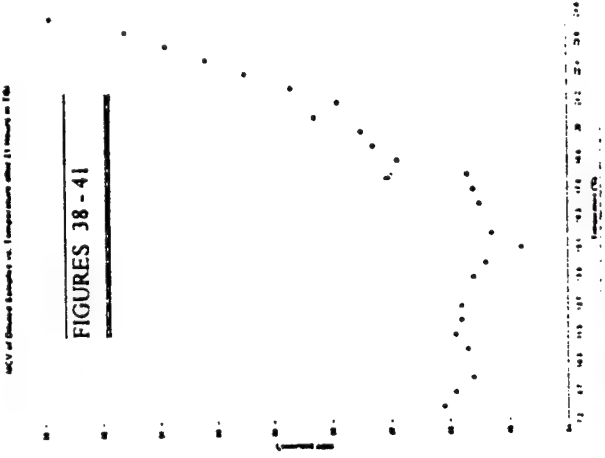
MCV of Diluted Samples vs. Temperature after Four Hours in TGI
94TGI08 (BD)



MCV of ESR Samples vs. Temperature after Six Hours in TGI
94TGI08 (BD)

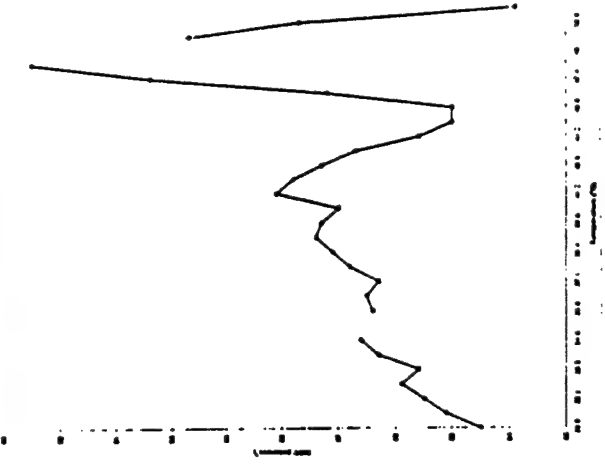


MCV of Diluted Samples vs. Temperature after 21 Hours in TGI
94TGI08 (BD)

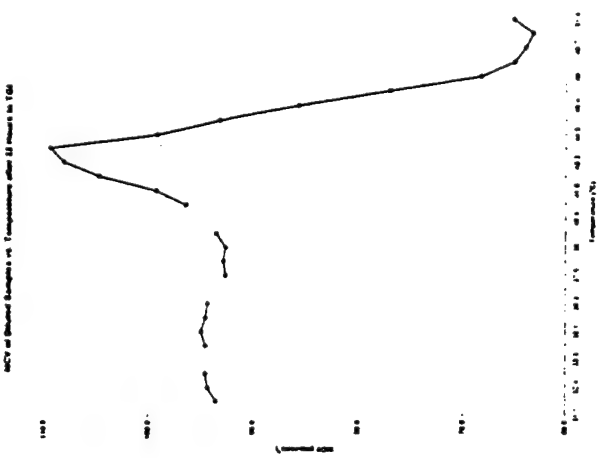


FIGURES 38 - 41

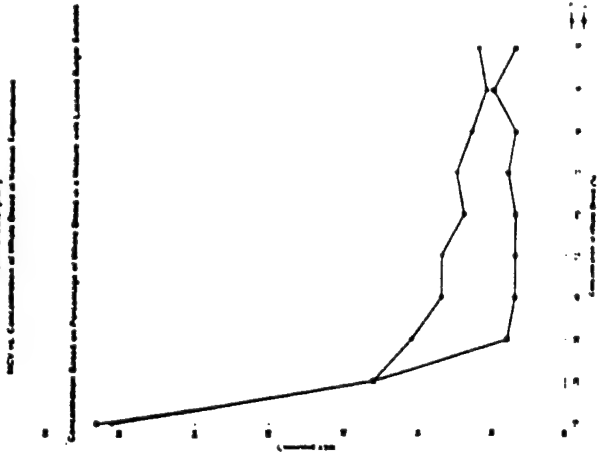
MCV of ESR Samples vs. Temperature after Five Hours in TGI
94TGI08 (DB)



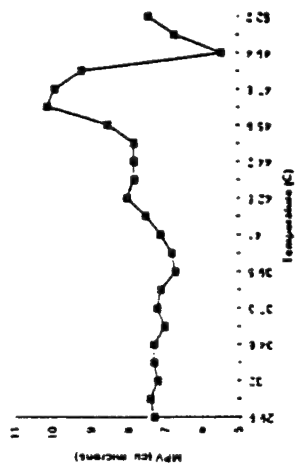
MCV of Diluted Samples vs. Temperature after 22 Hours in TGI
94TGI08 (DB)



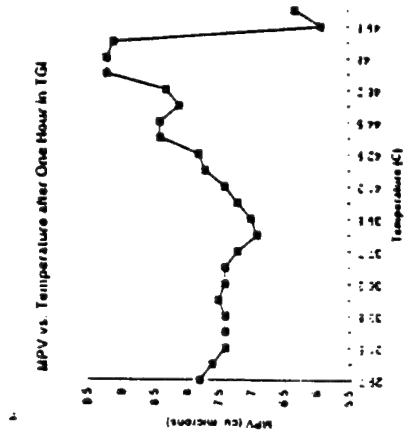
MCV vs. Concentration of Whole Blood after Three Hours Incubation at Various Temperatures
94TGI08 (BP)



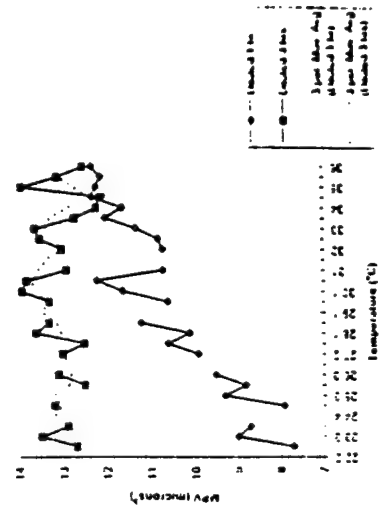
MPV vs. Temperature



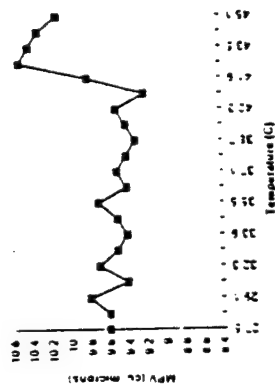
MPV vs. Temperature after One Hour in TGI



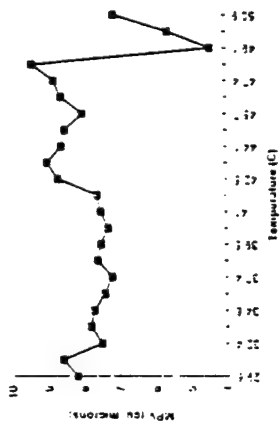
MPV of Diluted Samples vs. Temperature for Various Time Intervals



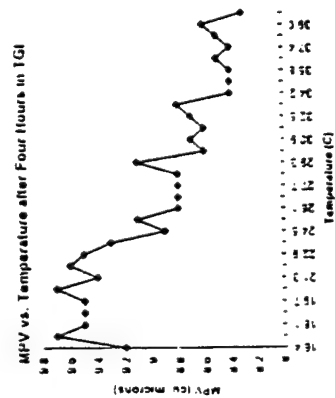
MPV vs. Temperature after Two hours in TGI



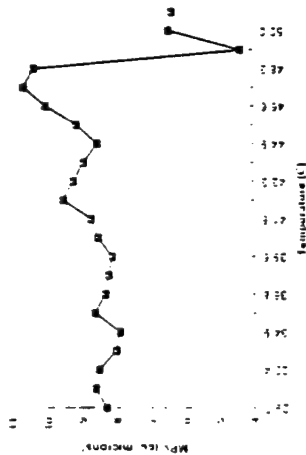
MPV vs. Temperature after Two hours in TGI



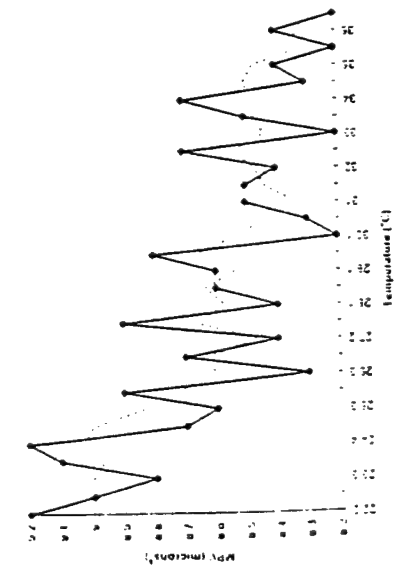
MPV vs. Temperature after Four hours in TGI



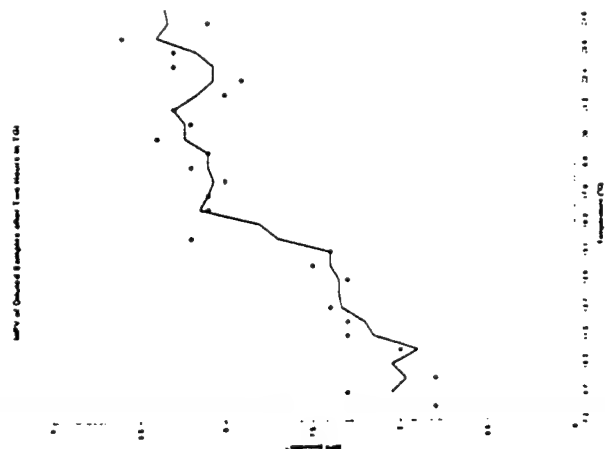
MPV vs. Temperature



MPV vs. Temperature after Four hours in TGI

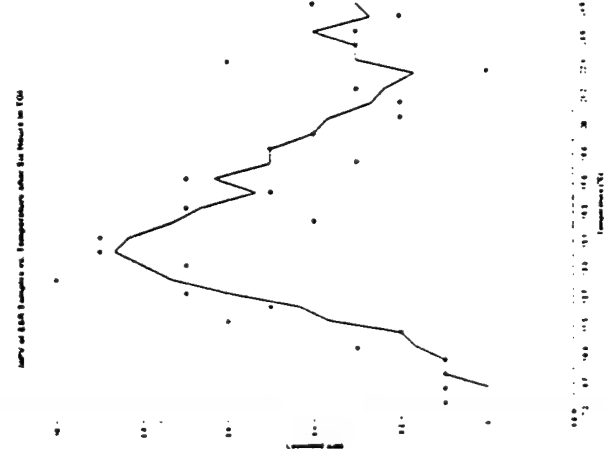


MPV of Diluted Samples vs. Temperature after Two Hours in TGI
S4(G119B) (BD)

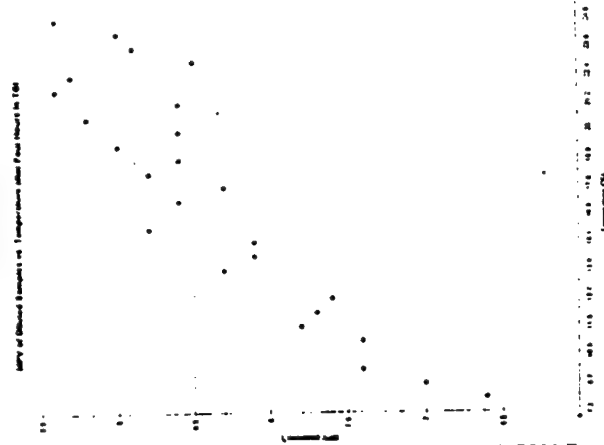


Samples Diluted with Lactated Ringer Solution
Time Point Showing Average Included

MPV of ESR Samples vs. Temperature after Six Hours in TGI
S4(G119B) (BD)



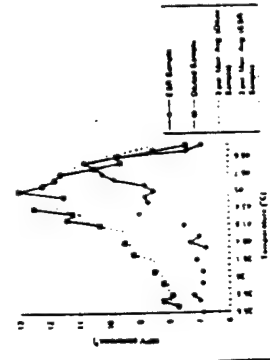
MPV of Diluted Samples vs. Temperature after Four Hours in TGI
S4(G119B) (BD)



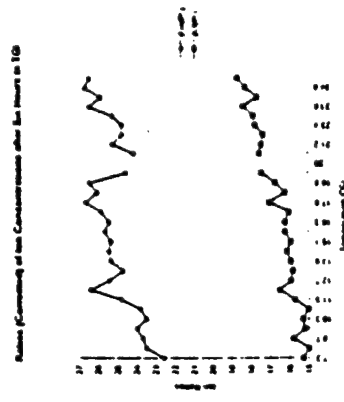
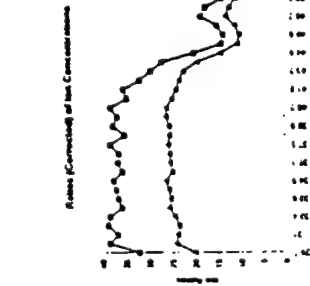
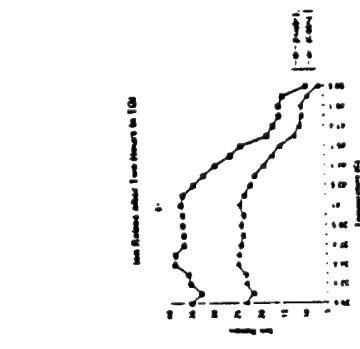
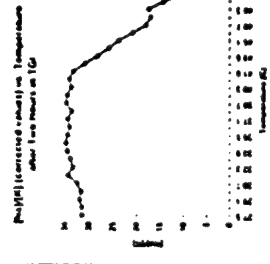
Samples Diluted with Lactated Ringer Solution

FIGURES 50 - 53

MPV vs. Temperature after 2 Hours in TGI



FIGURES 54 - 60



DATA ANALYSIS

ERYTHROCYTE SEDIMENTATION RATE DATA

Figs. 1 - 5 show typical ESR curves as function of temperature (for various settling times) from approx. 30 to 54 °C. The curve-shape is characteristic: a general increase from approx. 30 °C to about 43 (to 44) °C, followed by a pronounced, sometimes dramatic, drop (to effectively zero settling velocity) at higher temperatures. The scatter in the curves is usually remarkably small; frequently deviations from a smooth curve being less than 0.2 - 0.3 mm (see for instance Fig. 2) while in other cases the scatter may occasionally be somewhat larger, say ± 1 mm (Figs. 3, 5). Between approx. 30 and 43 °C, the increase in the ESR is essentially exponential as illustrated in Figs. 12 - 16. The linearity of the log-plots is often very good (Fig. 12) but (weak) systematic variations may occur (compare for instance the data for two hours of settling as shown in Fig. 12 and in Fig. 16 - note that the blood samples came from different subjects). However, in general it appears fair to conclude that good linearity is observed. Over the temperature range investigated, the temperature in °C and the reciprocal of the absolute temperature (in Kelvin) are very roughly proportional (see the Appendix for a justification of this). In view of this, plots of $\log[\text{ESR}]$ (or $\ln[\text{ESR}]$) vs. temperature (in °C) are essentially Arrhenius graphs ["poor man's Arrhenius Graphs"]. Thus, a single straight line in such a graph suggests that only one rate-controlling process is involved and the slope of the line is essentially proportional to the apparent energy of activation (ΔE_a) for the rate-controlling process. In general we find ΔE_a to be rather small, say of the order of 4 to 5 kcal/mole, suggesting that the rate controlling step may be a diffusion process or a viscous flow mechanism, for instance depending on the viscosity of whole blood or of the plasma. As the settling progresses, the slopes of the $\log[\text{ESR}]$ -vs-temp. curves tend to become smaller (and of course ultimately close to zero in those experiments where a final sedimentation height has almost been reached). We return to the question of the slopes of the settling graphs and their possible diagnostic value in the Discussion Section.

The abruptness of the change near the critical maximum temperature is particularly easily seen in Fig. 11 in which the ESR curve has been numerically differentiated. Note in this graph the abrupt drop for temperatures above 43.5 °C and the sharp minimum observed after two or more hours of sedimentation, centered near 44.9 °C - i.e. quite precisely the 45 °C for the third Drost-Hansen Thermal Transition Temperature. (T_k).

A number of measurements have been carried out also at lower temperatures. Such measurements were made because ESR measurements in the Clinical Laboratory are usually made at Room Temperature, i.e., generally 22 ° to 25 °C. In other series of measurements we have also determined the ESR over temperature ranges including 15 ° and 30 °C as these temperatures represent two other Thermal Transition Temperatures (T_1 and T_2 , respectively) for vicinal water.

In Fig. 6 the settling was followed for 4 hours but no evidence is found for an anomaly near 30 °C. Likewise, neither Figs. 7 nor 8 offer any evidence of a transition near T_2 ; on the other hand, in previous ESR measurement at CID in 1989 and 1991 anomalies were indeed seen near 30 °C. We have no immediate explanation for this variability.

Professor Glaser and co-workers in Berlin have published convincing data to show anomalies in the ESR (of *resuspended* RBCs) near 21 - 23°C. Only occasionally have we observed indications of such an anomaly in the ESR but from time to time we have seen a suggestion of an anomaly at this temperature range in *other* properties of the blood. In all probability the 22 ° anomaly is unrelated to the vicinal water structure; instead it most likely reflects a phase transtion in a cell membrane lipid. Note that the two curves in Fig. 7 and 8 do not appear to increase in similar manners with temperature and may indeed not be well represented by an exponential curve.

A few measurements have also been made at lower temperatures. Thus Figs. 9 and 10 show the erythrocyte settling over a range of temperatures from 7 to 24 °C. At these low temperatures the rate of settling is notably less than at the higher temperatures as would be expected if the viscosity of whole blood (or the blood plasma) exerts a rate controlling role. Similarly, the rates of other processes influencing the settling rate will also be affected, for instance the rate of rouleaux formation is likely also decreased at the lower temperatures. Because of the lower rates of settling, measurements were possible over longer time intervals; as an example settling data were obtained over a six hour period in experiment 94TGI19B. Unfortunately the scatter seen in both Figs. 9 and 10 makes it impossible to determine if an anomaly (due to vicinal water) exists near 15 °C (due to the vicinal water) or near 21 - 23 °C (due to a membrane lipid transition) as suggested by Glaser's data.

CELL VOLUME DATA

A large number of Cell Volume Data have been collected, both on RBCs as well as on Platelets, over a wide range of temperatures and in some instances after dilution of the samples with lactated Ringer solution and incubating at various temperatures over different time intervals. [All cell volumes expressed in cubic microns: $(\mu\text{m})^3 = 10^{-12}$ ml = a femtoliter (fl); 10^{-15} liter].

MEAN ERYTHROCYTE VOLUMES (MCV).

A) Figures 19 through 26 show MCV data obtained on erythrocytes from whole blood after incubation at various temperatures for different lengths of time. Overall the data resemble quite precisely the volume data we have collected in previous years. The typical variation in the MCV as a function of temperature is a relatively small, gradual increase over the range ca. 30 °C to about 43 ° to 44°C; the increase is usually 1 to 2 % (with one exception; see Fig. 26); note the rather small variations from a smooth curve, suggesting excellent reproducibility of the volumes as determined with the Baker Model 9000 Hematology Counter. Characteristically, the gradual increase up to nearly 44 °C is

followed by a distinct and sometimes dramatic drop over the range of temperature from about 44 ° to about 46.5 (+/- 0.5) °C. The minimum at this temperature is frequently very sharp, followed by a large, abrupt increase in the MCV up to about 51 °- 52 °C. Above this temperature range the MCV again drops and again the change may be quite dramatic (!) - see for instance Figs. 24 and 25. Note that in all cases observed (in this study as well as in those data collected in previous years on both human blood and blood from about a dozen different mammals) the MCV values near the relative maximum around 51.5 °C are much larger than the values below the 45 °C anomaly.

B) Measurements of MCV has been made also on RBCs from whole blood diluted with lactated Ringer solution; unless otherwise stated, the dilution is 5:1, -- Ringer:blood. [Undiluted samples are referred to as "ESR Samples" as these are the samples used for the ESR measurements].

In Fig. 27 is shown the MCV for whole, undiluted blood after 2 hours incubation in the TGI compared to the MCV of diluted samples after the same length in the TGI. The two curves are relatively similar but distinct differences do exist: a) over the whole range of temperatures the MCVs of the diluted samples are larger than for the undiluted samples. The difference in volumes below the thermal transition region [approximately around 42 ° (to 45 °)C] is 2%. This suggests that the lactated Ringer solution is not truly isotonic with the plasma in the whole blood. b) The variations with temperature of the RBC in the whole blood are typical of the general response of the MCV to temperature as discussed for Figs. 19 - 26. However, the drop in MCV at higher temperature for the diluted samples begins already at about 42 °C which is distinctly below the range generally observed, 44 ° - 45 °C; at this time we have no explanation for this behavior. c) The minimum in the MCV - vs - temp. curve for the diluted samples is centered around 44 °C, or ca. 2.5 ° below the value for the whole blood. d) the rise from the minimum to the maximum value of the MCV curve for the diluted samples is as steep as observed for the whole blood (the curves are essentially parallel), suggesting that the same mechanism may be responsible for the swelling in both the whole blood and the diluted samples (-hardly a surprising finding). e) The MCV curve for the diluted samples decreases sharply above the maximum temperature (although in the present example only two data points were obtained below the maximum). The presence of a sharp maximum is qualitatively identical to the behavior seen in whole blood but again the temperature of the maximum appears to be ca. 3 °C less than for the whole blood.

With increasing length of incubation at elevated temperatures, the volume curves for the diluted samples seem in general to be "down-shifted" as illustrated in Fig. 28. For the curve for 4 hours of incubation the minimum now occurs at about 45.5 °C. However, the differences between the volumes of the cells in whole blood and in the diluted samples are not always great as illustrated in Fig. 29. (Note in this Figure that the total changes in the observed MCV above and below the thermal transition temperature around 45 °C are not large).

Finally note in FIG. 30 the distinctly different behavior of the MCV upon long term exposure to elevated temperatures; the initial MCV below 45 °C was about 89 (mm)³ while after 22 hours of incubation the MCV is about 90 - 95 (mm)³. Note also that the drop in MCV begins at about 45 °C but the minimum usually seen near 46.5 °C has been eliminated or, at best, reduced to an inflection point in the curve but followed by a distinct if relatively broad minimum near 52 °C.

A number of other runs have been made at lower temperatures. FIG. 34 shows the variation of MCV as a function of temperature from approx. 7 °C to 25 °C, [with a parabola fitted to the data]. There is no indication in this case of an anomaly near 15 °C, but note that the total variation in MCV over this 18 ° interval is only 1.5 % (after 2 hours of incubation).

As would be expected, the rate of change in the RBC volumes is low at the lower temperature range. FIGS. 35 through 38 shows the change in MCV, measured on a sample of blood diluted with lactated Ringer solution, over an interval of 21 hours. While no obvious trends exist in the data in FIG. 35, measured after 2 hours of incubation, a distinct effect of temperature is seen in FIG. 38 after 21 hours of incubation: below 15 °C the MCV is nearly constant (dropping about 1 % between 7 ° and 15 °C) but increasing notably above this critical temperature ($T_{k=1}$). [The increase is 8 % over an 8 ° interval, or a temperature coefficient of 1% per degree!]

Another example of the effects of long term incubation on MCV of red cells in diluted samples of blood is shown in FIGS 39 and 40: In FIG. 39, after 5 hours of incubation, a distinct maximum is seen in the MCV near 41 °C, followed by a relatively sharp minimum near 45 °C and a subsequent very dramatic increase [9 % over a 3 ° interval !] followed by an equally decisive drop. On the other hand, after 22 hours of incubation, the overall features of the MCV curve have changed: the difference between the maximum observed value and the minimum observed value is nearly 50 % ! Below 40 °C the effect of temperature on the MCV is minimal but above ca. 40 ° and up to 44 °C, the MCV increases only to drop very dramatically above this temperature.

Finally, in FIG 41 is shown the effects of dilution with lactated Ringer solution on the MCV, at two different temperatures: 25 ° and 37 °C. The abscissa is the percentage of whole blood in the final solution while the ordinate is the MCV (measured after three hours of incubation). Note the pronounced increase in MCV for blood concentrations less than ca. 20 % for both isotherms and the remarkable temperature independence of the MCV, measured at 37 °C, from 30 to 100 % blood. In other words: over the physiologically important range, extending the blood plasma with lactated Ringer solution at body temperature does not cause any change in the MCV.

MEAN PLATELET VOLUMES (MPV)

Platelet volumes are as sensitive to temperature variations as RBC volumes, especially near the 45 °C anomaly of the cell-associated vicinal water, and vary strongly with temperature below the 30 °C anomaly.

A) In general, the MPV is relatively constant over the temperature interval from ca. 30 °C up to a range of transition temperatures extending from about 42 ° to about 48 °C (see FIGS. 42 through 46) but distinct variations occur even over this relatively narrow [12 °] temperature interval and large differences between otherwise similar runs are seen in the transition range from ca. 42 ° to 48 °C. As will become evident from some of the following illustrations, part of the large variability may be due to changes with time.

The main variation in MPV appears to be an increase starting around 45 °C followed by an abrupt drop near 47 ° - 48 °C, leading to a sharp minimum and an equally abrupt increase at higher temperatures [see particularly FIGS. 43, 44 and 45]. A slight modification on this behavior is seen in FIG. 42, where the initial rise before the abrupt drop occurs at about 41 °C; the data in FIG. 46 suggests that a minimum exists near 38 °C but this may be the result of insufficient time for equilibration as these data were obtained after only 1 hour of incubation. Note that the abrupt drop seen in the previous FIGURES are also seen here, starting at 49 °C.

B) Measurements of MPV have also been made at lower temperatures as well as on samples of blood diluted with lactated Ringer solution. FIG. 47 shows the MPV after four hours of incubation in the range of temperatures from ca. 22 ° to 37 °C. The net effect is a 10 % drop in the MPV over this temperature interval (with possibly a levelling-off for temperatures above 30 °C [?]). See also FIG. 48 which shows essentially the same behavior. (In both Figures note the scale: it would be possible to draw a smooth, single curve through the majority of data points with all deviations being less than $\pm 5\%$. In view of the nature of the quantity measured this is certainly not an unreasonable degree of scatter).

The variation in MPV in blood diluted with lactated Ringer solution is rather surprising. While such dilution (at 37 °C) did not seem to alter drastically the MCV, the effect on the platelets is quite surprising. In FIG. 49 one observes a dramatic *increase* in MPV after 1 hour of incubation on going from 22 ° to 37 °C whereas the MPV values in whole blood dropped approx. 10 % over the same temperature interval (compare FIG. 47).

On the other hand, after 3 hours of incubation, the MPV appears to be essentially temperature independent over the temperature interval studied - but at notably larger volumes! In fact, the swelling of the platelets over a 2 hour interval at 22 °C is more than 50 % ! This surely suggests that the lactated Ringer solution is not isotonic with the platelets at low temperatures and that the approach of the platelets to an "equilibrium"

volume is fairly slow. This is particularly surprising as the erythrocytes appear to change rather little upon dilution with the Ringer solution at room temperature (confer FIG. 41). Another example of changes with time in the MPV at even lower temperatures is shown in FIGS 50, 51 and 52. The temperature range (from ca. 7 ° to 25 °C) was chosen such as to place the vicinal water transition temperatures ($T_{k=1}$) of 15 °C near the midpoint of the observed range. After two hours of incubation (FIG. 50) a small but significant increase occurs between 7 ° and ca. 16 °C while the rate of increase is distinctly less at the higher temperatures. After 4 hours of incubation (FIG. 51) the MPV values have, on the average, increased a little less than 10 %, and no evidence is seen of the possible thermal anomaly near 15 °C. However, after an additional two hours of incubation, the MPV values have not only increased dramatically (by about 25 to 35 %) but a distinct maximum is now seen at 15 °C.

C) Finally, a few experiments have been made in the high temperature range on diluted samples as a function of time. FIG. 53 shows the MPV after 2 hours of incubation of whole blood ("ESR Samples") and blood diluted with lactated Ringer solution. Below the thermal transition temperature range (44 ° - 46 °C) the platelet volumes in the diluted samples are decidedly larger than the volumes in the whole blood (by about 10 to 20 %) but above this critical temperature range the volumes appear to be comparable.

Na/K RATIOS IN WHOLE BLOOD PLASMA

At normal body temperature, the ion ratio, R , defined as $[Na^+]/[K^+]$ in the plasma of whole blood, is approx. 35 (within 95% confidence level: 28 to 40. See Cogan, 1991). Any notable deviations from this range of values suggest the existence of some active ionic unbalance, generally requiring decisive clinical intervention. R is obviously related to the RBC volume control mechanisms, notably the sodium membrane pump.

We have made a series of measurements of R in blood plasma after incubation of whole blood at various temperatures for different lengths of time. Invariable, R decreases above a very broad maximum centered around a temperature not too far from the normal body temperature of 37 °C. The decrease in R above ca. 40 °C is often very substantial and as one approaches the critical thermal transition temperature of 45 °C, R may have dropped to half of the value near 37 °C. In other words, in the range of elevated temperatures such as seen in severe febrile states, R may differ very significantly from the normal range. Surely this must have important clinical implications (for instance for patients with high fevers, heat strokes, severe burns, or in hyperthermia therapy) but it is somewhat surprising that over the same range of temperatures the MCV only tends to increase a relatively small amount (see FIGS. 19 - 24). Thus it appears that different molecular mechanisms may be involved although traditional wisdom would anticipate a close correlation between cell volumes and Na^+/K^+ ratios.

NOTE: All the blood samples used in the present study were collected in syringes to which Na_4EDTA had been added. The contribution of this sodium is taken account of in the calculations: hence the data are referred to as "Corrected".

A series of measurements of R have been made and some of the results obtained at high temperatures (ca. 27 ° through 51 °C) are shown in FIGS. 54 through 58. In these graphs are also shown, where available, the ratio of the chloride ion concentration to potassium concentration ($[Cl^-]/[K^+] = J$). In general the J-curve follows the R-curve very closely.

It is of interest to note that in many instances, the R- and the J- curves appear to level out near 45 ° to 46 °C (see FIGS. 55 and 56), while in some cases (FIGS. 57 and 58) a new, distinct, relative maximum occurs near 48 ° or 49 °C [the J-curves behaving in a similar manner]. It is instructive to compare this finding with the MCV data in the same temperature range: an abrupt decrease is seen in some of the MCV data, for temperatures near or above 50 ° - 51 °C; see FIGS. 23, 24, 25 and 26. On the other hand, no unusual features are seen in the ESR curves in this temperature range in agreement with expectations [the ESR essentially becomes zero above, 47 ° or 48 °C].

Finally, we have made a number of R measurements at lower temperatures. Some typical results are shown in FIGS. 59 and 60. It is seen in both of these graphs that R is less than at normal body temperature and increases from a value of about 22 to the "normal" value, 35 (- 40), over the range of temperature from 7 °C to normal body temperature. Unfortunately not enough data have been obtained to allow a decision to be made whether or not anomalies exist near 15 ° and 30 °C. (Note: the data in FIGS. 59 and 60 should perhaps not be compared directly because of the different lengths of incubation). Note again, however, that the J-curve essentially follows the R-curve.

APPENDIX

I) The standard Arrhenius graph is a plot of $\log (\text{Rate})$ [or $\ln (\text{Rate})$] as a function of reciprocal, absolute temperature ($1/T$, K^{-1}). However, from around 0° to about 30 ° or 40 ° C, the temperature in °C is roughly proportional to $1/T$. This is easily seen from the expansion of $1/T$ namely

$$1/T = 1/(273.2 + t) = 1/273.2[1 + t/273.2] = 1/273.2 - t/(273.2)^2$$

which is of the form $1/T = a - bt$. Thus, $1/T$ is roughly proportional to t . This approximation is of course dependent on $t < (or <<) 273.2$; as long as this approx. is approximately fulfilled, graphs of $\log (\text{Rate})$ vs temperature in °C will resemble Arrhenius graphs.

II) The Temperature Gradient Incubator (TGI or "polythermostat") has been briefly described in previous reports and a detailed description given in one of our papers (Drost-Hansen, 1981). The device consists of a massive aluminum bar with wells drilled along the bar to accommodate test tubes, culture tubes or other small samples (such as Wintrobe tubes). The bar is thermally insulated on all sides; one end is maintained at a constant high temperature while the other end is maintained at a constant low temperature. A temperature gradient is thus established along the bar; in the present version the bar provides two sets of 30 different wells, each at a different, constant temperature. Hence, almost precisely simultaneous measurements may be made at 30 different, constant temperatures. The total span of temperatures (and hence the difference in temperatures between subsequent wells) is easily adjusted. Temperature intervals of 0.6 ° to 0.9 °C between adjacent wells have been used throughout this study, providing great thermal resolution in the measured quantities.

ABBREVIATIONS: TEMPERATURE RANGES:

	H	HIGH; APPROX. 30 ° - 52 ° C
	M	MEDIUM 20 ° - 40 ° C
	L	LOW 7 ° - 23 ° C
ROOM TEMPERATURE	rt	24 ° - 26 ° C

DILUTIONS:

Unless otherwise stated: whole blood (W)

W	WHOLE BLOOD
D	DILUTED (usually 5:1).

CONCLUSIONS AND RECOMMENDATIONS

All the hematological parameters measured in this study (ESR, MCV, MPV and [Na]/[K] ratio) show anomalies at 45 °C, within one or two degrees, in complete agreement with our previous findings (1989, 1991, 1992). It seems an inescapable conclusion that this must be a manifestation of critical roles for the cell-associated, vicinal water in these systems. These findings are also consistent with a wealth of independent observations showing a critical role of vicinal water in nearly all aspects of cell physiology, ranging from determining multiple growth optima and minima for many micro-organisms to determining body temperatures of mammals and birds. In some cases, the effects of the thermal transitions begin to be manifested at temperatures as low as 42 ° to 43 °C and this may play an important role in a variety of processes in the hyperthermic state, for instance in patience with severe fevers or during hyperthermia therapy of malignancies.

That the thermal anomalies of vicinal water plays a crucial role in many biological systems is now beyond doubt; what remains far less well understood is the question of the "site of action" of such solvent structural transitions. We have recently proposed (Drost-Hansen and Singleton, 1995) that the effects of the structural transitions of the vicinal water may be in the hydration of the biomacromolecules present in the cellular systems. One such sensitive site may be the vicinal hydration structure of some protein, for instance partially imbedded in the cell-membrane, regulating ion transport across the membrane. If the transport mechanism depends on the extent of dimerization (or oligomerization) of such a protein, a sudden change in the vicinal hydration of that protein at T_k will surely affect the equilibrium constant for the dimerization equilibrium and may thus suddenly change the transmembrane transport of a crucial ion, for instance required in the regulation of the osmotic equilibria of the cell.

On the basis of this hypothesis for the criticality of the vicinal water control, it is possible to make some predictions which may be tested experimentally. Thus it would be of interest to study those cell processes for which it is known that dimerization (or oligomerization) of a protein or enzyme is required for the process to take place. The prediction is that for such processes the rate might change dramatically at least near one of the thermal transition temperatures, T_k . Because of the number and sizes of the subunits in, for instance, the ATPases these are likely candidates for distinct thermal anomalies in their rates as ion-translocators. In fact, because of the frequent involvement of associated proteins in the cell-membrane *all* cell transport processes may be influenced by the vicinal hydration of the protein subunits involved.

Another possibility is the tissue deterioration caused by various venoms: we particularly propose to study the rates of proteolysis caused by the venom from the brown recluse spider (*Loxosceles reclusa*) as a function of temperature near 45 °C. Our prediction is that near this critical temperature the venom activity may be lessened considerably - or indeed completely eliminated - while the surrounding tissue may be able to withstand the required hyperthermia stress without irreversible damage (or with minimal deleterious effect).

ACKNOWLEDGEMENTS

The authors wish to thank the US Air Force, Office of Scientific Research, and the Clinical Investigation Directorate of Wilford Hall Medical Center for making this research possible and our sincerest thanks go as well to those at CID who so cheerfully and competently helped make this work much easier. Special thanks go to Dr. J. H. Cissik, (Col., USAF, ret.), Lt.Col. John Cody, Ph.D. and the Director, Col. E. S. Oertli, Ph.D., DVM, for their interest in this work and their continued encouragement. We also wish to thank those who so graciously volunteered to donate blood for this study. The efforts by RDL to facilitate the mechanics of this research opportunity is also appreciated.